TECHNISCHE
UNIVERSITÄT
DARMSTADT

# Organic Hole Transport Materials: Properties and Interface Formation

**Zur Erlangung des akademischen Grades Doktor-Ingenieur (Dr.-Ing.)**
**genehmigte Dissertation vorgelegt von Markus B. Frericks**
**geboren in Frankfurt am Main** **2022 – Darmstadt**

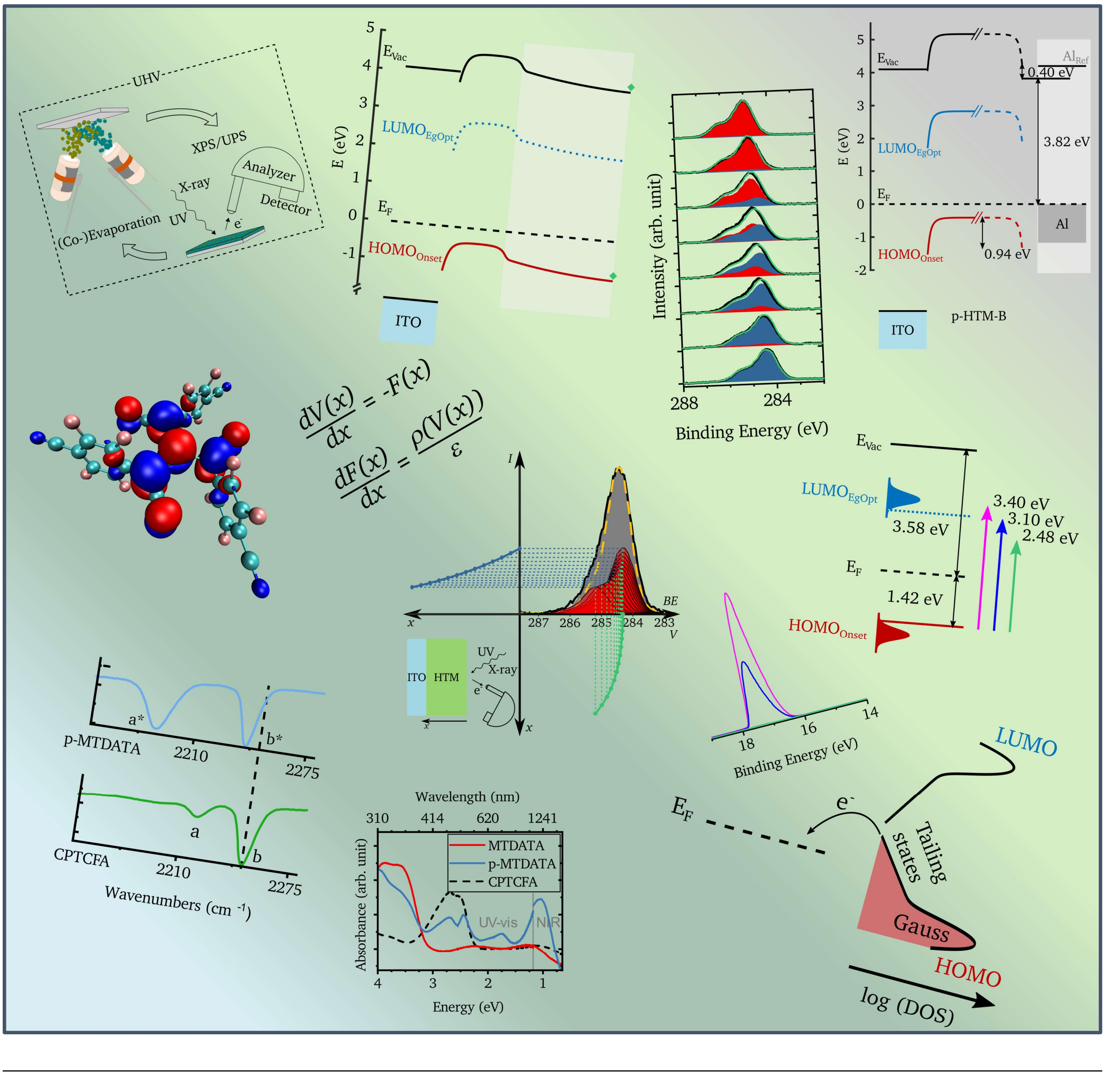

**On the cover:** The gradient background is an abstract representation of the layered sample structure from the indium tin oxide substrate in blue over the dark and light green doped and undoped hole transport materials, to the grey Al back-contact. The foreground is a scattered summary of important figures from the thesis.

Titel: Organic Hole Transport Materials: Properties and Interface Formation

Zur Erlangung des akademischen Grades Doktor-Ingenieur (Dr.-Ing.)
genehmigte Dissertation vorgelegt von Markus Benjamin Frericks M. Sc.
geboren in Frankfurt am Main

Fachgebiet: Oberflächenforschung
Fachbereich: Material- und Geowissenschaften
Technische Universität Darmstadt

Berichter: Prof. Dr. Wolfram Jaegermann
Technische Universität Darmstadt

Mitberichter: Prof. Dr. Wolfgang Ensinger
Technische Universität Darmstadt

1. Prüfer: Prof. Dr. Uli Lemmer
Karlsruher Institut für Technologie

2. Prüfer: Prof. Dr. Ralph Krupke
Technische Universität Darmstadt

Tag der Einreichung: 27.06.2022
Tag der Prüfung: 15.09.2022
Jahr der Veröffentlichung: 2022

Darmstadt 2022
D17

Please cite this document as:
URN: urn:nbn:de:tuda-tuprints-223973
URL: https://tuprints.ulb.tu-darmstadt.de/id/eprint/22397

## Erklärung zur Dissertation

Hiermit versichere ich, dass die elektronische Version mit der schriftlichen Version übereinstimmt. Ich versichere, dass zu einem vorherigen Zeitpunkt noch keine Promotion versucht wurde. Ich versichere, die vorliegende Dissertation, abgesehen von den in ihr ausdrücklich genannten Hilfen, nur mit den angegebenen Quellen und Hilfsmitteln selbstständig verfasst zu haben. Alle Stellen, die aus Quellen entnommen wurden, sind als solche kenntlich gemacht. Diese Arbeit hat in gleicher oder ähnlicher Form noch keinen Prüfungszwecken gedient.

Darmstadt,

(Markus B. Frericks)

# Abstract

This dissertation is related to organic semiconductor (OSC) materials for organic light emitting diode (OLED) applications investigated together with our project partner Merck KGaA. One often stated advantage of OSCs is the chemical flexibility to easily synthesize new molecules. A deeper understanding of the connection between molecular structure and device characteristics could lead to faster material screening and development. As contribution to this goal, the here presented work analyzes and discusses the properties of hole transport materials (HTMs) and especially their electronic interface properties.

Indium tin oxide (ITO) substrates, a commercially available p-dopant, CPTCFA, a literature-known HTM, m-MTDATA, a commercial HTM from Merck KGaA, HTM-B, and aluminum are characterized as thin films by photoelectron spectroscopy (PES) to obtain the materials' electronic properties. Ultraviolet, visible, near- and mid-infrared absorption spectroscopy on pure and p-doped HTM thin films correlated with density functional theory calculations provides insight into the doping mechanism. For CPTCFA:m-MTDATA, an integer charge transfer is observed. However, this is not the case for CPTCFA:HTM-B, suggesting the formation of a charge transfer complex in this case.

The electronic properties at ITO | (p-)HTM hetero- and p-HTM | HTM homointerfaces are studied by PES in step-by-step deposition experiments. A novel density of states-based model for fitting the PES data is presented. This model is able to reproduce the classically obtained results at the heterointerfaces while providing more details and accurate electrical potential distributions. More importantly the model allows for the analysis of the homointerfaces and reveals an unexpected space charge region in the p-doped HTM layer. After the model is advanced, an increased number of states in the energy gap for the molecules of the undoped layer right at the interface is predicted.

The interfaces between Al back-contacts and HTM as well as p-doped HTM layers are investigated. These interfaces are relevant for hole-only devices which are used to study effects on less complex device structures. It is shown that Al tends to diffuse into the organic thin film where it reacts with the dopant molecule, redopes the material, and strongly changes the electronic properties. This could be a problem, as this HTM | Al back-contact interface appears to have a strong influence on the properties of hole-only devices, potentially leading to conclusions which do not hold for full devices, where this interface does not exist.

Finally, a low excitation energy electron emission (termed L4E) effect is observed. Free electrons are emitted by shining an ultraviolet LED on m-MTDATA thin films even though the photon energy is lower than the ionization potential of the material. The effect is most likely related to a triplet-triplet-annihilation mechanism and an application as room temperature electron source is discussed.

## Zusammenfassung

Diese Dissertation untersucht organische Halbleiter (OHL) für die Anwendung in organischen Leuchtdioden (OLED) in Zusammenarbeit mit unserem Projektpartner Merck KGaA. Eine häufig genannte Eigenschaft von OHL ist die chemische Vielseitigkeit, welche es erlaubt neue Moleküle leicht zu synthetisieren. Ein tieferes Verständnis der Beziehung von molekularer Struktur zu Bauteileigenschaften könnte hier zu einer schnelleren Sichtung und Entwicklung neuer Materialien führen. Als Beitrag zu diesem Ziel, analysiert und diskutiert diese Arbeit die Eigenschaften von Lochtransportmaterialien (HTM) mit Fokus auf den elektronischen Eigenschaften.

Die elektronischen Eigenschaften von Indium-Zinnoxid (ITO) Substraten, einem kommerziellen p-Dotanden, CPTCFA, einem literaturbekannten HTM, m-MTDATA, einem HTM von Merck KGaA, HTM-B, und Aluminium werden an Dünnschichten mittels Photoelektronenspektroskopie (PES) bestimmt. Absorptionsspektroskopie im ultravioletten, sichtbaren, sowie infraroten spektralen Bereich an reinen und p-dotierten HTM-Dünnschichten, in Verbindung mit Dichtefunktionaltheorieberechnungen, gibt Aufschluss über den Dotiermechanismus. Das System CPTCFA:m-MTDATA zeigt einen ganzzahligen Ladungsübertrag, während CPTCFA:HTM-B diesen nicht zeigt. Letzteres deutet auf die Bildung eines Ladungsübertragkomplexes hin.

Die elektronischen Eigenschaften an ITO | (p-)HTM Hetero- und p-HTM | HTM Homogrenzflächen werden während schrittweisen Abscheidungsexperimenten mit PES untersucht. Ein neues Modell basierend auf Zustandsdichten zum Fitten von PES-Daten wird vorgestellt. Dieses Modell ermöglicht es die auf klassischem Wege erhaltenen Ergebnisse an den Heterogrenzflächen zu reproduzieren. Zusätzlich bietet es mehr Details und eine genauere Beschreibung des elektrischen Potentialverlaufs. Des Weiteren erlaubt das Modell erst die Analyse der Homogrenzflächen. Dies führt zur Entdeckung einer unerwarteten Raumladungszone in der p-dotierten HTM Schicht. Nach einer Weiterentwicklung des Modells wird eine erhöhte Anzahl von Zuständen innerhalb der Energielücke für Moleküle in der undotierten HTM-Schicht direkt an der Grenzfläche vorausgesagt.

Die Grenzflächen zwischen dem Al-Rückkontakt und den HTM bzw. p-HTM Schichten werden untersucht. Diese Grenzfläche ist für reine Lochtransportbauteile relevant. Diese Lochtransportbauteile werden genutzt, um Effekte an weniger komplexen Bauteilstrukturen zu studieren. Es wird gezeigt, dass Al dazu neigt in die organische Schicht zu diffundieren, dort mit dem Dotiermolekül zu reagieren, das Material zu redotieren, und die elektronischen Eigenschaften stark zu verändern. Dies könnte ein Problem sein, da diese HTM | Al-Grenzfläche anscheinend einen starken Effekt auf die Eigenschaften von reinen Lochtransportbauteilen hat und so zu Schlussfolgerungen führen kann, welche sich nicht auf komplette Bauteile übertragen lassen, da diese Grenzfläche dort nicht vorkommt.

Abschließend wird ein Effekt der niederanregungsenergetischen Elektronenemission (genannt L4E) beobachtet. Freie Elektronen werden durch die Beleuchtung einer m-MTDATA Dünnschicht mit einer ultravioletten LED erzeugt, obwohl die Photonenenergie niedriger ist als das Ionisationspotential des Materials. Dieser Effekt steht höchstwahrscheinlich im Zusammenhang mit einer Triplet-Triplet-Annihilationsmechanismus und eine Anwendung als (gepulste) Raumtemperatur Elektronenquelle wird diskutiert.

## Acknowledgments – Danksagung

An dieser Stelle möchte ich mich bei allen bedanken die diese Arbeit möglich gemacht haben und mich dabei in den letzten Jahren unterstützt haben.

Zuallererst danke ich meinem Doktorvater Prof. Dr. Wolfram Jaegermann und Dr. Thomas Mayer für ihre Betreuung der Arbeit, für die vielen intensiven und manchmal sicherlich anstrengenden Diskussionen, und für den Freiraum diese Arbeit zu gestalten. Außerdem möchte ich mich bei Dr. Eric Mankel und Dr. Maybritt Münch bedanken, die mir vor allem am Anfang eine große Hilfe waren.

Zudem geht mein Dank an Prof. Dr. Wolfgang Ensinger, dass er die Rolle des Gutachters für diese Arbeit übernimmt, und an Prof. Dr. Uli Lemmer und Prof. Dr. Ralph Krupke für ihr Bereitschaft als Prüfer Teil meiner Prüfungskommission zu sein.

Des Weiteren möchte ich mich bei unserem Projekt Partner Merck KGaA für die finanzielle Unterstützung und die Breitstellung der Materialien bedanken. Insbesondere bedanke ich mich auch bei Dr. Christof Pflumm für die inhaltliche Unterstützung.

Ebenfalls bin ich dankbar für die von der TU Darmstadt zur Verfügung gestellte Rechenzeit am Lichtenberg Hochleistungsrechner. An dieser Stelle möchte ich mich auch bei Jochen Rohrer, Ph.D. für seine Erklärungen zur DFT und den nötigen Installationen bedanken.

Ich danke dem gesamten Fachgebiet Oberflächenforschung mit seinem neuen Leiter Prof. Dr. Jan Philipp Hofmann für die tolle Zeit, die ich dort hatte. Besonders möchte ich noch Sun-Myung Kim für ihre ausgezeichnete Arbeit während ihrer Bachelor-Thesis und Dr. Victoria Wißdorf-Nowald für die gute Zusammenarbeit danken. Auch danke ich der Werkstatt des Fachbereichs, insbesondere Michael Weber, für die Hilfe bei diversen Reparaturen.

Ein großer Dank geht auch an das InnovationLab, wo ich den Großteil meiner Experimente durchgeführt habe. Auch hier möchte ich mich bei meinen Kollegen Dr. Valentina Rohnacher, Dr. Xiaokun Huang, Dr. Patrick Reiser, Dr. Florian Ullrich, Rainer Bäuerle, und Adriana Salazar für die gute Zusammenarbeit und gegenseitige Hilfe bedanken.

Bei Dr. Daniel Utt möchte ich mich für die vielen Gespräche, Diskussionen und die Unterstützung bedanken, die mir oft bei dieser Arbeit geholfen haben. Ich schätze deine Meinung sehr, danke dir!

Zuletzt möchte ich mich ganz besonders bei meinen Freunden, meinen Eltern, meiner Schwester und meiner Freundin Lu bedanken, für so manches geteilte Leid, aber vor allem die vielen großartigen Momente und Erinnerungen – ohne euch gäbe es diese Arbeit nicht. Von ganzem Herzen, **vielen Dank!**

## Table of Contents

## List of Abbreviations

| | |
|---|---|
| 2PE | *Two Photon Excitation* |
| AFM | *Atomic Force Microscopy* |
| ASE | *Atomic Simulation Environment* |
| ASF | *Atomic Sensitivity Factor* |
| CBM | *Conduction Band Minimum* |
| CNL | *Charge Neutrality Level* |
| cps | *counts per second* |
| CPTCFA | *2,2',2"-(cyclopropane-1,2,3-triylidene)-tris[2-(4-cyanoperfluorophenyl)-acetonitrile]* |
| CTX | *Charge Transfer Complex* |
| DFT | *Density Functional Theory* |
| DOGS | *Density of Gap States* |
| DOS | *Density of States* |
| $E_F$ | *Fermi Level* |
| ERE | *Electron Relaxation Excitation* |
| FT | *Fourier Transform* |
| FWHM | *Full Width at Half Maximum* |
| GPAW | *DFT Python code based on the PAW method* |
| HOD | *Hole-Only Device* |
| HOMO | *Highest Occupied Molecular Orbital* |
| HTM | *Hole Transport Material* |
| HTM-B | *HTM of the project partner Merck KGaA* |
| ICT | *Integer Charge Transfer, Integer Charge Transfer* |
| ID | *Interface Dipole* |
| IDIS | *Induced Density of Interface States* |
| IMFP | *Inelastic Mean Free Path* |
| IP | *Ionization Potential* |

| | |
|---|---|
| IPES | *Inverse Photoemission Spectroscopy* |
| IR | *Infrared* |
| IRA | *Infrared Reflection Absorption* |
| ISC | *Intersystem Crossing* |
| ITO | *Indium Tin Oxide* |
| L4E | *Low Excitation Energy Electron Emission* |
| LED | *Light Emitting Diode* |
| LUMO | *Lowest Unoccupied Molecular Orbital* |
| MIR | *Mid-Infrared* |
| *MMFF94s* | *A type of force field method* |
| m-MTDATA/MTDATA | *4,4‘,4“-Tris[phenyl(m-tolyl)amino]triphenylamine* |
| NIR | *Near-Infrared* |
| OFET | *Organic Field Effect Transistor* |
| OLED | *Organic Light Emitting Diode* |
| OPV | *Organic Photovoltaic* |
| OSC | *Organic Semiconductor* |
| OVITO | *Atomistic visualization software* |
| PAE | *Photon Absorption Excitation* |
| PAW | *Projector-Augmented Wave* |
| PBE | *Perdew, Burke, Ernzerhof exchange-correlation functional* |
| PES | *Photoelectron Spectroscopy* |
| RMS | *Root-Mean-Square* |
| SAM | *Self-Assembling Monolayer* |
| SCR | *Space Charge Region* |
| SEC | *Secondary Electron Cut-Off* |
| SEM | *Scanning Electron Microscopy* |
| SPAE | *Secondary Photon Absorption Excitation* |
| SSA | *Singlet-Singlet Annihilation* |

| | |
|---|---|
| TCNQ | *7,7,8,8-Tetracyanoquinodimethane* |
| TCO | *Transparent Conductive Oxide* |
| TTA | *Triplet-Triplet Annihilation* |
| UHV | *Ultra-High Vacuum* |
| UP | *Ultraviolet Photoelectron* |
| UPS | *Ultraviolet Photoelectron Spectroscopy* |
| UV | *Ultraviolet* |
| VB | *Valence Band* |
| VBM | *Valence Band Maximum* |
| vis | *Visible* |
| WF | *Work Function* |
| XP | *X-ray Photoelectron* |
| XPS | *X-ray Photoelectron Spectroscopy* |
| $\theta$ | *Take-Off Angle* |

# 1 Introduction

The research on organic semiconductors (OSCs) started with the observation of semiconducting properties in molecular crystals. Here, an important step were the reports by Pope in 1963[1] and by Helfrich and Schneider in 1965[2] and 1966[3] on the electroluminescence in anthracene crystals. Due to the thickness of the crystals, a few hundred volts were required for the charge injection. Much lower operation voltages were achieved by Tang and VanSlyke who prepared evaporated amorphous molecular thin films to obtain a light emitting diode (LED) with a driving voltage below 10 V.[4] The research of OSCs was further progressed by the work of Heeger, MacDiarmid, and Shirakawa on the doping of polymers starting in 1977.[5] Their work was awarded the Nobel Prize in Chemistry in 2000.[6] Today, the field of OSC spans from organic photovoltaics (OPVs) over organic field effect transistors (OFETs) to organic light emitting diodes (OLEDs). Since OPV research switched from fullerene to non-fullerene acceptors, relatively stable small area OPV lab cells with record efficiencies exceeding 15% have been developed. For larger modules, Distler, Brabec, and Egelhaaf achieved record power conversion efficiencies of 12.6% for a 26.2 $cm^2$ module and 11.73% for a 204.0 $cm^2$ module in 2020.[7] OFETs are especially interesting for sensing applications and the flexible sensors are perfectly suited for wearable electronics and the medical field.[8] Finally, OLEDs are already well established in modern consumer electronics such as television screens and smartphone displays.[9] Besides these well-known applications, organic materials are also investigated in the fields of solar water splitting,[10] piezoelectric materials,[11] and thermoelectric materials.[12]

The advantages of OSC devices in comparison to inorganic semiconductor-based devices lie in the available processing methods and the chemical flexibility of the OSCs. Devices from small molecule OSCs can be produced by evaporation-based thin film deposition techniques, while polymer OSCs allow for liquid processing routes, which include spin-coating and printing techniques. These methods are relatively cost effective, e.g., in comparison to the single crystal growth for silicon wafers. Furthermore, OSCs allow for flexible substrates. In addition, with organic chemistry very many different OSC materials and derivatives can be synthesized to tailor the specific properties of the obtained material.[13] However, as can be seen from the work by Kühn et al., the resulting device characteristics cannot be easily predicted even for similar molecules.[14,15] But, attempts to predict the device characteristics just based on the molecular structure and properties is the underlying motivation of the here presented work, as will be explained in the following.

This work and also the just mentioned work by Kühn et al. were conducted in a cooperation with Merck KGaA in Darmstadt. With their *livilux* product line, they offer a series of OSC materials for OLED device production. Thus, even though this work represents a more fundamental research direction, it can be considered for the application field of OLEDs. An OLED consists of several functional layers in a "sandwich" structure (see Figure 1-1a), where the outermost layers are made up of the contacts. Under applied voltage, these contacts act as a positive anode for the hole injection and a negative cathode for the electron injection. Often, injection layers (HIL and EIL) are added to both contacts to obtain reduced injection barriers for the charge carriers.

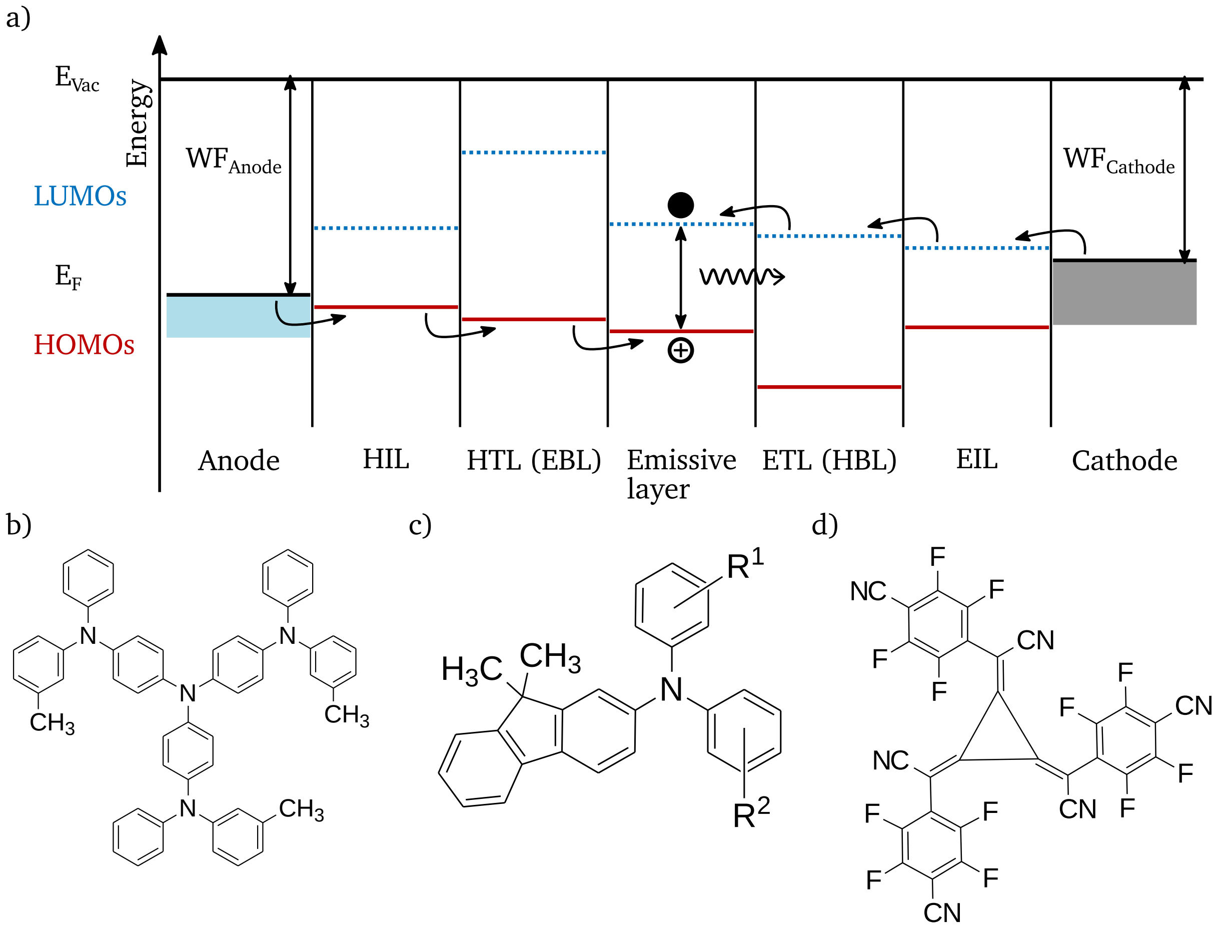

Figure 1-1: a) Example of a Multi-layer OLED "sandwich" structure. Adapted from Adapted from A. Köhler and H. Bässler.[13] b) Molecular structure of 4,4',4''-Tris[phenyl(m-tolyl)amino]triphenylamine (m-MTDATA). Adapted from Shirota et al.[16] c) Reduced structure of the commercial HTM herein called HTM-B. $R^1$ and $R^2$ mark the position of two aryl groups which cannot be shown to protect the interests of the project partner Merck KGaA. d) Structure of the CPTCFA p-dopant molecule. c) and d) adapted from Wißdorf et al.[17]

Next, there are the hole and electron transport layers (HTL and ETL, sometimes named electron and hole blocking layers EBL and HBL, respectively), which conduct the respective charge carriers to the emissive layer in the center of the OLED and confine them there. In this emissive layer, the holes and electrons then combine to form excitons followed by electron-hole recombination, leading to the desired light emission.[13] For the development of new materials, a company like Merck is interested in gaining a better understanding on how the chemical structure of a molecule will determine the final device characteristics, e.g., the current voltage curve of an OLED. Ideally, the theory of every factor of influence from the molecular structure to the final device should be known well enough to model the entire process. These factors can be grouped as the molecular properties, the morphology and related thin film properties which depend on deposition and processing recipes, the interface properties, and, finally, the device characteristics. Consequently, if each group of properties and their interconnections would be understood, new materials could be easily screened by a computer to select promising candidates for further testing. Based on this motivation and as a part of this extended research goal, this dissertation studies the electronic properties of hole transport materials (HTMs) at interfaces and aims to model the experimental data for a detailed discussion and understanding of the obtained behavior.

Going more into detail, two different HTMs are studied for comparison to verify if a certain behavior is solely related to one specific material's properties. The two HTMs are the "starburst"-type molecule 4,4',4"-Tris[phenyl(m-tolyl)amino]triphenylamine (m-MTDATA) which is a well-known HTM from literature[18–20] and a commercially available HTM from Merck KGaA which will be called HTM-B (see Figure 1-1b and c)). To obtain a higher conductivity, the HTMs can be p-doped by addition of high electron affinity molecules which increases the number of holes. Doping of organic semiconductors is an important method to obtain high performance devices, as it can lead to very narrow space charge regions at the contacts which allow the transfer of charge carriers by tunneling, thus leading to a better charge injection. Consequently, the driving voltages of OLEDs are reduced which lowers the power consumption.[21–26] Due to the impact of doping for devices, it cannot be neglected in the interface study of this work. Here, a commercially available molecular p-dopant, which will be called CPTCFA (see Figure 1-1d), is used and co-evaporated with the HTMs to dope them. As CPTCFA and HTM-B are not known from literature, it is important to characterize their thin film properties especially with respect to their electronic properties before they are studied in interface experiments. To obtain a well-defined starting point for this work, all materials used will be characterized as thin films in Chapter 4. Furthermore, the influence of doping and the underlying mechanism should be analyzed. In literature, two doping models are discussed: the integer charge transfer (ICT) and the charge transfer complex (CTX).[27] Salzmann et al. suggest that the ICT model is valid for OSC polymers while the CTX model applies for small molecule OSCs.[28] However, as this rule is not verified for a large set of different dopant:host combinations, the doping behavior and mechanism for the investigated materials will be examined in the second part of Chapter 4. In fact, it will be shown that the CPTCFA:m-MTDATA combination shows signs of ICT while the CPTCFA:HTM-B pair seems to be better described by the CTX model.

Beside the beneficial influence of doping at the contact interface, a doped transport layer at the interface to the emission or absorption layer can be detrimental for the functionality of an OLED or OPV device. The high concentration of charge carriers can lead to a quenching of the excitons lowering the efficiency of the device. Thus, the doped transport layer is often separated from the active emission or absorption layer by an intrinsic (i), i.e., undoped, HTM layer.[22,24,25,29] As a result, interfaces of doped and undoped (p-i or n-i) transport layers can often be found in device structures. OSC heterointerfaces, where two different materials are brought into contact, are widely studied.[15,18,30–38]But, often the host material is the same in the doped layer as in the undoped layer, forming a homointerface. Such homointerfaces can be found in literature for studies where devices are characterized by electrical measurements.[39–43] Reports on dedicated interface experiments, however, could not be found. The reason for a lack of dedicated homointerface studies is probably related to a spectroscopic problem. Due to the fact that the same host molecule is used on both sides of the interface, the spectral data will also be dominated by this molecule for the doped as well as for the undoped layer. Thus, it is nearly impossible to distinguish the contributions from the two layers and therefore to analyze the contact formation. In this work, this spectroscopic challenge of homointerfaces is met by using a model-based fitting method. Here, different approaches from literature[44–47] are combined to derive a new density of states (DOS)-based model. This model includes a distribution of acceptor states as well as a density of tailing gap states to calculate the electric potential distribution. Thus, it is possible to fit photoelectron spectroscopy data to a valid contact potential distribution. In Chapter 5 of this work, first, an ITO | (p-)HTM heterointerface will be analyzed by classical procedure.[48] The results serve as benchmark for the new DOS-based model which is first introduced in detail and then tested at the heterointerfaces. The model, which uses a depth-independent description of the DOS, will prove to reproduce the results obtained by the classical procedure while also providing insights for an improved discussion of the influence of acceptor and gap states. After the successful introduction of the model, it can then be used also on the p-HTM | i-HTM homointerfaces. From the analysis of the homointerface using the fitting model, it is found that a significant space charge region appears in the doped HTM layer, which is unexpected from a classical semiconductor physics standpoint. Again, using the model and advancing it towards a depth-dependent description of the DOS, the unexpected behavior is resolved by introducing a high number of gap states in the undoped layer right at the interface. This solution is in line with literature reports where a finite number of electronic states in the energy gap of an OSC is used to explain the electronic structure at an interface: Mankel et al.[49] use a distributed states model with a constant number of states across the whole energy gap. Vázquez, Kahn, and coworkers[32,50–52] use an induced density of interface states. In the review article of Yang et al.[47] the ”origin and role of [tailing] gap states” in different experiments is discussed. The question about the origin of gap states at the homointerface remains unanswered, but the presented results demonstrate how homointerfaces can be analyzed and open up the possibility for further systematic studies on a broader range of materials.

Another work, which can be placed in the greater framework of relating molecular design to device properties, is the work by V. Wißdorf who modelled and fitted current voltage and impedance measurements of hole-only devices (HODs) trying to extract material property parameters.[17,53] HODs are simplified device structures which are used to lower the complexity and enable the study of specific effects. As one result of that work, the interface at the Al back contact appeared to have a strong influence on the electric characteristics of the HOD. Furthermore, the experiments also make use of HTM-B and the same molecular p-dopant (CPTCFA) as in this work. Thus, this interface became of interest for further studies and the photoelectron spectroscopy results of (p-)HTM | Al interface experiments will be shown in Chapter 6. It will be demonstrated, that the (p-)HTM | Al interface is not as well defined as it is assumed in the model for the HODs and that the Al atoms tend to strongly interact with CPTCFA.

Finally, as last chapter of experimental results, a surprising emission of electrons from low excitation energy photons is investigated in Chapter 7. This effect, which will be labeled as low excitation energy electron emission (L4E), describes the emission of electrons from m-MTDATA at an excitation energy between 2.5 eV and 3.4 eV, even though m-MTDATA has an ionization potential of 5 eV. The emission of photons with higher energy than the exciting photons is known as up-conversion.[54–56] However, reports on the emission of electrons and the underlying mechanism could not be found. Thus, the dependency of the effect on excitation energy, layer thickness, temperature, p-doping, and air exposure is studied. Furthermore, the electron emission intensity versus irradiation intensity is measured, leading to a discussion of possible mechanisms. At the end, the involvement of long lifetime triplet states and a triplet-triplet-annihilation process is proposed as the most probable explanation. In addition, some potential applications of the effect are discussed.

Outlining the written structure of this thesis, the next chapter will provide the needed theoretical information of organic semiconductors which is useful for the understanding of the presented results later on. Furthermore, Chapter 3 provides information on the experimental methods, which are used in this work, before the results of these methods are presented and discussed starting with Chapter 4. Each chapter of experimental results and discussion is concluded with a summary. At the end, a complete survey and resume of this work as well as an outlook (Chapter 8 and 9) will be given.

# 2 Theory of Organic Semiconductors

## 2.1 General Information and Electronic Structure

In this section, some general information about organic semiconductors will be given with focus on the electronic structure and properties of this material group. The information is taken from *Electronic Processes in Organic Semiconductors* by A. Köhler and H. Bässler[13] where further details can be found.

As the name suggests, organic semiconductors (OSCs) belong to organic carbon-based compounds. Their semiconducting properties originate from an energy gap of about 2 to 3 eV which matches the energy range of visible light and allows for the usage of OSCs in optoelectronic applications, i.e., organic light emitting diodes or organic solar cells. In comparison to their inorganic counterparts, e.g., Si, the energy gap is still quite large and thus the density of mobile charge carriers in undoped OSCs is much lower. The group of OSCs can be further divided into small molecules and polymers. Small molecules have lower molar masses which allows to deposit thin films by evaporation without degradation of the molecules. Depending on the molecular structure, the molecules orient themselves as crystals bound by van-der-Waals forces or as amorphous layers with no long-range order. Polymers are too heavy to be evaporated, as during heating the covalent bonds would break before the long-chained molecule is evaporated. Instead, polymer OSCs can be processed by spin-coating or printing methods. They are also better suited for blending which is utilized in organic solar cells.

In contrast to many other organic compounds or materials, OSCs are extended π-conjugated systems, which result from the molecular structure with alternating single and double bonds. These structures contain C in the $sp^2$-hybridization (see Figure 2.1-1a). The overlap of two $sp^2$-

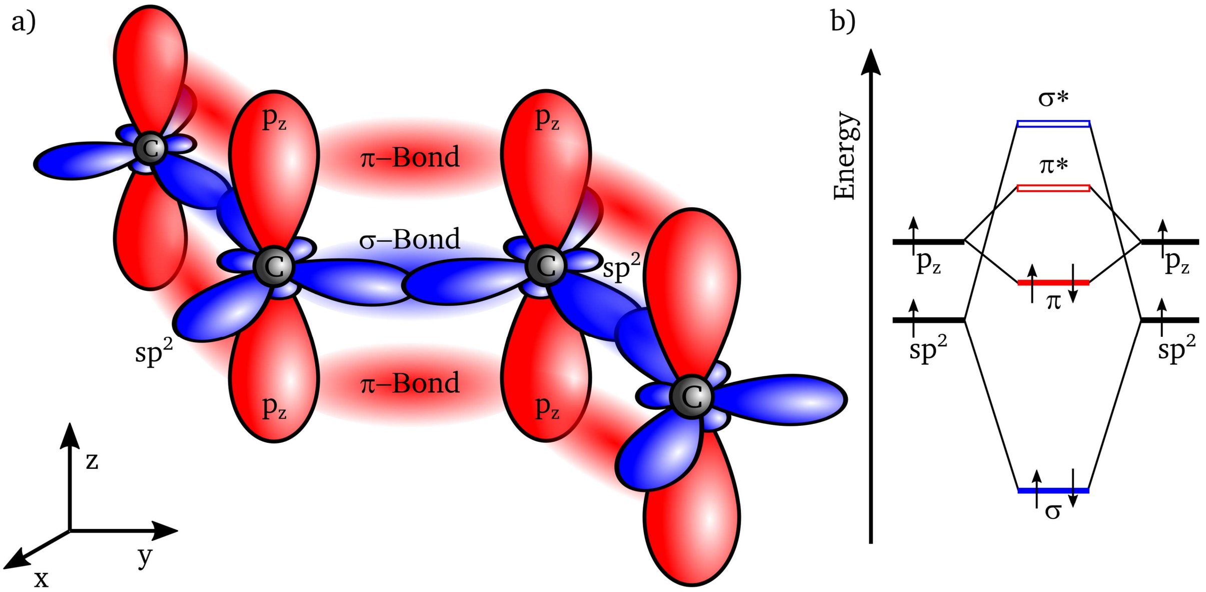

Figure 2.1-1: a) Schematic of an $sp^2$-hybridized carbon chain. The $sp^2$-orbitals (blue) form the directional σ-bonds with localized electrons while the $p_z$-orbitals form the π-bonds (red) with electrons delocalized along the chain. b) Energetic splitting of the bonding π-/σ- and anti-bonding π*-/σ*-states. Adapted from Maybritt Kühn's dissertation.[57]

orbitals leads to the formation of directional σ-bonds where the electrons are localized. In addition, the overlap of the remaining unhybridized p-orbitals leads to the formation of π-bonds where the electrons are more delocalized. The energetic splitting of the bonding σ- or π-orbital to the anti-bonding σ*- or π*-orbital is larger for the σ-bond than for the π-bond (see Figure 2.1-1b). Often additional atoms as N, O, S, etc. are also included in the C sp2 based backbone, which leads to σ (σ*) and π (π*) states of related but energetically shifted electron states. The π-orbital often forms the highest occupied molecular orbital (HOMO) and the π*-orbital the lowest unoccupied molecular orbital (LUMO), which together define the energy gap of the molecule. In other words, the formation of π-bonds with a smaller energetic splitting between bonding and anti-bonding states leads to the smaller energy gap, which leads to semiconductor properties and related applications.

Going from the orbitals of a single molecule to the electronic states of a condensed thin film, crystalline and amorphous structures need to be distinguished. For molecular crystals, electronic band structures are formed. However, due to the weak interaction between the molecules, the electrons are delocalized mainly on just the individual molecules, resulting in energetically quite narrow bands with a high effective mass. More important for this work are amorphous thin films. Here, the varying orientation of molecules and changing distances between them leads to a random distribution of energy levels around a mean value, i.e., a Gaussian distribution (see Figure 2.1-2a). Additionally, there might be polarization effects which influence the energy gap of a molecule.[58] In both cases of amorphous and crystalline OSCs, the electronic states can be considered as mostly localized, which is in contrast to the electron gas in inorganic semiconductors. Thus, charge carrier mobilities are much lower and the transport properties require a different description which is the so-called *hopping* mechanism.

Furthermore, in a solid, polarization effects of the surrounding molecules will lower the energy of excited states. The permittivity in OSCs is lower than in inorganic semiconductors. Thereby,

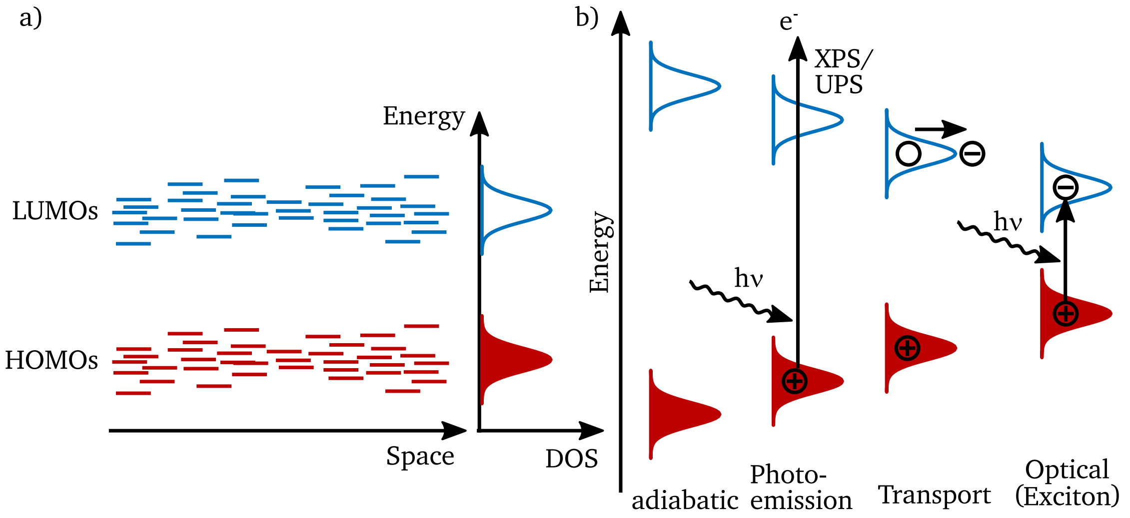

Figure 2.1-2: a) In an amorphous OSC, the varying orientation of molecules and changing distances between them leads to a random distribution of HOMO and LUMO energies around a mean value. The resulting density of states is well approximated by a Gaussian distribution. No polarization effects which influence the energy gap are considered. b) Different energy gaps in organic semiconductors. Different excited states are compared to the adiabatic ground state. Adapted from Eric Mankel's dissertation.[59]

the screening of charges is low and the coulomb interaction between electron-hole pairs is high (up to 1 eV). This can be observed when comparing different methods to determine the energy gap of an OSC thin film (see Figure 2.1-2b). Using photoelectron spectroscopy and inverse photoelectron spectroscopy to determine the ionization potential and the electron affinity, respectively, yields the so-called photoemission gap $E_{\mathrm{g}}^{\mathrm{Photoemission}}$ which is close to the transport gap. For both processes, an electron is removed or added to a molecule, resulting in polarization effects without an exciton formation. However, as the photoemission process is faster than the charge transport, the corresponding photoemission gap is not, or only partially, influenced by the slower intra-molecular and inter-molecular relaxations. In contrast, optical absorption spectroscopy leads to the excitation of an electron, creating an exciton that is bound by the strong Coulombic interaction of electron and hole. The resulting energy gap is called optical gap $E_{\mathrm{g}}^{\mathrm{optical}}$.[59,60] Djurovich et al.[61] measured the electrical and optical gap for different OSCs and derived an empirical formula which, in a first approximation, can be used to translate optical gap energies to electrical gap energies:

$$E_{\mathrm{g}}^{Photoemission} = 1.39 \cdot E_{\mathrm{g}}^{\mathrm{optical}} - 0.46\ \mathrm{eV}\,. \tag{1}$$

The next section will discuss further details on the optical properties of OSCs.

## 2.2 Optical Properties

The information given in this section is taken from *Electronic Processes in Organic Semiconductors* by A. Köhler and H. Bässler[13]

At the end of the previous section, two different methods for determining the energy gap of an organic semiconductor (OSC) are mentioned: photoelectron spectroscopy (PES) and optical absorption spectroscopy. For PES, a photoelectron is removed from an electronic state leaving an unpaired electron behind which interacts with the other electrons in the atom and molecule. These interactions change the energy of the electronic state the photoelectron was removed from also affecting the energy of the removed photoelectron. This influence is termed final state effect.[62] For absorption and emission spectroscopy, an electron is not removed but excited into a higher electronic state. Here, the excited electron interacts with the remaining hole and the other electrons. These interactions, again, will influence the energy of the electronic states and are included in the measured absorption and emission spectra. These electron-electron interactions make it difficult to picture the optical absorption or emission process as the excitation or relaxation of a single electron. Thus, usually, a state picture, which does not try to specifically represent one electronic configuration, is used to describe different energetic transitions. The Jablonski-diagram shown in Figure 2.2-1 summarizes different processes. When the spin of an excited electron and the remaining unpaired electron is considered, singlet $S_i$ and triplet $T_j$ states need to be distinguished. For a singlet state, the spin of the unpaired electron is opposite while for a triplet state both electrons have the same spin.

The ground state is marked by the index 0 and the 1., 2., and higher excited states are indicated with incrementing index. Triplet and singlet states are electronic states (thick solid horizontal lines in the Jablonski-diagram) where a transition involves the change of the electronic configuration. As these electronic states represent a configuration of many electrons, they must

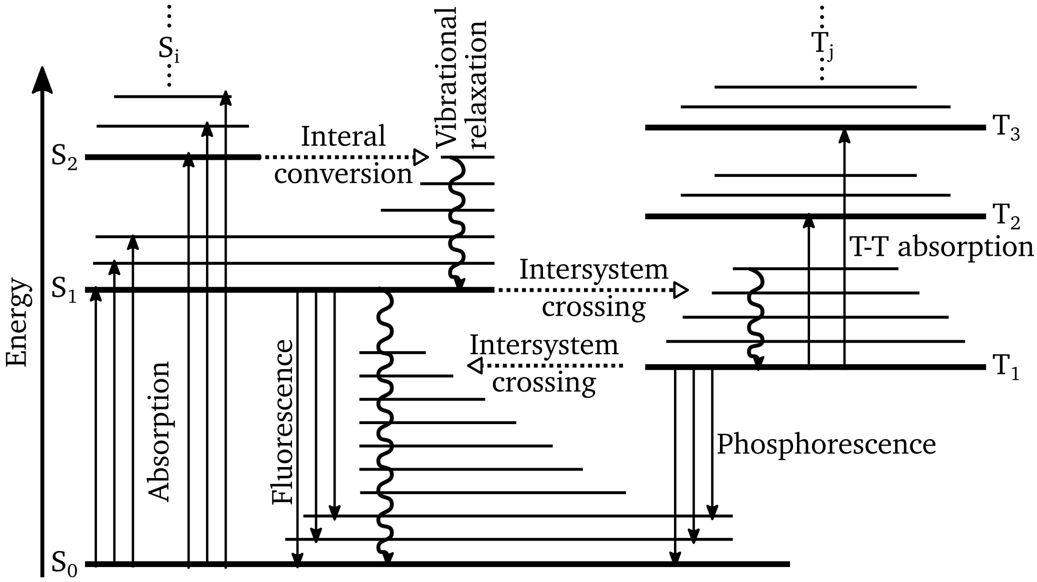

Figure 2.2-1: Jablonski-diagram illustrating the different radiative and non-radiative transitions between singlet $S_i$ and triplet $T_j$ states. Adapted from A. Köhler and H. Bässler.[13]

not to be confused, e.g., with the energy levels of electrons in an atom. For each of these electronic states, several vibrational states or modes (shown as thin solid horizontal lines for each electronic state in the Jablonski-diagram) can be found. Transitions between the electronic states require energies in the range of some eV and can thus be excited by visible light photons. Transitions between vibrational states take less energy and are typically excited by light in the infrared range.

Often, all electrons are paired with opposite spins in the ground state, forming a singlet state $S_0$. Radiative transitions usually keep the spin of an electron, because the change of the magnetic field due to the electromagnetic wave is too small to have an effect. Thus, only transitions from singlet to singlet or triplet to triplet state are likely. Absorption is the radiative process of excitation while the fluorescence is the radiative process of recombination. In addition to these "spin-allowed" transitions, there are also "spin-forbidden" radiative transitions involving a spin flip. Contrary to their name, "spin-forbidden" transitions can still occur but at a lower rate. In the case of strong spin-orbit coupling, the wavefunctions of the ground state and excited state are not purely singlet or triplet and a change in spin angular momentum can be compensated by a change in orbital angular momentum. Thus, "spin-forbidden" transitions become more likely. The radiative transition from the first excited triplet state $T_1$ to the singlet ground state $S_0$ is such a well-known "spin-forbidden" transition that is termed phosphorescence.

Beside the radiative transitions, non-radiative transitions may also occur. Vibrational relaxations take place when a molecule is excited into a higher vibrational state of an excited electronic state and then relaxes down to the lowest vibrational state of that excited electronic state. Internal conversion happens, e.g., from a higher excited singlet state $S_{n+1}$ into a vibrational state of the next lower excited singlet state $S_n$ which is similar in energy. The rates of internal conversion are usually high with about $10^{12}$ $s^{-1}$. After the internal conversion process, vibrational relaxation will relax the molecule into the lowest vibrational state of the $S_n$

electronic state. Another non-radiative transition is the intersystem crossing. Here, the molecule converts from a singlet state into a triplet state or vice versa (sometimes called reverse intersystem crossing). Strong spin-orbit coupling favors this transition, and the transition rates can vary from $10^6$-$10^{12}$ $s^{-1}$. The process is again facilitated if the involved electronic and vibrational states are close in energy. The so far mentioned transitions describe the excitation or relaxation of only one molecule. However, there are also transitions with two excited molecules, like the singlet-singlet-annihilation (SSA) or triplet-triplet-annihilation (TTA). SSA is typically irrelevant, as the short lifetime of singlet states (sub-nanosecond range) requires for very high concentrations of excited singlet states for SSA to be observed. In contrast, the lifetime of triplet states can be much longer (from milliseconds to seconds) and TTA might be observed, also depending on the diffusion rate of the triplet states. For TTA, the total spin of the formed triplet-pair $(TT)^*$ has to be considered. Thus, TTA might either just lead to non-radiative quenching of one of the triplet states if they have a total spin of 1, or TTA might cause the transition into an excited singlet state if the triplet-pair carries a total spin of 0. The latter case initiates delayed fluorescence when the excited singlet state decays under emission of a photon. The theoretical formation of a quintet state for a total spin of 2 is not observed.

$$(\mathrm{TT})^* \rightarrow \begin{cases} \mathrm{S}_1 + \mathrm{S}_0 + \text{heat}, & \text{if total spin 0} \\ \mathrm{T}_1 + \mathrm{S}_0 + \text{heat}, & \text{if total spin 1} \\ (Q_1 + S_0 + \text{heat}, & \text{if total spin 2)} \end{cases} \tag{2}$$

## 2.3 Doping

The conductivity of a material depends on the number of mobile charge carriers, their charge, and their mobility. In case of electronic conductivity, the charge carriers are electrons or holes carrying one elementary charge. For ionic conductivity, multiples of the elementary charge are possible depending on the type of mobile ion. Ionic conductivity will not be further discussed as it is irrelevant for this work.

In an intrinsic inorganic semiconductor, the number of mobile charge carriers, i.e., electrons and holes, depends on the band gap and the temperature. The charge carrier mobility depends on the effective mass given by the band structure of the inorganic semiconductors. For intrinsic organic semiconductors, the number of thermally activated mobile charge carriers is negligible due to relatively large energy gaps and the mobility of these charge carriers is low because of the strong Coulomb energies for electron-hole pairs leading to exciton trapping. Thus, for these materials to be reasonable conductive, charge carriers need to be introduced either by injection from contacts in a device structure, optical generation, e.g., as in a solar cell, or by doping.[13] The doping procedure shall be further discussed.

Classically, in the case of inorganic semiconductors, parts of the host material atoms are substituted with a different element which creates a defect that will either donate electrons into the conduction band (n-type doping) or accept an electron from the host material's valence band, thereby creating a hole in the valence band (p-type doping). In inorganic semiconductors the Coulomb interaction between the created electron or hole and respectively ionized donor or acceptor is weak due to high values of the dielectric constant. Thus, the doping efficiency is high and only low concentrations of acceptors or donors in the range of $10^{-6}$ to $10^{-3}$ mol% are

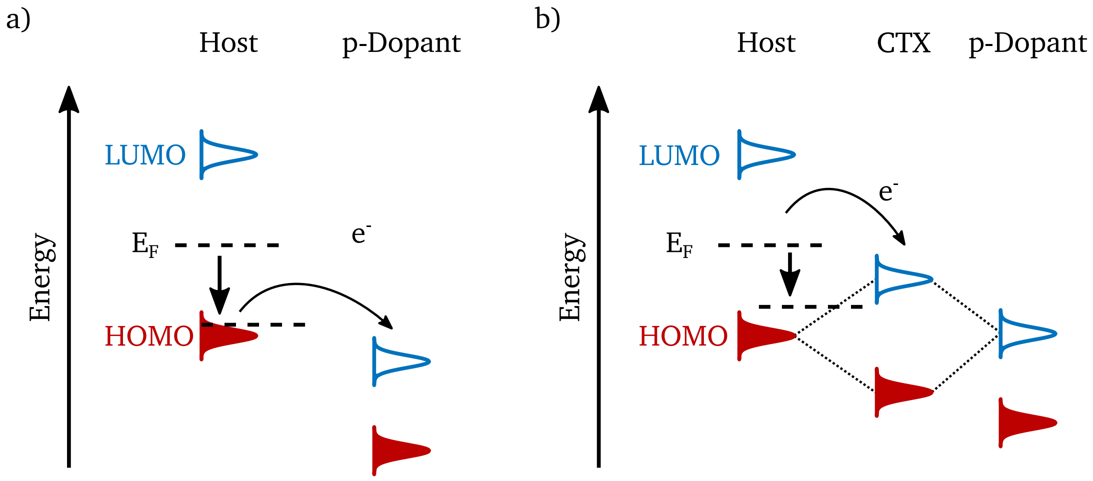

Figure 2.3-1: Schematic representation of two doping mechanism models for the case of p-doping: a) Integer charge transfer (ICT) where an electron gets transferred from the HOMO of the host molecule to the LUMO of the p-dopant molecule, and b) charge transfer complex (CTX) formation where the HOMO of the host molecule and LUMO of the p-dopant molecule overlap and form a complex with a new HOMO and LUMO state. The electron gets then transferred from the HOMO of the host molecule to the LUMO of the complex. Adapted from Salzmann et al.[46]

needed. In contrast, the Coulomb energy in organic semiconductors is high due to the low dielectric permittivity resulting in low doping efficiencies. As a result, much higher dopant concentrations in the range of $10^{-3}$ to $10^{-1}$ mol% are needed. In organic semiconductors, halogens (e.g., iodine) and alkali metals (e.g., lithium) were used in the beginning as p- and n-dopants. However, the problem of these atomic dopants is their diffusivity which leads to unstable devices.

Less susceptible to diffusion are molecular dopants. These are molecules which are chemically designed to have an energetically very low LUMO (high electron affinity) for p-dopants to accept electrons from the matrix molecule's HOMO or which have a high HOMO (low ionization potential) for n-dopants to donate electrons to the matrix molecule's LUMO. Their tendency to donate electrons renders n-dopants to be prone to oxidation which poses a challenge. The description of orbital energetic position leads to two doping mechanisms which are discussed in literature: the integer charge transfer (ICT) model and the charge transfer complex (CTX) model (Figure 2.3-1). According to the work by Salzmann et al.[28], the former is typically observed for organic conjugated polymers while the latter is typical for organic conjugated small molecules. Both models are briefly discussed here and will be brought up again in Subsection 4.2.7 when discussing the measurements on two different dopant:host systems.

### Integer Charge Transfer Model

As the name integer charge transfer suggests, a "full" electron is transferred from the host molecule to the dopant molecule (p-doping, see Figure 2.3-1a) or vice versa (n-doping). Using the example of p-doping, this transfer leads to a positively charged host molecule and a negatively charged dopant molecule.[28] A change in the spectral signature between the neutral molecules and the charged ones can be observed by light absorption spectroscopy[13,27,28] as will be later shown in Section 4.2. If the hole on the host molecule can dissociate from the electron, it can function as a mobile charge carrier. Furthermore, by increasing the number of holes the Fermi level of the material will shift closer to the HOMO of the host material with increasing dopant concentration. If the energetic position of the dopant's LUMO is below the energetic position of the host's HOMO, even degenerate doping might be observed, i.e., the Fermi level position shifts into the matrix's HOMO.[28]

### Charge Transfer Complex Model

The charge transfer complex model as introduced by N. Koch and coworkers[27,28,46,63,64], again discussed for the case of p-doping, assumes an overlap of the matrix molecule's HOMO with the dopant molecule's LUMO which leads to a hybridization of the two orbitals. This hybridization results in the formation of a complex with its own bonding and anti-bonding orbital, i.e., the complex's HOMO and LUMO respectively (see Figure 2.3-1b). While the complex's HOMO is occupied by the electrons from the complex forming host molecule's HOMO, the complex's LUMO is unoccupied. Thus, the complex's LUMO can serve as electron acceptor for electrons from another host molecule which is not part of the complex. In their work, Méndez et al.[27] and Salzmann et al.[28] use a Hückel-like model to calculate the energy gap $E_g^{\mathrm{CTX}}$ between the complex's HOMO and LUMO:

$$E_g^{\mathrm{CTX}} = \frac{1}{2}\left(H_{\mathrm{Host}} + L_{\mathrm{Dopant}}\right) \pm \sqrt{\left(H_{\mathrm{Host}} - L_{\mathrm{Dopant}}\right)^2 + 4\beta^2}\,, \tag{3}$$

where $H_{\mathrm{Host}}$ is the energetic position of the host molecule's HOMO, $L_{\mathrm{Dopant}}$ is the energetic position of the dopant molecule's LUMO, and $\beta$ is the resonance integral which depends on the intermolecular coupling and is stated with a value between 0.4 and 0.6 eV.[28]

As it is the complex formed between host and dopant molecule which acts as the acceptor, no fully charged dopant molecules appear as spectral signature in light absorption spectroscopy, but the spectra change as if a partial charge transfer would have happened.[27] Furthermore, as the anti-bonding state of the complex, the complex's LUMO will be energetically above the host molecule's LUMO. Thus, with increasing dopant concentration, the Fermi level shifts towards the host molecule's HOMO but then saturates between the complex's LUMO and host molecule's HOMO.[27] Thus, this model can provide an explanation for the often observed saturation of the Fermi level above the host molecule's HOMO even though a larger shift of the Fermi level into the HOMO would be expected from the LUMO position of the dopant molecule.

Finally, it should be pointed out that both models assume a homogeneous distribution of the dopant molecules in the matrix. However, at higher concentrations the dopants might form clusters and precipitates. Then, the internal interface charge transfer doping model by Mayer et al.[65] needs to be considered. Instead of the interaction between individual molecules, they describe the doping as a charge transfer at interfaces between matrix phase and dopant phase in the precipitates.

## 2.4 Interfaces

When it comes to (organic) semiconductor devices, the interface properties of the different layers play a significant role. In this section, first, general semiconductor contact formation shall be summarized and, second, different types of interface dipoles (IDs) for different organic semiconductor (OSC) interfaces shall be discussed.

### Semiconductor Contact Formation

If two materials with different electrochemical potentials, i.e., Fermi levels, are brought into contact, a charge transfer between the two materials will happen due to the rules of thermodynamics to reach electronic equilibrium, i.e., Fermi level alignment. Based on this rule, classical models like the Schottky model[66,67] and Anderson alignment[68,69] can be used to describe and predict the electronic structure at metal-semiconductor and semiconductor-semiconductor interfaces (see Figure 2.4-1). First, the electronic level diagrams of two materials are drawn aligned with respect to the vacuum level (see Figure 2.4-1(i)). Second, an ID, if present, needs to be added as abrupt potential difference between the two diagrams (see Figure 2.4-1(ii)).

Finally, the remaining energetic difference between the Fermi levels of the two materials will cause a charge transfer which induces the formation of space charge regions at the interface. These space charge regions give rise to a change of the electrical potential, which leads to a bending of the electronic states towards the interface and an alignment of the Fermi levels (see Figure 2.4-1(iii)). The potential drop across the interface is given by the difference of the Fermi levels of the two materials. However, the distribution of the potential drop between the two materials and the related widths of the space charge regions depend on the charge carrier density in the materials. The higher the charge carrier density, the thinner the space charge region. In addition, the lower the charge carrier density in one material with respect to the charge carrier density in the other material, the more of the potential will drop across the space charge region of the material with the lower charge carrier density. An extreme result of this set of rules can be seen at the metal-semiconductor interface. Here, the metal has such a high number of charge carriers that all transferred charges in the metal will accumulate right at the interface forming more a charged surface layer than a space charge region. In the semiconductor, the charges have less available electronic states to occupy leading to a lower charge density; the counter charges are more spread out in a space charge region. As a result,

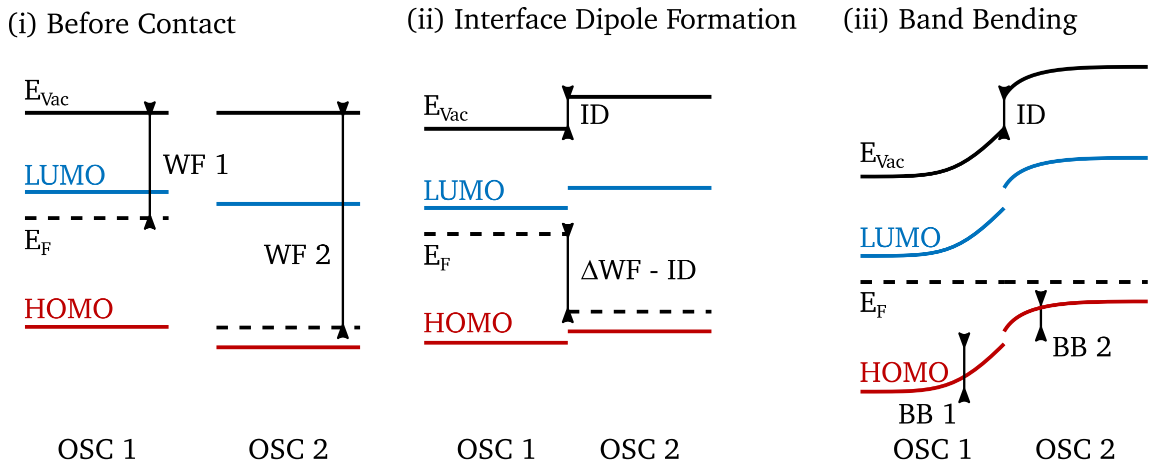

Figure 2.4-1: Illustration of the energy alignment model for semiconductor interfaces. (i) Before contact, the energy levels of the semiconductors are aligned at the vacuum level highlighting their work function difference ΔWF. (ii) When brought into contact the energy levels are offset by an interface dipole (ID) which changes the energetic distance of the Fermi levels. (iii) The remaining energetic difference in Fermi level positions leads to charge transfer, the formation of a space charge region, and a bending of the energy levels (band bending – BB). Adapted from Maybritt Kühn's dissertation.[57]

band bending of the electronic states towards the metal contact is observed in the semiconductor, forming a typical Schottky barrier.

In this work, the electronic structure at OSC interfaces is studied by interface experiments as described in Section 3.1 and 5.1. The formation of a space charge region and the related change of the electrical potential shift all electronic states which can be measured with photoelectron spectroscopy for thin layers close to the interface and for thick layers further away from the interface. Thus, from the shift of the spectra the band bending can be determined. In addition, the energy difference of the Fermi level to the valence band maximum and to the work function of the pure sublayer and the thick adlayer far away from the interface can be determined. Thereby, an energy level diagram of the interface can be drawn. If the difference in the measured work functions does not match the observed band bending, the reason might be the formation of an ID or similar charge separation at the interface that causes a quasi-abrupt change of the electric potential at the interface. This quasi-abrupt change in the electrical potential might be seen as an abrupt change of the work function in the secondary electron cut-off spectra from the pure sublayer to the first deposited thin adlayer. There may be various reasons for the formation of an ID or similar dipole moment at OSC interfaces which are discussed in the following.

### Interface Dipoles at Organic Semiconductor Contacts

As described in a review article by Braun et al.,[35] the formation of an ID at an OSC contact depends on the strength of interaction between the OSC and the second material. The following paragraphs are mainly based on this review. The term interface dipole (ID) will be used for any charge separation in close proximity of the interface which causes a quasi-abrupt change of the electrical potential.

First, the physisorption of an OSC on a metal surface without any chemical reaction or charge transfer is considered. For such a metal-OSC interface, the distinction between a clean metal surface, e.g., cleaned by Ar-ion etching (sputtering), and a “passivated” metal surface, e.g., by adsorbed hydrocarbon species from exposure to air, has to be made. For a clean metal surface, the electron density in the solid slightly decreases towards the surface and extends on the other side into the vacuum. This creates an electric double layer, equivalent to an electric dipole moment, which in combination with the chemical potential in the bulk defines the work function of the clean metal (see Figure 2.4-2a). The physisorption of another species on the clean metal surface reduces the tailing of the electron density which lowers the corresponding dipole moment and reduces the work function of the metal. This effect is known as the push-back effect (see Figure 2.4-2b). For the deposition of an OSC on a clean metal surface this push-back effect and the resulting change of the work function has to be taken into account and will appear as ID at the interface. In case of a “passivated” metal surface which was exposed to air and has hydrocarbon species already adsorbed on the surface, the push-back effect is already present and the deposition of an OSC on such a surface will not lead to a further push-back effect related work function change. It should be noted that in both cases the effective work function of the metal is reduced by the push-back effect. Besides the adsorption of hydrocarbons, the formation of oxide or hydroxide species on some substrate surfaces may occur during air exposure passivating the surface and affecting the substrates work function.

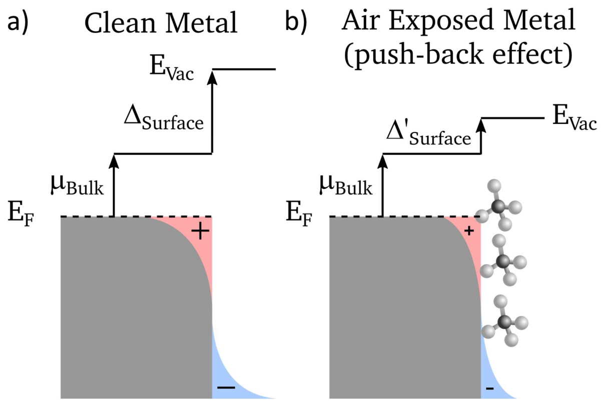

Figure 2.4-2: a) Surface dipole of a clean metal. The electron density decreases towards the surface and extends into the vacuum. This creates dipole moment between the positive net charge in the material (red area – "missing" electron density) and the negative net charge in the vacuum (blue area – "additional" electron density) which influences the surface potential. b) Air exposed metal surface with push-back effect. The adsorption of hydrocarbons reduces the tailing of the electron density across the surface and lowers the dipole moment. Adapted from Heimel et al.[71]

Furthermore, especially when experimenting with single crystals substrates, e.g., silicon wafers, the crystal orientation and termination influences the work function.[70]

In case of a "passivated" metal surface and depending on the energetic position of the molecular orbitals with respect to the Fermi level of the metal, integer charge transfer (ICT) at the interface might occur. This ICT, shown in Figure 2.4-3, takes place by tunneling through the passivating layer of adsorbed species. The transferred electrons or holes occupy localized electronic states of the molecules right at the interface. The energetic position of these transfer states is different from the molecular HOMO and LUMO energetic positions as it is changed by relaxation effects of the molecule and the Coulomb interaction with the counter charges in the metal surface. This charge separation right at the interface creates a double layer dipole moment which results in a quasi-abrupt change of the electrical potential at the interface, i.e., an ID. Such a process can also occur for an organic-organic interface if the energetic positions of the donating and accepting transfer states suggest a charge transfer.

For a clean metal surface and a stronger interaction between the OSC molecules and the metal surface, the induced density of interface states (IDIS) model by Vázquez, Kahn, and coworkers[32,50–52] might need to be considered. In this model, a resonance between the molecular orbitals and the quasi continuum of states in the metal broadens the molecular orbitals which results in a continuous density of states (DOS) right at the interface. Furthermore, an intrinsic

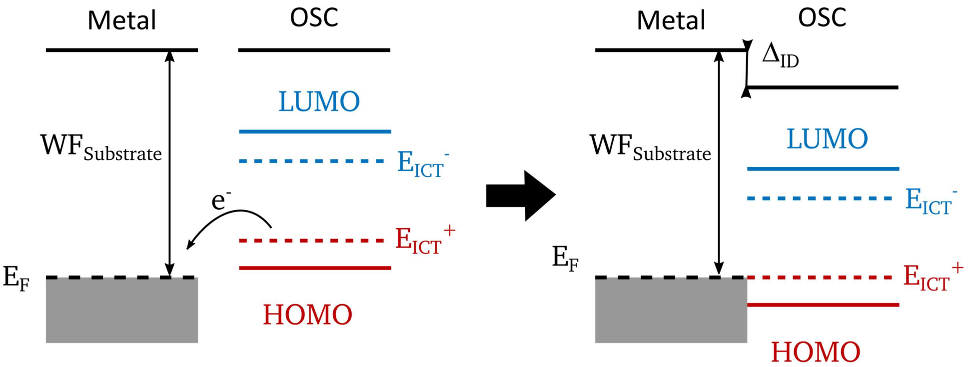

Figure 2.4-3: Integer charge transfer (ICT) at a metal | OSC interface; left: vacuum level alignment before contact; right: energy alignment with dipole formation due to the charge transfer after contact. The energy difference in electronic states before contact which determines the charge transfer is between the Fermi level of the metal and the ICT states of the OSC. The ICT states are the electronic states which take the relaxation effects originating from the charge transfer into account. Adapted from Braun et al.[35]

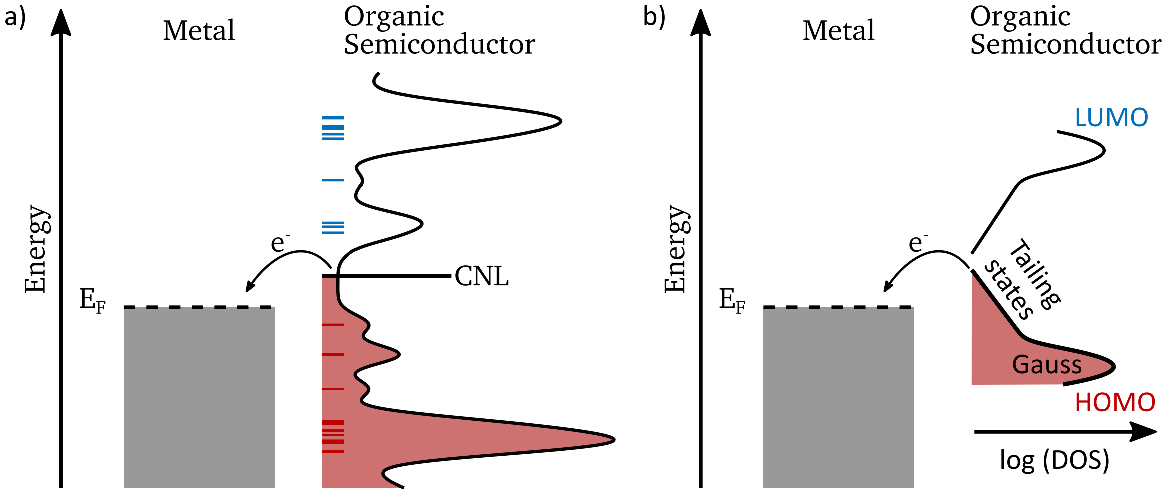

Figure 2.4-4: a) Induced density of interface states by Vázquez et al. A resonance between the molecular orbitals and the quasi continuum of states in the metal broadens the molecular orbitals which results in a continuous density of states (DOS) at the interface. The charge neutrality level (CNL) marks the level up to which the broadened DOS is occupied and determines the energy level alignment under contact formation. Adapted from Vázquez et al.[52] b) Charge transfer at an metal | OSC interface due to the presence of electronic states which tail into the energy gap. The electrons which occupy these tailing states above the metal's Fermi level will transfer under contact formation. According to Yang et al.[47] the origin for these tail states lies in structural or electronic disorder. The often by an exponential function described distribution of tailing states appears linear on the logarithmic scale.

charge neutrality level (CNL) for the OSC has been defined.[a] The difference between this CNL and the Fermi level of the metal causes a charge transfer (see Figure 2.4-4a). Due to the continuous DOS, electronic states are available throughout the energy gap range enabling charge transfer and an alignment of the Fermi level of the metal and the CNL of the OSC. As this charge transfer is again occurring in the adsorbed molecular layer right at the interface, a short-range charge separation and ID formation is observed. Vázquez, Khan, and coworkers extend the model to organic-organic interfaces describing charge transfer at the interface by difference in CNLs.[52] In their review article, Braun et al.[35] question this approach. They argue that a strong resonance interaction as between metal and OSC is no longer given for weakly (van-der-Waals based) interacting organic molecules. Thus, the assumption of a continuous induced DOS might not be justified.

For the model used in this work (see Section 5.2), tailing gap states as described in the more recent review by Yang et al.[47] are assumed to describe the experimentally observed behavior at OSC interfaces (see Figure 2.4-4b). These tailing gap states are related to structural or electronic disorder and are often described by an exponential distribution which extends the density of occupied HOMO states beyond the typical Gaussian distribution into the energy gap. The measurement of these tailing states requires for specialist setups and the low signal intensities coming from the tailing states is only visible on a logarithmic scale.

The effect of both approaches – IDIS by Vázquez et al. and tail states by Yang et al. – is similar as becomes already clear from the illustration in Figure 2.4-4. Both mechanisms result in electronic states for a charge transfer at the interface. It is just the origin of the states which

---

[a] The term "charge neutrality level" (CNL) is usually strictly used for inorganic semiconductors. Here, the CNL is the level up to which the surface states are occupied and which determines the effect of Fermi level pining.[72].

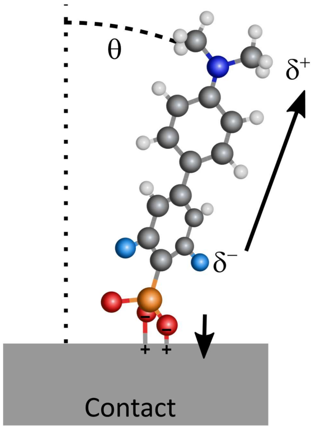

Figure 2.4-5: Molecule for a self-assembling monolayer bound to a contact surface. The molecule is designed with an electric dipole moment which shall reduce the work function of the contact material. The chemisorption of the molecule to the surface comes with a charge transfer between anchor group and contact material. The related electric dipole moment points in the opposite direction of the molecular dipole moment. In addition, only two of the three anchor group atoms have bound to the surface leading to a tilted molecule which reduces the effective molecular dipole moment. Overall, the effective work function change will be smaller as it would be expected just from the molecular dipole moment. Adapted from Benneckendorf et al. [73]

diverges. It shall be noted that the transition from an ID to a space charge region in these models depends on the separation distance of transferred charges to the interface. If charges are just transferred into localized states right at the interface, the resulting quasi-abrupt potential drop appears as an ID. If charges are also transferred into electronic states in the OSC further away from the interface, i.e., into a space charge region, the potential drop is more gradual.

Finally, molecular dipoles and strong interacting OSC contacts, where chemisorption appears, shall be considered in this summary of interface charge transfer and dipole formation. Both, molecular dipoles and chemisorption appear in the case of self-assembling monolayers (SAMs); see Figure 2.4-5. Molecules which carry a molecular dipole moment are designed to react with and bind to the contact surface to form a monolayer of aligned molecules. The dipole moments of the molecules add up and change the resulting work function of the contact. Ideally, the work function of the contact can be freely tailored by using molecules with different molecular dipoles. However, besides the molecular dipole other factors of influence have to be taken into account. The chemical reaction which binds the molecules to the contact material creates a charge transfer which results in a dipole moment which may be contrary to the molecular dipole. Additionally, the molecular dipole moments might not be aligned perfectly perpendicular to the contact surface which reduces the effective dipole moment. Lastly, in case of a metal contact, the before mentioned push-back effect also needs to be considered.[71]

# 3 Methodology

In this chapter, experimental and theoretical methods for this work will be described. A theoretical background as well as practical information will be given. The chapter starts with a presentation of the integrated ultra-high vacuum system and process of performing interface experiments, which can be seen as central part of this work. It is followed by a description of the substrate and sample preparation. The second section gives detailed information on photoelectron spectroscopy, which is the main experimental technique for this work. The last three sections are on ultraviolet-visible-near-infrared (UV-vis-NIR) absorption spectroscopy, Fourier transform (FT) infrared reflection absorption (IRA) spectroscopy, and density functional theory (DFT).

## 3.1 Interface Experiments and Sample Preparation at the Clustertool

The experiments for this work were conducted at a clustertool which is an integrated ultra-high vacuum (UHV) system. It is located at the InnovationLab GmbH in Heidelberg, Germany, in a joint laboratory of universities and industry partners. The clustertool combines several vacuum chambers for sample preparation and characterization as well as a glovebox. In Figure 3.1-1, the parts of the clustertool which are important for this work are highlighted in color: the photoelectron spectrometer (blue), the Al evaporation chamber (grey), the organic evaporation

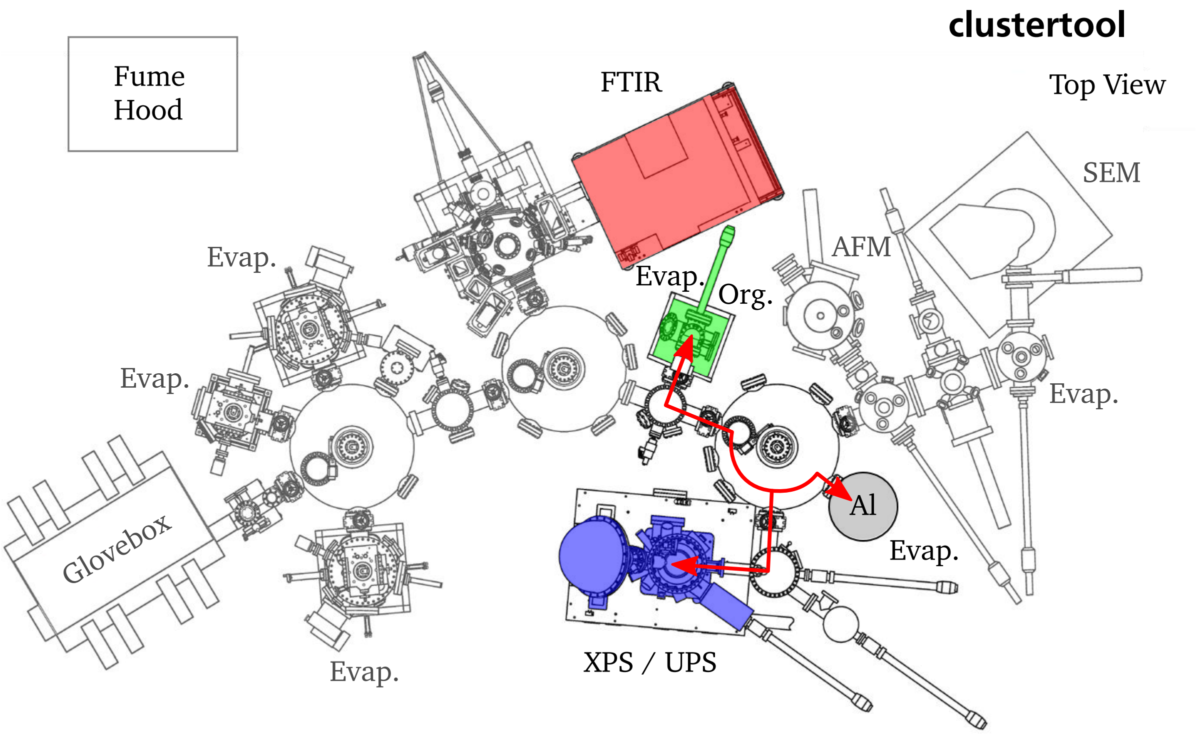

Figure 3.1-1: Top view of the clustertool at InnovationLab GmbH, an integrated ultra-high vacuum system. It consists, of several evaporation and characterization chambers, as well as an integrated glovebox. The fume hood for the substrate preparation is also shown. The irrelevant parts for this work are shaded while the important parts of the clustertool are color coded: photoelectron spectrometer (blue), FTIR spectrometer (red), organic evaporation chamber (green), and aluminum evaporation chamber (grey). The path for the in-situ sample transfer is drawn as red line. The FT-IR spectrometer was accessed from the outside. Adapted from Maybritt Kühn's dissertation.[57]

chamber (green), and the FT-IR spectrometer (red). In this setup, thin films can be deposited in vacuum and then analyzed in-situ without breaking the vacuum.

The most important experimental process for this work is the interface experiment. The procedure is illustrated in Figure 3.1-2a. For an interface experiment, a substrate is introduced to the UHV system and measured by X-ray and ultraviolet photoelectron spectroscopy (XPS and UPS). Next, the substrate is transferred to an evaporation chamber (see red path with arrows in Figure 3.1-1) where a short deposition step is performed. The sample is then transferred back for an XPS and UPS measurement followed by another deposition step. Hereby, the influence of the interface on the photoelectron spectra can be studied by observing the changes in the spectra with increasing layer thickness, i.e., from close to the interface to further away from the interface. The process is repeated until the spectra show no further change with increasing layer thickness.

Figure 3.1-2b shows the layer stacks and corresponding interfaces which are analyzed in this work. The substrate chosen for the experiments in this work is indium tin oxide (ITO) on glass. The substrates were provided by Merck KGaA, the project partner of this work. The substrates are 15 × 15 mm$^2$ and the ITO has a conductivity of about 13 Ω/cm$^2$. Before the ITO substrates are introduced into the UHV system, they are cleaned in an ultrasonic bath (*USC100TH* by VWR) using first acetone for about 10 min and then isopropanol for another 10 min. After the ultrasonic bath, the substrates are blown dry with nitrogen. XPS measurements show that after this procedure there are still hydrocarbon species on the surface. Different methods, i.e., Ar-plasma, UV-Ozone, and Ar-ion etching (sputtering) treatment, to remove these residuals are evaluated and their effect is discussed in Subsection 4.1.1. For the Ar-plasma treatment, the *Nano* low-pressure plasma system from Diener Electronic is used. The process is run for 190 s, at full power, and 0.15 mbar. The UV-Ozone treatment is performed with the *PR-100* UV-Ozone Photoreactor from UVP for 15 min. Both treatments are performed ex-situ and the substrates are in contact to air before they are introduced into the UHV system. The Ar-ion etching, however, can be performed in-situ at the photoelectron spectrometer. Here, a sputter-gun is

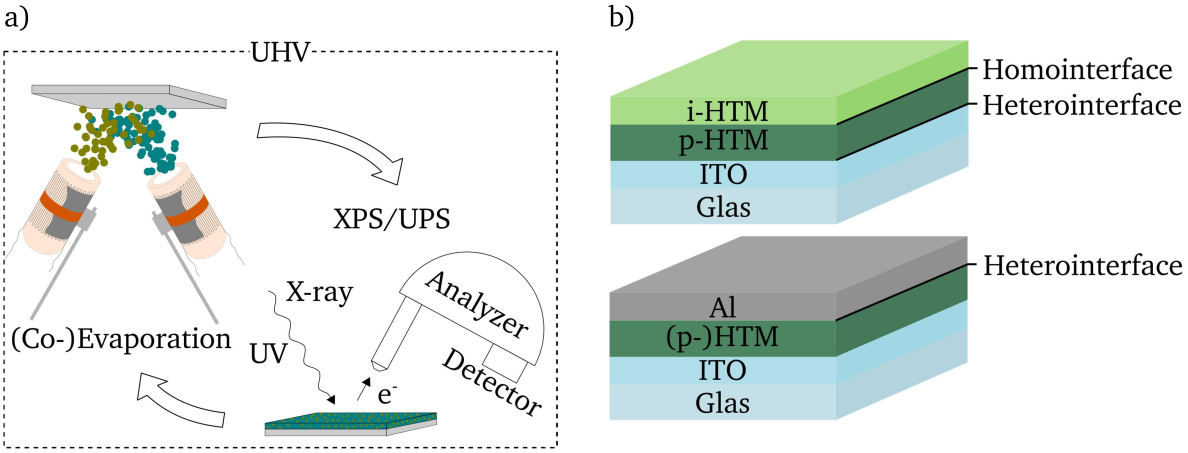

Figure 3.1-2: a) Illustration of the interface experiment process. A thin film is deposited layer by layer with consecutive XPS and UPS measurements. The whole cycle is performed in-situ without breaking the vacuum. b) Sample layer stacks which are analyzed in this work. As substrate ITO on glass is chosen. On top of the ITO, a p-doped HTM thin film is deposited by co-evaporation of the HTM and dopant molecules forming a heterointerface. Next, either an undoped HTM layer is deposited for the analysis of the formed homointerface (top), or an Al back contact is deposited forming another heterointerface (bottom). Adapted from Frericks et al.[74]

used to scan an area of 8 × 8 $\mathrm{mm}^2$ on the substrate surface for 2 min at an acceleration voltage of 3 kV.

On the ITO substrate, p-doped hole transport materials (HTMs) are deposited by co-evaporation forming a heterointerface with the ITO. For the co-evaporation process, the HTM matrix molecules and the p-dopant molecules are evaporated from two home-build effusion cell evaporation sources with aluminum oxide crucibles, Ta heating wires, and K-type thermocouples. The evaporation rate and deposition time are manually controlled by the heating current and turning the sample surface towards or away from the evaporation sources. The second type of analyzed interfaces is the homointerface between the p-doped HTM thin film and another undoped thin film of the same HTM deposited on top of the doped film (see Figure 3.1-2b top). Finally, also the heterointerface towards an aluminum back contact are analyzed. For the evaporation of Al, a commercial cold lip cell (CLC) form CreaTec is used. In this cell the rim of the pyrolytic boron nitride (PBN) crucible is positioned about 2 cm above the heated area. According to the manufacturer, this setup is especially designed for the evaporation of Al which tends to creep out of the crucible which shall be prevented by the cold lip. This evaporation cell has a shutter which can be used to control the deposition time manually. After this description of the sample preparation, the next section will cover photoelectron spectroscopy which is the main characterization technique for this work.

## 3.2 Photoelectron Spectroscopy (PES)

X-ray and ultraviolet photoelectron spectroscopy (XPS and UPS) are powerful methods regularly used in surface science. XPS allows for a chemical analysis of thin film samples including the stoichiometric composition and ionization state. Furthermore, thicknesses of thin layers in the Å to nm range can be determined. In addition, XPS and UPS are sensitive to the valence states of a material and deliver important information on the electronic structure like the work function (WF) and ionization potential (IP) of a material.[62] In the first subsection, the general principles of PES will be described and in the then following subsections more specific aspects used in this work will be addressed. The subsection about energy resolution discusses the effects on the peak width and compares the resolution in XPS and UPS measurements. The subsection about UPS deals with the He-discharge lamp and specific data analysis procedures, which are used in the analysis of ultraviolet photoelectron (UP) spectra, i.e., the removal of ghost lines and the determination of onsets by a tangent procedure. The secondary electron cut-off (SEC) is a specific spectral feature that allows for the determination of the work function of a material. Different important aspects and pit falls will be outlined. Next, the information depth of XPS and UPS and the determination of the layer thickness of thin films will be detailed. In the subsection about stoichiometry analysis the important parts of this quantification method will be presented. Finally, charging effects and their reduction by using photoconductivity are explained. The information given in the following subsections is taken from Stephan Hüfner's book *Photoelectron Spectroscopy*,[62] and the chapter *Photoelectron Spectroscopy in Materials Science and Physical Chemistry: Analysis of Composition, Chemical Bonding, and Electronic Structure of Surfaces and Interfaces* by Klein et al. in the book *Methods in Physical Chemistry*.[48]

### 3.2.1 General Principles

Historically, photoelectron spectroscopy (PES) goes back to experiments by Heinrich Hertz in 1887 and the explanation of the photoelectric effect by Albert Einstein in 1905 receiving the Nobel Prize in physics in 1921. An electron absorbs the energy of a photon and gets excited. If the excitation energy is high enough, the electron can leave the sample. In a PES setup, the kinetic energy of the electrons is analyzed, and the number of electrons per time is detected. This allows to plot the intensity in electron counts per second against the kinetic energy of the electrons. Typically, the kinetic energy of the electrons is converted to the binding energy as illustrated in Figure 3.2-1. Even though, PES on gases is possible, the following descriptions will focus on solid state samples.

The electron of an atom in a sample which absorbs the energy of a photon gets excited overcoming its binding energy with respect to the Fermi level of the sample. It can then transit from the sample to the vacuum by overcoming the WF of the sample. The remaining energy of the electron is in form of kinetic energy and can be analyzed. Finally, the electron is detected in the spectrometer. If the sample is conductive and properly connected to the spectrometer, the Fermi levels of sample and spectrometer align. As the electron is detected in the spectrometer, not the WF of the sample but the WF of the spectrometer has to be known or calibrated. Knowing the WF of the spectrometer and the energy of the exciting photons $h\nu$, the binding energy of the electron $E_\mathrm{B}$ can be calculated from the measured kinetic energy of the electron $E_\mathrm{kin}$:

$$E_\mathrm{B} = h\nu - E_\mathrm{kin} - \mathrm{WF}_\mathrm{Spectrometer} \tag{4}$$

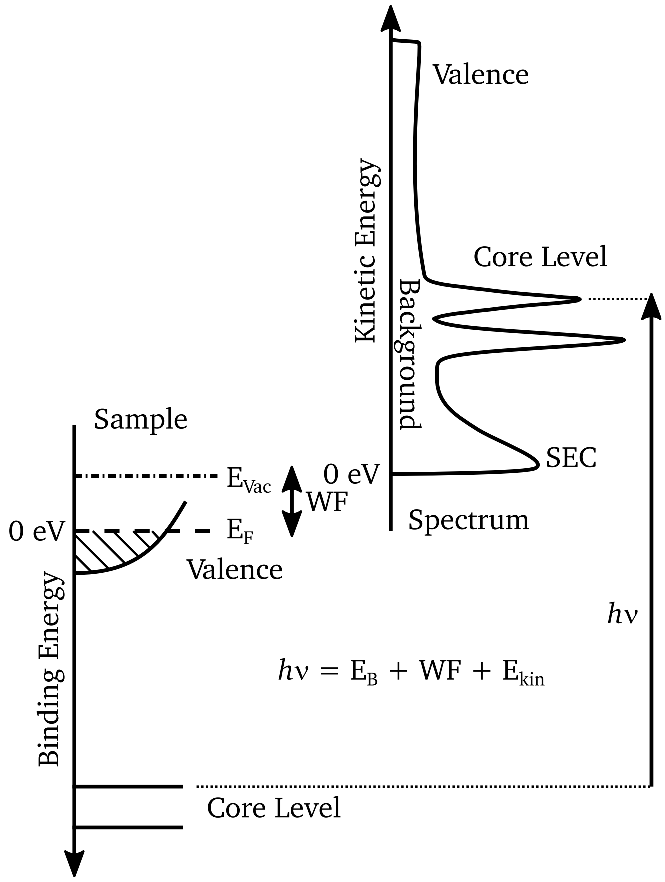

Figure 3.2-1: Illustration of the relation between binding energy and kinetic energy of the photoemitted electrons. Electrons which absorb the defined energy of a photon overcome their binding energy with respect to the Fermi level ($E_\mathrm{F}$) and the work function (WF). The electron holds the remaining energy in form of kinetic energy which can be analyzed. Adapted from Stefan Hüfner's book *Photoelectron Spectroscopy*.[62]

The binding energy of an electron is characteristic for the element and the respective core level from which the electron is excited. This allows for a qualitative chemical analysis of the sample, to identify the elements that are present in the sample or on its surface. Furthermore, the intensity, i.e., the number of electrons, which is measured for a specific element is proportional to the amount of the element present in the sample. Thus, also a quantitative analysis of the stoichiometry is possible as is further described in Subsection 3.2.7.

Besides identifying the element, also information on the oxidation state of the element can be gathered by XPS. The so-called chemical shift describes the fact that the binding energy of an electron in a core level is slightly influenced by the electron density around the respective atom. If the energy resolution, which is further discussed in Subsection 3.2.3, is fine (high) enough, these chemical shifts can be resolved.

Furthermore, the binding energy of the electrons is not only influenced by the chemical surrounding of the atoms but also by the electrostatic potential distribution in the sample. This means that, if the electrostatic potential distribution of the sample changes, e.g., due to charging effects or the presence of a space charge region, the energetic position of the electronic levels is shifted with respect to the position of the Fermi level, i.e., the measured binding energy changes. This effect allows for the analysis of the electronic structure at interfaces. If a material is deposited step by step in an interface experiment as described in Section 3.1, the shift of the spectra with increasing layer thickness can reveal the formation of a space charge region at the interface (see Section 2.4).

### 3.2.2 Photoelectron Spectroscopy Setup

A PES setup might look like the one that was used for this work and is shown in Figure 3.2-2. In general, a PES setup consists of an X-ray source, a sample stage, electron optics, an analyzer and a detector, and additional optional equipment. As the emitted electrons strongly interact with matter, ultra-high vacuum conditions are needed for the electrons to reach and pass the analyzer. The system used for this work is a *VersaProbe 5000* system from Physical Electronics Inc. The X-ray source is a monochromatized Al-K$\alpha_{1,2}$ source with an excitation energy of 1486.6 eV and an approximate line width (full width at half maximum) of 0.26 eV.[75] The X-ray beam has a diameter of about 200 $\mu$m and is smaller than the area covered by the electron optics. Thus, the X-ray beam size determines the analyzed area. The beam power of the electrons generating the X-rays is 50 W. The installed *hot/cold* sample stage of the *VersaProbe 5000* system allows for adjusting the position, tilt, and rotation of the sample as well as heating or cooling the sample with a specific sample holder. If not specified differently, spectra in this work were recorded at a take-off angle θ of 90° to the sample surface plane. The electrons optics of the setup include a retardation field which allows to scan the electron kinetic energies and operate the analyzer with a constant pass energy which keeps the energy resolution constant (see next Subsection 3.2.3).

The detector is a multichannel detector operating with a pair of microchannel plates and a sixteen channel anode.[75] Additionally, the setup has a He-discharge lamp, an Ar-sputter gun, and an ultraviolet (UV) light emitting diode (LED) installed. The He-discharge lamp which serves as UV photon source is further described in Subsection 3.2.4. The Ar-sputter gun is used

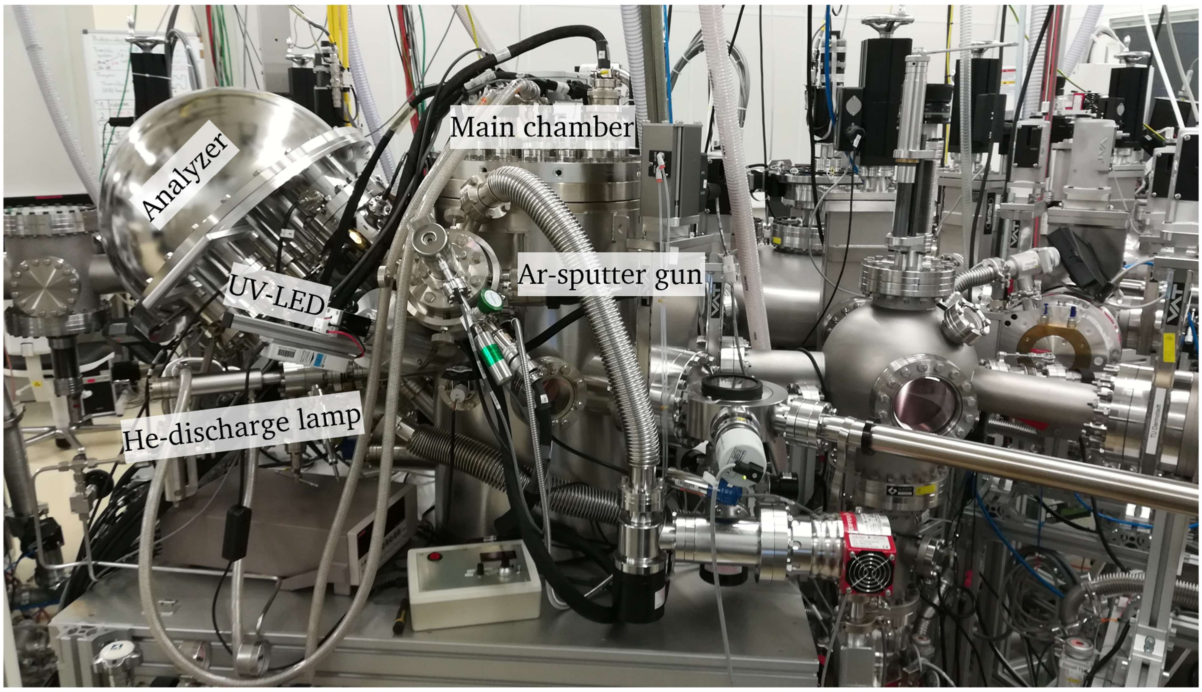

Figure 3.2-2: PES setup VersaProbe 5000 which was used in this work and is connected to the integrated UHV system named clustertool in Heidelberg at InnovationLab GmbH. The cylindrical main chamber with the monochromatized X-ray source and sample stage are barely visible behind the several attachments, cables, and tubes. Furthermore, the analyzer, He-discharge lamp, UV-LED, and Ar-sputter gun are labeled.

for cleaning surfaces by Ar-ion etching as described in Section 3.1. Last but not least, the UV-LED is used to avoid charging effects by using the photoconductivity in organic semiconductors as described in Subsection 3.2.8.

### 3.2.3 Energy Resolution

The energy resolution of a photoelectron spectrometer is influenced by the line width of the excitation source and the energy resolution of the analyzer. As mentioned before, the line width of the monochromatized X-ray beam is stated with 0.26 eV full width at half maximum (FWHM) in the manual by the manufacturer.[75] The energy resolution of the analyzer depends on the pass energy. The analyzer used in the setup for this work is a spherical capacitor analyzer or sometimes also called hemispherical analyzer. It is built up by two concentric hemispheres which are oppositely charged to create an electric field which deflects the beam of incoming electrons. Only the electrons with the right energy, i.e., the pass energy, can pass the analyzer. The electrons which are too slow hit the inner hemisphere and the electrons which are too fast hit the outer hemisphere. A lower pass energy will result in a smaller energy spread, i.e., a better energy resolution, but at the cost of a lower signal. Vice versa, higher pass energies lead to a higher signal but broader energy resolution. The FWHM of the analyzer energy resolution is stated to be 0.015 times the pass energy.[75] In this work, for the detailed core level spectra measured by XPS a pass energy of 11.75 eV is chosen which results in FWHM of the analyzer energy resolution of 0.176 eV.

For UPS measurements of the valence region, the signal is more intense and thus the pass energy can be chosen lower at 2.95 eV resulting in an FWHM of 0.044 eV for the analyzer energy resolution. Furthermore, survey spectra of the full accessible binding energy range of XPS are

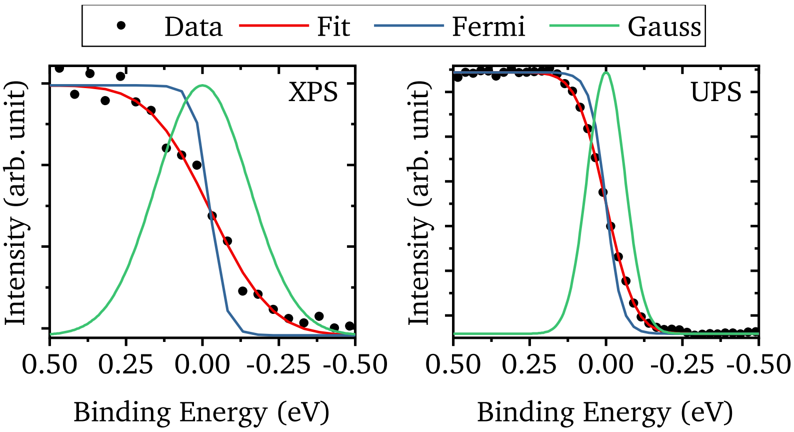

Figure 3.2-3: Experimental method to determine the spectrometer energy resolution. The Fermi edge of a clean Ag sample is measured and then fit by the convolution of the Fermi-Dirac distribution at 20°C and a Gaussian function. The width of the Gaussian function gives the energy resolution of the setup. Shown are spectra, fits, and fit components for an XPS measurement at 11.75 eV pass energy and a UPS measurement at 2.95 eV pass energy.

measured at 187.85 eV pass energy to get enough intensity in a quick measurement for a general overview. UPS measurements of the secondary electron cut-off are measured at 0.59 eV pass energy because the high signal allows for a very precise energy resolution. In addition, the detector can only handle a signal of $1.6 \cdot 10^7$ counts per second and thus the pass energy can be used to reduce the intensity of the passing electron beam to protect the detector. An experimental method to determine the energy resolution of the spectrometer is shown in Figure 3.2-3. The Fermi edge of clean Ag sample is measured and then fit by convolution of the Fermi-Dirac distribution function and a Gaussian function. The broadening of the Fermi-Dirac distribution is fixed to a room temperature of 20°C. However, the width of the Gaussian function serves as fit parameter and represents the energy resolution of the spectrometer. The fitting of the Fermi edge measured by XPS results in a Gaussian FWHM of 0.358 eV while the fitting of the respective UP spectrum yields an FWHM of 0.146 eV. For XPS, this result is slightly larger than from the line width and pass energy expected value of 0.314 eV. For UPS, the line width of the He-I emission should be negligibly small in the range of some meV[76] and the analyzer energy resolution is much smaller than the actual spectrum broadening. Thus, other components of the spectrometer, e.g., the electron optics, seem to play a significant role at low pass energies. Still, the energy resolution in UP spectra is better compared to the X-ray photoelectron (XP) spectra and thus, UPS is better suited to determine precise electronic property values of a material.

### 3.2.4 Ultraviolet Photoelectron Spectroscopy (UPS)

The UP spectra for this work were measured by excitation with the He-I emission from a He-discharge lamp. In the He-discharge lamp, He flows through a small capillary where a plasma is glowing, emitting the characteristic light of the excited He and also excited He-ions. The lamp is setup up with differential pumping in two stages: a rough vacuum stage and an ultra-high vacuum stage. The differential pumping keeps the pressure difference between the capillary and the spectrometer's main chamber. The pressure in the capillary influences the ratio between the different emission lines of the excited He and He-ions. Lowering the pressure increases the mean free path in the plasma and increases the number of ions. The more ions the higher the intensity of the He-II emission.[77–79] For the measurements in this work, the He-discharge lamp was operated at a pressure of $10^{-1}$ mbar in the rough pumping stage and at a current of 80 mA to obtain a strong He-I emission. In case the He-II emission is used, the pressure is lowered to $2 \cdot 10^{-2}$ mbar and the current is increased to 200 mA.

Beside the He-I emission with an excitation energy of 21.2 eV and the He-II emission with an excitation energy of 40.8 eV, other weaker emission lines of He exist. These other emission lines are called satellite lines and cause additional spectral features in UP spectra. For example, the next strongest satellite line of the He-I emission is 1.87 eV higher in energy.[79] As a results, this satellite line excites electrons from the same valence states as the He-I emission, but the electrons have a 1.87 eV higher kinetic energy. Thus, these electrons appear at 1.87 eV lower binding energies in comparison to the electrons which were excited by the He-I emission. In conclusion, the spectra measured by the He-discharge lamp are a convolution of the true spectrum shifted and scaled by the energy difference of the He-emission lines and their relative intensity, respectively. To deconvolute the spectrum the following system of linear equations is solved (adapted from Patrick Reiser[80]):

$$\mathbf{S}\,\mathbf{t} = \mathbf{m} \tag{5}$$

where **t** is the data vector of the true spectrum and **m** is the data vector of the measured spectrum. **S** is the square matrix that contains the information of the He-emission satellites. It is the identity matrix plus the satellite intensities on selected side diagonals. The rows of the data vector and the columns of the satellite matrix correspond to the data points with a constant binding energy step size while the value contains the intensity information. After filling the satellite matrix based on the relative energy and intensity of the He-emission lines, the system can be solved for the true spectrum **t**.[80] The energy difference between the He-emission lines is well-known but their relative intensities depend on the pressure and the setup. Thus, the values were optimized based on the reference valence spectrum of a clean Ag sample. Still, by comparing a broad set of Ag calibration spectra from several experiment days, it is found that the conditions vary too much to obtain a ghost line removal sufficient for the detection of gap states on a logarithmic scale. However, the analysis of the data on a linear scale the procedure is sufficient. To truly obtain a ghost line free spectrum, a monochromator for the He-discharge lamp is needed.

Once the ghost lines are removed from the UP spectra, they can be analyzed for their relevant spectral features. These features are the valence band maximum onset or highest occupied molecular orbital (HOMO) onset in the case of organic semiconductors, and the onset of the secondary electron cut-off. The standard procedure to determine these onsets is a tangent procedure, as shown for the example of the HOMO onset of a m-MTDATA thin film in Figure

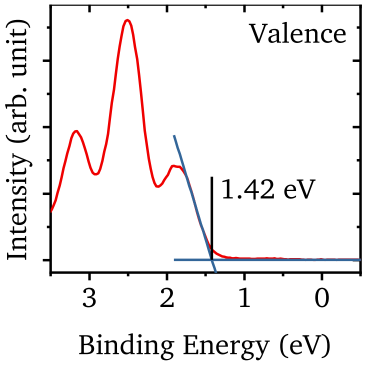

Figure 3.2-4: Illustration of the tangent procedure to determine the HOMO onset in this valence spectrum of a m-MTDATA thin film. One straight line is fit to the side of the first spectral feature and one straight line is drawn horizontally at the averaged value of the background above the Fermi level. The intersection of both lines marks the onset.

3.2-4.[57,81] In this procedure, the low binding energy side of spectral peak is fit by a straight line. Therefor, the limits for the linear fit are set at 75% and 25% of the maximum peak intensity. Furthermore, the average of the background above the Fermi level is taken and a horizontal line is placed at this constant value. Finally, the intersect of the tangent to the peak side and the constant average background marks the onset. In some cases, the limits of the linear fit need to be adjusted. In the case of a Gaussian spectral profile and a tangent that goes straight through the inflection point, the intersect, i.e., onset, will be two times the Gaussian standard deviation ($2\sigma$) from the peak maximum of the Gaussian profile.[47] Another way to determine the valence onset is applying the tangent procedure to a logarithmic intensity plot of the spectrum. This method is often found in field of metal halide perovskite absorber materials for solar cells.[82] However, as pointed out by Tim Hellmann[83] and similarly observed during the work for this thesis, the background of the spectrum is also significantly increased in the logarithmic plot. Thus, especially for non-monochromatized UPS measurements, the distinction between the background noise and states which tail into the energy gap is difficult or nearly impossible. For this reason, this logarithmic method was not used in this work.

### 3.2.5 Secondary Electron Cut-off and Work function

The secondary electron cut-off (SEC) is an important spectral feature for the analysis of the electronic structure of a material as it allows for the determination of the work function (WF). The SEC can be understood with the model of the three-step process in PES which is depicted in Figure 3.2-5. This model is important because often the emission of a photoelectron is imagined as a one step process of excitation and immediate emission.

The first step is the photoexcitation of an electron from an occupied state in the material to an excited unoccupied state. This step marks the usual photoemission process, and the excited electrons are called primary electrons. If these primary electrons leave the sample without losing energy due to inelastic scattering processes, they are detected with their characteristic binding energy.

The second step is the transport of the excited primary electrons to the surface of the sample. Some of the primary electrons scatter inelastically during the transport transferring part of their energy to other electrons which are thereby excited. These electrons which are excited by inelastic scattering events are called secondary electrons. The amount of energy that is transferred during the inelastic scattering processes may vary and thus the secondary electrons will be excited into unoccupied states at all available energies down to the conduction band minimum for an inorganic semiconductor, the Fermi level for a metal, or the LUMO for an organic semiconductor. Thus, the secondary electrons create a background signal for the primary electrons.

The third step is the transfer from the sample through the surface into vacuum. For this transfer, the electrons (primary or secondary) have to overcome the vacuum energy (also called vacuum level). Thus, only the electrons which occupy states energetically above the vacuum level can leave the sample into the vacuum. All electrons of lower energy remain in the sample and cannot be detected forming the characteristic cut-off. As the electrons in the states around the vacuum level energy are usually secondary electrons, the spectral feature is called secondary electron cut-off.

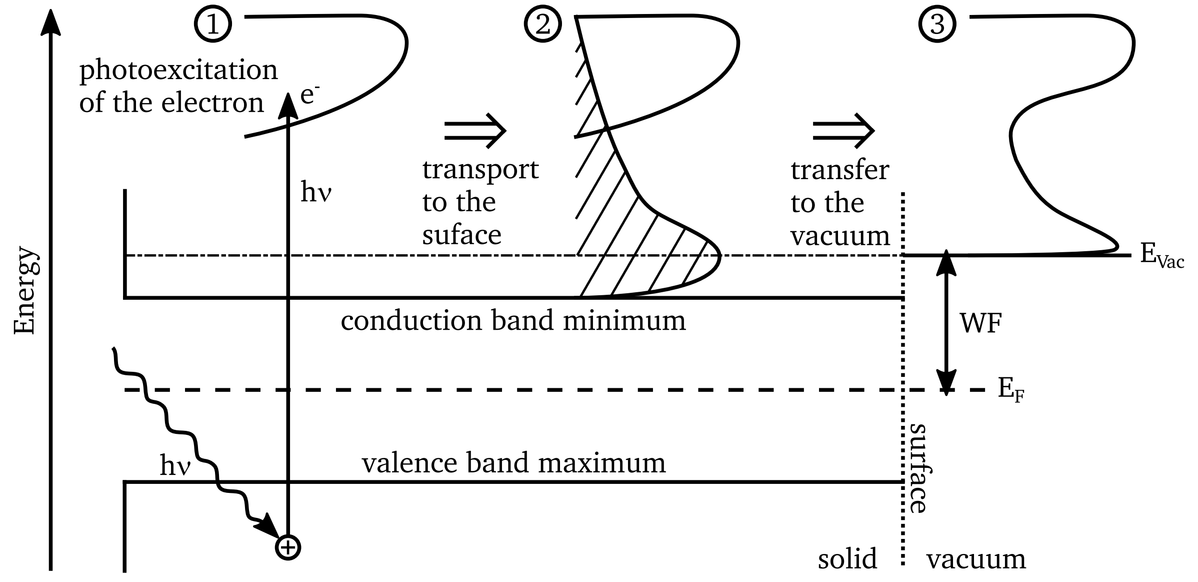

Figure 3.2-5: Illustration of the three-step model for secondary electron cut-off. First, primary electrons get excited into an unoccupied state of the sample by absorption of photons with energy $h\nu$. Second, the primary electrons are transported to the surface. Some of the primary electrons scatter inelastically during the transport process exciting secondary electrons which occupy unoccupied states of lower energy down towards the conduction band minimum of a semiconductor. Third, only the primary and secondary electrons which are in excited states energetically above the vacuum level can transfer from the sample to the vacuum. The electrons of lower energy get cut-off, remain in the sample, and cannot be detected. Adapted from Stefan Hüfner's book *Photoelectron Spectroscopy*.[62]

The electrons which have just enough energy to overcome the vacuum energy, thus, have only very little kinetic energy after the transition to the vacuum. In consequence, these electrons are too slow to reach and pass the analyzer. It is therefore necessary to accelerate these electrons by applying a negative bias potential to the sample. It shall be mentioned that this bias potential affects all energy levels including the vacuum level and thus does not enable electrons with too little energy to transfer to the vacuum but only accelerates the electrons which already have enough energy for the transition.[84] The spectra, which were measured with applied bias, are afterwards corrected for it. The bias used in this work for the SEC measurements is -7 or -5 V. After the respective correction, the different bias does not affect the position of the cut-off, i.e., the WF, but the intensity of the cut-off as the stronger acceleration allows for more electrons to reach and pass the analyzer. As it was found that the bias of -7 V led in some cases to overly high signals, the bias was reduced to -5 V.

As shown by Helander et al.,[84] it is important that the SEC measurement with applied bias is recorded under a take-off angle of 90° to the surface plane, i.e., normal to the surface and straight towards the electron optics and the analyzer entrance slit. Otherwise, electrons of very low kinetic energy which mark the SEC onset and define the WF cannot reach the electron optics as they get accelerated normal to the sample surface, i.e., past the electron optics at take-off angles smaller 90°. The slowest electrons are most strongly affected by the electric field, while the faster electrons with higher kinetic energy are less affected. Thus, electrons of higher kinetic energy still reach the analyzer and get detected as cut-off electrons as their higher energy results in a higher WF than which would be measured under 90° take-off angle.[84]

Besides the take-off angle, also inhomogeneities of the sample surface affect the determined WF.[84–86] In the work of Schultz et al.[85,86] and Helander et al.,[84] the researchers study defined patterned surfaces with areas of different WFs. The SEC spectra of these mixed WF surfaces show spectral features of two SECs. One SEC at lower kinetic energy (higher binding energy) for the low WF areas and one SEC at higher kinetic energy (lower binding energy) for the high WF areas. Depending on the resulting spectral shape of the two overlapping SECs, it could easily be the case that only the low WF SEC gets recognized while the higher WF SEC is unnoticed.

Especially, if a surface is not well defined patterned but simply has a inhomogeneous structure with areas of several WFs, only the lowest WF will be determined.[86] Furthermore, on the other side of the spectral range, the determination of the valence band maximum onset of an inorganic semiconductor or HOMO onset of an organic semiconductor would take the signal that is closest to the Fermi level.[86] The ionization potential of a material can be taken from the sum of the WF and the HOMO onset to Fermi level energetic distance. If the analysis of the measurements on an inhomogeneous surface obtains the smallest WF and the HOMO onset closest to the Fermi level, the determination of the ionization potential of a material with an inhomogeneous electronic surface structure will always lead to a too small value.[86]

### 3.2.6 Information Depth and Layer Thickness

As the name reveals, photoelectron spectroscopy (PES) probes electrons which are charged particles that strongly interact with matter. Thus, the inelastic mean free path (IMFP) of electrons in a material, i.e., the distance electrons can travel on average before they scatter inelastically, is rather small, in the range of some nanometers. Therefore, the electrons which are detected in PES are coming from just 10-15 nm below the surface rendering PES a quite surface sensitive technique.

The often cited work by Seah and Dench[87] shows a *universal curve* as sketched in Figure 3.2-6 for the dependence of the IMFP on the kinetic energy of the electrons. The inelastic scattering processes limiting the IMFP of the electrons are mainly electron-electron collisions. At high energies, the electrons can be treated as free electron gas resulting in a universal character for approximately all materials. However, at lower energies material specific properties like the energy gap of a semiconductor or the plasmon energy play an important role revoking the universal character. While the *universal curve* is useful for some general estimations, there are other methods to estimate the IMFP for a specific material. The so-called *TPP-2M* equation was derived by Tanuma, Powell, and Penn who measured several organic materials.[88] The equation is implemented in the *NIST* database software[89] and considers different material properties, like stoichiometric composition, number of valence electron, energy gap, and density. As the *TPP-2M* equation was specifically designed based on organic materials it is used in this work to obtain IMFPs for the studied materials.

Assuming an exponential Lambert-Beer type damping (6) of a substrate signal by a deposited overlayer, the thickness of the overlayer $d$ can be determined. The intensity of the substrate signal damped by an overlayer $I_{\mathrm{Substrate}}$ is given by:

$$I_{\mathrm{Substrate}} = I^{0}_{\mathrm{Substrate}} \exp\left(-\frac{d}{\lambda \sin\theta}\right) \tag{6}$$

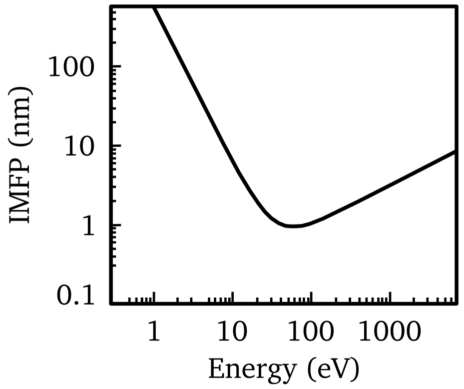

Figure 3.2-6: Sketch of the so-called *universal curve* which shows the inelastic mean free path of an electron in a material dependent on the electron's kinetic energy. Adapted from Seah and Dench.[87]

where, $I^0_{\mathrm{Substrate}}$ is the intensity of the substrate signal without an overlayer, $\lambda$ is the effective attenuation length and $\theta$ is the take-off angle with respect to the surface plane.[90] For this work, $\theta$ is 90° and thus sinus is one.

The effective attenuation length and IMFP are often used interchangeably, however, this is not entirely correct. For the path of the electrons towards the surface, not only inelastic scattering but also elastic scattering which changes the path of the electrons plays a role.[90] The influence of elastic scattering is especially strong for small take-off angles and high atomic numbers.[91] In this work, the IMFP is still substituted for the effective attenuation length as the organic materials contain elements of relatively small atomic numbers and a large take-off angle of 90° is used. In this case, the simplification might lead to an error of about 10% in the layer thickness determination.[91]

In this work, the layer thicknesses of the organic layers deposited on ITO are determined from the damping of the In $3d_{5/2}$ emission peak following Eq. (6). This is possible as long as there is still an In $3d_{5/2}$ signal detected. At larger adlayer thicknesses where the In $3d_{5/2}$ signal is insufficiently weak or has vanished, the thickness can no longer be found out directly. In this case, a deposition rate is calculated from the layer thicknesses and deposition times of the first deposition steps. Then, the thickness of the thicker layers is extrapolated by the deposition rate, which is assumed to be constant for the rest of the experiment and deposition time. For UPS, the kinetic energy of the emitted electrons is small and the material specific differences in the effective attenuation length therefore might be large. Overall, there are only a few reports of the effective attenuation length for the valence region of organic semiconductors. The articles of Ozawa et al.[92] and Graber et al.[93] state values between 0.3 and 3 nm strongly dependent on the kinetic energy of the electron. For this work, the effective attenuation length is determined specifically for the used materials, as described in Subsection 5.1.1.

### 3.2.7 Stoichiometry Analysis

In this work, the stoichiometric composition of the deposited layers is analyzed, and the atom ratios are cross checked with the expected ratios from the molecular structure. A stoichiometric analysis by XPS is based on the intensity of the orbital emissions from the different elements present in a sample. The ratio $x_{\mathrm{i}}$ of an element i with respect to all elements n in the sample is given by:

$$x_{\mathrm{i}} = \frac{\tilde{I}_{\mathrm{i}}}{\sum_{\mathrm{i}}^{\mathrm{n}} \tilde{I}_{\mathrm{i}}}, \qquad \text{with} \qquad \tilde{I}_{\mathrm{i}} = \frac{I_{\mathrm{i}}}{ASF_{\mathrm{i}}}, \tag{7}$$

where $I_{\mathrm{i}}$ is the area under the peak of element i, and $ASF_{\mathrm{i}}$ is the corresponding atomic sensitivity factor.

Before the area under a peak can be determined, the secondary electron background signal has to be subtracted, as the background is not related to the amount of an element present in a sample. In this work, a Shirley type[94,95] or linear background function is used depending on the spectrum.

The atomic sensitivity factor is a correction term that is necessary because the intensity of the orbital emission from an element does not only depend on the amount of the element but has several influencing factors. Therefore, the ASF is given by:

$$ASF = \sigma(h\nu, element, orbital) \cdot f(\beta, \alpha) \cdot T(E_{\mathrm{kin}}, E_{\mathrm{Pass}}) \cdot ED(E_{\mathrm{kin}}) \tag{8}$$

Here, $\sigma$ is the photoionization cross section which depends on the excitation energy of the used light source, the element, and the electronic orbital. It is a quantum mechanical value that is calculated and tabulated by Scofield for the typical excitation energies 1254 eV (Mg $\mathrm{K}_\alpha$) and 1487 eV (Al $\mathrm{K}_\alpha$).[96] $f$ denotes a correction term for the angular distribution of the photoelectron emission which varies among different electronic orbitals. $f$ requires the asymmetry parameter $\beta$ which is tabulated by Reilman et al.[97] as well as the angle $\alpha$ between the source and the analyzer. $f$ is given by:

$$f(\beta, \alpha) = 1 + \frac{\beta(element, orbital)}{4}(1 - 3cos^2\alpha) \tag{9}$$

For $\alpha = 54.73°$ the term $1 - 3\cos^2\alpha$ gets zero and $f$ can be neglected. Therefore, the angle of 54.73° is also called magic angle and thus $f$ is sometimes referred to as magic angle correction.

$T$ is a correction factor that depends on the spectrometer and is called transmission function. It depends on the kinetic energy of the electrons and the pass energy of the analyzer that is selected. For the setup used in this work, the transmission function is approximated by the following equation and the parameters $a$ and $b$ are obtained from a calibration measurement:

$$T(E_{\mathrm{kin}}, E_{\mathrm{pass}}) = E_{\mathrm{pass}} \left( \frac{a^2}{a^2 + \left(\frac{E_{\mathrm{kin}}}{E_{\mathrm{pass}}}\right)^2} \right)^b \tag{10}$$

Finally, $ED$ is the escape depth correction of the electrons. It corrects for the fact that electrons with higher kinetic energy can escape from greater depth in the sample and thus the corresponding element is probed in a larger volume resulting in comparably higher intensity. If the sample contains an element with two different orbital emissions in the accessible spectral range and the other parameters for the ASF value are known as described, the escape depth correction can be evaluated. Ideally, the ASF corrected intensities of two different orbital emissions from the same element should yield the same value. For this work, this method is unfortunately not possible. Thus, the stoichiometry in this work is analyzed with the software CasaXPS and the *TPP-2M* (see Subsection 3.2.6) option is chosen for the escape depth correction. In general, it should be noted that there are many influencing factors when determining the stoichiometry with XPS and that the analysis considers a homogeneous distribution of the elements.[48]

### 3.2.8 Charging Effects and Counter Measures

This subsection is mainly based on the articles by Cros[98] and Yu et al.[99]

As mentioned in Subsection 3.2.1, a prerequisite for the there presented energy scheme is a high conductivity and properly grounding of the sample. If, however, an insulating sample or a low conducting sample is measured by PES, charging effects will appear. The photoionization process generates positive charges which need to be compensated by a current from the ground. If the resistance of the measured sample is too high, positive charges cannot be compensated in time and will accumulate at the surface. The result is a potential drop across the sample. The respective energy level diagram of a low conductivity organic thin film deposited on a conductive ITO substrate is shown in Figure 3.2-7. The ITO substrate is connected to the spectrometer and its Fermi level is well aligned with the one of the spectrometer.

At the surface of the organic semiconductor, however, positive charges have accumulated creating a potential which shifts the electronic states of the semiconductor with respect to the spectrometer Fermi level. As a result, the measured photoelectron peaks from the organic thin film will be shifted to higher binding energies. The diagram is a simplified sketch, and the distribution of the charges and the resulting potential might be more complex. Furthermore, if the potential varies laterally on the surface due to inhomogeneities or the potential change is steep with respect to the information depth of XPS, a superposed signal from electronic states at different potentials, i.e., effective binding energies, will lead to a broadening of the measured peaks (see Section 5.2).

To counter act the charging of insulating or low conductivity samples and still enable a PES measurement, different methods are available of which some are mentioned in the following.

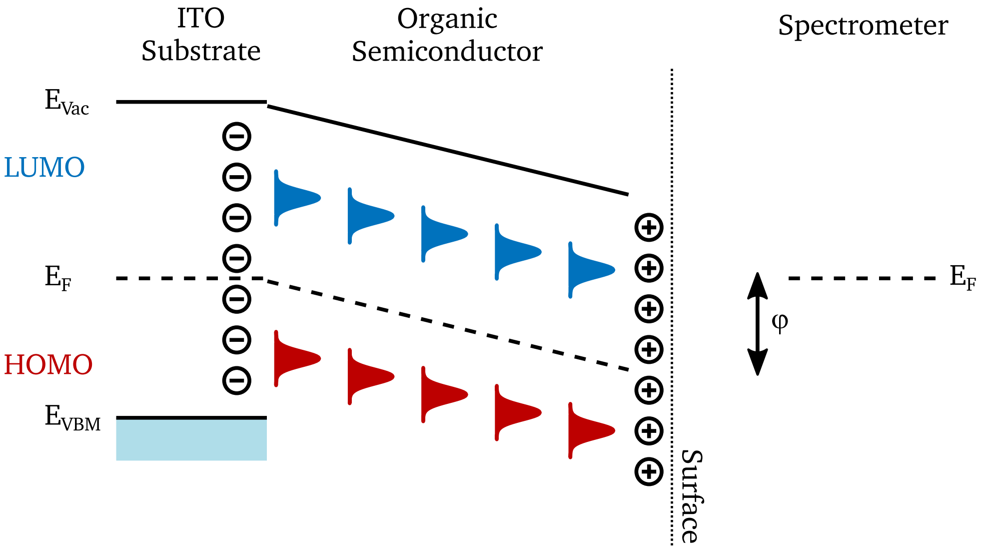

Figure 3.2-7: Energy level diagram for an insulating or low conductivity thin film on a conducting substrate in PES. The conducting substrate is grounded, and its Fermi level is aligned with the Fermi level of the spectrometer. Due to the low conductivity of the deposited thin film, the positive charges generated by the photoionization at the surface cannot be compensated. A potential drop across the thin film shifts its electronic states by $\varphi$ with respect to the spectrometers Fermi level. Adapted from A. Cros.[98]

Very common is the use of an electron flood gun. Here, low energy electrons are directed to the sample surface to compensate for the emitted photoelectrons. This technique is quite effective, but it is difficult to determine the right amount of compensation, and often an overcompensation is obtained. A meaningful interpretation of the Fermi level position is not possible.[48] An additional problem in the case of organic materials is the damage of molecules by the incoming electons.[100] Another method is to study only very thin samples. This method relies on the fact that the resistance increases with the thickness of the sample. Thus, if only thin films are measured on a conductive substrate, the resistance might be low enough to avoid significant charging effects. The available thickness strongly depends on the conductivity of the material which is studied. In principle, this technique allows for the study of the electronic structure of poorly conductive materials. However, the thickness of the film needs to be thin enough to avoid charging effects and thick enough not to be affected by interface effects, e.g., space charge regions.[48]

Finally, Koch et al. showed that for organic semiconductors photoconductivity can be utilized to enhance the conductivity of organic thin films and enable a PES measurement.[100,101] If light with an energy higher than the optical energy gap of the material is shone onto the sample, excitons are created of which some will dissociate providing additional mobile charge carriers and increasing the conductivity.[13,100] The method was tested before at the same setup used in this work by using an UV-LED lamp with a wavelength of 365 nm.[57,102] It proved to be very effective, especially for undoped organic semiconductors. At small thicknesses, where charging effects do not yet play a role, the electronic structure is the same with or without the light from the UV-LED. At large thicknesses using the UV-LED revokes the charging induced shifting and broadening of the spectra resulting in unshifted and sharp peaks.[57] For this reason, the same UV-LED which is an 11 W RSW-P11-365-0 High Efficacy UV LED Emitter from *Roschwege*[103] was also used for the measurements in this work. Furthermore, a peculiar effect of photoelectron emission excited by this LED was observed although the photon energy should be too small to generate photoelectrons (see Chapter 7). During the study of this effect, two other LEDs were tested: a 10 W RSW-P10-400-0 High Efficacy UV LED Emitter from *Roschwege*[104] with a wavelength of 400 nm and a combination of three L1C1-CYN1000000000 LUXEON C Color Line LEDs from *Lumileds*[105] with a wavelength between 490-510 nm.

Additionally, surface photovoltage effects[83,106,107] may be induced and should be considered when using these LEDs. A surface photovoltage is build up in the same way as the open circuit voltage in a solar cell. Electron hole pairs are generated by photon excitation and separated by the electric field of a space-charge region. The resulting electrostatic potential counteracts the energy level bending at the space-charge region and changes the binding energy of the electronic states with respect to the Fermi level. The requirements for a surface photovoltage are: i) generation of electron hole pairs, ii) a space-charge region which separates the charge carriers, iii) a layer stack structure where the top layers are connected to ground only through the bottom electrode, and iv) sufficiently high mobility and lifetime, i.e., diffusion length, of the charge carriers. The lifetime will be influence by recombination processes in the bulk as well as on the surface.[83,106,107] While requirements i) and ii) are fulfilled for some of the samples studied, requirements iii) and iv) are probably not given. The investigated thin films are deposited by evaporation without a shadow mask and therefore unlikely to be strictly grounded only through the bottom contact. In addition, the charge carrier mobility in organic materials is low and it is difficult to separate electron hole pairs due to a low dielectric permittivity and the related high coulombic potential (see Section 2.1). Consequently, a surface photovoltage seems less likely to occur for the experiments in this work. Also, a surface photovoltage was not found in the similar studies using these LEDs mentioned above.[57]

## 3.3 UV-vis-NIR Absorption Spectroscopy

UV-vis-NIR absorption spectroscopy is a method to analyze the absorption of light in a material in the range from ultraviolet (UV) over visible (vis) to near-infrared (NIR) in the electromagnetic spectrum. In the UV-vis spectral range, electronic transitions are excited by the incident light. For NIR, mostly overtones and combinations of fundamental vibrational excitations of the sample are analyzed.[13,108] For the measurements in this work, a very simple setup is used as shown in Figure 3.3-1. The sample is placed over a hole in the table. Above the sample a collimating lens with an optical fiber is mounted from which the light source comes. The light source is a combination of a halogen (for vis and NIR) and a deuterium (for UV) lamp (AvaLight-DH-S-BAL) from *avantes*.

Below the hole, a collimating lens and an optical fiber collect the light that is transmitted through the sample and guide it to the spectrometer. To access the UV-vis range (200-1100 nm) an AvaSpec ULS3648 and for the NIR range (1050-2050 nm) an AvaSpec NIR256-2.2TEC spectrometer from *avantes* is used. Thus, the UV-vis-NIR absorption spectra are recorded in two steps: first, the UV-vis spectrometer is connected, and the respective range is measured. Second, the NIR spectrometer for the NIR range measurement is applied. Both spectrometers can be connected to a computer where a software records the spectra. Different integration times and numbers of repetition have to be chosen for the two different measurements which lead in some cases to a vertical offset at the transition between the two spectral ranges. The software calculates the absorbance from the transmittance which is the measured transmission spectrum divided by a reference spectrum recorded beforehand. The absorbance is the negative logarithm of the transmittance.[108,109] Influences by scattering, diffraction, or reflection are neglected and might lead to artifacts or errors in the spectra.

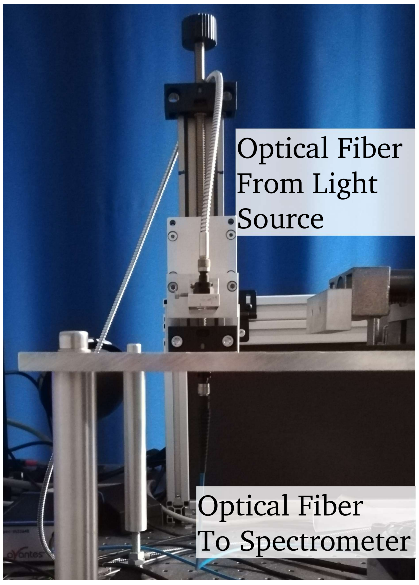

Figure 3.3-1: UV-vis-NIR absorption spectroscopy setup. The sample is placed over a hole in the table where an optical fiber cable with a collimating lens is attached and leads to the spectrometer. Above the sample is a second optical fiber with a collimating lens mounted which comes from the light sources.

## 3.4 Fourier Transform Infrared Reflection Absorption Spectroscopy (FT-IRAS)

Infrared (IR) spectroscopy is a technique where information on a material is obtained by analyzing the absorption of light in the IR range. In this work, the mid IR range from 700 cm$^{-1}$ to 4000 cm$^{-1}$ where molecular vibrations are excited is studied. In the so-called fingerprint region up to around 1500 cm$^{-1}$ where the whole molecule contributes, the resulting complex spectral shapes are unique for a specific molecule.[109] In this region, it is often difficult to assign defined vibrational modes to a specific vibration of a molecular bond. At higher wavenumbers vibrational modes of specific functional groups are found, e.g., the C-H stretching vibration around 2700-3100 cm$^{-1}$ or the C≡N stretching vibration around 2100-2260 cm$^{-1}$.[109]

For the measurements in this work, a VERTEX 80V Fourier transform IR spectrometer from *Bruker* is used. It works like a Michelson interferometer, where a broad band beam from an IR light source is sent onto a beam splitter. Here, the beam gets split, and the two parts are separately transmitted onto two mirrors. One mirror is fixed while the other mirror is moved. After reflection at the mirrors, the beams join again at the beam splitter and are directed at a detector. If the movable mirror is displaced, the path of the respective beam is increased or shortened with respect to the path of the other beam creating an optical path difference that leads to interference. Then, the combined beam passes through the sample and a detector measures the intensity of the interfering beams in a broad range of wavenumbers with respect to the mirror displacement. This interferogram is then Fourier transformed to calculate the spectral intensity as function of the wavenumber.[110] Instead of a transmission spectrum where the beam passes through a sample, IR spectroscopy can also be performed in reflection. Here, the reflection unit A513 from *Bruker* is used, which was modified to allow for the automated measurement of two samples (see Figure 3.4-1).[111] The organic thin films studied in this work are deposited onto indium tin oxide substrates which reflect the IR light in the observed spectral range.[112,113] Thus, the beam which enters with an angle of 15° to the sample surface has to pass through the organic thin film with a much longer distance in comparison to a transmission setup where the effective length is simply the layer thickness. The measurements are performed in a vacuum of about 3 mbar, with an aperture of 2.5 mm, and a resolution of 4 cm$^{-1}$. Each spectrum is the average of 200 scans.

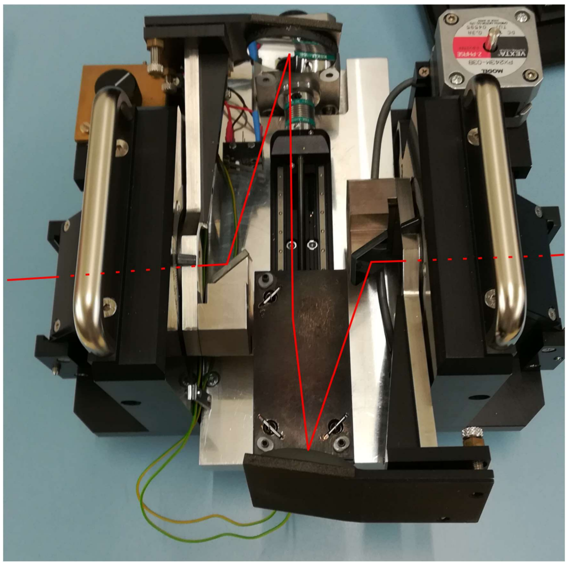

Figure 3.4-1: IR spectrometer reflection unit A513 from *Bruker*. The red line shows the path of the IR beam which enters from the right side in the picture, gets reflected by two mirrors, hits the sample surface on the movable table, is reflected, and leaves the unit after reflection at two more mirrors on the left side of the picture. The positions of the two center mirrors can be changed to obtain different reflection angles.

## 3.5 Density Functional Theory (DFT)

Density functional theory (DFT) is used in this work to calculate the relative binding energies of electrons from different atoms in the studied organic molecules and thereby allows to deduce the photoemission spectral profile that can be expected for these molecules. The measured spectra can be compared to the expected profile verifying the successful evaporation of the intact molecules. Furthermore, DFT is used to calculate IR absorption spectra and assist in the interpretation and discussion of doped and undoped hole transport materials and the involved doping mechanism.

### General Description of Density Functional Theory

Density functional theory allows for the calculation of the electronic structure in condensed matter and of the material properties which originate from it. In the following, the rough idea and basis of the theory will be outlined. For a detailed description, please refer to a textbook, e.g., the book of Richard M. Martin.[114] DFT dates back to the work of Hohenberg and Kohn[115] as well as Kohn and Sham.[116] Hohenberg and Kohn showed that the properties of a system of many-electrons, e.g., a molecule, are described by functionals of the ground state electron density $n(\boldsymbol{r})$. The advantage that lies in this statement is that the ground state density is one scalar function which depends only on the position within the molecule while otherwise the many-body system depends on the position of every single electron. Furthermore, if a functional of the electron density is defined which yields the energy of the system, the ground state density can be found by minimizing this functional with respect to the density.[114] Next, Kohn and Sham introduced the idea of approximating the many-body system of interacting particles with a system of non-interacting particles. As a result, a system of coupled independent-particle equations, i.e., the so-called Kohn-Sham-equations, has to be solved. The basis of the interacting and non-interacting systems is the same ground state density. In addition, the Kohn-Sham approach approximates all the interaction of the many-body system in an exchange-correlation functional of the density.[114] The Kohn-Sham equations can be written as:[117]

$$\overbrace{\left[-\frac{1}{2}\nabla^2 + \underbrace{v_{\text{ext}} + \int d\boldsymbol{r}' \frac{n(\boldsymbol{r}')}{|\boldsymbol{r}-\boldsymbol{r}'|} + \frac{\delta E_{\text{xc}}[n(\boldsymbol{r})]}{\delta n(\boldsymbol{r})}}_{V_{\text{eff}}[n(\boldsymbol{r})]}\right]}^{\hat{H}_{KS}} \Phi_i^{\text{KS}}(\boldsymbol{r}) = \epsilon_i \Phi_i^{\text{KS}}(\boldsymbol{r}), \tag{11}$$

where $\Phi_i^{\text{KS}}(\boldsymbol{r})$ are the single particle Kohn-Sham orbitals and $\epsilon_i$ are their corresponding energy eigenvalues. The effective Hamiltonian operator $\hat{H}_{KS}$ in the square brackets can be separated into two parts. The first term represents the kinetic energy contribution while the second to fourth term can be combined as effective potentials $V_{\text{eff}}[n(\boldsymbol{r})]$. The single components of the effective potential are (from left to right), first, the external Coulombic potential contribution which contains the influence of the atomic nuclei, second, the Coulomb interaction between the electrons sometimes referred to as Hartree term, and third, the exchange-correlation term which approximates the missing interactions from the many-body system. All three terms depend on the electron density $n(\boldsymbol{r})$ which is linked to the Kohn-Sham orbitals by:[117]

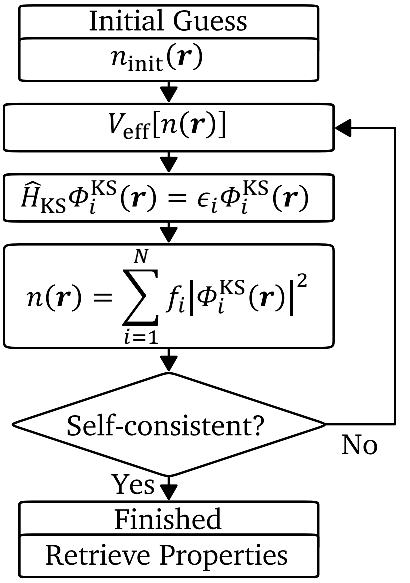

Figure 3.5-1: Illustration of the self-consistent cycle of the Kohn-Sham approach. It starts with an initial guess of the electron density. Based on this guess the effective potential can be calculated which is needed to solve the Kohn-Sham equations to obtain the Kohn-Sham orbitals. From these orbitals a new electron density can be calculated. If the density agrees with the one from the previous iteration, the calculation is finished. Otherwise, the new electron density is used to calculate a new effective potential, etc. Adapted from D. A. Barragan-Yani.[117]

$$n(\boldsymbol{r}) = \sum_{i=1}^{N} f_i\left|\Phi_i^{\text{KS}}(\boldsymbol{r})\right|^2, \tag{12}$$

with $f_i$ being the occupation numbers for the Kohn-Sham orbitals.

From Eq. (11) and (12) it can be understood that the solution of the Kohn-Sham equations for the Kohn-Sham orbitals depends on the electron density while, in turn, the electron density depends on the solution for the Kohn-Sham orbitals. Therefore, a self-consistent cycle is used to solve this non-linear problem. As illustrated in Figure 3.5-1, the cycle starts with an initial guess for the electron density $n_{\text{init}}(\boldsymbol{r})$. Based on this guess, the effective potential term is calculated which then allows to solve the Kohn-Sham equations, Eq. (11), to obtain a solution for the Kohn-Sham orbitals. Next, a new electron density can be calculated from this solution of Kohn-Sham orbitals. From here, the cycle starts anew with the calculation of the effective potential based on the new electron density and so forth.

The iterations stop when the new calculated electron density is consistent with the density from the previous cycle. Then, properties like the total energy or forces between the atoms of a molecule can be retrieved. The actual implementation of this approach into a software can take many forms with different descriptions of, e.g., the Kohn-Sham orbitals or the approximation of the exchange-correlation functional. In the following, the dedicated methods, software and settings used in this work shall be described.

### Density Functional Theory Setup

For the DFT calculations in this work, the open software GPAW is used.[118,119] The software uses the atomic simulation environment (ASE)[120] and is based on the projector-augmented wave (PAW) method.[121] Thereby, the GPAW algorithm does not consider the core electrons explicitly but describes them by so-called PAW setups. The pseudo wave functions, or Kohn-Sham orbitals are calculated only for the valence electrons. Here, a finite difference method is chosen where the pseudo wave functions, electron densities, and effective potential are calculated on a real space grid. This method can be well parallelized, which means that the calculations can be run efficiently with several cores on a cluster computer. The calculations were conducted on the *Lichtenberg* high performance computer of TU Darmstadt. All calculations were performed on single molecules in the vacuum. To get closer to the properties of a condensed film, more molecules in a larger simulation cell would have to be considered. This would have quickly increased the required time and computational resources. Furthermore, the studied thin films are amorphous which poses an additional challenge. To simulate the randomness of an amorphous layer, the calculations would need to be repeated for several structural orientations and then be statistically analyzed. Consequently, such efforts exceed the scope of this dissertation.

**Binding Energy and Chemical Shift Calculations**

As mentioned in the beginning of this section, one application of DFT in this work was the calculation of core level electron binding energies for the comparison with photoemission spectroscopy data. The process is based on the Delta Kohn-Sham (ΔK-S) method described, e.g., by Ljungberg et al.[122] and shall be explained for the example of a 1s orbital electron on a carbon atom of an organic molecule. First, the total energy of the ground state of the molecule $E_{\mathrm{Total}}^{\mathrm{Ground\ State}}$ is calculated. Second, a PAW setup for a C-atom with a missing 1s electron is generated using the respective functionality of GPAW. Next, the total energy of the molecule is calculated again, however, this time using the modified PAW setup on the C-atom of interest ($E_{\mathrm{Total}}^{\mathrm{Core\ Hole}}$). Finally, the binding energy $E_{\mathrm{BE}}$ of the corresponding electron is obtained by calculating the difference in total energy of the ground state molecule and the core hole molecule, i.e., the molecule with the removed core electron:

$$E_{\mathrm{BE}} = E_{\mathrm{Total}}^{\mathrm{Ground\ State}} - E_{\mathrm{Total}}^{\mathrm{Core\ Hole}}\,. \tag{13}$$

The process needs to be repeated for every atom of interest in the molecule.

As the binding energy values are calculated for a single molecule in the vacuum, the respective binding energy values are referenced to the vacuum level and not to the Fermi level of a condensed layer of the molecule.[123,124] This results in a binding energy offset when compared to photoelectron spectroscopy data which are referenced to the Fermi level of the measured thin film. In addition, there are relaxation and screening effects in the condensed film which are not present for a single molecule in vacuum[123] and the usage of effective core potentials[125] which further influence this offset.[124] Therefore, it is only reasonable to compare the relative binding energy shifts, i.e., the chemical shifts. Thus, the energetic distances of the calculated binding energies for each atom of one type of element, e.g., all carbon atoms, are calculated. Based on these relative binding energies, the modelled spectral shape, e.g., of the carbon 1s emission, for the molecule can be generated and then be fitted to the measured spectrum. The calculated energy values are sharp energy positions while the measured spectra contain a broadening from the disorder in the condensed layer (see Section 2.1) and the spectrometer broadening (see Subsection 3.2.3). Thus, to generate and fit the modelled spectral shape, the calculated sharp energy values need to be broadened to match the measured spectrum. Each calculated binding energy $E_{\mathrm{BE}}^{i}$ for the $n$ atoms of one element, e.g., all carbon atoms, in the molecule is broadened by a Gaussian function. At the end, the calculated spectrum $CS$ can be fitted to the measured spectrum using three parameters: an overall binding energy offset $\mu$, one Gaussian standard deviation value $\sigma$, and an intensity scaling pre-factor $a$:

$$CS = a \sum_{i}^{n} \frac{1}{\sigma\sqrt{2\pi}} \exp - \frac{E - E_{\mathrm{BE}}^{i} - \mu)^2}{2\sigma^2} . \qquad (14)$$

In the following paragraph, some practical information on the calculations is given. The calculations are performed on a single molecule in vacuum with open boundary conditions. The size of the cuboid simulation cell is increased until an increase of the minimum free space around the molecule by 1 Å leads to a change in total energy smaller than 1 meV. The grid spacing is chosen at 0.1 Å. In addition, the structure of the molecule is pre-relaxed by the *MMFF94s* force field method in the software *Avogadro*[126] and then further relaxed by GPAW and the *BFGSLineSearch* algorithm from the *optimize* method from ASE minimizing the forces between the atoms below a maximum force of 0.05 auf [b]. The chosen exchange-correlation functional is the PBE (Perdew, Burke, Ernzerhof)[127] functional of the generalized gradient approximation type. This functional was used before in binding energy calculations for m-MTDATA which is also used in this work.[19] In addition, it was shown that the PBE functional in comparison to other exchange-correlation functionals performs well for chemical shift calculations.[125] Furthermore, calculations were spin-polarized with a Fermi-Dirac broadening of 0.0 eV. For some core hole cases, no convergence was reached, and the Fermi-Dirac broadening[c] had to be increased. In these cases, calculations for some non-zero broadening values up to 0.2 eV were conducted and the trend of the total energies was linearly extrapolated to a broadening of zero.

### Infrared Absorption Spectra Calculations

In Chapter 4, thin films of the organic molecules studied in this work are characterized by infrared reflection absorption (IRA) spectroscopy (see Section 4.1). To assist the interpretation of the measured IRA spectra, DFT can be used to calculate infrared absorption spectra. For these spectra two pieces of information are needed: the vibrational frequencies of the vibrational modes, and the intensity of the absorption mode. For a more detailed description of the following method please refer to the work of Porezag et al.,[128] Pederson et al.,[129] and Mortensen et al.[118]

In a molecule, the oscillations of each individual atom combine to one vibration of a coupled oscillator. An oscillation can be described by the balance of kinetic and potential energy. In Cartesian coordinates, the kinetic energy is given by the motion of each atom individually. The potential energy, however, depends on the interactions and forces between the atoms (“spring constants”) and thus their relative motion to each other (position of each atom). As a consequence, a mathematical description of the potential energy in a Cartesian coordinate system involves many cross-terms which renders calculations complicated. To solve this issue, a unitary transformation from linear algebra can be used to change to a new coordinate, called the normal coordinate. To change the coordinate, the eigenvectors of the cross-term matrix have to be found. These eigenvectors then define the change of basis matrix used for the

---

[b] Atomic unit of force as it is used by ASE

[c] This broadening has no physical reasoning but allows for non-integer occupations of the Kohn-Sham orbitals which in some cases helps the conversion of the self-consistent cycle.

transformation to the normal coordinate. An eigenvalue problem has to be solved to find the eigenvectors and eigenvalues of the cross-term matrix for the potential energy. In the normal coordinate, the kinetic and potential energy terms are free of cross-terms and the vibration of the coupled oscillator can be separated into oscillations at each atom. Each vibration is called a normal mode, corresponds to an eigenvector, and its frequency is given by the respective eigenvalue.[110] As the vibrations are relatively small compared to the bond length in the molecule, the harmonic approximation can be used.[110] The Hessen matrix of a system is the second derivative of the potential energy with respect to the position of each atom. It can be regarded as the matrix which holds the “spring constants” for all cross-terms of the atomic interactions. Thus, the eigenvectors of the Hessian matrix correspond to the normal modes and the eigenvalues are the frequencies of these normal modes. After defining the Hessen matrix, the normal modes can be determined by finding the eigenvectors of the Hessian matrix.[128]

The Hessen matrix of a system is obtained by a numerical differentiation of the forces, which are the first derivative of the energy with respect to the displacement of the atoms, at each atom of the molecule. As mentioned before, in this work, the software GPAW together with ASE is used. The forces at each atom of the molecule are obtained as a result of the GPAW algorithm.[118] Using the *Infrared* class of ASE, the forces are calculated separately for a positive and negative displacement of each atom from its relaxed position along all three directions (x, y, z). Next, calculating the differences of the forces for the positive and negative displacement divided by twice the displacement is the numerical derivative. With these derivatives the Hessian matrix can be constructed and is then weighed by the atomic masses. Thereby, the vibrational frequencies can be obtained from the eigenvalues of the mass weighed Hessen matrix.[128] For the intensity of the vibrational absorption modes, the change of the dipole moment with displacement along the normal mode coordinate is needed. As for the forces, the dipole moment is obtained as result of the GPAW algorithm[118] and in the same way the change of the dipole moment can be obtained by displacement of each atom along each direction. Again, the eigenvectors of the Hessian matrix are used to transform the change of the dipole moment with respect to the atomic coordinate into a change with respect to the normal mode coordinate. This result squared is proportional to the infrared absorption intensity and can be used to obtain a normalized infrared absorption spectrum.

Quite conveniently, these calculations are performed by the ASE class *Infrared* with the *run()* method. Furthermore, using the *write_spectra()* method, the sharp frequencies of the vibrational modes are broadened by Gaussian functions (width is 10 cm$^{-1}$) which are scaled by the normalized calculated intensities. Thereby, a calculated spectrum is obtained which can be directly compared qualitatively to a measured IRA spectrum. As the calculations are performed on single molecules in the vacuum, the calculated spectra diverge from the measured once. Still, the strongest modes usually can be identified, and the actual vibrations of the molecules, i.e., the motion of the atoms, can be visualized using a software like OVITO.[130] For consistency with the binding energy calculations the same PBE functional and settings were also used for the IR spectra calculations. This might be not the optimal choice and the more commonly used B3LYP hybrid functional might lead to better results.[131] However, GPAW is not able to perform force calculation for hybrid functionals. Thus, to use the B3LYP functional a different DFT software would have needed to be chosen.

# 4 Materials

In this chapter, thin films of the materials used in this work will be characterized by X-ray and ultraviolet photoelectron spectroscopy (XPS and UPS), ultraviolet-visible-near-infrared (UV-vis-NIR) absorption spectroscopy, infrared reflectance absorption (IRA) spectroscopy, and other methods. The goal is to characterize the bulk properties of the thin films before the effects at interfaces are studied in Chapters 5 and 6. For the well-known materials indium tin oxide (ITO), 4,4‘,4“-Tris[phenyl(m-tolyl)amino]triphenylamine (m-MTDATA), and aluminum, the obtained results will be compared to the literature. For the also studied commercial state-of-the-art organic p-dopant, herein called CPTCFA, and hole transport material (HTM), herein called HTM-B, little to no information can be extracted from the literature and results from own characterizations are crucial to gain knowledge about the materials. The main target are the electronic properties of the materials. The chapter is divided into two parts. First, the thin films of the pure materials will be studied and second, p-doped HTM thin films will be characterized and discussed.

## 4.1 Pure Material Thin Films

This section contains general information and characterization of pure material thin films used in this work. It starts with ITO which is the main substrate used in this work. Different surface treatments will be compared using XPS and UPS to find a reliable method to prepare a clean surface which is free from organic residues and leads to reproducible results. The substrate is also characterized regarding its optical properties as its absorption spectrum serves as reference for following absorption spectra of organic thin films deposited on the substrate. Finally, the surface morphology is examined as roughness of the surface might influence the deposition of the organic thin films. The section about ITO is followed by the characterization of the thin films of a commercial organic p-dopant molecule herein called CPTCFA, the well-known HTM m-MTDATA, and a commercial HTM herein after called HTM-B. All organic materials are characterized by XPS to check for undesirable molecular degradation during thermal evaporation. Furthermore, UPS is used to determine the electronic properties. Finally, absorption spectroscopy is performed to obtain reference spectra of the pure materials. These reference spectra can then be used for comparison with spectra from the p-doped HTMs in the second part of the chapter. The last material is aluminum which is commonly used as back contact material. Here, the properties of the evaporated thin film will be compared to a clean Al foil sample. The results, especially on the electronic properties, for all the materials are summarized at the end. Based on this summary, expectations will be developed regarding the later studied energy alignment at the interfaces of these materials.

### 4.1.1 Indium Tin Oxide Substrate

ITO is one of the most commonly used transparent conductive oxides (TCOs).[132] It is used for light emitting diodes (LEDs) and solar cells, as well as in displays and as infrared reflective coating on windows.[133] As required for an TCO, ITO provides good transparency in the visible range of the electromagnetic spectrum while showing also high electronic conductivity.[134,135] The material is based on indium oxide ($In_2O_3$) degenerately doped with Sn. The thermodynamically stable phase of $In_2O_3$ under standard conditions is cubic bixbyite structure.[136] By substituting In with Sn, the higher number of valence electrons of Sn leads to an increase in the number of free electrons and thereby the conductivity. Typically, the concentration of Sn in ITO is in the range of some percent.[136] The Fermi level ($E_F$) then shifts up to 0.5 eV above the conduction band minimum.[133] The band gap of ITO was under discussion for some time as will be described below in the UV-vis-NIR absorption subsection. Now, the fundamental band gap is known to be 2.8 eV.[133] The work function (WF) of ITO can be varied in a wide range from 4.1 to 5.2 eV or sometimes even higher by either changing the processing conditions or subsequent surface treatments. Surface treatments change the surface dipole potential as seen by the ionization potential in Figure 4.1-3.[135,137,138] ITO films with a low WF are used for example as electron extraction contact for solar cell applications, and ITO films with a high WF serve as hole injection layer for light emitting devices.[139] In the next subsections, differently surface treated ITO films will be characterized by XPS and UPS, the optical properties will be briefly discussed, and finally the analysis of the surface by scanning electron microscopy (SEM) and atomic force microscopy (AFM) is shown.

### X-ray and Ultraviolet Photoelectron Spectroscopy

As mentioned above there are different surface treatments available to clean the ITO surface from unwanted residuals and potentially modify the surface dipole and thus the WF.[138] In this subsection, different surface treatments are compared using XPS and UPS to find a method that leads to a clean surface and reproducible results for the WF. Standard solvent cleaned ITO is compared to three additional surface treatments: in-situ Ar-ion etching (‘sputtered’), Ar-plasma cleaning, and UV-ozone cleaning (see Section 3.1). Figure 4.1-1 shows the X-ray photoelectron (XP) survey spectra from 0 to 1400 eV binding energy and detail spectra of the core level emissions O 1s around 531 eV, Sn $3d_{5/2}$ at about 487 eV, and In $3d_{5/2}$ around 445 eV for the four different surfaces.[140] The survey spectra of all surfaces are similar except for the binding energy region from 200 to 350 eV shown in the inset. Here, a C 1s emission at 285 eV is detected for the surface that was just cleaned with acetone and isopropanol in the ultrasonic bath.[140] This emission indicates the presence of hydrocarbon species which could not be removed by simple solvent cleaning or stem from solvent residues. Concurrently, the absence of this C 1s emission in the other spectra shows that all three surface treatments are effective in removing organic residues from the surface. Furthermore, the survey spectrum of the Ar-ion etched surface shows an emission peak at about 240 eV which can be assigned to the Ar 2p emission and results from the implantation of Ar during the cleaning procedure. Comparing the detail spectra of the O 1s, Sn 3d, and In 3d emission it can be clearly seen that the peaks of the Ar-plasma treated surface are all shifted to lower binding energies. This indicates that the $E_F$ is closer to the valence band (VB) compared to the other cases of surface treatment. The electronic structure is further discussed below. The intensity of the peaks for the solvent cleaned surface is reduced which is likely due to a damping of the signal by the organic residues on top.[48,138] For the Ar-ion etched surface, only the In 3d intensity is increased which probably shows that more Sn and O than In is removed during the treatment.[138] Finally, the UV-ozone treated surface shows that the emissions are all shifted to slightly lower binding energies compared to the solvent cleaned and Ar-ion etched surface but not as low as the one from the Ar-plasma treated surface. The asymmetry of the emission peaks can be attributed to the interaction of photoelectrons with the

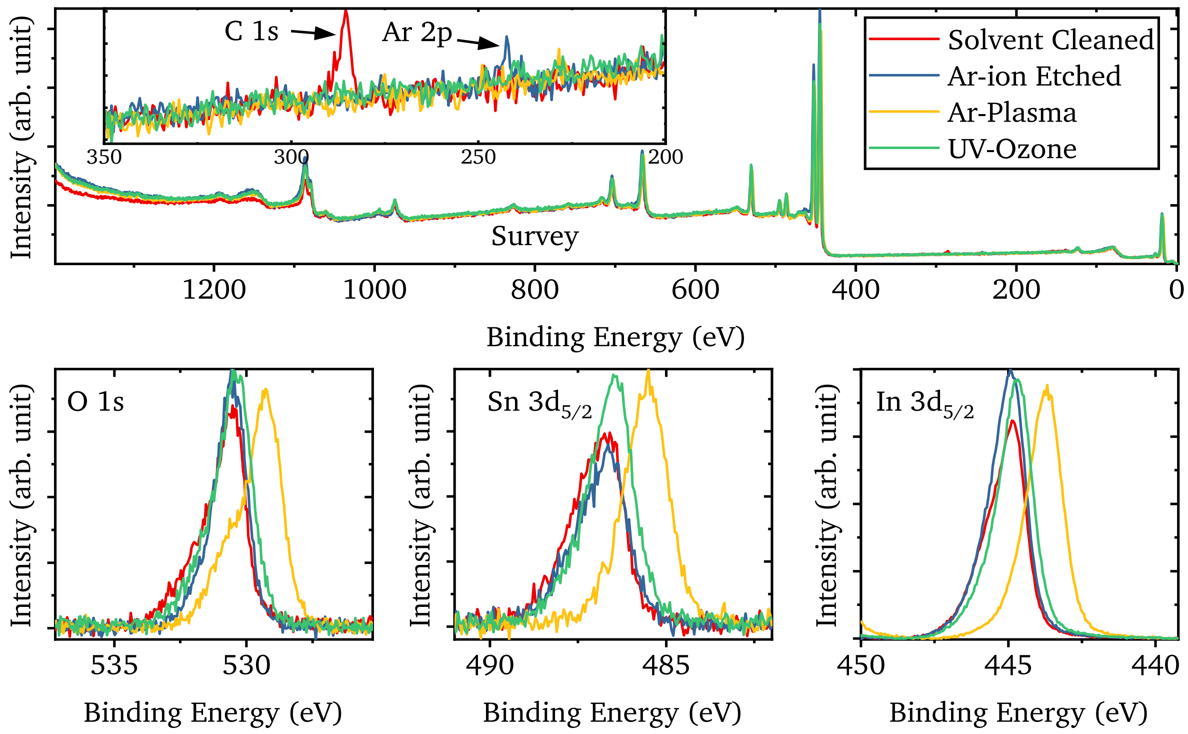

Figure 4.1-1: XP survey spectra and detailed spectra of the core level emissions O 1s, Sn 3d$_{5/2}$, and In 3d$_{5/2}$ for differently surface treated ITO films: Solvent cleaned, Ar-ion etched, Ar-plasma cleaned, UV-ozone cleaned.

high number of electrons in the conduction band due to the high doping of ITO as discussed below.[62,136] In the case of the O 1s spectrum of the Ar-plasma treated surface, an additional spectral feature towards higher binding energy appears which indicates some additional presumably oxy- or hydroxy-species at the surface.

Besides the XP spectra, also ultraviolet photoelectron (UP) spectra of differently treated ITO surfaces were taken and plotted in Figure 4.1-2. From the valence region the VB onsets are determined and from the secondary electron cut-off (SEC) onsets the WF is given. Both onsets are determined via a tangent procedure (see Subsection 3.2.4). The sum of the two values then yields the ionization potential (IP). These three values are given for all four surfaces in an energy level diagram in Figure 4.1-3.

Figure 4.1-2: UP spectra of the valence and SEC region for differently surface treated ITO films: Solvent cleaned, Ar-ion etched, Ar-plasma cleaned, and UV-ozone cleaned. The SEC region is plotted against the difference of the excitation energy hν (21.22 eV) and the binding energy. Thus, the WFs can be read from the x-axis at the SEC onsets.

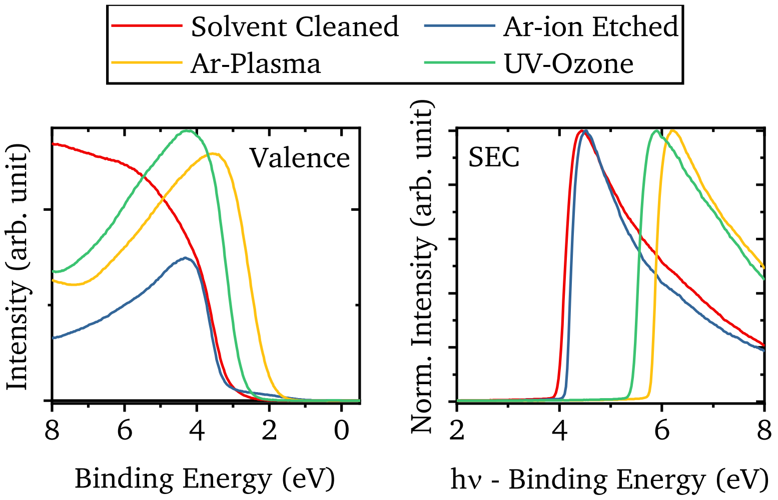

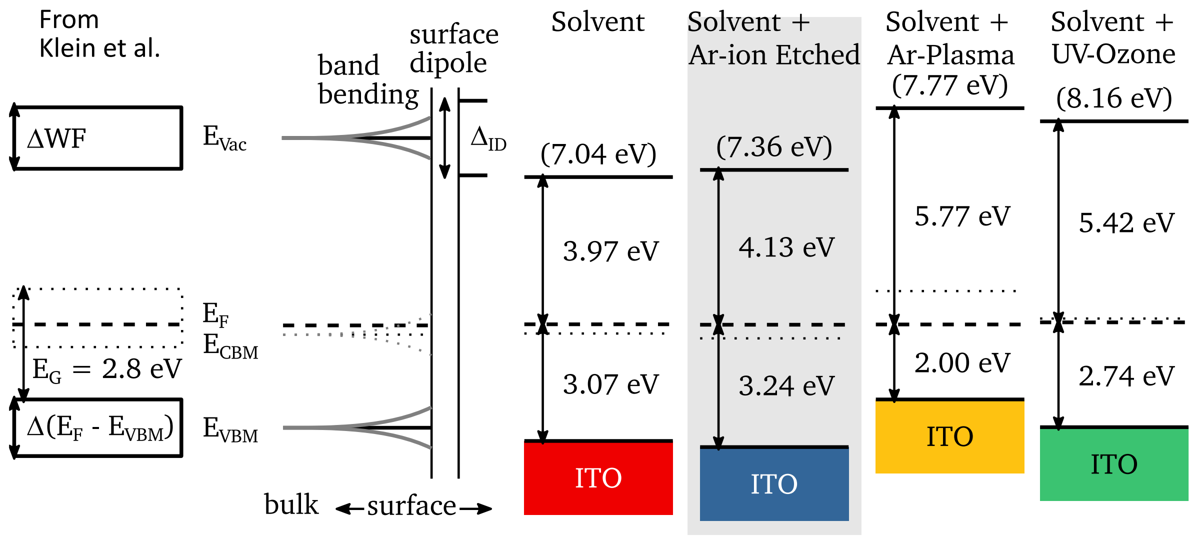

Figure 4.1-3: Energy level diagrams of the electronic properties at the surface for the different surface treated ITO substrates. The treatment will mainly influence the electronic properties at the surface by inducing a band bending or change of surface dipole. The treatment is stated above the respective diagram and the IP is given in parentheses. The energy values are based on the VB onset and SEC onset values determined from the spectra shown in Figure 4.1-2. As a reference, a range for the energetic difference of $E_F$ to $E_{VBM}$ and the WF determined by Klein et al.[133] is given. Ar-ion etched ITO film which is mainly used as a substrate in this work is highlighted by a grey background.

As discussed above, the solvent cleaned surface has some organic residuals on it which will influence the WF and probably also cause the continuous intensity increase towards higher binding energies above 4 eV as this is where the carbon $sp^2$ or $sp^3$ valence states are expected.[141,142]

The valence band maximum (VBM) to $E_F$ has an energetic distance of 3.07 eV and is 0.27 eV larger than the fundamental band gap of 2.8 eV[133] meaning that the $E_F$ is well above the conduction band minimum (CBM, dotted lines). For the Ar-ion etched surface, the $E_F$ is even 0.44 eV above the conduction band. Both values indicate degenerate doping where the Fermi level is shifted above the conduction band minimum as it is expected for a TCO with sufficient conductivity.[133] The resulting high number of charge carriers in the conduction band leads to the before mentioned asymmetry of the core level spectra. Furthermore, the spectrum of the Ar-ion etched surface shows some emission above the VBM, clearly visible between 1.5 and 3 eV. This could be due to the selective etching of the Sn, discussed above which might lead to locally different electronic structures. The UV ozone treatment leads to a slightly lower $E_F$ of 2.74 eV above the VBM and the Ar plasma treatment results in an even lower $E_F$ energetic position of 2.00 eV above the VBM. Both is in line with the lower binding energies for the core level emissions mentioned above.

In addition, the WF values do not change proportionally, leading to different IPs for the different surface treatments. This means that the treatments do not only change the respective $E_F$ energetic position by a change of the band bending situation at the surface or by a local change of the dopant concentration but affect the surface dipole. For the further experiments in this work, the Ar-ion etching was chosen as standard surface treatment for two reasons. First, the treatment can be performed in-situ and the substrate can be transferred directly to the deposition chamber without breaking the vacuum and risking contamination. Second, the

Figure 4.1-4: UV-vis-NIR absorption spectra of the Ar-ion etched ITO on glass substrate with reference to air. The absorbance is calculated from the transmission neglecting the reflection. The UV-vis and NIR regions are indicated and were measured with different detectors and optical fibers.

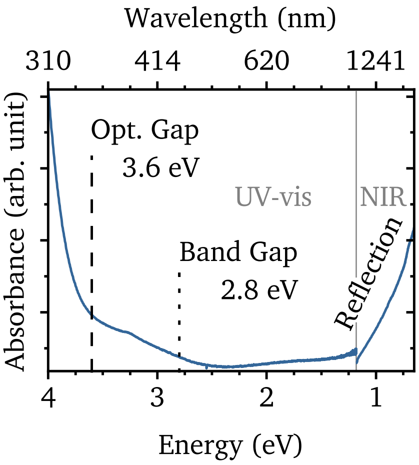

obtained WF is close to the WF values of the two HTMs characterized in the later subsections. Furthermore, after several substrates were prepared by solvent cleaning and subsequent Ar-ion etching it is found that the WF is highly reproducible with a value of 4.10±0.03 eV (mean value and standard deviation from 11 prepared substrates).

### UV-vis-NIR Absorption Spectroscopy

As the ITO/glass substrates are used as reference for the UV-vis-NIR absorption spectroscopy of the organic thin films, the UV-vis-NIR absorption spectrum of ITO/glass with respect to air is shown here in Figure 4.1-4. The absorption in the UV-vis range starts around 2.5 eV but stays low before it strongly increases above 3.6 eV. This is in line with literature where the lower energy absorption is assigned to formally forbidden transitions and the actual optical energy gap is found 0.8 eV above the fundamental band gap of 2.8 eV.[133,143,144]

For the NIR range, it has to be considered, that in the used measurement setup the absorption is calculated from the measured transmission and is neglecting reflection. For ITO, it is known that the high charge carrier concentration leads to a metallic behavior in conductivity with a plasma frequency resulting in increased reflection in the NIR to mid-infrared (MIR) range.[112,113] Thus, the observed increasing absorption is in fact a reflection due to the high number of free charge carriers in the conduction band. This effect also allows to use the ITO as substrate for the later shown IRA spectroscopy results for the organic thin films.[111]

### Topography Characterization

In this subsection, SEM and AFM is used to study the ITO substrate topography. While SEM provides a more qualitative impression on a larger surface area, the analyzed area in AFM is smaller but AFM gives quantitative roughness information. SEM micrographs were taken with the help of Dr. Xiaokun Huang[d]. The aim was to check the homogeneity of the Ar-ion etched ITO surface. Figure 4.1-5 shows the micrographs of the surface at two different magnifications. In a) an area of 42.6 $\mu$m x 56.8 $\mu$m is shown presenting a smooth and homogeneous surface. No clear structure is visible on this scale. An about five times larger magnification covering an

---

[d] Dr. Xiaokun Huang, InnovationLab GmbH

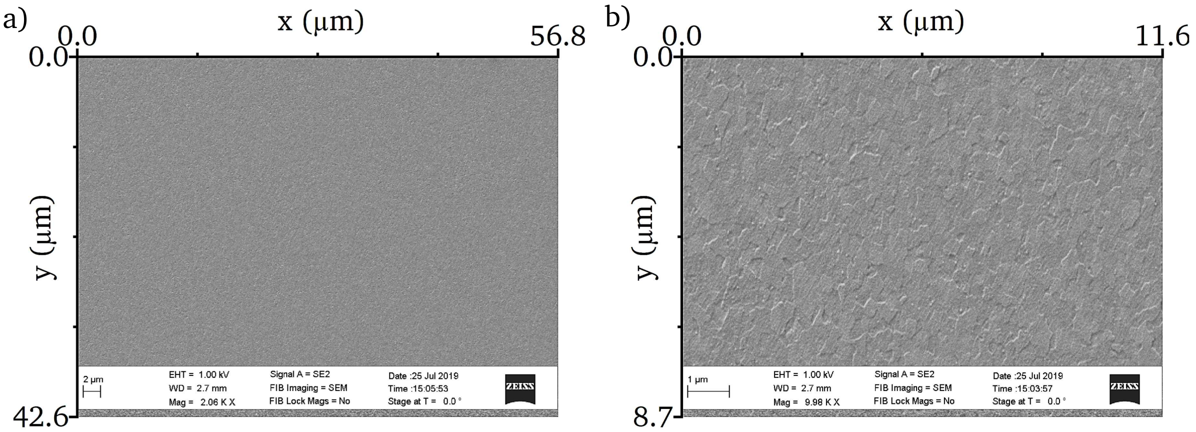

Figure 4.1-5: SEM micrographs of the ITO substrate surface. a) shows the surface at about a 5th of the magnification compared to b). The dimensions can be taken from the axes at the left and top of each graph.

area of 8.7 $\mu$m x 11.6 $\mu$m is shown in b). Here, a patch-like structure is visible. The structural features are in the range of some hundred nanometers.

To further characterize this structure and the roughness of the ITO surface, AFM micrographs were taken and are discussed in the following. AFM micrographs of the ITO surface were taken by Dr. Valentina Rohnacher[e]. The micrographs were post-treated with the software *Gwyddion*[145]. The *remove scars* method is used to automatically remove disrupted parts of a scanning line, *align rows* is used with a median method to level the data and subtract the background, and finally the height is shifted by the *fix zero* method so that the scale starts at 0 nm.[146] Figure 4.1-6a shows the micrograph for an area of 5.0 $\mu$m x 5.0 $\mu$m. The same patch-like structure as in Figure 4.1-5b is visible. The height scale ranges from 0 to 28.7 nm and the root-mean-square (RMS) roughness is calculated to be 2.8 nm. The RMS is calculated by the following Eq. (15):

$$RMS = \sqrt{\frac{1}{N}\sum_{n=1}^{N}(z_n - \bar{z})^2} \tag{15}$$

Where $N$ is the number of data points, $z$ the height value of the data point, and $\bar{z}$ the mean value over all height values.[146]

Compared to the polished and unpolished commercial ITO substrates produced by radio frequency or direct current sputtering which were analyzed in the study of Tamanai et al.[112], the observed patch-like structure is similar for these samples and the RMS roughness is among the smoother surfaces. This proves that the used substrates are of similar quality as the ones typically used in the field. Furthermore, a five times larger magnification micrograph covering an area of 1.0 $\mu$m x 1.0 $\mu$m is shown in Figure 4.1-6b. Here, the height scale ranges from 0 to 19.9 nm. While the previously identified patch-like structure with a feature size in the range of

---

[e] Dr. Valentina Rohnacher, Kirchhoff-Institut für Physik, Ruprecht-Karls-Universität Heidelberg

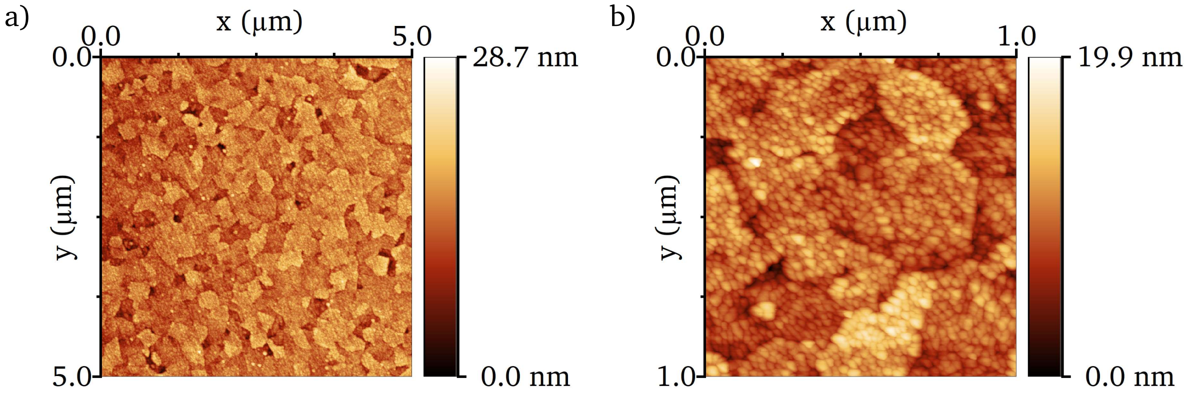

Figure 4.1-6: AFM micrographs of the ITO substrate surface. a) shows the surface at a lower magnification compared to b). The dimensions can be taken from the axes at the left and top of each graph. The color gradient scale for the height is given on the right of each graph.

some hundred nanometers is still visible, an additional fine structure is revealed in this micrograph. This fine structure shows that each patch consists of many smaller humps which are supposedly particle grains. An analysis of the height profile along some of these grains reveals that the measured height of each grain is about 2 nm, and the width is around 20-30 nm. This aspect ratio (width/height) of about 10 to 15 shows that the substrate surface is rather flat for the molecules during deposition, especially in comparison to the size of the molecules which is between 1 to 2 nm for the longest dimension. Thus, it can be concluded that the surface roughness is no obstacle for a smooth layer-by-layer growth of the organic materials. In the next subsection, the commercial p-dopant molecule will be characterized as the first example of the organic materials investigated in this work.

### 4.1.2 CPTCFA p-Dopant

The p-dopant used in this work is 2,2',2"-(cyclopropane-1,2,3-triylidene)-tris[2-(4-cyanoperfluorophenyl)-acetonitrile] (herein called CPTCFA). It is a commercially available molecule and there are only few reports in literature not providing any reference values of the electronic structure or the spectral PES signature.[23,26] It has the molecular formula $C_{30}F_{12}N_6$ and its structure is shown in Figure 4.1-7. It is a trimer where the monomers are connected by a cyclopropane group in the center of the molecule. The monomers consist of one inner and one outer cyano group with a tetrafluorophenyl ring in between. The conformation of the molecule after force field relaxation (see Section 3.5) is rather flat than bulky. A virtual cuboid around the molecule would have a height of about 5 Å and length and width around 12 Å. Its synthesis is described in United States patent 8,057,712 B2.[147]

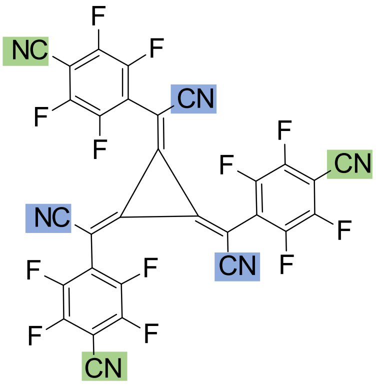

Figure 4.1-7: Structure of the CPTCFA p-dopant molecule. There are two types of C≡N groups: the inner ones highlighted in blue, and the outer ones highlighted in green. Adapted from Wißdorf et al.[17]

In the following subsections, thin films of the pure dopant on ITO will be characterized by photoemission and absorption spectroscopy to get more information on this electronically mostly uncharacterized material. The XP spectra will be used to check for any degradation of the molecule during the evaporation and from the UP spectra the WF and IP will be determined. UV-vis-NIR absorption allow for determining the optical energy gap and the infrared reflection absorption (IRA) spectra of the pure CPTCFA thin film will be later used for the interpretation and discussion of the IRA spectroscopy of the p-doped HTMs in Section 4.2.

### X-ray and Ultraviolet Photoelectron Spectroscopy

To characterize a pure thin film of CPTCFA by XPS and UPS, a 20 nm thick layer is evaporated onto an ITO substrate. The layer thickness was determined from the deposition rate which is obtained from the XP core level emission signal damping.[48] First, the XP spectra are analyzed to check for any signs of a degradation of the molecules during deposition.

The spectra are shown in Figure 4.1-8. The survey spectrum shows the 1s orbital and Auger emissions of C, N, and F. No unexpected signal from any other element is found. The detailed spectra of C, N and F show single peaks for N 1s (399.1 eV) and F 1s (687.6 eV), and two peaks for C 1s (286.2 and 287.5 eV). The two C 1s emissions can be related to chemical shifts which are discussed below. Besides these main emissions, small humps at higher binding energies are detected. These are most likely shake-up or shake-off satellites where photoelectrons which have excited other electrons above the energy gap or vacuum level appear at higher binding energies due to the related energy loss. The stoichiometric analysis of the detailed regions for the three elements results in a composition of 27% / 62% / 11% (F / C / N) which is close to the expected ratio of 25% / 62.5% / 12.5%. The small deviation might stem from the uncertainties in the estimation of the required atomic sensitivity factors as described in Subsection 3.2.7. In addition, the detailed spectra of N and F show that their emission peaks are symmetrical. This means, that there is no difference in the electron density of the twelve F atoms as it is expected. But there is also no significant difference in electron density for the N atoms of the two differently positioned cyano groups which are highlighted in blue and green in Figure 4.1-7.

This observation is cross checked with density functional theory (DFT) calculations for the binding energies as described in detail in Section 3.5. For the CPTCFA molecule the calculated binding energies of the F 1s electrons diverge only by a few meV for the different F atoms. For the two structurally different N atoms, the binding energies of the electrons still diverge by only 20 meV. Furthermore, the calculated binding energies can be used to generate spectra which can be fit to the measured ones. The measured emissions are broadened by lifetime effects, the spectral width of the excitation source, and the analyzer energy resolution (see Subsection 3.2.3). Furthermore, the DFT calculations are performed on a single molecule in vacuum while the XP spectra are recorded of thin film samples. This leads to an energetic offset[124] and further spectral broadening effects. The energetic offset is caused by energetic relaxation effects in the thin film and the referencing of the XP spectra to the Fermi level while the calculated binding energies are referenced to the vacuum level. The further spectral broadening effects are due to the amorphous structure, orientation, and conformation of the molecules (see Section 2.1). Thus, the calculated binding energies are adjusted by Gaussian functions with a constant

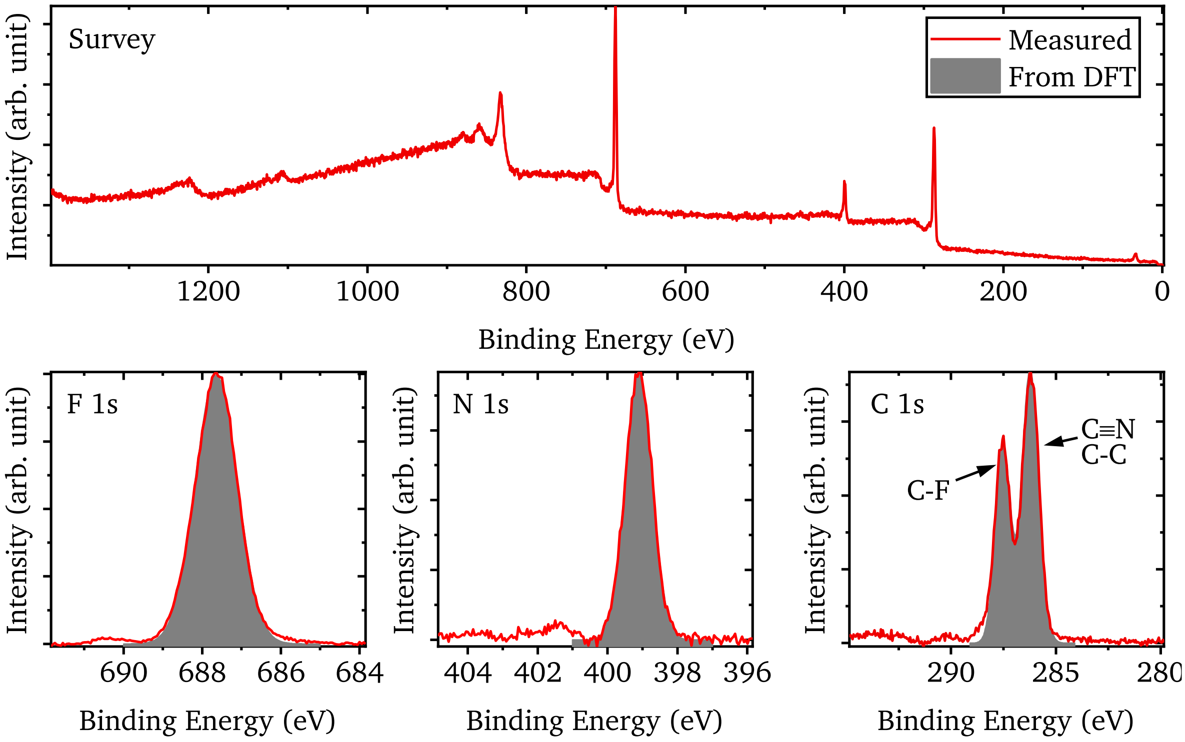

Figure 4.1-8: XP survey spectra and detailed spectra of the core level emissions F 1s, N 1s, and C 1s for a 20 nm CPTCFA film on ITO. Fits based on DFT binding energy calculations are given as grey shaded areas. The calculated sharp binding energies are broadened by Gaussian functions, scaled, and offset by a constant energy to fit the measured data.

standard deviation and offset for each element to fit the measurements. The relative binding energy differences between the different atoms of one element among the molecule are not affected. The resulting fit spectra (grey shaded areas) are in good agreement with the measured spectra (red lines) as can be seen in Figure 4.1-8. Finally, the C 1s spectrum shows two well separated peaks. Again, DFT calculations for the binding energies were performed and theoretical spectra with good agreement were generated. From the calculations the different contributions to the spectral signature can be distinguished. The peak at higher binding energies results from the C atoms which are bound to F. Due to its high electro negativity, F significantly reduces the electron density at the C atoms bound to it. The second peak which is about 1 eV lower in binding energy consists of the emissions from the other C atoms. The divergence in calculated binding energies for the different C atoms is only about 60 meV between the C atoms bound to F and about 150 meV among the other C atoms. The C atoms on the most inner position of the aromatic rings have a binding energy which is even lower with about 340 meV below the next in binding energy lowest C atom. However, these differences are still too small to be visible for the used spectral resolution. Besides the possibility to distinguish the different spectral contributions, the DFT spectra also serve as reference for a non-degraded molecule. If the molecules would have degraded during deposition by thermal evaporation, it would be expected that measured spectra of the degradation products would not lead to such a good agreement. Thus, the calculations help to prove the absence of any unexpected spectral features. Based on the obtained results, it can be assumed that the evaporation does not lead to a degradation of the molecule within the sensitivity of XPS (detection limit of about 1 at%).[148]

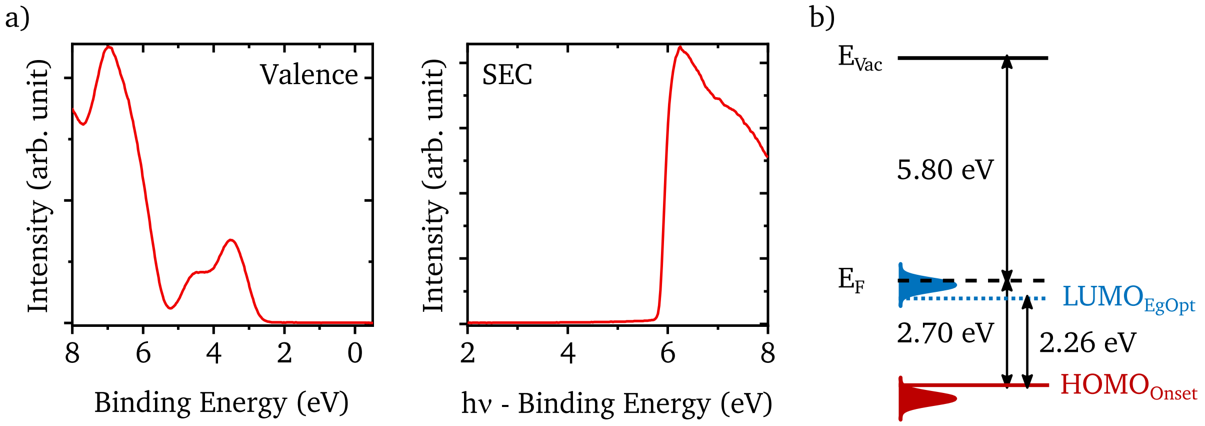

Figure 4.1-9: a) UP spectra of the valence and SEC region for a 20 nm CPTCFA film on ITO. The SEC region is plotted against the difference of the excitation energy hν (21.22 eV) and the binding energy. Thus, the WF can be read from the x-axis at the SEC onset. b) Energy level diagram based on the HOMO onset and SEC onset values determined from the spectra which are shown in (a). The LUMO onset is taken from the optical energy gap determined from the UV-vis absorption data shown in Figure 4.1-10 with respect to the HOMO onset.

Now, the UP spectra can be analyzed to obtain the WF and IP and draw an energy level diagram of CPTCFA. This information is later used when doping of the HTMs is discussed. In Figure 4.1-9a, the valence and SEC regions are plotted from the UPS data.

From the valence region the highest occupied molecular orbital (HOMO) onset is determined by a tangent procedure (see Subsection 3.2.4) to be 2.70 eV below the $E_F$. The SEC onset yields by the same procedure a WF of 5.80 eV. Together the two values add up to an IP of 8.50 eV. The energy level diagram is drawn in Figure 4.1-9b using the optical energy gap determined from the UV-vis absorption spectra shown in the next subsection for the lowest unoccupied molecular orbital (LUMO) energetic position. There, also the energetic position of the Fermi level above the optical energy gap will be discussed.

### UV-vis-NIR and Infrared Reflection Absorption Spectroscopy

The UV-vis-NIR absorption spectrum for CPTCFA presented in Figure 4.1-10 was taken from a 100 nm thin film on ITO with respect to a clean ITO substrate. Using a tangent procedure an optical energy gap of 2.26 eV is determined. As mentioned in Section 2.1, the value of the energy gap determined for an organic semiconductor may depend on the method used to measure it. Applying the empirical Eq. (1) by Djurovich et al.[61] to calculate the respective

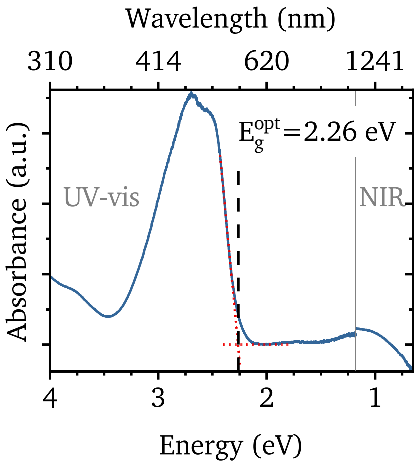

Figure 4.1-10: UV-vis-NIR absorption spectra of a 100 nm CPTCFA film on ITO with reference to an ITO substrate. The absorbance is calculated from the transmission neglecting the reflection. The UV-vis and NIR regions are indicated and were measured with different detectors and optical fibers. The optical energy gap was determined by a tangent procedure (red dotted lines).

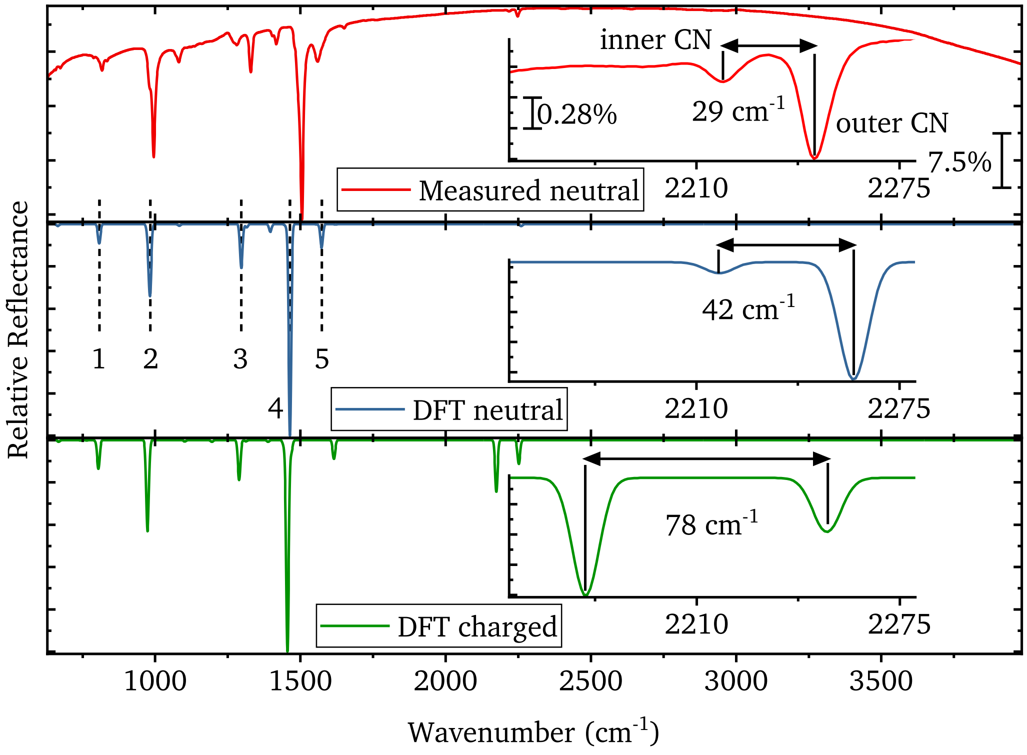

Figure 4.1-11: IRA spectrum of a 100 nm CPTCFA film on ITO (top) in comparison to DFT calculation-based spectra of the neutral (center) and singly negatively charged (bottom) molecule in vacuum. The calculated sharp vibrational modes are broadened by Gaussian functions. The x-axes of the insets are aligned among each other and show the region from 2150 to 2280 cm$^{-1}$. The relative reflectance scale for the measured spectrum is indicated by the percentage value for the tick distance. The scale for the calculated spectra ranges from 0 to 1. The labels (1) to (5) help to identify the modes discussed in the main text.

photoemission energy gap yields a value of 2.68 eV. This value is close to the $E_F$ energetic position of 2.70 eV above the HOMO onset (see Figure 4.1-9b). The high energetic position of $E_F$ close to the LUMO state probably originates from defects in the thin film. As CPTCFA is designed with a high electron affinity, it can accept electrons from defects which are likely to have a smaller ionization energy.

The same sample used for the UV-vis-NIR absorption spectroscopy is also used for IRA spectroscopy[f]. The obtained spectrum is plotted in the top panel of Figure 4.1-11. For comparison, DFT calculations were performed to obtain the vibrational modes and respective dipole moments to generate a theoretical spectrum using Gaussian functions for each absorption frequency. The calculations were done for a neutral (middle panel) and a singly negatively charged (bottom panel) molecule in vacuum. This leads to slightly different frequencies and absorption strengths. However, the theoretical spectra can help to identify the measured modes. In the so-called fingerprint region of the molecule, typically up to a wavenumber of about 1500 cm$^{-1}$, it is difficult to exactly assign a mode to the vibration of one specific chemical group as the vibration is usually more complex involving more atoms.

---

[f] Infrared Reflectance Absorption Spectroscopy was performed with the help of Rainer Bäuerle, OCI Heidelberg University.

Nevertheless, the strongest calculated modes and their main vibrational contributions will be described as example for the respective wavenumber range.

The mode around 810 cm$^{-1}$ labeled with (1) originates mainly from C-C stretching that includes bonds in all parts of the molecule and has some smaller contribution of C-F stretching. Mode (2) around 980 cm$^{-1}$ can be assigned to the stretching of C-F bonds mainly. The next three modes (3-5) around 1300, 1460, and 1570 cm$^{-1}$ originate from C-C stretching in different parts of the molecule. Mode (5) can be mainly assigned to the stretching in the central cyclopropane group, while modes (3,4) are due to stretching in the tetrafluorophenyl groups. For mode (3), the carbon atoms vibrate in an alternating pattern – three inwards and three outwards – in the plane of the ring. For mode (4), one bond of the ring shortens while the opposite bond stretches and vice versa while the atoms on both sides move accordingly. Besides these modes in the fingerprint range, the C≡N stretching modes at 2248 and 2219 cm$^{-1}$ shown in the insets are of special interest. For the well-studied p-dopant 7,7,8,8-Tetracyanoquinodimethane (TCNQ) and its derivatives it is known, that the shift of this vibration scales linearly with the amount of charge transferred to the dopant molecule.[149,150] Based on the calculations we can assign the absorption at 2219 cm$^{-1}$ to the stretching of the inner C≡N groups closer to the center of the molecule while the absorption at 2248 cm$^{-1}$ stems from the stretching of the outer C≡N groups further away from the center of the molecule (see structure in Figure 4.1-7). Comparing the calculations for the neutral and the charged molecule, it can be seen that the outer C≡N absorption shifts by only 8 cm$^{-1}$ while the inner C≡N absorption shifts by 44 cm$^{-1}$ to lower values. As a result, the distance in wavenumber between the two absorptions changes from 42 to 78 cm$^{-1}$ which is a factor of 1.86.

The stronger influence of the charge on the vibrations of the inner cyano groups can be understood when looking at the pseudo wave functions of the LUMO in Figure 4.1-12 extracted from the DFT calculations of the neutral molecule. The LUMO is mainly located in the center of the molecule and thus an additional charge will influence more strongly the inner cyano groups than the outer ones. Besides the shift of the absorptions, also their intensities, especially for the inner C≡N groups, increase. The discussed observations will be later used in Section 4.2 when the doping of the HTMs is characterized.

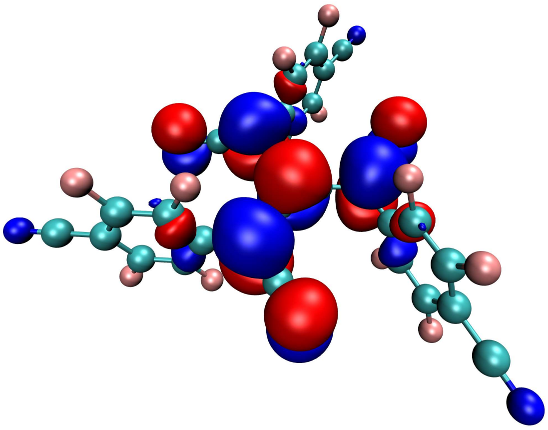

Figure 4.1-12: CPTCFA molecule with pseudo wave functions of the LUMO as obtained by DFT calculations plot as iso-surfaces (isovalues of 0.05 Å-3/2 – blue and -0.05 Å-3/2 – red) . The colors of the atoms are C – turquoise, F – rose, and N – blue.

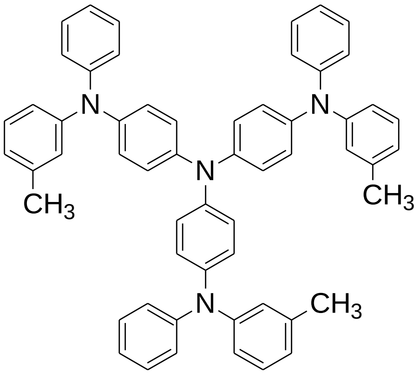

Figure 4.1-13: Structure of the HTM m-MTDATA. Adapted from Shirota et al.[16]

## 4.1.3 m-MTDATA Hole Transport Material

The “starburst” molecule 4,4‘,4“-Tris[phenyl(m-tolyl)amino]triphenylamine (m-MTDATA) is a well-known HTM.[18–20] It forms spontaneously amorphous stable thin films with a glass transition temperature of 75°C.[151,16] The molecular formula of m-MTDATA is $C_{57}H_{84}N_{4,}$ and the structure is shown in Figure 4.1-13. The molecule is a trimer where the monomers are connected by a central amine group. Each monomer, again, consists of an amine group with three phenyl rings of which one has a methyl group attached. The conformation of the molecule after force field relaxation (see Section 3.5) is rather flat than bulky. A virtual cuboid around the molecule would have a height of about 5 Å and length and width around 19 Å.

In the following subsections, undoped thin films of m-MTDATA on ITO will be characterized by photoemission and absorption spectroscopy. As in the previous subsections for CPTCFA, the XP spectra will be used to check for any degradation of the molecule during the evaporation and from the UP spectra the WF and IP will be determined. UV-vis-NIR absorption allows for determining the optical energy gap, and the infrared reflection absorption spectra of the pure m-MTDATA thin film will be later compared to spectra of p-doped m-MTDATA to characterize the doping mechanism in Section 4.2. As the characterization follows closely the one described for CPTCFA in Subsection 4.1.2., the description of the analysis of the different methods is shortened.

### X-ray and Ultraviolet Photoelectron Spectroscopy

A 20 nm thick pure m-MTDATA layer was deposited in-situ onto an ITO substrate for the characterization by XPS und UPS. The layer thickness was determined from the deposition rate which is obtained from the damping of the In $3d_{5/2}$ core level emission signal.[48] The obtained XP and UP spectra are shown in Figure 4.1-14 and Figure 4.1-15a. The XP survey spectrum shows only the expected emissions for C and N. No contamination from another element is found. The broadly increased background signal around 200 eV and between 500 and 1000 eV originates still from the ITO substrate and decreases for greater layer thicknesses. The detailed spectra of C, N show single peaks for N 1s (400.4 eV) and C 1s (285.2 eV). The shoulder of the C 1s emissions can be related to chemical shifts which are discussed below. Besides these main emissions, a small hump at higher binding energy is detected. This is most likely a shake-up or shake-off satellite where photoelectrons which have excited other electrons above the energy gap or vacuum level appear at higher binding energies due to the related energy loss. The stoichiometric analysis of the detailed spectra results in a composition of 93.2% / 6.8% (C / N)

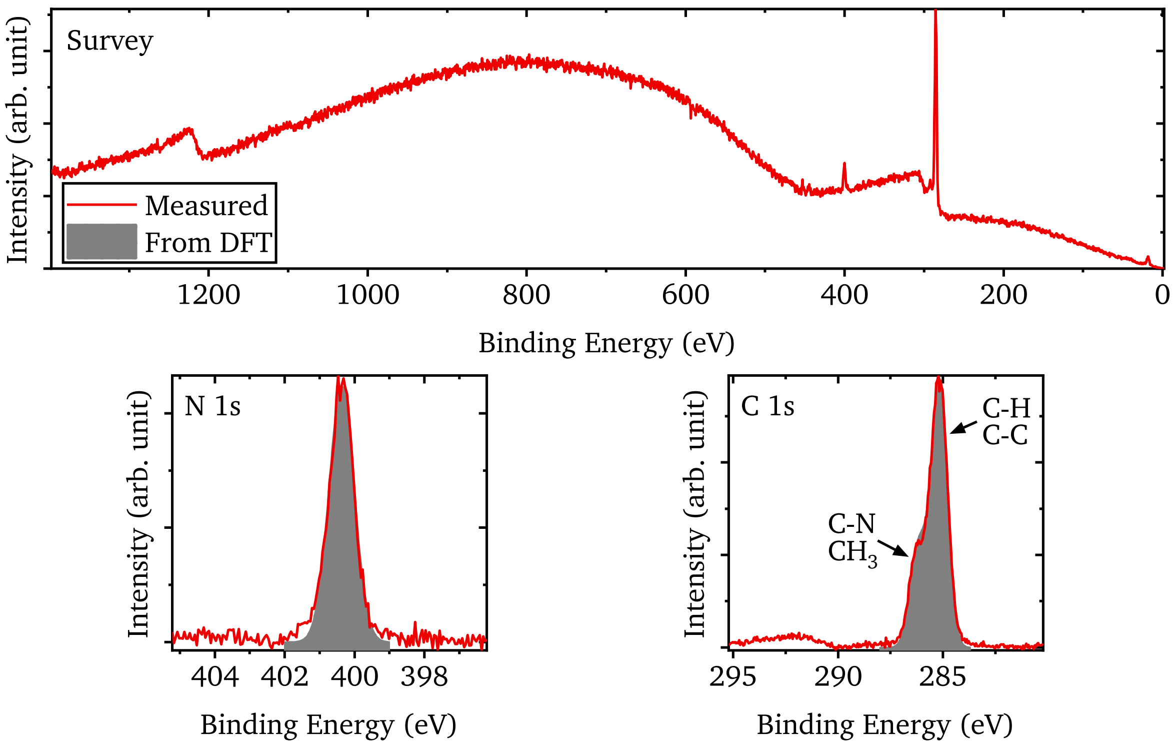

Figure 4.1-14: XP survey spectra and detailed spectra of the core level emissions N 1s and C 1s for a 20 nm m-MTDATA film on ITO. Fits based on DFT binding energy calculations are given as grey shaded areas. The calculated sharp binding energies are broadened by Gaussian functions and then scaled and offset to fit the measured data.

which is very close to the expected ratio of 93.4% / 6.6%. The little deviation might arise from uncertainties in the used atom sensitivity factors (see Subsection 3.2.7). The good agreement of the stoichiometry suggests non-degraded molecules. Furthermore, the detailed spectra are again compared to fits based on DFT binding energy calculations as explained in the previous subsection for CPTCFA. The aim is again to distinguish the spectral contributions of the different atoms in the molecule and check for unexpected spectral features in the measured spectra indicated a degradation of the molecule. The binding energies for the 1s electrons diverge between the one central and the three outer N atoms by only 80 meV with the lower values for the central N atom. Hence, the spectrum shows a symmetrical peak with no shoulder to any side. The C 1s peak shows a shoulder at higher binding energies. This shoulder can be assigned to the emissions from the C atoms which are bound to N and the C atoms of the three methyl groups. As for CPTCFA, the calculated fit spectra (grey shaded areas) are in good agreement with the measured spectra (red lines) which in turn show no additional spectral features, and hence show no sign of degradation of the molecules due to the evaporation process.

The UP spectra are used to determine the HOMO onset (1.42 eV) from the valence region and the WF (3.58 eV) from the SEC onset. Both values sum up to an IP of 5.00 eV and are used to draw the energy level diagram shown in Figure 4.1-15b. The determined IP corresponds well to the values reported in literature between 5.0 and 5.1 eV.[24,151–153] The LUMO is placed above the HOMO onset by the optical energy gap as determined from the UV-vis absorption spectrum shown in the next subsection. The obtained energy level diagram will be later used in the summary of this section (see Subsection 4.1.6) to develop expectations regarding the effects at

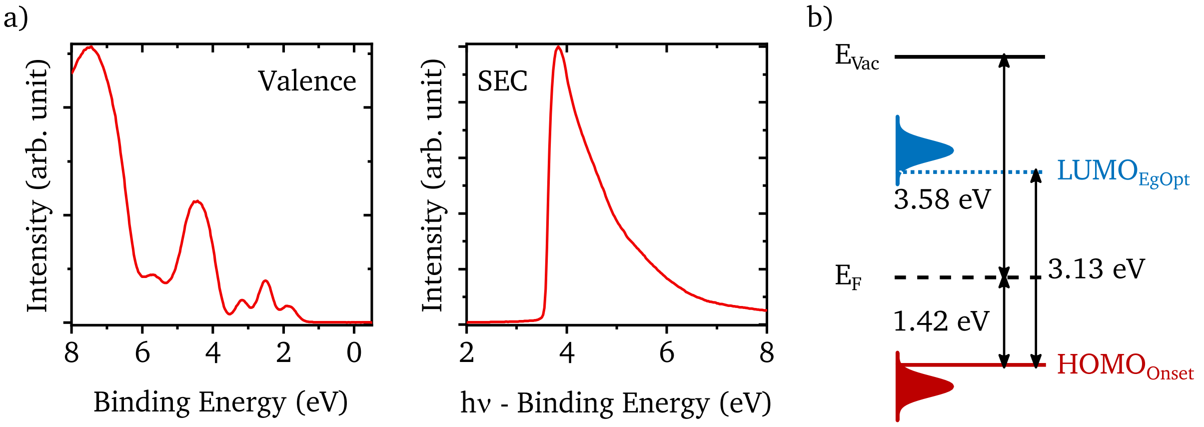

Figure 4.1-15: a) UP spectra of the valence and SEC region for a 20 nm m-MTDATA film on ITO. The SEC region is plotted against the difference of the excitation energy hν (21.22 eV) and the binding energy. Thus, the WF can be read from the x-axis at the SEC onset. b) Energy level diagram based on the HOMO onset and SEC onset values determined from the spectra shown in (a). The LUMO onset is based on the optical energy gap determined from the UV-vis absorption data shown in Figure 4.1-16 with respect to the HOMO onset.

the interface with ITO and Al. Furthermore, it is used to discuss the p-doping of the material in Section 4.2.

### UV-vis-NIR and Infrared Reflection Absorption Spectroscopy

A 100 nm thick m-MTDATA film is deposited onto an ITO substrate for the characterization by absorption spectroscopy. The obtained UV-vis-NIR spectrum with reference to a bare ITO substrate is plotted in Figure 4.1-16. The onset of the absorption is determined by a tangent procedure (see Subsection 3.2.4) and yields a value of 3.13 eV for the optical absorption gap. This value corresponds well to a reported IP to electron affinity difference of 3.2 eV.[154,155] The photoluminescence peak energy for the first excited singlet state S1 is reported to be 2.9 eV.[156] The small absorption features at lower energy are probably artifacts from the simple setup which, e.g., does not account for changes in reflection.

For the MIR range, the reflection absorption spectrum[g] is shown in Figure 4.1-17. Here, the measured spectrum (top panel) is compared to a spectrum generated from DFT calculations

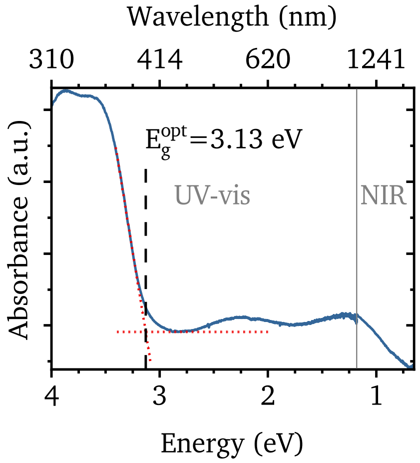

Figure 4.1-16: UV-vis-NIR absorption spectrum of a 100 nm m-MTDATA film on ITO with reference to an ITO substrate. The absorbance is calculated from the transmission neglecting the reflection. The UV-vis and NIR regions are indicated and were measured with different detectors and optical fibers. The optical energy gap was determined by a tangent procedure (red dotted lines). The increased absorbance at lower energies is tentatively assigned to the simple measurement setup.

---

[g] Infrared Reflectance Absorption Spectroscopy was performed with the help of Rainer Bäuerle, OCI Heidelberg University.

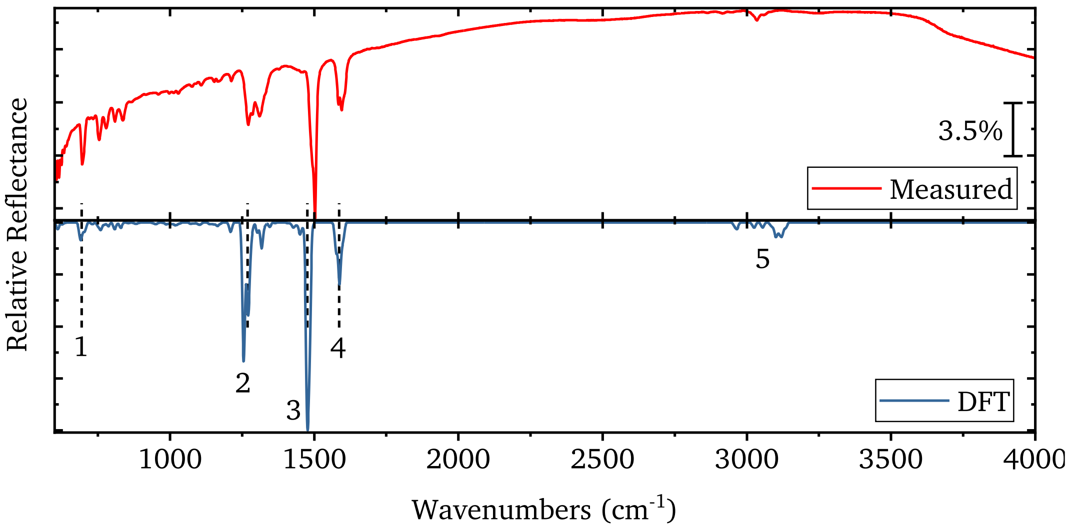

Figure 4.1-17: IRA spectrum of a 100 nm m-MTDATA film on ITO with reference to an ITO substrate (top) in comparison to DFT calculation-based spectra of the molecule in vacuum (bottom). The calculated sharp vibrational modes are broadened by Gaussian functions. The relative reflectance scale for the measured spectrum is indicated by the percentage value. The scale for the calculated spectrum ranges from 0 to 1. The labels (1) to (5) help to identify the modes discussed in the main text.

(bottom panel). Even though the calculation was again performed on a single molecule in vacuum, the similarities are clearly visible. As for CPTCFA spectrum, the dominant vibrations of the molecule are assigned to one mode for each wavenumber range using the DFT calculations. The modes are labeled in the calculated spectrum. Mode (1) around 700 cm$^{-1}$ originates from bending vibrations of the C-H bonds out of the plane of the phenyl ring. For mode (2) around 1270 cm$^{-1}$, stretching vibrations of the C-N amine bonds are observed with some C-H bending vibrations which move in the plane of the phenyl rings. Mode (3) around 1480 cm$^{-1}$ can be mainly assigned to C-H bending vibrations in the plane of the phenyl rings. While for mode (2) the bending corresponds to a rocking-like movement it is more like a scissoring movement for mode (3). For mode (4) around 1590 cm$^{-1}$, C-C stretching vibrations are dominant. The modes around 3000 cm$^{-1}$, label (5), are outside of the fingerprint range and originate from C-H stretching vibrations. The modes at lower wavenumbers are assigned to the C-H bonds of the methyl groups while the modes at higher wavenumber result from the C-H stretching vibrations of the phenyl rings. The UV-vis-NIR as well as the IRA spectra will be used below when discussing the p-doping of m-MTDATA.

### 4.1.4 HTM-B Hole Transport Material

The second HTM used in this work is molecule of the project partner Merck KGaA. To protect their interests, the official name and complete chemical structure cannot be given, and the results cannot be compared to reference values from the literature. However, the full structure is known to the author and was used for the later mentioned DFT calculations. In this work, it will be referred to as HTM-B. Its stoichiometric formula is $C_{52}H_{37}N$ and the reduced structure is shown in Figure 4.1-18. It consists of a central amine group with three aryl groups attached two of them are marked as R$^1$ and R$^2$ in the structure. The conformation of the molecule after force field relaxation (see Section 3.5) is less flat and bulkier than for m-MTDATA and CPTCFA. A virtual cuboid around the molecule would have a height of about 8 Å, a length of 14 Å and

Figure 4.1-18: Schematic structure of the commercial HTM herein called HTM-B. R¹ and R² mark the position of two aryl groups which cannot be shown to protect the interests of the project partner Merck KGaA. The C atoms of the fluorene group are indexed to help the description in the main text. Adapted from Wißdorf et al.[17]

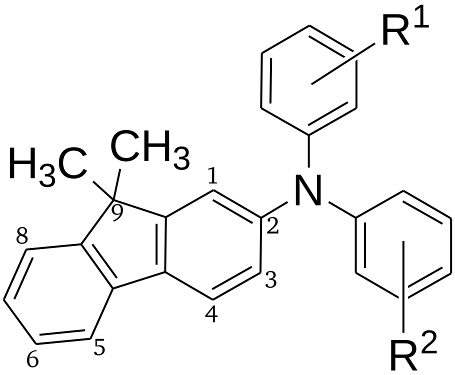

width around 17 Å. Due to the non-flat structure of the molecule and the deposition by evaporation onto a substrate at room temperature the deposited thin films are expected to be amorphous.[13,157] Its synthesis is described in United States patent 9,312,495 B2.[158]

In the following subsections, thin films of undoped HTM-B on ITO will be characterized by photoemission and absorption spectroscopy. As in the previous subsections for CPTCFA and m-MTDATA, the XP spectra will be used to check for any degradation of the molecule during the evaporation and from the UP spectra the WF and IP will be determined. UV-vis-NIR absorption allow for determining the optical energy gap, and the infrared reflection absorption spectra of the pure HTM-B thin film will be later used for the analysis and discussion of the p-doped HTM-B in Section 4.2. As the characterization follows closely the one described in Subsection 4.1.2., the description of the analysis of the different methods is shortened.

### X-ray and Ultraviolet Photoelectron Spectroscopy

For the characterization of HTM-B by XPS and UPS, a pure layer of 20 nm is deposited onto ITO. The XP spectra are given in Figure 4.1-19. The survey spectrum consists of emissions of C and N only. No indication for a contamination by another element is found. The broadly increased background signal around 200 eV and between 500 and 1000 eV originates still from the ITO substrate and decreases for greater layer thicknesses. The detailed spectra of C, N show single peaks for N 1s (400.3 eV) and C 1s (285.2 eV). The asymmetry of the C 1s emissions can be related to chemical shifts which are discussed below. Besides the main emission, a small hump at higher binding energy is detected. This is most likely a shake-up or shake-off satellite where photoelectrons which have excited other electrons above the energy gap or vacuum level appear at higher binding energies due to the related energy loss. The stoichiometry analysis of the detail spectra of the C 1s and N 1s regions leads to a composition of 97.9% / 2.1% (C / N) which is close to the expected ratio of 98.1% / 1.9%. As in the previous subsections, this agreement of determined and expected composition indicates no degradation of the molecules during evaporation. Furthermore, the spectra are compared to fits generated from DFT binding energy calculations to analyze the spectral contribution of the different atoms in the molecule and check for unexpected spectral signatures. The 1s emission of the single N atom simply results in a symmetric peak. The structure of the molecule is quite complex with many slightly different binding energies for the different C atoms. Hence, it is not possible to clearly assign the slight shoulder towards higher binding energies of the C 1s peak. However, in an attempt to simplify, this shoulder stems from the three C atoms bound to the N atom, those of the methyl groups and the one in the 9th position of the fluorene group (see Figure 4.1-18). Finally, the good

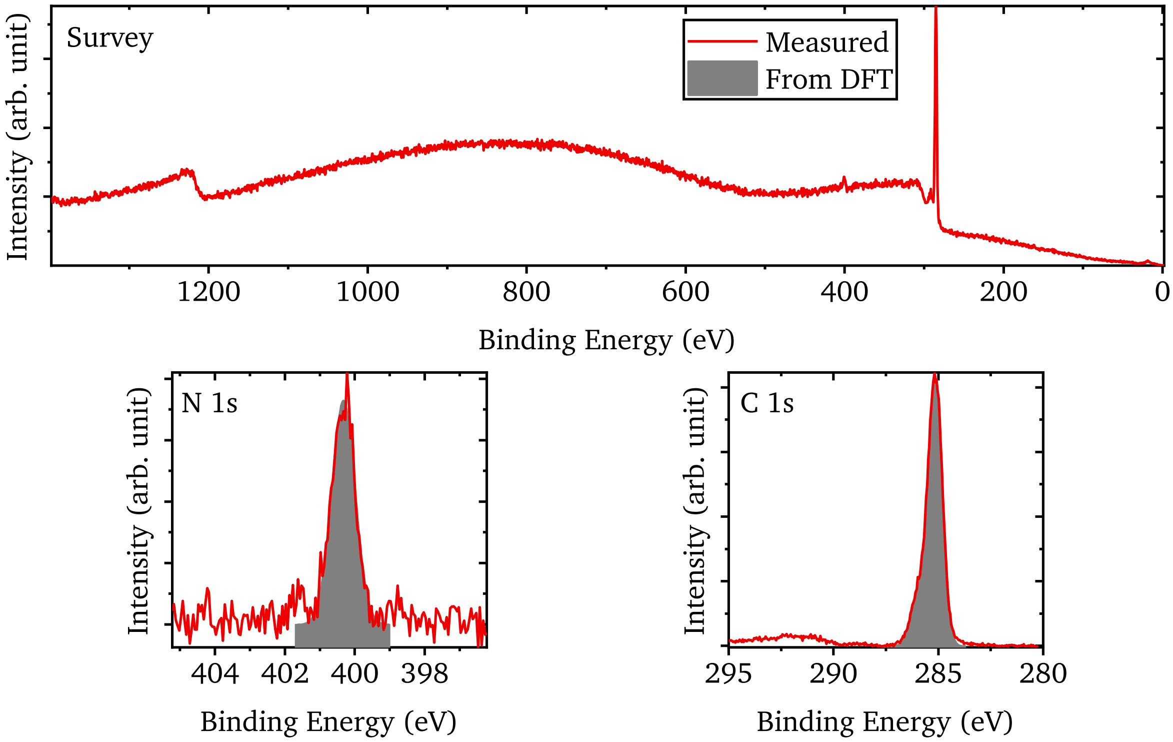

Figure 4.1-19: XP survey spectra and detailed spectra of the core level emissions N 1s and C 1s for a 20 nm HTM-B film on ITO. Fits based on DFT binding energy calculations are given as grey shaded areas. The calculated sharp binding energies are broadened by Gaussian functions and then scaled and offset to fit the measured data.

agreement between the calculated fit spectra (grey shaded areas) and the measured spectra (red lines) proves the absence of unexpected features supporting that no degradation of the molecule occurs during deposition.

The UP spectra of HTM-B are given in Figure 4.1-20a. Here, the HOMO onset is taken from the valence region and the WF value is determined from the onset in the SEC region. Both onsets are found by a tangent procedure. The HOMO onset yields 1.88 eV and the WF value is 3.70 eV. Both values are used for the energy level diagram in Figure 4.1-20b. Here, the LUMO is given

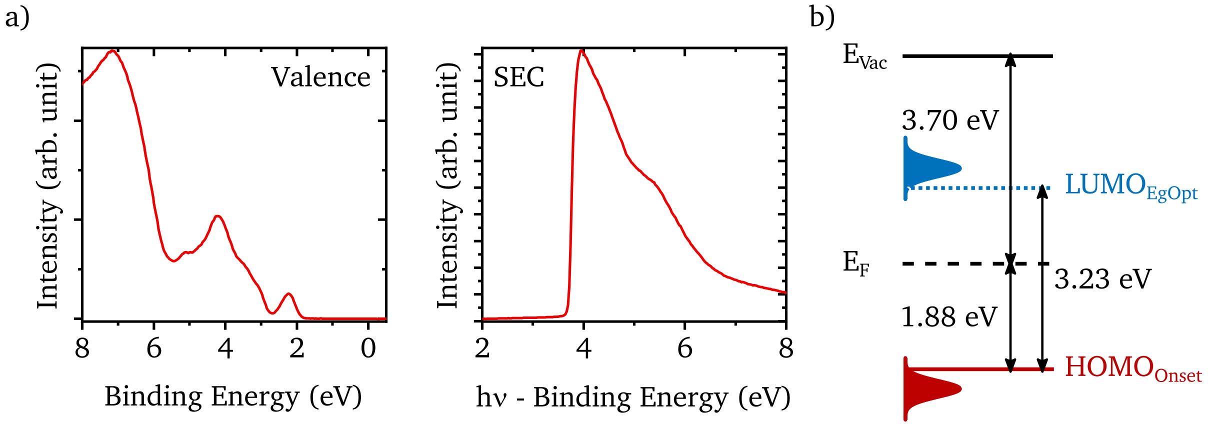

Figure 4.1-20: a) UP spectra of the valence and SEC region for a 20 nm HTM-B film on ITO. The SEC region is plotted against the difference of the excitation energy hν (21.22 eV) and the binding energy. Thus, the WF can be read from the x-axis at the SEC onset. b) Energy level diagram based on the HOMO onset and SEC onset values determined from the spectra shown in (a). The LUMO onset is based on the optical energy gap determined from the UV-vis absorption data shown in Figure 4.1-21 with respect to the HOMO onset.

using the optical energy gap of 3.23 eV as determined in the next subsection from the UV-vis absorption spectrum. The obtained energy level diagram will be later used in the summary of this section (see Subsection 4.1.6) to deduce theoretically expectations of the interface formation to ITO and Al. Furthermore, it is used to discuss the p-doping of the material in Section 4.2.

### UV-vis-NIR and Infrared Reflection Absorption Spectroscopy

To further characterize HTM-B with absorption spectroscopy in the UV, vis, NIR, and MIR range, a thicker film compared to the one used for the photoemission spectroscopy of 100 nm was deposited on ITO. The measurements are taken with an ITO substrate as reference. The UV-vis-NIR absorption spectrum is shown in Figure 4.1-21. Here, the optical energy gap can be determined from the onset of the adsorption by a tangent procedure and is found to be 3.23 eV. The small absorption features at lower energy are probably artifacts from the simple setup which, e.g., does not account for changes in reflection.

The absorption in the MIR range is measured under reflection[h] and is plotted in Figure 4.1-22 (top panel) in comparison to a spectrum generated from DFT calculations (bottom panel). The calculations of the molecular vibrations were performed on a single molecule in vacuum and thus the obtained wavenumbers and intensities diverge from the measured spectrum. In summary the main lines as given in Figure 4.1-22 are similar to the ones of m-MTDATA can be assigned to: (1) around 740 $cm^{-1}$ originates from the C-H bending vibrations out of the plane of the phenyl ring; (2) around 1280 $cm^{-1}$ is mainly coming from the C-N stretch vibration of the amine part of the molecule, together with some rocking type C-H bending vibration in the phenyl ring plane; (3) around 1430 $cm^{-1}$ stems from a different, more scissoring like C-H bending vibration; (4) around 1600 $cm^{-1}$ shows C-C stretching vibrations in the fluorene group; finally, (5) around 3000 $cm^{-1}$, stems from C-H stretching vibrations – C-H bonds of the methyl groups vibrate at lower wavenumbers while the C-H bonds of the phenyl rings vibrate at higher wavenumbers.

Figure 4.1-21: UV-vis-NIR absorption spectra of a 100 nm HTM-B film on ITO with reference to an ITO substrate. The absorbance is calculated from the transmission neglecting the reflection. The UV-vis and NIR regions are indicated and were measured with different detectors and optical fibers. The optical energy gap was determined by a tangent procedure (red dotted lines). The absorbance at energies below the optical gap is tentatively assigned to the simple measurement setup.

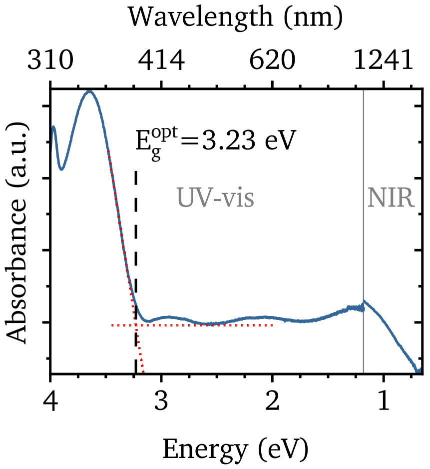

---

[h] Infrared Reflectance Absorption Spectroscopy was performed with the help of Rainer Bäuerle, OCI Heidelberg University.

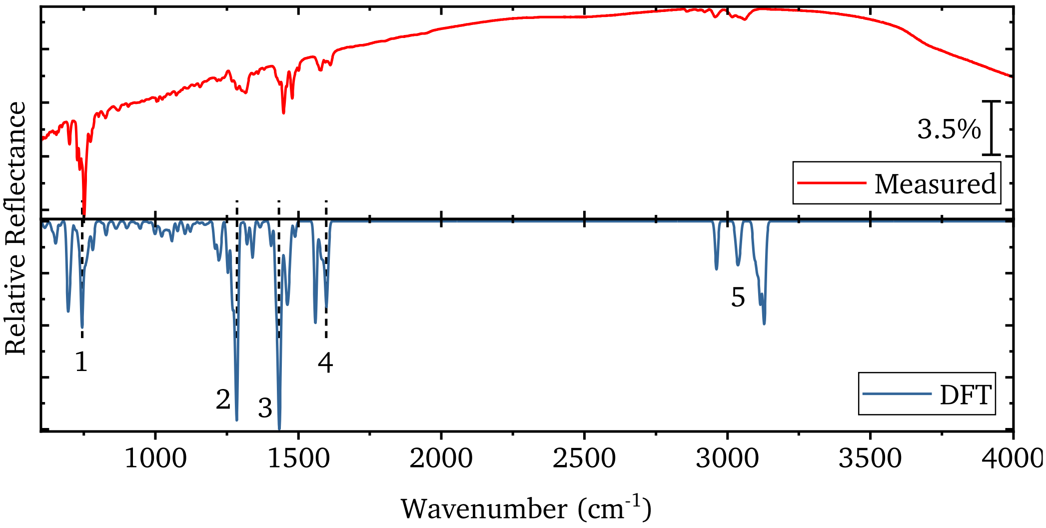

Figure 4.1-22: IRA spectrum of a 100 nm HTM-B film on ITO with reference to an ITO substrate (top) in comparison to DFT calculation-based spectra of the molecule in vacuum (bottom). The calculated sharp vibrational modes are broadened by Gaussian functions. The relative reflectance scale for the measured spectrum is indicated by the percentage value. The scale for the calculated spectrum ranges from 0 to 1. The labels (1) to (5) help to identify the modes discussed in the main text.

### 4.1.5 Aluminum Back Contact

Since the early days of organic light emitting devices, aluminum is used as cathode material.[159,160] While it is argued that aluminum is a suitable cathode material due to its low expected WF, its actual WF, depends strongly on the deposition conditions. Under experimental ultra-high vacuum (UHV) conditions with pressures of $10^{-9}$ mbar only little to no oxygen is taking part in the deposition process resulting in a WF around 4.3 eV. However, setups for device fabrication often have vacuum pressures of just $10^{-6}$ mbar leading to the incorporation and adsorption of oxygen and a lower WF.[161,162] Here, also the deposition rate affects the amount of oxygen uptake – the slower the deposition, the more oxygen is taking part in the film formation.[161–163] The aluminum thin films in this work are evaporated under UHV conditions and are thus on the low oxygen, high WF side. In the following, an evaporated aluminum thin film is compared to an Ar-ion etched piece of aluminum by XPS and UPS.

#### X-ray and Ultraviolet Photoelectron Spectroscopy

To characterize the Al back contact layers which are deposited in UHV by thermal evaporation, a 20 nm thick film was deposited onto an Ar-ion etched Si wafer and then analyzed by XPS and UPS. To check the quality of the evaporated thin film, a piece of an Al sputter target is measured for comparison which was Ar-ion etched until no O 1s signal was detected anymore. The obtained spectra are shown in Figure 4.1-23 and Figure 4.1-24a. The survey spectra show the Al 2p and 2s emissions with their satellite structure around 73 and 118 eV. For the Ar-ion etched sputter target piece, the signal from the Ar 2p and 2s emissions around 240 and 320 eV is detected as well. These emissions stem from the Ar-ions that were implanted during the bombardment of the surface. No O 1s signal is visible in the survey spectrum of any sample (see dashed line), but the detailed spectrum of the O 1s emission reveals that the evaporated thin film contains some oxygen while the Ar-ion etching of the sputter target piece removed all

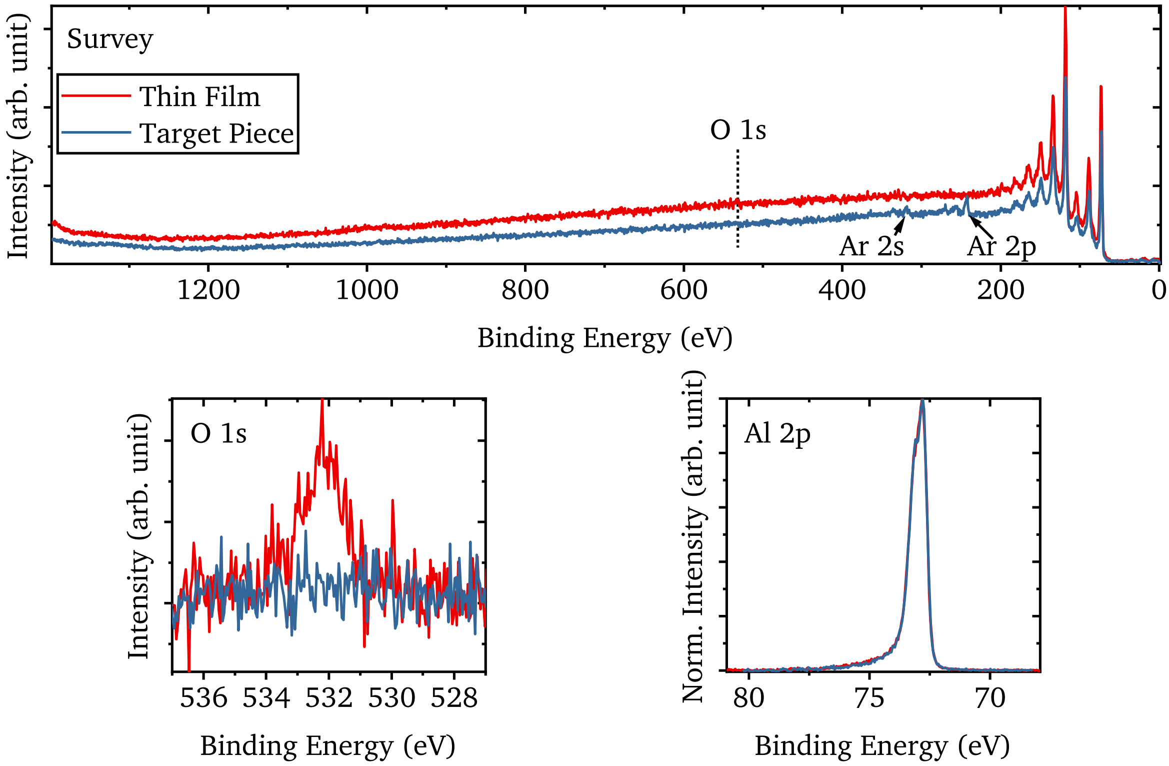

Figure 4.1-23: XP survey spectra and detailed spectra of the core level emissions O 1s and Al 2p for two different Al samples: 20 nm evaporated Al film on an Ar-ion etched Si wafer and an Ar-ion etched piece of an Al sputter target. The Al 2p spectra are normalized and aligned on the binding energy scale to allow for a better comparison of the spectral shape.

oxygen from the surface. The amount of oxygen on the thin film is difficult to put in perspective against the oxygen free sample.

Therefore, the Al 2p spectra are compared to check for a spectral signature of oxidized Al in the thin film spectrum. The spectra are normalized in intensity to allow for a comparison of the spectral shape. There is a very good agreement between the two samples in the Al 2p peak shapes. No additional shoulder or hump towards higher binding energies, which would indicate an oxidized Al species, is detected in the spectrum of the evaporated thin film. This suggests that the amount of oxygen on the evaporated thin film is comparably small. Furthermore, the Fermi edge and SEC energetic positions in Figure 4.1-24 are the same for both samples which also supports this evaluation of only minor oxygen contents as discussed in the following.

When comparing the valence region of both samples in Figure 4.1-24a, it can be clearly seen that the Fermi edges of both samples are at 0 eV binding energy as expected. A difference, however, can be noted above 4 eV binding energies. Here, the evaporated thin film shows a broad peak around 6-8 eV which can be assigned to O 2p states.[164] As UPS is very surface sensitive and the O signal appears in the UP spectrum, it can be assumed that the oxygen detected for the evaporated thin film is mainly situated on the surface of the film. The sharper peak in the UP spectrum of the sputtered sample at about 9.5 eV is probably due to the Ar 3p emission of the implanted Ar atoms.[165] As also mentioned above, the SEC onsets of both samples are very close and yield WFs of 4.21 eV for the evaporated film and 4.29 eV for the Ar-ion etched

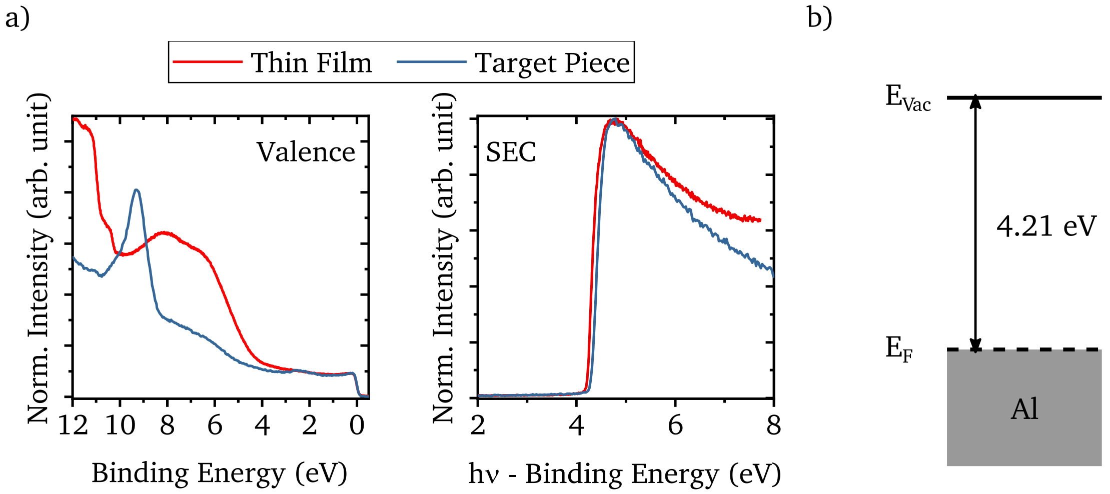

Figure 4.1-24: a) UP spectra of the valence and SEC region for two different Al samples: 20 nm evaporated Al film on an Ar-ion etched Si wafer and an Ar-ion etched Al sputter target. The spectra are normalized for better comparison. The SEC region is plotted against the difference of the excitation energy hν (21.22 eV) and the binding energy. Thus, the WFs can be read from the x-axis at the SEC onsets. b) Energy level diagram for the evaporated thin film based on the SEC onset value determined from the spectrum shown in (a).

sample. These values correspond well to the reported WF decrease of Al with the exposure to oxygen by Blyth et al.[162]

In their study, the WF values range from 4.3 to 3.4 eV with a steep decrease in the first 1000 L[i] of oxygen exposure. Therefore, the WF of the evaporated thin film is still in the range of low oxygen content. It is reported in literature that the oxygen on Al(111) surfaces is distributed in islands of chemisorbed oxygen and oxides on the surface.[167] Figure 4.1-24b presents the WF of the evaporated Al thin film in an energy level diagram which will be referenced to the energy levels of the other materials in the next subsection.

### 4.1.6 Summary

In this chapter, the thin films of the pure materials used in the rest of this work were characterized. The surface of the ITO substrates is cleaned from hydrocarbons by Ar-ion etching which results in a WF of 4.10 eV and has the advantage over the UV-ozone and Ar plasma treatments that it can be performed in-situ with the equipment used for this work. Furthermore, the surface of the ITO substrate is rather smooth with an RMS roughness of 2.8 nm and grain sizes in the range of 20-30 nm. The XP spectra for the p-dopant, CPTCFA, and the HTMs, HTM-B and m-MTDATA, show no unexpected features. Furthermore, DFT was used to calculate the binding energy differences of the photoelectron emissions from the different atoms in the molecules. These calculations were used to generate spectra which could be fitted to the measured data. This allowed do distinguish the spectral contributions of the different atoms in the molecules and the remarkable agreement of the fits supports the impression that no undesired degradation products with different emission signatures are present in the thin films. In addition, the obtained stoichiometries are close to the expected compositions for all

---

[i] L for Langmuir, a practical unit for exposure. 1 L is equivalent to the exposure for 1 second at a pressure of $10^{-6}$ Torr.[166].

molecules. Therefore, it can be assumed that the molecules are stable under evaporation and do not degrade during deposition.

Besides the calculations of the binding energies, DFT was also used to obtain reference spectra for the IRA spectra which were recorded for CPTCFA, m-MTDATA, and HTM-B thin films. With the help of these calculated reference spectra the main contributions to the vibrational modes could be identified. Furthermore, the calculated absorption spectrum of a charged CPTCFA molecule was compared to the one of the neutral molecule. This comparison revealed that the additional electron has a stronger effect on the C≡N stretching vibrations of the cyano groups in the inner part of the molecular structure compared to the more outer located cyano groups. As a result, the vibrational mode of the inner cyano groups was shifted more strongly towards lower wavenumbers on the charged molecule. This effect could be explained by visualizing the pseudo wave functions of the LUMO on the molecule, i.e., the position where an additional electron would be added. The image revealed that the LUMO is located around the center of the molecule including the inner cyano groups but not the outer ones. This analysis and the IRA spectra of the pure organic material thin films will be important for the discussion of the doped HTMs in the next section.

Also, UP spectra from all materials are used to extract the WF and the VBM or HOMO onset. These values, together with the optical energy gaps determined from UV-vis absorption spectra, are then used to construct energy level diagrams of the materials. These diagrams are summarized in Figure 4.1-25. This comparison of the energy level positions shows that the WF of ITO after Ar-ion etching is close to the values of the HTMs. Applying the concepts of semiconductor contact formation described in Section 2.4, smaller space charge regions are expected when depositing the pure HTMs on the ITO substrates as if ITO substrates with a higher work function would be used. It is assumed that the difference in $E_F$ between two materials leads to the formation of space charge regions with a potential variation of the same magnitude as the $E_F$ difference. In case of ITO | m-MTDATA the difference is 0.52 eV and for ITO | HTM-B it is 0.40 eV. In case of a contact formation between the HTMs and Al, the 0.11 eV larger WF of Al has to be taken into account. This simple picture, however, is no longer valid if

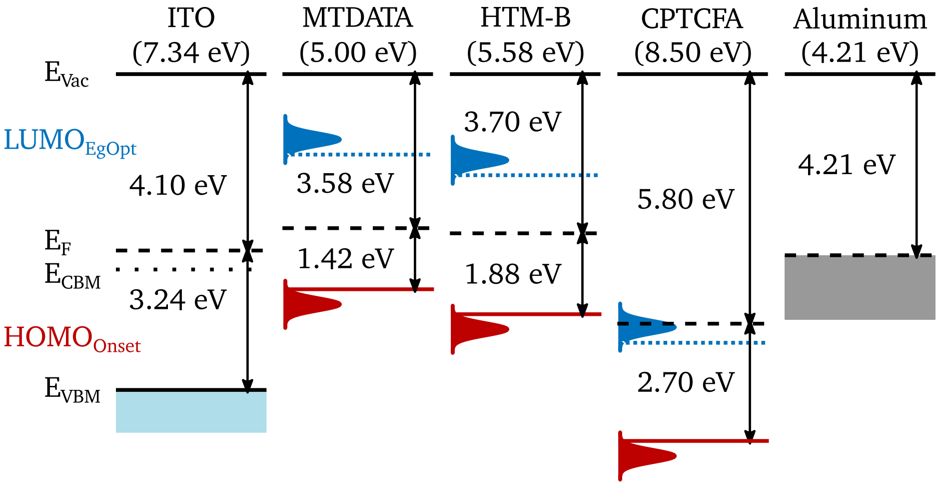

Figure 4.1-25: Summary of the energy level diagrams of the materials characterized in the previous sections. The material is stated above each diagram with its IP in parentheses. Energetic distances HOMO onset to $E_F$ and WFs are determined from UPS while the LUMO onset is based on the optical energy gaps determined from UV-vis absorption spectra. Adapted from Frericks et al.[74]

a double layer potential drop right at the interface of the two materials is formed altering the energy level alignment at the interface.[69]

To reveal the actual energetic alignment at these ITO | HTM and HTM | Al interfaces, interface experiments are conducted, and their analysis and discussion is presented in Chapters 5 and 6. Also, p-doped HTM thin films are analyzed. As can also be seen from the diagram in Figure 4.1-25, CPTCFA shows a much larger WF of 5.80 eV than the HTMs, and the LUMO onset is also well below the HOMO onset of the HTMs. Thus, a p-doping effect where electrons are transferred from the HTMs to the p-dopant molecules creating holes in the HTMs can be expected when co-evaporating the p-dopant with one of the HTMs. This doping of the HTMs would shift the $E_F$ closer towards their HOMO levels and potentially below the $E_F$ of ITO and Al. In that case, the charge transfer between ITO or Al and the p-HTMs would be reversed in comparison to the case of undoped HTMs. The p-doping of the HTMs will be further analyzed and discussed in the next section.

## 4.2 p-Doping of Hole Transport Materials

Doping of transport materials is often used to increase the conductivity and lower charge transfer barriers at the contacts of an organic electronic device.[21–25] Therefore, in Chapters 5 and 6, the interfaces of undoped as well as doped HTM layers are studied. The understanding of the doping process and the electronic properties of the doped transport materials is of great interest. The mechanism can change for different dopant:host systems as will be discussed at the end of this section.[23,27] Even though the main goal of this work is not to study the doping mechanism in organic semiconductors on a broad scale, it is still interesting and part of the characterization process for the used materials. The information gathered in this section on the p-HTMs will be important for the analysis and discussion of the interface experiments in Chapters 5 and 6. There, heterointerfaces between p-HTM and ITO or Al are studied, as well as homointerfaces between p-HTM and layers of the same undoped HTM. To dope the HTMs of this work, m-MTDATA and HTM-B, the commercial p-dopant, CPTCFA, is co-evaporated with the HTMs. In this section, these p-doped HTM layers are first characterized regarding the dopant concentration, the dopant distribution, and the diffusion of the dopant molecule in the matrix. These steps are important to make sure the doped layers are processed as intended. Furthermore, the influence of the dopant on the electronic structure is analyzed to check if the expected doping effect is obtained. Finally, absorption spectroscopy is used to get information on the doping mechanism for the two different HTMs. Salzmann et al. suggest, that an integer charge transfer (ICT) model applies for polymer OSCs, while a charge transfer complex (CTX) model has to be considered for small molecules OSCs.[28] It will be seen if this distinction also holds for the used materials of this work.

### 4.2.1 Dopant Concentration

The doped HTM layers in this work are prepared by co-evaporation where the evaporation rates of the HTM and CPTCFA molecules determine the dopant concentration. The evaporation rates of the molecules are controlled manually via the heating current of the evaporation sources. Therefore, setting an exact dopant concentration is difficult and it is even more important to determine the dopant concentration of the deposited layer afterwards. To determine the dopant

Figure 4.2-1: XP detailed spectra of the F 1s core level emission for a pure CPTCFA film (red) and a p-doped HTM-B film (blue). The shaded areas under the peaks are obtained by integration and used to calculate the volumetric dopant concentration following Eq. (16). In this case the dopant concentration is 14 vol%.

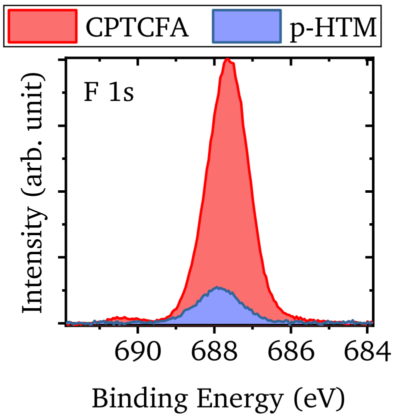

concentration of the deposited thin films, the F 1s emission of the p-doped HTM is compared with the emission from a pure CPTCFA layer. For this analysis, both layers need to be thicker than the information depth of XPS.

As given in Eq. (16) and illustrated by Figure 4.2-1, the blue shaded area under the F 1s peak of the doped layer divided by the red shaded area below the peak of the pure CPTCFA layer approximately yields the volumetric dopant concentration $X$.

$$\frac{\int I^{\mathrm{F1s}}_{\mathrm{p-HTM}}}{\int I^{\mathrm{F1s}}_{\mathrm{CPTCFA}}} \cdot 100 \ \approx X\ (vol\%) \tag{16}$$

This approximation assumes that the volume probed by the measurement stays the same which would mean that the effective attenuation length of the photoelectrons is the same in the pure CPTCFA layer and the CPTCFA:HTM mixture. In addition, it is assumed that the volume per dopant molecule is similar in both layers and that the dopant is homogeneously distributed. This method is limited by the detection limit of XPS, and the precision is dependent on the signal to noise ratio. Thus, the error is larger for low dopant concentrations and concentrations below 1 vol% cannot be evaluated reliably. Besides these drawbacks, this analysis characterizes the actual deposited film and is not based on the pre-determined deposition rates of the pure components as it is the case when working with quartz microbalances. In addition, the method is simple, and the accuracy of the results is sufficient to identify the dopant concentration related trends of this work.

### 4.2.2 Dopant Distribution

The dopant concentration which is discussed in the previous subsection is an average value for the analyzed volume. However, it does not give any information on the distribution of the CPTCFA molecules in the HTM matrix. In literature, inhomogeneous doping profiles were observed and assigned to different sticking coefficients of dopant and matrix molecules on the substrate as well as interdiffusion of the dopant molecule towards the substrate.[168,169] Therefore, it is important to check the processed layers for inhomogeneities. A potential diffusion of the dopant is discussed in the next subsection. Here, the dopant distribution in the p-doped HTM layers during deposition is investigated by a step-by-step deposition of p-m-MTDATA monitored by XPS. The dopant concentration of the final film is determined to be 7 vol%. This concentration is representative for the p-doped layers studied in the interface experiments

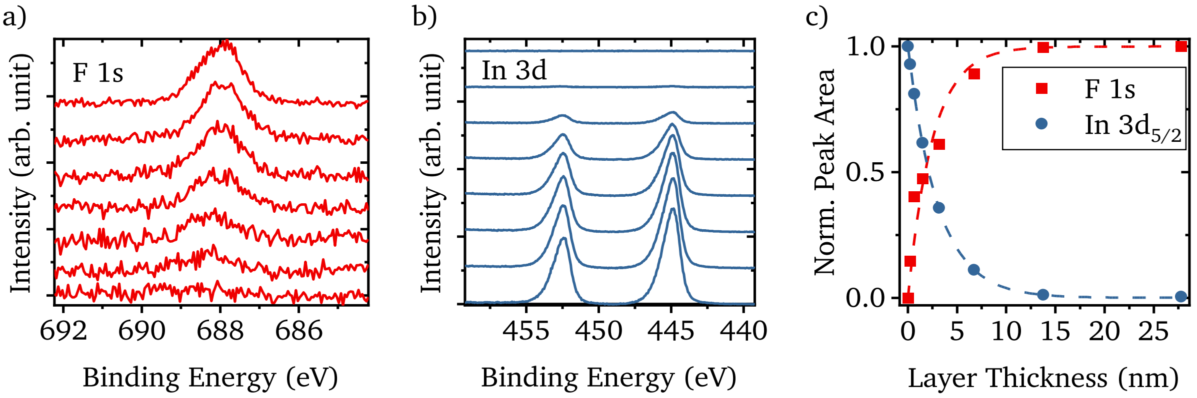

Figure 4.2-2: XP detail spectra of the core level emissions a) F 1s and b) In 3d for the layer-by-layer deposition of p-(7 vol%)-MTDATA on ITO. The adsorption layer thickness increases for the spectra from bottom (0 nm) to top (28 nm). In c), the integrated intensities of the F 1s and In $3d_{5/2}$ peaks are given as normalized scatter plot. The dashed lines indicate exponential Beer-Lambert type behavior. Adapted from Frericks et al.[74]

shown in Sections 5.1 and 5.4 which range from <1 to 11 vol%. The evolution of the F 1s emission from CPTCFA molecules and the In 3d emission from the ITO substrate are plotted in Figure 4.2-2. As expected, the F 1s signal increases and the In 3d signal decreases with increasing film thickness (bottom to top). The areas under the F 1s and In $3d_{5/2}$ peaks are determined and plotted against the film thickness in the right panel of Figure 4.2-2.

The values are normalized to the respective maximum areas. In addition, Beer-Lambert type exponential functions are fit to the data points showing a good agreement for both orbital emissions with a slightly worse agreement for F 1s in comparison to In 3d which can be explained by the reduced signal to noise ratio of F 1s. The good agreement for the ITO substrate signal indicates a homogeneous layer growth. Based on this homogeneous layer growth, the good fit for the CPTCFA signal indicates a homogeneous dopant distribution profile where the amount of dopant is proportional to the layer thickness. As mentioned at the beginning of this subsection, the diffusion of CPTCFA might still lead to some inhomogeneous distribution of the CPTCFA molecules. Therefore, an experiment to test for diffusion is presented in the next subsection.

### 4.2.3 Dopant Diffusion

In the previous subsection, it is shown that the dopant concentration profile right after deposition is homogeneous. However, it is also mentioned that the diffusion of the dopant might cause inhomogeneity after deposition.[169] To check for the diffusion of CPTCFA, a layer stack of 20 nm undoped HTM-B on top of 20 nm 6 vol% p-doped HTM-B is prepared. The stack is measured by XPS and UPS right after deposition and after a period of 5 days during which the sample was kept under UHV conditions. The spectra are shown in Figure 4.2-3. As the undoped layer is thick enough, the F 1s detail spectrum shows no signal from CPTCFA right after deposition. This remains to be the case also after 5 days. Furthermore, no change in the C 1s or valence region is observed. The intensity of the C 1s peak after 5 days is slightly lower, which might be due to some variations in the intensity of the X-ray source but is no sign for a diffusion of the CPTCFA. If the dopant would diffuse into the undoped layer due to the concentration gradient between doped and undoped layer, a F 1s signal should be detected and an $E_F$ shift should occur resulting in a shift of the HOMO onset and C 1s emission towards lower binding

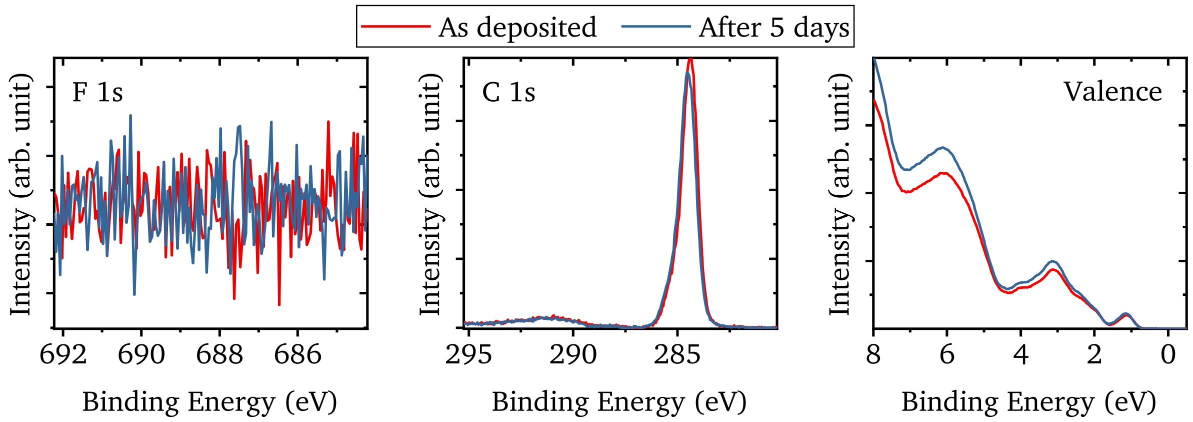

Figure 4.2-3: XP detail spectra of the core level emissions F 1s and C 1s as well as UP valence region spectra for the layer stack HTM-B 20 nm/p-(6 vol%)-HTM-B 20 nm/ITO right after deposition and after 5 days in UHV.

energies. As this is not the case and the time span of 5 days does exceed the time scale of the experiments in this work, the diffusion of the CPTCFA molecules can be excluded for the presented experiments. In addition, it can be mentioned that devices fabricated by the project partner Merck KGaA containing doped and undoped layers showed similar electric characteristics even after some month. This would also not be expected, if the CPTCFA molecules were to diffuse.

### 4.2.4 Electronic Structure

As mentioned in the introduction to this Section 4.2, doping is used to increase the conductivity of transport layers and also reduce charge transfer barriers at the interfaces. Therefore, the doping should change the electronic structure leading to an increased number of charge carriers. This increased number of charge carriers will be visible by a shift of the Fermi level.[23] In this subsection, the doping effect will be evaluated. Comparing the energy level diagrams of the HTMs and the p-dopant shown in the summary of the previous chapter (Figure 4.1-25), a charge transfer from the hole transport molecules to CPTCFA molecule can be expected as the $E_F$ of CPTCFA is significantly lower than the one of the HTMs. This charge transfer will lead to

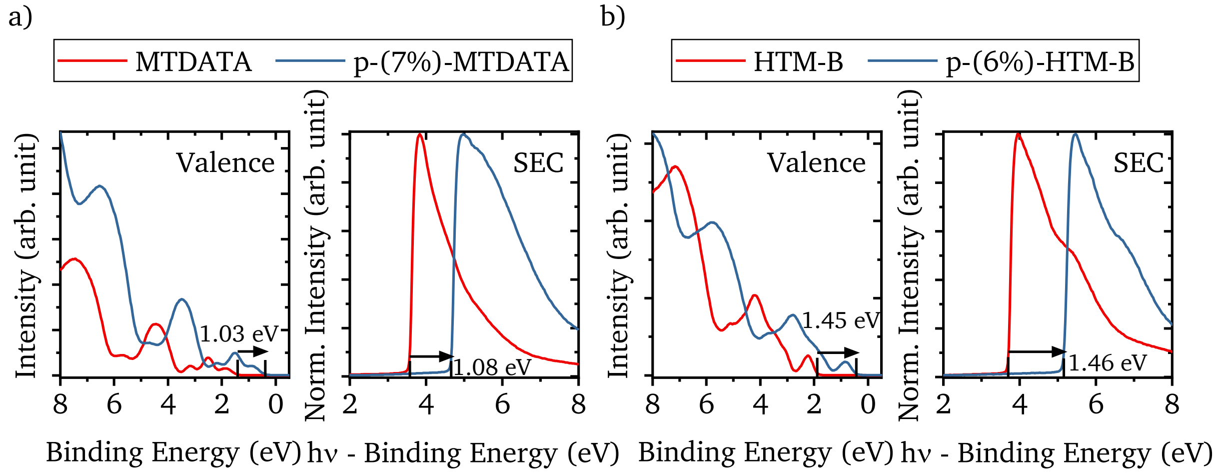

Figure 4.2-4: UP spectra of the valence and SEC region for 20 nm undoped and doped (a) m-MTDATA and (b) HTM-B films on ITO. The SEC regions are plotted against the difference of the excitation energy hν (21.22 eV) and the binding energy. Thus, the WFs can be read from the x-axis at the SEC onsets. The arrows indicate the energetic shift due to the doping induced $E_F$ shift towards the HOMO.

a doping effect with a hole in the HOMO of the HTM and a resulting shift of the HTM's $E_F$ towards the HOMO onset. UP spectra of doped and undoped m-MTDATA and HTM-B are shown in Figure 4.2-4. For m-MDTATA, it can be seen that the HOMO onset in the valence region shifts by 1.03 eV towards lower binding energies and the SEC onset shifts by 1.08 eV in the same direction. This means that the energetic distance HOMO onset to $E_F$ is reduced while the WF increases by about the same value. As a result, the IP remains about the same for doped and undoped layer, but the $E_F$ shifts towards the HOMO as expected. For HTM-B, the observed shifts are 1.45 eV and 1.46 eV in the valence and the SEC region for the comparison of doped and undoped samples. This leads to an energetic distance HOMO onset to $E_F$ of 0.39 eV for m-MTDATA and 0.43 eV for HTM-B. These values are close to the ones which Paula Connor determined in her master thesis[102] for the same CPTCFA:HTM combinations: 0.38 eV for m-MTDATA and 0.5 eV for HTM-B. In that work, she also studied the $E_F$ shift vs. the dopant concentration and found that the $E_F$ shift saturates around a dopant concentration of 2 vol%. This observation is also made in this work and will be further discussed in Section 5.3.

### 4.2.5 Dopant Influence on Valence States

It is known that the presence of dopant molecules in a matrix cannot only lead to the intended electronic doping effect but also to an electronic and steric increased disorder.[170–172] An increased disorder would lead to a broadening of the density of states which would also result in a broadening of the valence features in UP spectra. A related change of molecular orientation or conformation could also change the energetic distance between the valence features.[47,170,173] Additionally, trapped charge carriers forming polaron states in an organic matrix may also lead to changes in the molecular structure. To check for these effects, the UP spectra of differently doped m-MDATA and HTM-B are analyzed in Figure 4.2-5. The spectra are shifted on the binding energy scale to be aligned at their HOMO onset energetic positions. In addition, the spectra are normalized with respect to the maximum around 3 eV below the HOMO onset for m-MTDATA and about 2.5 eV for HTM-B. These modifications favor a comparison of the spectral shape and clearly reveal a broadening of the spectra for the doped layer. This broadening seems to increase stepwise with dopant concentration from 0 over 2 to 7 vol% for

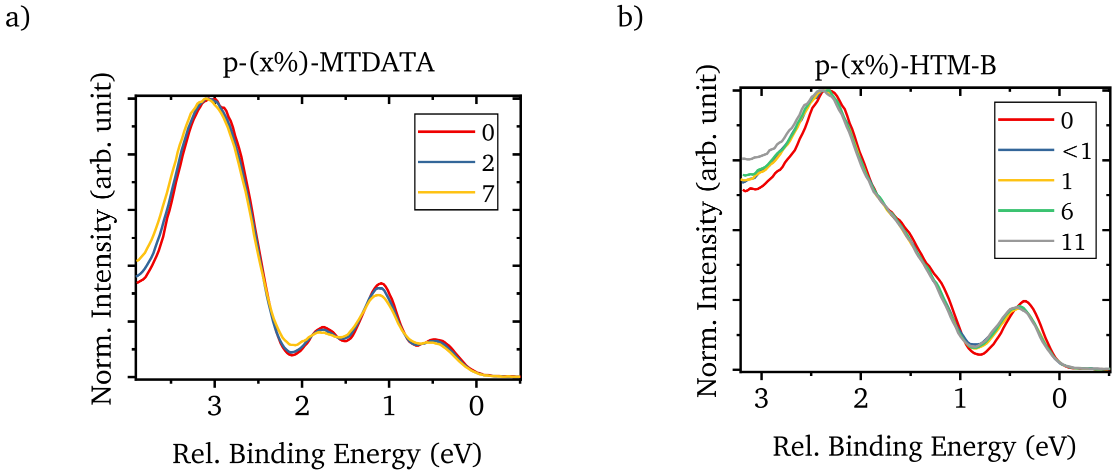

Figure 4.2-5: UP spectra of the valence region for differently doped m-MTDATA and HTM-B films on ITO. For a better comparison of the spectral shape, the intensities are normalized, and the spectra are shifted on the binding energy scale. The legend gives the dopant concentration in vol%. Adapted from Frericks et al.[74]

m-MTDATA while for HTM-B it appears right at the lowest concentration of <1 vol% and then does not become stronger for higher dopant concentrations. This small difference could indicate a different interaction of CPTCFA with m-MTDATA in comparison to HTM-B. In the following subsections, this difference becomes more obvious and will be discussed further.

### 4.2.6 UV-vis-NIR and Infrared Reflection Absorption Spectroscopy

The doping mechanism in organic semiconductors can vary among different dopant:host systems.[27] Therefore, it is interesting to characterize the studied material combinations regarding their doping mechanism. Especially, as CPTCFA and HTM-B molecules are well-performing commercially available materials which are barely discussed in literature. Based on previous work in the literature, including the p-dopant TCNQ and its fluorinated derivatives, absorption spectroscopy in the UV, vis, NIR, MIR range is performed and will lead to a discussion of the doping mechanism in the next subsection.[27,170] The UV-vis and the NIR range of the spectra are separated by a line at 1.18 eV as they were measured with the same light source but different detectors and optical fibers. These different setup configurations explain the offset that is visible in the graphs around this spectral range transition. Figure 4.2-6a shows the UV-vis-NIR absorption spectra of pure m-MTDATA and CPTCFA films (see Figure 4.1-16 and Figure 4.1-10) in comparison to a highly p-doped m-MTDATA layer with a dopant concentration of 25 vol%. For visualization purposes, the intensity of the spectrum of the pure CPTCFA film is divided by two. All spectra were measured at 100 nm thick films on ITO substrates. It is unambiguously visible that the p-m-MTDATA film shows absorption features at about 1.1 and 1.7 eV that are not present in either of the two pure component layers. This difference suggests a charged m-MTDATA ion as is later discussed in Subsection 4.2.7. Furthermore, the two local maxima at 2.4 and 2.7 eV are well separated and also different from the absorption of pure CPTCFA around the same energy range. Finally, the absorption above 3.2 eV changes between the undoped and the doped m-MTDATA film. For the undoped film,

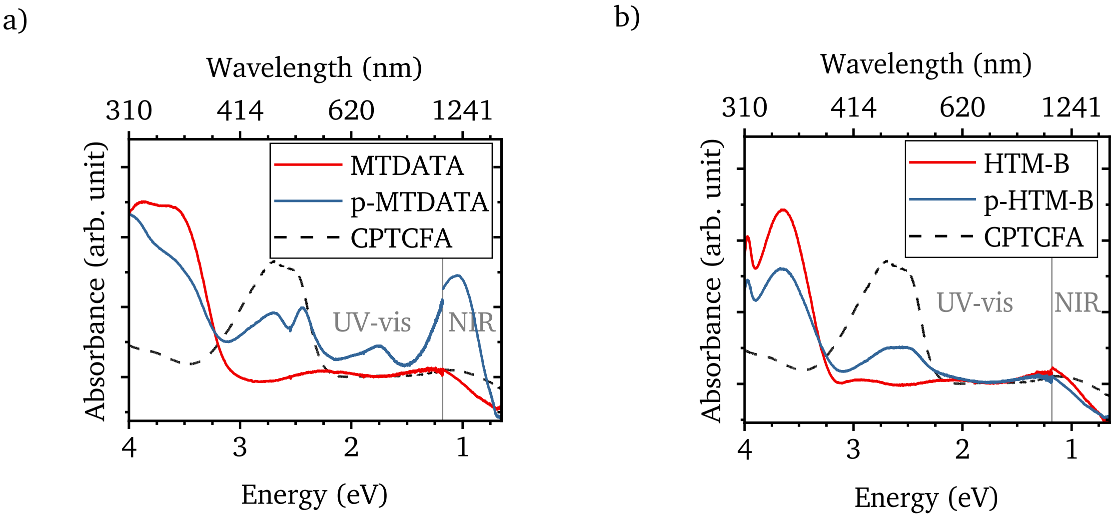

Figure 4.2-6: UV-vis-NIR absorption spectra of 100 nm undoped and doped m-MTDATA (a) and HTM-B (b) films on ITO. An ITO substrate is taken as reference. All spectra are normalized. The intensity of the spectrum of the pure CPTCFA film is divided by two and is plotted for comparison. The dopant concentrations are 25 vol% for m-MTDATA and 19 vol% for HTM-B. The absorbance is calculated from the transmission neglecting the reflection. The UV-vis and NIR regions are indicated and were measured with different detectors and optical fibers. The new absorption peaks in the p-m-MTDATA film around 1.1 and 1.7 eV are discussed in Section 4.2.7.

the absorption appears to consist of two peaks of similar intensity while the doped film shows a less intense shoulder at lower energies and a more intense feature shifted to higher energies.

For HTM-B in Figure 4.2-6b, the same comparison does not reveal obvious differences between dopant:matrix mixture and pure material thin films. The p-doped HTM-B film spectrum rather appears as superposition of the pure HTM-B absorption above 3.2 eV and with reduced intensity of the CPTCFA absorption between 2.2 and 3 eV. Still, it might be argued that there is a slight deviation between 2 and 2.25 eV where the absorption of the doped HTM seems to be broader and tailing to lower energies than the pure CPTCFA absorption. This might be the indication for some interaction of dopant and host molecule. This different behavior in the UV-vis-NIR absorption for the doping of m-MTDATA and HTM-B suggest a different doping mechanism which is discussed in the next Subsection 4.2.7.

By IRA spectroscopy[j], significant differences for the p-doped HTMs are found as well. Figure 4.2-7 shows the IRA spectra of pure m-MTDATA (top panel), 25 vol% p-doped m-MTDATA (center panel), and pure CPTCFA (bottom panel). The insets show the wavenumber range from 2150 to 2280 $cm^{-1}$. The vibrational modes of the pure components are already assigned in Subsections 4.1.2 and 4.1.3 and can be looked up there. Here, the new modes given by the added labels in Figure 4.2-7 will be discussed. The goal is to describe differences between the measured p-m-MTDATA spectrum and a spectrum that would simply be a superposition of the two pure component spectra.

The vibrational modes (1) and (5) of m-MTDATA do not overlap with any strong modes from pure CPTCFA and are also clearly visible for the p-m-MTDATA film. The other modes (2-4) overlap with modes from pure CPTCFA (7-9) and thus cannot be easily separated from these in the mixture. Still, the vibrational mode (9*) of the p-m-MTDATA layer does not seem to be a simple superposition of the modes (9) and (4). Also, the shape of mode (6*) is significantly changed in comparison to (6). Furthermore, a strong new mode (11) appears in the p-m-MTDATA layer. Finally, the C-N stretching vibrational modes of the CPTCFA molecule (a, b) shown in the insets change from the pure CPTCFA film to the CPTCFA:MTDATA mixture (a*, b*). The two modes from pure CPTCFA of the inner (a) and outer (b) cyano groups at 2219 and 2248 $cm^{-1}$, respectively, shift towards lower wave numbers in the mixed film. The outer cyano group mode (b*) shifts to 2240 $cm^{-1}$ and the inner cyano group (a*) to 2188 $cm^{-1}$. As discussed, when comparing the pure CPTCFA spectrum to DFT calculations of the neutral and charged CPTCFA molecule in Subsection 4.1.2, the inner cyano group mode is affected more strongly by an additional charge. For the spectra calculated by DFT, the wavenumber difference between the two C-N stretching modes changes from 42 to 78 $cm^{-1}$ from the neutral to the charged molecule. This is an increase by a factor of 1.86. In addition, the inner cyano group mode becomes more intense for the charged molecule. The wavenumber difference of the two modes in the measured spectrum of pure CPTCFA is 29 $cm^{-1}$ and the one obtained for the p-m-MTDATA film is 52 $cm^{-1}$ which yields a factor of 1.79. This is surprisingly close to the calculated one even though the calculations were performed on single molecules in vacuum and clearly diverge from the measured spectra. Also, in agreement to the calculations, the inner

---

[j] Infrared Reflectance Absorption Spectroscopy was performed with the help of Rainer Bäuerle, OCI Heidelberg University.

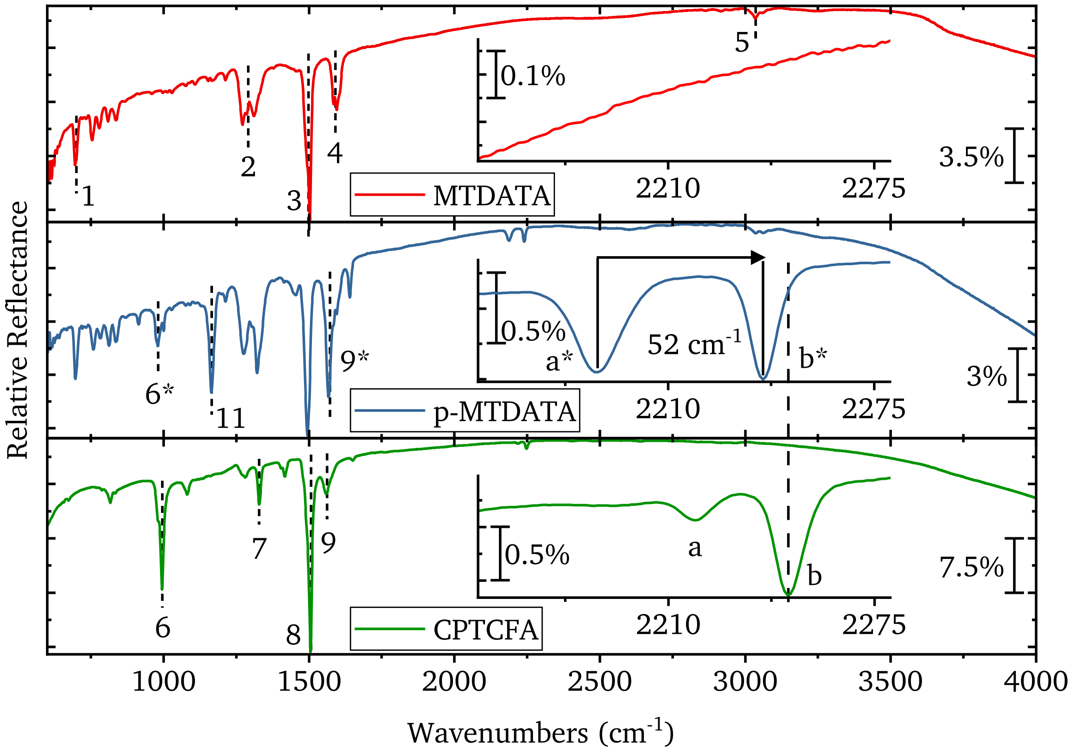

Figure 4.2-7: IRA spectra of 100 nm thin films of m-MTDATA (top), p-(25 vol%)-m-MTDATA (center), and CPTCFA (bottom) on ITO. The x-axes of the insets are aligned among each other and show the region from 2150 to 2280 cm$^{-1}$. The relative reflectance scale for the graphs is indicated by the percentage values.

cyano group mode in the p-m-MTDATA spectrum is more intense than in the pure CPTCFA spectrum. These observations suggest the presence of a negatively charged CPTCFA molecule which will be further discussed in the next Subsection 4.2.7.

The same comparison of IRA spectra is also done for HTM-B and is shown in Figure 4.2-8 with the pure HTM-B film at the top, the doped HTM-B film in the center, and the pure CPTCFA film at the bottom panel. As for the case of m-MTDATA, the vibrational modes of the pure components were already assigned in Subsections 4.1.2 and 4.1.4, and are now simply discussed by the labels added in Figure 4.2-8.

The vibrational modes (1) and (5) of the HTM-B layer have no overlap with modes from CPTCFA and appear unchanged in the p-HTM-B layer. The other HTM-B modes (2-4) overlap with modes (7-9) from pure CPTCFA but seem to be simply superposed in the p-HTM-B layer. Mode (6) also appears in the CPTCFA:HTM-B mixture without a strong change in shape. The strong new mode (11 in Figure 4.2-7) for p-m-MTDATA cannot be found for p-HTM-B. Finally, the C-N stretching vibration modes (a, b) of the CPTCFA molecule shown in the insets are compared. For p-HTM-B, the outer cyano group mode (b*) appears nearly at the same wavenumber as in the pure CPTCFA film (b) at about 2248 cm$^{-1}$ but with a more triangular than Gaussian shape. Below this absorption feature, there is some broad absorption (a*) visible from 2174 to 2228 cm$^{-1}$. This is quite different from the case of m-MTDATA where the inner cyano group mode became significantly more intense and appeared as clearly identifiable Gaussian shaped absorption. Overall and in contrast to the m-MTDATA case, the absorption spectrum of the p-HTM-B layer appears as mere superposition of the pure HTM-B and CPTCFA IRA spectra.

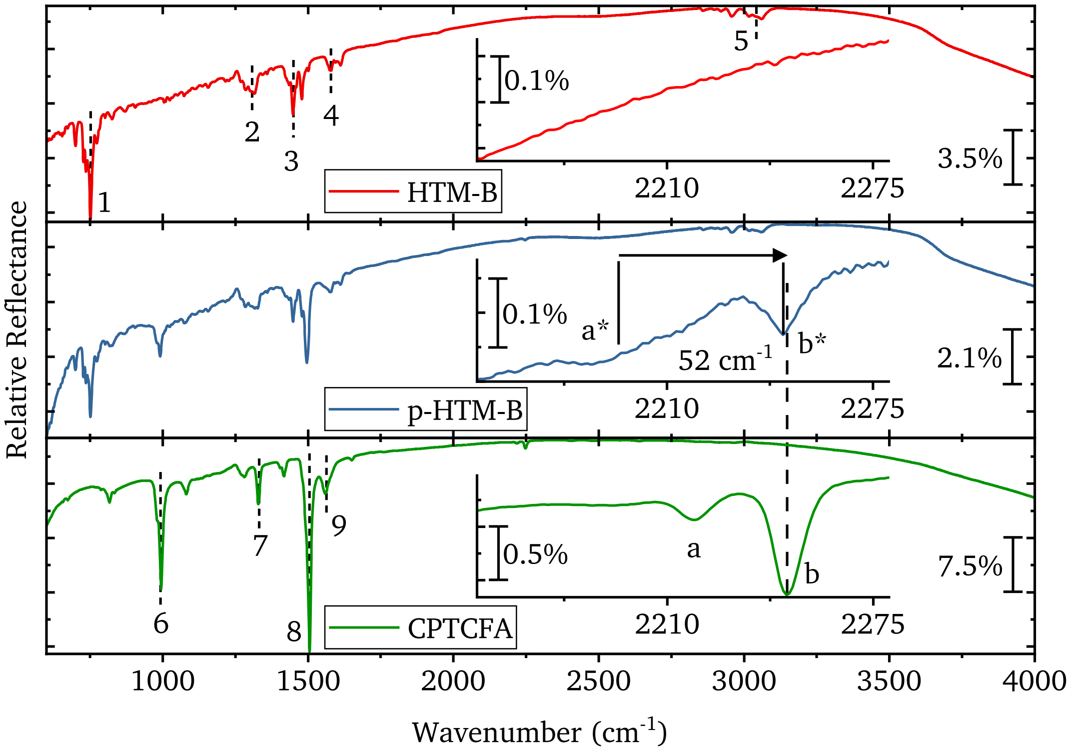

Figure 4.2-8: IRA spectra of 100 nm thin films of HTM-B (top), p-(19 vol%)-HTM-B (center), and CPTCFA (bottom) on ITO. The x-axes of the insets are aligned among each other and show the region from 2150 to 2280 cm$^{-1}$. The relative reflectance scale for the graphs is indicated by the percentage values for the tick distances.

Thus, no indication of a charged molecular species due to a charge transfer between the dopant and host molecule is found. This different behavior of m-MTDATA and HTM-B under p-doping is further discussed in the next subsection with the aim to assign known doping mechanisms to the two dopant:HTM systems.

### 4.2.7 Doping Mechanism Discussion

In this subsection, the observations of the UV-Vis-NIR absorption and IRA spectroscopy (previous Subsection 4.2.6) will be discussed regarding the doping mechanism in the two dopant:host systems relevant for this work: CPTCFA:m-MTDATA and CPTCFA:HTM-B. For a deeper understanding of the here briefly mentioned ideas, the reader may please refer to the works of Lüssem et al.,[23] Salzmann et al.,[28,46,63] and Tietze et al.[81,174–176] which are the basis for the performed discussion. Some more general information on the doping of organic semiconductors and an illustration of the discussed doping models (see Figure 2.3-1) can be found in Subsection 2.3.

At first sight, the doping of organic semiconductors can be understood similarly as for inorganic semiconductors. An acceptor or donor species is introduced into a host system where it accepts or releases charges to create free holes or electrons and thus enhances the conductivity of the material. However, the electronic structure of organic semiconductors does not consist of delocalized bands as in the case of their inorganic counterparts but of localized states due to the weak interatomic interactions. In addition, the low dielectric constants of organic semiconductor materials lead to strong Coulombic interactions. As result, the charge transfer between matrix and dopant does not lead directly to a free charge carrier but to a localized polaron state. Besides other possibilities, molecular dopants are often used especially as p-dopants due to their better morphological stability than, e.g., halide atoms.

The explained charge transfer between dopant and matrix describes the so-called integer charge transfer (ICT) doping mechanism (see Figure 2.3-1a in Section 2.3). Here, the participating matrix molecule forms the cation and the doping molecule the anion for p-doping or vice versa in the case of n-doping. These ions show absorption spectra strongly different to their neutral versions in the UV-vis-NIR as well as the MIR range. For example, studies on the dopant:matrix combinations of $F_4$TCNQ:P3HT[k] and $MoO_3$:CBP[l] could clearly identify the $F_4$TCNQ anion or the CBP cation.[177,178] The second doping mechanism discussed in literature, is the so-called charge transfer complex (CTX). It was proposed by Salzmann et al. and describes the formation of a dopant:host complex where the frontier orbitals of both molecules overlap and form new bonding and anti-bonding states.[63] For the example of p-doping, it is the HOMO of the matrix molecule that hybridizes with the LUMO of the dopant molecule leading to partial charge transfer and forming a complex with a new HOMO and LUMO. The new LUMO of the complex can then act as electron acceptor and can lead to a doping effect (see Figure 2.3-1b in Section 2.3). In this model, there are no electronically separated anions and cations as the charge transfer per molecule is only partial.

Hence, the absorption spectra of such systems should not correspond to the ones of the ionic molecules. Instead, the absorption spectra are expected to show signs of partial charge transfer, e.g., a slight shift of a vibrational mode or the optical transition across the energy gap of the new complex as described by Mendez et al.[27] In the work of Mendez et al., the doping mechanism of the host materials P3HT and 4T[m] in combination with the dopant TCNQ and its fluorinated derivatives ($F_x$TCNQ) is studied. Their data for the $F_x$TCNQ:P3HT systems show clear signs of an ICT with $F_x$TCNQ anion features in the UV-vis-NIR as well as the MIR range. On the other hand, the $F_x$TCNQ:4T system does not show absorption features of the $F_x$TCNQ anions in the UV-vis-NIR but a new absorption band that they assign to the proposed CTX. In the MIR spectrum of the doped layers, Mendez and coworkers find the C≡N stretching vibration mode of $F_x$TCNQ shifted to lower wavenumbers compared to pristine dopant films but not as much as in the combination with P3HT. From this shift the degree of partial charge transfer can be calculated and is determined to be around 0.25.

Based on these models and the related observations, the analysis of the absorption spectra of the p-doped HTMs from the previous subsection can be discussed. In the case of p-m-MTDATA, a strong variation from the absorption spectra of the pure components is observed. This suggests that an ICT is taking place for the CPTCFA:MDTATA mixture. As a result, CPTCFA becomes the anion and m-MTDATA the cation. This leads to respective changes for the absorption in comparison to the neutral molecules. More precisely, this explanation matches the good agreement of the change in the cyano group stretching vibrations between doped and undoped layer with the calculations for the charged and neutral CPTCFA molecule. Furthermore, the

---

[k] $F_4$TCNQ Tetrafluorotetracyanoquinodimethane; P3HT Poly(3-hexylthiophene)

[l] CBP 4,4′-Bis(N-carbazolyl)-1,1′-biphenyl

[m] Quaterthiophene

changed UV-vis absorption above 3.2 eV and the new absorption around 1.1 eV for p-m-MTDATA are the same as in a spectrum reported for $MoO_3$:m-MTDATA. Here, $MoO_3$ is used to oxidize m-MTDATA and obtain a reference spectrum for the m-MDTATA cation.[179] In analogy to this argumentation, the absence of any new absorption features in the case of p-HTM-B can be explained by the CTX model. However, if following the observations on $F_x$TCNQ:4T the complex should be visible as new transition in the UV-vis-NIR spectrum. The p-HMT-B IRA spectrum also shows barely any difference that would indicate even a partial charge transfer. The C≡N stretching vibration modes are marginally shifted. Maybe, the broad absorption visible from 2174 to 2228 $cm^{-1}$ is the result of a variety of slightly different complexes due to several slightly different orientations of matrix and dopant molecules leading to different degrees of charge transfer. These different degrees of charge transfer would then cause different strongly shifted vibrational modes which would appear as a broad absorption. In comparison to the crystallite system $F_x$TCNQ:4T, the molecules in this work are larger and are expected to form amorphous layers (see Subsections 4.1.3 and 4.1.4). As a consequence, differently orientated complexes explaining the absence of a clear complex-induced absorption seem possible. Following the argumentation of Salzmann et al.,[28] the formation of a CTX could explain the observed saturation of the $E_F$ above the matrix HOMO onset with increasing dopant concentration. The new complex LUMO would be saturated above the matrix HOMO and thus the $E_F$ would be pinned between the two levels.[28] For m-MTDATA, however, this explanation cannot hold as it seems that an ICT is taking place. Considering that the LUMO of CPTCFA is below the HOMO onset of m-MTDATA, degenerate-like doping where the $E_F$ shifts into the HOMO of m-MDATA would be expected for high dopant concentrations. This kind of degenerate doping is, e.g., observed for doping of P3HT. For P3HT, a finite density of states that pins the $E_F$ is observed by photoemission spectroscopy. The origin of these states is claimed to be a polaron lattice.[28,180] Still, for p-m-MTDATA no such states are observed. Another explanation for the saturation of $E_F$ above the HOMO onset, is given by the internal interface charge transfer doping model introduced by Mayer et al.[65] In this study, Mayer and coworkers found that the dopant is forming precipitates in the matrix creating an interface between dopant and matrix phase. At this internal interface, electric double layers are formed which limit the shift of $E_F$. However, in the case of m-MTDATA the saturation starts already at a rather low dopant concentration of 2 vol% which makes the formation of precipitates less likely.

In conclusion, the introduction of the p-dopant, CPTCFA, into m-MTDATA and HTM-B leads to a shift of the $E_F$ by about 1.03 and 1.45 eV towards the HOMO onset. Absorption spectra reveal the presence of a p-dopant anion and a m-MTDATA cation indicating an ICT. For HTM-B, the absorption spectra show barely any signs of a charge transfer which might be a sign for the formation of a CTX. Still, a final answer to the question of the doping mechanism in HTM-B and m-MTDATA cannot be given here and further studies with a focus on this complicated subject are necessary. These studies might require a systematic choice of materials and a wider range of methods, e.g., inverse photoemission spectroscopy (IPES) to measure the energetic position of unoccupied acceptor states.[32,62]

## 4.3 Conclusion

In this chapter, at first, thin films of the pure materials relevant for this work were characterized and, second, the p-doping of the used hole transport materials was investigated. The characterization of the ITO substrates in combination with different surface treatments revealed that Ar-ion etching removes the hydrocarbon contaminations which are present after the solvent cleaning of the substrates and creates a substrate surface with a reproducible WF of 4.1 eV. Furthermore, the Ar-ion etching can be performed in-situ and is thus preferred over other surface treatments. Beside the WF, an IP of 7.4 eV was determined by UPS. The topographical characterization by SEM and AFM, showed a rather smooth surface with an RMS roughness value of 2.8 nm. The structure at the surface consists of grains with 2 nm height and 20-30 nm diameter. This is relatively flat and wide compared to the size of the organic molecules which is in the range of 1-2 nm. Thus, a smooth layer-by-layer growth of the organic thin films on the ITO substrates can be expected.

The organic molecules, a commercially available p-dopant, CPTCFA, a literature-known HTM, m-MTDATA, and a commercial HTM of Merck KGaA, HTM-B, were characterized by XPS, UPS, UV-vis-NIR absorption, and IRA spectroscopy. Via XPS, it could be confirmed (within the XPS restrictions) that the molecules are not decomposed during the thermal evaporation process. To draw this conclusion, the stoichiometric ratio of the atoms in the molecule were checked and the XP spectra were compared to simulated spectra based on DFT calculations. From the valence and SEC regions of the UP spectra, the WF/IP of the materials were determined to be 3.6/5.0 eV for m-MTDATA, 3.7/5.6 eV for HTM-B, and 5.8/8.5 for CPTCFA. The optical energy gap of the materials was evaluated from the UV-vis-NIR absorption spectra: 3.1 eV (m-MTDATA), 3.2 eV (HTM-B), and 2.3 eV (CPTCFA). The IRA spectra of the organic thin films were recorded for an evaluation of the doping mechanism in the second part of this chapter. DFT calculations were used to distinguish the different vibrational modes. For CPTCFA, the vibrational modes of a negatively charged molecule were calculated. This calculation revealed that the stretching modes of the cyano groups in the inner part of the molecule were more strongly affected by the added charge than the cyano groups in the outer part of the molecule. This observation was linked to the calculated pseudo wave functions which showed that the LUMO is located mostly around the center of the molecule than at the outer parts.

Finally, a thermally evaporated Al thin film was compared to an Ar-ion etched clean Al surface revealing only minor amounts of oxygen on the evaporated thin film. The WF of the evaporated Al thin film was determined at 4.2 eV. The electronic structure of all materials was summarized in energy level diagrams at the end of the first Section 4.1.

In the second Subsection 4.2, the quality of the p-doped m-MTDATA and HTM-B layers was checked. First, the data analysis process for the dopant concentration was explained. Then, experiments on the distribution and diffusion of the dopant molecules were discussed. It was shown that the distribution of the CPTCFA molecules across the deposited layer is homogeneous and no signs for diffusion of the CPTCFA molecules were found. The evaluation of the electronic structure of the doped layers showed that the Fermi level is shifted by 1.1 eV for m-MTDATA and 1.5 eV for HTM-B towards the HOMO levels of the molecules. Furthermore, the introduction of the dopant lead to a broadening of the valence spectra in both molecules which indicates a disturbance of the structure, orientation, or conformation of the host molecules by the CPTCFA molecules.

UV-vis-NIR absorption and IRA spectra of the p-m-MTDATA and p-HTM-B layers in comparison to the undoped layers showed a clear difference between the two HTMs. For p-m-MTDATA, new UV-vis-NIR absorption features were found which do not correspond to the pure m-MTDATA or CPTCFA spectrum. The features could be assigned to m-MTDATA cations. In addition, the cyano group stretching vibrations of CPTCFA were shifted similar as in a DFT calculated spectrum for the negatively charged CPTCFA molecule. For this reason, an integer charge transfer is expected to occur in the CPTCFA:MTDATA system. This observation is contradicting the suggestion by Salzmann et al.[28] who expect a charge transfer complex formation for small molecules. It remains unclear why the Fermi level saturates above the HOMO level of m-MTDATA when the LUMO level of CPTCFA is well below. In contrast, the p-HTM-B absorption spectra appeared as mere superposition of the spectra from the pure materials showing barely any feature that could be addressed to a charged species. Therefore, it is believed that the doping mechanism in the CPTCFA:HTM-B system is based on the formation of a charge transfer complex. Here, the electronic states of the formed complex act as acceptor states for the electron causing the p-doping effect without the formation of a cation-anion pair. Further experiments using IPES could be used to identify these new acceptor states in the CPTCFA:HTM-B system.

In the next chapter, the interfaces with the doped and undoped HTMs will be investigated and the doping mechanism of the two HTMs will be further discussed.

# 5 Modeling of Interface Experiment Photoelectron Spectra

In the previous chapter thin films of indium tin oxide (ITO), a commercially available p-dopant, herein called CPTCFA, the well-known hole transport material (HTM) m-MTDATA, a commercially available HTM, herein called HTM-B, and aluminum were characterized regarding their bulk electronic structure. Furthermore, doping of the HTMs with CPTCFA was investigated. Now, in this chapter, the electronic structure at the interfaces of these materials will be studied. These interfaces typically play an important role in organic electronic devices as, e.g., the presence of space charge regions at the interface can hinder or enable charge injection[23], or can lead to a shift of the onset voltage of a device[14,15]. Furthermore, a model approach that goes far beyond a classical Schottky model and is based on an approximated density of states (DOS) will be used to calculate the electric potential distribution at the interfaces and generate photoelectron spectroscopy data that can be fitted to the experiments. The aim of this chapter is to introduce the model, test it against a classical analysis approach, and show the advantages and additional insights provided by this sophisticated method. At first, the classical analysis is applied to ITO | (p-)HTM heterointerfaces where the HTM can be undoped or p-doped. This will provide the test case for the DOS-based model. Next, the DOS-based model is introduced. The same ITO | (p-)HTM heterointerface data analyzed by classical methods are fitted by the modeled data and the results are compared. In addition, an in-depth discussion enabled by the modeling is given. Finally, the model is applied to p-HTM | HTM homointerfaces where a classical analysis fails. Here, the model is further advanced and predicts the formation of a high density of tailing gap states right at the interface. These predicted gap states will be discussed with respect to literature where a density of states in the energy gap is a recurring explanation for the electronic structure of organic semiconductors at heterointerfaces.[32,47,49–52] The results of this chapter were published in:

*Frericks, Markus; Pflumm, Christof; Mankel, Eric; Mayer, Thomas; Jaegermann, Wolfram (2021): Space Charge Regions at Organic p-i-Homointerfaces from Advanced Modeling of In Situ-Prepared Interfaces Analyzed by Photoelectron Spectroscopy. In: ACS Appl. Electron. Mater. 3 (3), S. 1211–1227. DOI: 10.1021/acsaelm.0c01062.*[74]

## 5.1 Classical Analysis of Heterointerface Experiments

Before the sophisticated DOS-based model is introduced and tested, the typical approach of analyzing photoelectron spectroscopy interface experiments (see Section 3.1) shall be demonstrated. Thus, this classical approach as, e.g., outlined by Klein et al.[48] will be used to study the ITO | (p-)HTM heterointerface where the in-situ layer-by-layer deposition is monitored by X-ray photoelectron spectroscopy (XPS) and ultraviolet photoelectron spectroscopy (UPS) measurements. As mentioned before, ITO is a commonly used transparent conductive oxide (TCO) which is often used in organic light emitting diodes (OLEDs) as anode material. There, the role of ITO is to inject holes into the HTM. Frequently, the HTM is doped to increase the conductivity and to reduce the contact resistance by lowering the electronic interface barrier or reducing the barrier width far enough that the charges can tunnel through.

This section is divided into the first part investigating the undoped HTMs, and the second part studying the interfaces of the p-doped HTMs. The results of this section serve as benchmark for testing the DOS-based model.

### 5.1.1 Heterointerfaces with Undoped Hole Transport Materials

The undoped HTMs, m-MTDATA and HTM-B, were deposited layer by layer in an in-situ evaporation process. The film growth was monitored by consecutive XPS and UPS measurements. The respective spectra are shown in Figure 5.1-1 for m-MTDATA and Figure 5.1-2 for HTM-B. The analysis and trends for both materials are the same and therefore discussed together. The C 1s emission spectra are the strongest core level signal for the organic molecules and are shown in a). The N 1s emission (not shown) is much weaker and has a worse signal to noise ratio. Still, the observed trends are similar. It can be clearly seen that the C 1s intensity increases with increasing film thickness until the films are thicker than the information depth of XPS (about 15 nm). The In 3d substrate emission (not shown) decreases in intensity as the signal is damped by the adlayer. The binding energy position of the C 1s peaks is determined by fitting only the top part (around a quarter of the maximum intensity) by a Gaussian. The determined binding energy positions are indicated by black markers in the figure. It can be observed, that the C 1s peaks shift slightly to higher binding energies with increasing layer thickness. The analysis of the valence spectra in b) is already more complicated. Here, the emission from the substrate and the adlayer overlap and need to be separated by a fitting procedure. For the fitting, the spectrum of the bare substrate (first spectrum from the bottom) and the pure spectrum of the adlayer (second spectrum from the top) are interpolated. The

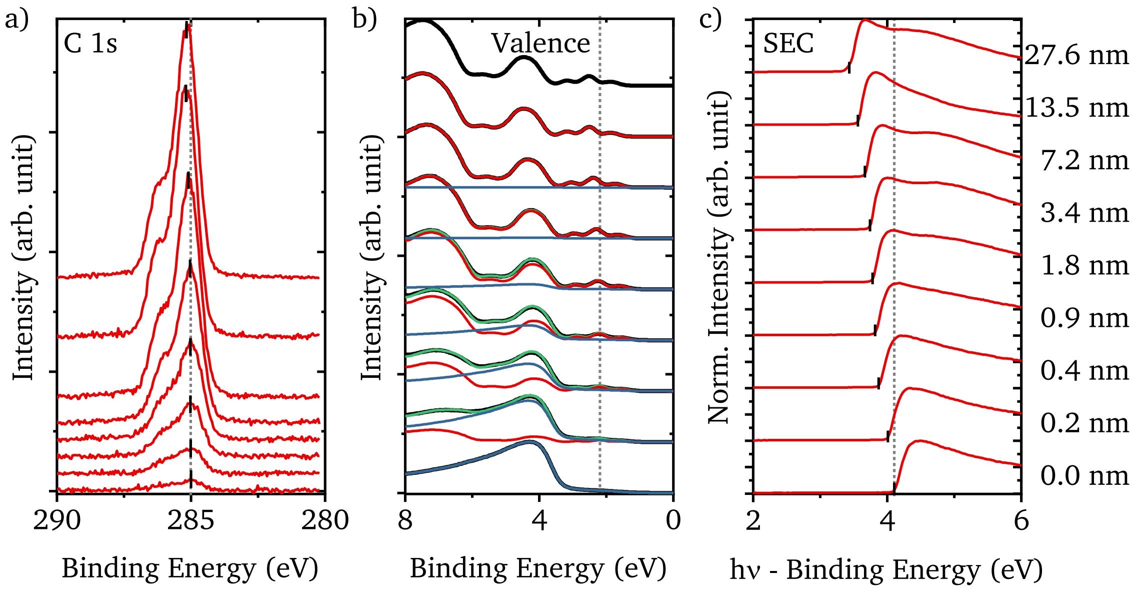

Figure 5.1-1: Photoemission spectra of the interface experiment ITO | undoped m-MTDATA. The spectra of the layer-by-layer deposition steps are stacked for increasing layer thickness from bottom to top. The layer thicknesses are given on the right side. a) The C 1s spectra start with the first deposition step (0.2 nm). For the C 1s emission peak and c) the secondary electron cut-off (SEC) onset, the binding energy positions are indicated by small black markers. b) The valence spectra are plotted in black and are fitted by a superposition (green) of the substrate (blue) and the adlayer (red). The SEC region is plotted against the difference of the excitation energy hν (21.22 eV) and the binding energy. Thus, the WFs can be read from the x-axis at the SEC onsets. Grey dotted lines serve as guide to the eye and help to observe the shift of the spectra.

spectrum of the adlayer has to be chosen from a deposition step where the layer thickness exceeds the information depth and thus the intensity of the adlayer emission has saturated.

Then, these reference spectra of substrate and adlayer can be used to fit the intermediate deposition steps by scaling the intensity of the reference spectra and shifting them on the binding energy scale. Four fitting parameters are obtained at each deposition step: one scaling factor and one shift offset for each reference spectrum. The intensity scaling factors are useful as they allow to estimate the effective attenuation length of the electrons emitted by the ultraviolet (UV) excitation with their low kinetic energies around 15 eV.

The *TPP-2M* equation[88] which is based on material properties and used in the *NIST* database software[89] to calculate the inelastic mean free path for the core level electrons in XPS, cannot be applied in this low kinetic energy range. In addition, the inelastic mean free path is not equal to the effective attenuation length due to elastic electron scattering (see Subsection 3.2.6). Therefore, the intensity scaling factors are plotted against the layer thickness and then fitted by a Beer-Lambert type exponential equation (see Eq. (6) in Subsection 3.2.6) resulting in an effective attenuation length of about 0.5 nm. Related values reported in literature are between 0.3 and 3 nm with a strong dependence on the kinetic energy.[92,93,171] The here determined value of 0.5 nm agrees with this range and as it is determined from the used materials and range of kinetic energies it is further on used in this work. Besides the analysis of the intensity scaling fit parameters, the binding energy offsets can be directly compared to the observed shifts vs layer thickness of the other emissions.

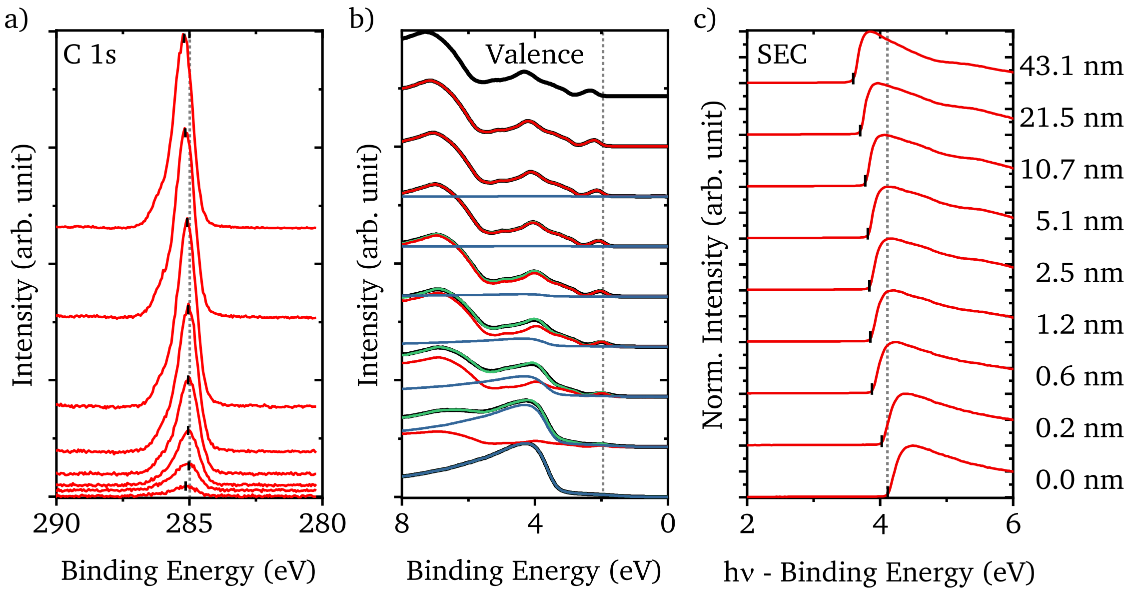

Figure 5.1-2: Photoemission spectra of the interface experiment ITO | undoped HTM-B. The spectra of the layer-by-layer deposition steps are stacked for increasing layer thickness from bottom to top. The layer thicknesses are given on the right side. a) The C 1s spectra start with the first deposition step (0.2 nm). For the C 1s emission peak and c) the SEC onset, the binding energy positions are indicated by small black markers. b) The valence spectra are plotted in black and are fitted by a superposition (green) of the substrate (blue) and the adlayer (red). The SEC region is plotted against the difference of the excitation energy hν (21.22 eV) and the binding energy. Thus, the WFs can be read from the x-axis at the SEC onsets. Grey dotted lines serve as guide to the eye and help to observe the shift of the spectra.

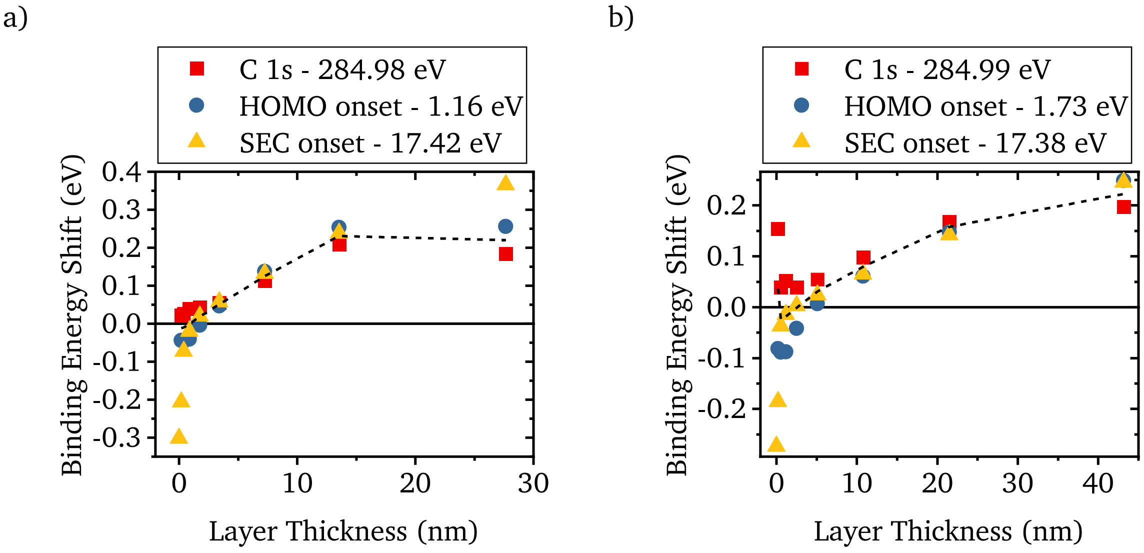

Figure 5.1-3: Classical analysis procedure of plotting adlayer binding energy shifts vs. deposition layer thickness. The shifts of the C 1s emission peaks, HOMO onsets, and SEC onsets for the interfaces of ITO with a) m-MTDATA and b) HTM-B are shown. The binding energies of the different emissions are offset to be comparable. The respective offsets are stated in the legends. The dashed line marks the mean value between C 1s and HOMO onset and serves as a guide for the eye.

The valence spectra of the substrate do not shift identically to the In 3d substrate emissions (not shown). Additionally, the valence spectra of the adlayer shift to higher binding energies with increasing layer thickness, similarly to the C 1s emissions. For the secondary electron cut-off (SEC) onset, determined by a tangent procedure, the trend is similar – binding energy positions are again indicated by black markers.

The determined shift of the SEC is larger than the one of the C 1s spectra and the highest occupied molecular orbital (HOMO) onsets of the adlayer. As it is commonly done in the classical analysis procedure[48], all extracted shifts of the adlayer are plotted in Figure 5.1-3. a) Shows the shifts observed for the interface ITO | m-MTDATA and b) the interface ITO | HTM-B. The values of the C 1s emission peak, the HOMO onset, and the SEC onset binding energy positions are offset by the values given in the legend of each graph. Overall, a similar shift to higher binding energies of the C 1s emissions and HOMO onsets can be seen, which is highlighted by the dashed lines that mark the mean value at every deposition step.

The shift is about 240 meV for m-MTDATA and 180 meV for HTM-B. For the ITO | HTM-B interface, the first C 1s peak binding energy position diverges from the trend. This is most likely due to an error in the fitting caused by the low signal because of the very thin layer (0.2 nm). There is no change in the spectral signature of the C 1s and valence emissions that could indicate a chemical reaction. Thus, this shift can be attributed to a change in the electrical potential causing an upwards bending of the energy levels in the HTMs towards the interface.[48] Presumably, this change in electric potential results of an electron transfer from the HTMs to ITO leading to the formation of a space charge region (SCR) at the interface.[48] More details on the formation of a SCR are given in the following subsections. It should be mentioned that the shifts to higher binding energy might be caused by a transition from the influence of the SCR to a charging effect at larger film thicknesses. As described in Subsection 3.2.8, counter measures against charging are taken in form of irradiation by an UV-LED, still a slight charging effect might be present for the thick undoped HTM layers. For layer thicknesses greater than about 2 nm, the SEC onsets are parallel to the other shifts. It should be mentioned that this SEC onset shift contrasts with an alternative explanation for the shifts of the HOMO onset with increasing layer thickness found in literature. The reports assign similar HOMO onset shifts to relaxation effects in the organic layer that cause a change of the energy gap with increasing layer thickness and thus distance to the interface. However, in that case the work function (WF) and thus the SEC onset would stay constant which is not the case here.[36,181,58]

In contrast to the agreement of all different binding energy shifts at layer thicknesses above 2 nm, there is a larger shift in the SEC onsets and therefore also in the WF, for about the first two deposition steps, which is not matched by the C 1s emission and the HOMO onset. Depending on the growth mode, the orientation, and conformation of the molecules, these two deposition steps up to about 1 nm may coincide with the formation of the first monolayer (see dimensions of the single molecules in vacuum in Subsections 4.1.3 and 4.1.4) and indicate the formation of an electric dipolar layer right at the interface.[47] The determined potential drops are about 310 meV for m-MTDATA and around 230 meV for HTM-B.

Such a dipolar layer at an inorganic | organic heterointerface can have different origins depending on the type of interaction. In the case of self-assembling monolayers, the charge transfer during chemisorption of the molecules can lead to a double layer potential drop.[35] Speaking of self-assembled monolayers, molecular dipoles aligned at the interface or induced by polarization of the electron density can also result in an interface dipole.[71] For interfaces with clean metal substrates as, e.g., Au, the electron wavefunctions that would otherwise extend beyond the surface are pushed back by the adsorbed layer. This so-called “push back effect” causes a change in electron density and thus a dipolar layer.[35] Finally, a charge transfer dipole can also build up when charges are transferred into localized states right at the interface.[47,182] The former interactions seem unlikely for the here discussed interfaces as no metal substrate is used, no indication for a chemical reaction is found, and the molecular layers are amorphous with no sign of oriented interlayers (see Subsections 4.1.3 and 4.1.4). A transfer of charges into localized states, however, could be an explanation for the observed dipolar charges. This kind of double layer potential drop is similar to the formation of a space charge region. However, the difference lies in the spatial distribution of the transferred charges. For the electrostatic potential drop, the charges are strongly localized right at the interface, in contrast to the more spread-out charges in the SCR. Alternatively, the observed dipolar layer could also result from a change of the surface dipole of the Ar-ion etched ITO substrate under deposition.

For further investigation of the first deposition steps and possible effects on the formation of an interface dipole, difference spectra of the valence region are calculated. To calculate a difference spectrum, the results of the above presented fitting of the valence spectra can be used. For each deposition step, the substrate reference spectrum is shifted and scaled as determined by the fit and then subtracted from the measured spectrum. This results in the actual emission from the adlayer assuming no changes in the spectral signature of the substrate. In Figure 5.1-4, the obtained spectra of the first three deposition steps are compared to the spectrum of the thick adlayer for m-MTDATA (a) as well as for HTM-B (b). To compare the spectral shape, the spectra are aligned to the HOMO onset and normalized in intensity. It can

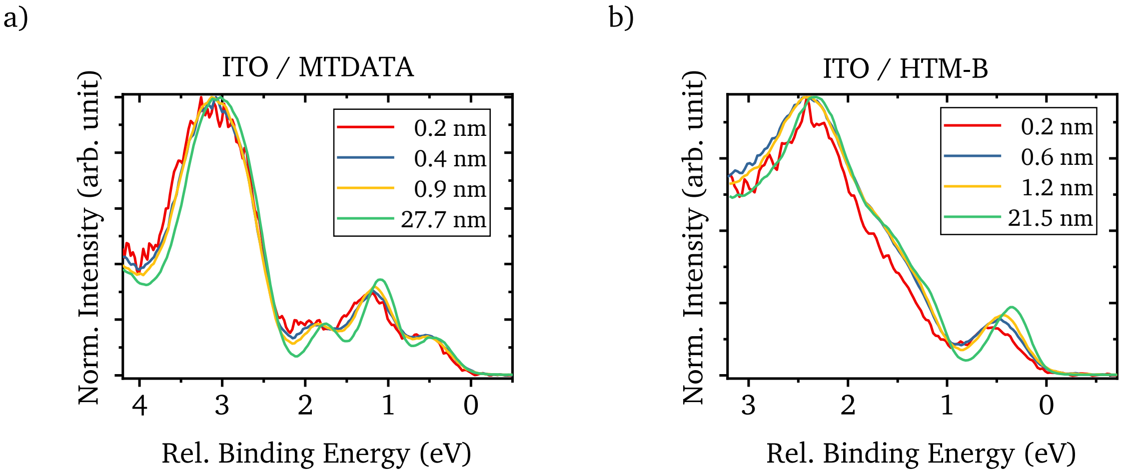

Figure 5.1-4: Difference valence spectra of the adlayer from the interface experiments a) ITO | m-MTDATA and b) ITO | HTM-B. The spectra are obtained by subtracting the substrate signal and are then normalized in intensity and aligned to the HOMO onset. The layer thicknesses are given in the legend. For the thickest layers, no subtraction is needed. Adapted from Frericks et al.[74]

be seen that the spectra are broader in the first deposition step and then become sharper with increasing layer thickness.

Furthermore, the energetic difference between the peak at lower binding energies and the one at higher binding energies becomes larger. Similar to the observations on doped and undoped layers in Subsection 4.2.5, these differences could stem from an increased structural or electronic disorder in combination with a change in conformation or orientation of the molecules right at the interface. These effects could be introduced by the charge transfer between ITO and HTMs and could be linked to the observed dipolar layer as they coincide with the strong changes in the WF.

Summarizing, the classical analysis of the ITO | MTDATA interface yields an upwards bending of the energy levels of 240 meV in the MTDATA thin film towards the interface and an interface dipole of 310 meV. For the ITO | HTM-B interface a similar energy level bending of 180 meV and an interface dipole of 230 meV is found. In the classical analysis, usually, these values, the WFs of the substrate and the adlayer at final thickness, and the HOMO onset to Fermi level ($E_F$) energetic difference of the adlayer at final thickness are now taken to construct and draw the self-consistent energy level diagram of the interface. The exact distribution of the electric potential is not known from the classical analysis and can only be approximated. Next, the interfaces of the doped HTMs will be also first analyzed by the classical procedure and afterwards the results of the modeling approach will be shown in the then following subsections. Finally, the results for the electrical potential changes of the undoped interfaces determined by the just described classical analysis are given in Table 5.3-1 in Subsection 5.3.1 together with the values from the interfaces of the doped HTMs and in comparison with the values derived from the modeling approach. In addition, the energy diagrams of all ITO | (p-)HTM heterointerfaces are then drawn in Figure 5.3-2 based on the modeled electrical potential distribution.

### 5.1.2 Heterointerfaces with p-Doped Hole Transport Materials

After the classical analysis was used on the undoped HTM interfaces, it is now applied to the interfaces between ITO and the doped HTM thin films. To investigate the influence of doping on the HTMs at the interface with ITO, several interface experiments with differently doped HTMs were performed. Dopant concentrations of 2 and 7 vol% for m-MTDATA and <1, 1, 6, and 11 vol% for HTM-B were tested. In this subsection, one example for each HTM is selected and analyzed following the same classical approach as for the undoped layers of the previous subsection. The spectra of the interface experiment ITO | p-(2 vol%)-m-MTDATA are shown in Figure 5.1-5 and the extracted binding energy shifts are plotted in Figure 5.1-6a. For the interface experiment ITO | p-(6 vol%)-HTM-B, only the extracted binding energy shifts are plotted in Figure 5.1-6b. The trends for both interfaces are again similar and can be discussed together. As for the undoped layers, the C 1s spectra in Figure 5.1-5 a) show an increasing intensity with increasing layer thickness and otherwise no signs of a chemical reaction in form of a new spectral feature. In contrast to the undoped layers, the C 1s peaks of the doped layers shift to lower binding energies. The same shift can be also seen for the valence spectra (black) in b) which are again fit by the superposition (green) of substrate (blue) and adlayer (red) reference spectra (see description in the previous subsection). The evolution of the SEC onsets in c) is slightly more complicated. From the substrate spectrum to the second deposition step for p-m-MTDATA and first deposition step for p-HTM-B, the SEC onsets shift to higher binding energies (lower WF). In the following deposition steps, the SEC onsets follow the trend of the C 1s and valence emissions and shift to lower binding energies (higher WF). Again, no shifts of the substrate emission are detected. Following, the classical method, the binding energy shifts

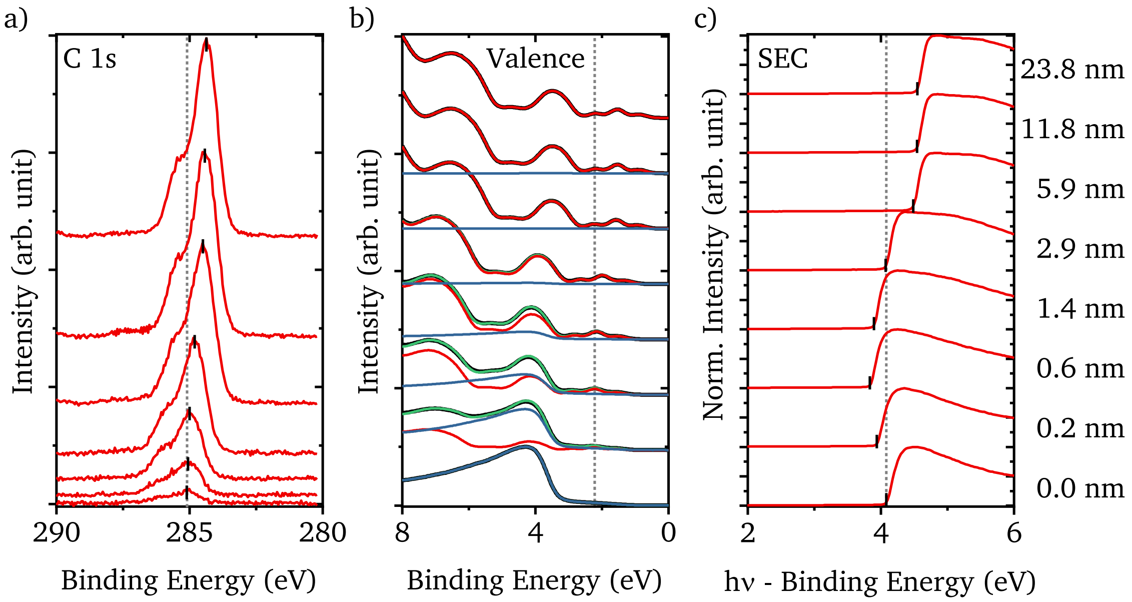

Figure 5.1-5: Photoemission spectra of the interface experiment ITO | p-(2 vol%)-m-MTDATA. The spectra of the layer-by-layer deposition steps are stacked for increasing layer thickness from bottom to top. The layer thicknesses are given on the right side. a) The C 1s spectra start with the first deposition step (0.2 nm). For the C 1s emission peak and c) the SEC onset, the binding energy positions are indicated by small black markers. b) The valence spectra are plotted in black and are fitted by a superposition (green) of the substrate (blue) and the adlayer (red). The SEC region is plotted against the difference of the excitation energy hν (21.22 eV) and the binding energy. Thus, the WFs can be read from the x-axis at the SEC onsets. Grey dotted lines serve as guide to the eye and help to observe the shift of the spectra. Adapted from Frericks et al.[74]

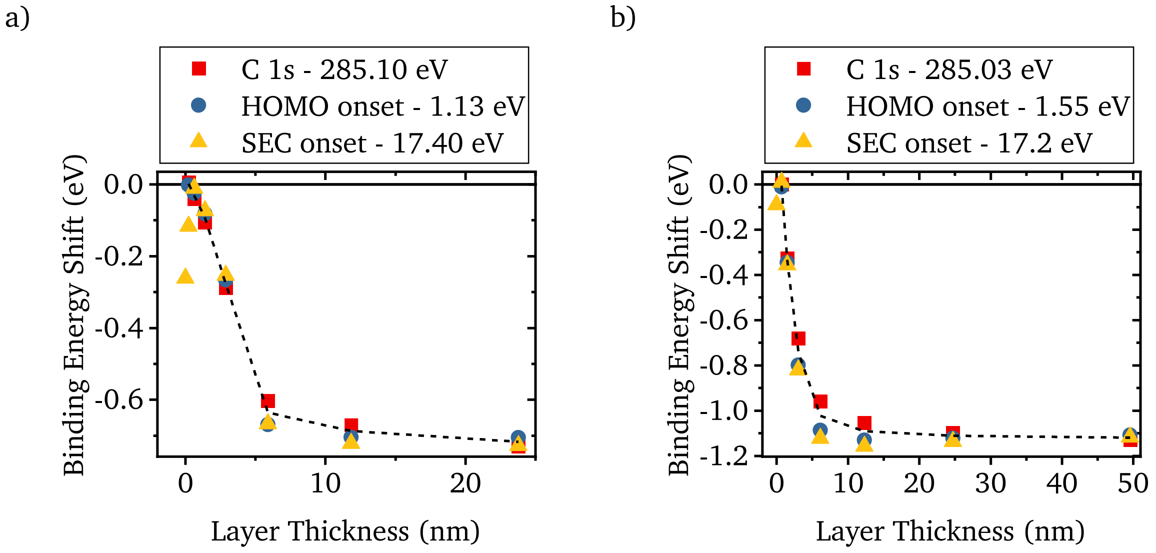

Figure 5.1-6: Classical analysis procedure of plotting adlayer binding energy shifts vs deposition layer thickness. Here, the shifts of the C 1s emission peaks, HOMO onsets, and SEC onsets for the interfaces of ITO with a) p-(2 vol%)-m-MTDATA and b) p-(6 vol%)-HTM-B are shown. The binding energies of the different emissions offset to be comparable. The respective offsets are stated in the legends. The dashed line marks the mean value between C 1s and HOMO onset and serves as a guide for the eye.

of the adlayer emissions are plotted in Figure 5.1-6. Here, it can be seen that the shifts are about -0.7 eV for m-MTDATA and -1.1 eV for HTM-B. Analogous to an inorganic Schottky diode metal-semiconductor interface, these shifts can again be assigned to a change in the electric potential which stems from the formation of a SCR.

As the shift is opposite to the case of the undoped HTMs, also the charge transfer needs to proceed in the other direction meaning that electrons are transferred from the ITO substrate to the p-doped HTM. This is because the doping introduces holes in the HOMO of the HTM lowering the $E_F$ below the one of the ITO substrate and thereby creating the driving force for the electron transfer to the HTM.[67] The transferred electrons recombine with the holes on the HTMs leaving the ionized acceptor states of the p-dopants uncompensated. These negative charges then build up the SCR. The charges of the SCR are compensated in the ITO. However, as ITO has a high number of mobile charge carriers the region of compensating charges is very narrow right at the interface and thus does not lead to a potential drop in the ITO.[66,67,183,184]

The decrease of the WF in the first deposition steps, indicated by the shift of the SEC onset to higher binding energies, can very likely be attributed to a formation of an electrical dipolar layer right at the interface, as it was discussed in the previous subsection. For p-m-MTDATA, the dipole related potential drop is about 250 meV and thereby only slightly smaller than for the undoped m-MTDATA (300 meV). For HTM-B, the dipole related potential drop is around 100 meV and thus reduced compared to the undoped case (250 meV). As discussed above, different mechanisms can be involved in the formation of an interface dipole, thus a reason for this different behavior cannot be given at this point without further dedicated studies on the doping mechanisms in these two HTMs. The dipole and SCR related potential drops are extracted for all studied interfaces of differently doped HTMs with ITO (doping concentrations of 2 and 7 vol% for m-MTDATA and <1, 1, 6, and 11 vol% for HTM-B). Overall, a typical semiconductor junction formation process is found. The potential drop across the SCR increases with dopant concentration as the Fermi level shifts closer to the HOMO onset of the organic semiconductor, increasing the Fermi level offset before contact. In addition, the width of the SCR becomes narrower with increasing dopant concentration due to the higher charge density and resulting in higher electric fields. All extracted values are summarized in Table 5.3-1 and compared to the values obtained by modeling approach in the Section 5.3. There, also energy level diagrams of the various ITO | (p-)HTM interfaces can be found. However, before the comparison to the model approach can be made, the DOS-based model is first explained in the next section.

## 5.2 Density of States Based Model

In this section, the density of states (DOS) based model, used to model photoelectron spectra for interface experiments, is introduced and the fitting of the measured data is explained. In a new and more complex way, this model combines different approaches from literature which, so far, were only applied to data analysis or interpretation separately. The calculation of the electrical potential is based on the work of Oehzelt et al.[45] The description of the DOS which enters the electrical potential calculation incorporates the ideas of Salzmann et al.[46] on how to introduce acceptor states, and Yang et al.[47] for using a density of gap states (DOGS). Finally, the model convolutes the calculated electrical potential distribution over the layer depth with the decay function of the photoelectron emission with layer depth as it is done in the work by Ohashi et al.[44] To the authors knowledge, for the first time, the here presented model generates photoelectron spectra of different emission regions based on a sophisticated calculation of the electrical potential distribution and fit the modeled spectra directly to sets of experimental spectra.

As it is shown in the previous section, interface experiments can be used to study the electronic structure at the interface of two materials. By observing the shifts of the photoelectron spectra on the binding energy scale with increasing layer thickness, the formation of space charge regions (SCRs) can be identified. More precisely, the drop of the electrical potential across a SCR and its width is detected and quantified in the simple classical approach. However, the actual distribution of the electrical potential $V(x)$ along the deposited layer thickness $x$ is not known.

### Formal Description of the Electric Potential Calculation

To calculate $V(x)$, the following one-dimensional ordinary[n] differential Poisson equation,

$$\frac{dV(x)}{dx} = -F(x), \qquad \frac{dF(x)}{dx} = \frac{\rho\big(V(x)\big)}{\varepsilon}, \tag{17}$$

has to be solved. Here, $F$ is the electric field, $\rho$ is the charge density, and $\varepsilon$ is the dielectric permittivity which can be separated as

$$\varepsilon = \varepsilon_{\mathrm{r}} \cdot \varepsilon_0 \,, \tag{18}$$

---

[n] Ordinary differential equations are differential equations with only one independent variable (here x) in contrast to partial differential equations which include more independent variables (e.g., x, y, z in 3 dimensions).

where $\varepsilon_\mathrm{r}$ is the material specific dielectric permittivity and $\varepsilon_0$ is the dielectric permittivity of the vacuum.

At this point, in the classical approach often the Schottky model[66,67] is used to approximate the solution. In the Schottky model, the SCRs are assumed to have a defined width with a constant non-zero value for $\rho$ inside the SCR and a value of zero outside the SCR. After integrating the constant value of $\rho$, a linear dependence for $F$ is obtained. A second integration then leads to a parabolic description of $V$. Thereby, a very simple but also very rough description for $V$ is obtained, as will be further discussed in the next section where the DOS-based model is tested and compared to the classical analysis approach.

For the DOS-based model of this work, $\rho$ is described as a sum of the contributions from different charge carriers:

$$\rho\big(V(x)\big) = e\big[p\big(V(x)\big) - n\big(V(x)\big) - NA^{-}\big(V(x)\big) + ND^{+}(V(x))\big], \tag{19}$$

with $p$ the density of holes, $n$ the density of electrons, $NA^{-}$ the density of ionized acceptors, and $ND^{+}$ the density of ionized donors.

Each of these contributing charge carrier densities depends on the convolution of a respective DOS with the Fermi function $f$, as shown for the example of $p$:

$$p\big(V(x)\big) = \int \mathrm{DOS}_{\mathrm{HOMO}}\,\big(E, V(x)\big) f_p(E) dE \tag{20}$$

Analogously, $n$, $NA^{-}$, and $ND^{+}$ are described using $\mathrm{DOS}_{\mathrm{LUMO}}$, $\mathrm{DOS}_{\mathrm{Acc}}$, and $\mathrm{DOS}_{\mathrm{Don}}$, respectively. Each of these DOS depends on $V$ as it shifts the position of the states on the energy scale $E$ with respect to the Fermi level $E_F$. Depending on the type of charge carriers, the Fermi function $f_n$,

$$f_n = \frac{1}{1+\exp\left(\frac{E-E_\mathrm{F}}{k_\mathrm{B}T}\right)}\,, \tag{21}$$

with temperature $T$ and Boltzmann's constant $k_\mathrm{B}$, for electrons and ionized acceptors, or $f_p$,

$$f_p = 1 - f_n\,, \tag{22}$$

for holes and ionized donors has to be used.

As just mentioned, the energetic position of the DOS with respect to $E_F$ depends on $V$ and allows to calculate $\rho$. However, by the Poisson Eq. (17) $V$ depends on $\rho$ rendering this a non-linear problem which allows for a non-constant charge density but also has to be solved numerically.

From the Eq. (17) to (22), it should become clear that the key parameter in this model is the description of the DOS. For the materials used in this work, the DOS for the HOMO is described as,

$$DOS_{\mathrm{HOMO}}\big(E, V(x)\big) = N_0(1 - r_{\mathrm{Acc}})\big[(1-t)G\big(E, V(x)\big) + tH\big(E, V(x)\big)\big], \tag{23}$$

which is a combination of a Gaussian,

$$G\big(E,V(x)\big)=\frac{1}{\sqrt{2\pi\sigma^2}}\exp\left(-\frac{[E-E_{\mathrm{HOMO}}+V(x)]^2}{2\sigma^2}\right), \tag{24}$$

and an exponential function,

$$H\big(E,V(x)\big)=\frac{1}{l}\exp\left(-\frac{E-E_{\mathrm{HOMO}}+V(x)}{l}\right), \tag{25}$$

for the HOMO states broadened by disorder and gap states tailing into the energy gap, respectively (see Figure 5.2-1). Here, $N_0$ is the total state density, $t$ the tail states ratio, $\sigma$ the Gaussian standard deviation, $l$ the exponential decay parameter, and $E_{\mathrm{HOMO}}$ the energy level expectation value. The description of the HOMO by a Gaussian function and the DOGS by an exponential function is in line with previous literature reports.[67,185–188] As described by Yang et al.[47], gap states seem to play an important role for the energetic alignment of organic semiconductors. In addition to these reports, the following sections will also show the importance and influence of the DOGS.

For the modeling of the p-doped layers used in this study, acceptor states are introduced using a Gaussian function as in the work of Salzmann et al.[46],

$$DOS_{\mathrm{Acc}}\big(E,V(x)\big)=N_0 r_{\mathrm{Acc}} G\big(E,E_{\mathrm{Acc}}+V(x)\big), \tag{26}$$

with the acceptor state energy expectation level $E_{\mathrm{Acc}}$ and the volumetric acceptor concentration $r_{\mathrm{Acc}}$.

In the same manner as for the acceptor states, donor states could be introduced for a case of n-doping. However, as n-doped layers are not studied here, no description for donor states is needed. Similarly, an exact description of LUMO states is not required for the modeling in this work. Thus, LUMO states are simply modeled as mirror image of HOMO states with respect to the center of the energy gap. From Eq. (23) to (26), it can be seen that the DOS is mainly described by the parameters $\sigma, l, t, r_{\mathrm{Acc}},$ and $E_{\mathrm{Acc}}$.

### Influence of the DOS parameters

The influence of the DOS parameters $\sigma, l, t, r_{\mathrm{Acc}},$ and $E_{\mathrm{Acc}}$ is illustrated in Figure 5.2-1 and will be discussed in the following. A detailed description of all parameters and how they are determined or estimated is given at the end of this Section 5.2. In a), the influence of the Gaussian standard deviation $\sigma$ is shown. This parameter is found to have only a small effect in this work as the Fermi level at the modeled interfaces varies with distance to the interface[o] mainly in the energy regime above the HOMO onset where the number of tailing gap states dominates. Furthermore, the HOMO onset is taken as descriptor for the HOMO states energetic position. As a consequence, the influence of $\sigma$ is further reduced as the HOMO onset is defined as $2\sigma$ above $E_{\mathrm{HOMO}}$ (see further description below).

---

[o] In the description of the model, the DOS shifts with respect to the Fermi level due to the change of the electrical potential with distance to the interface. Vice versa, this can be seen as shift of the Fermi level with respect to the DOS.

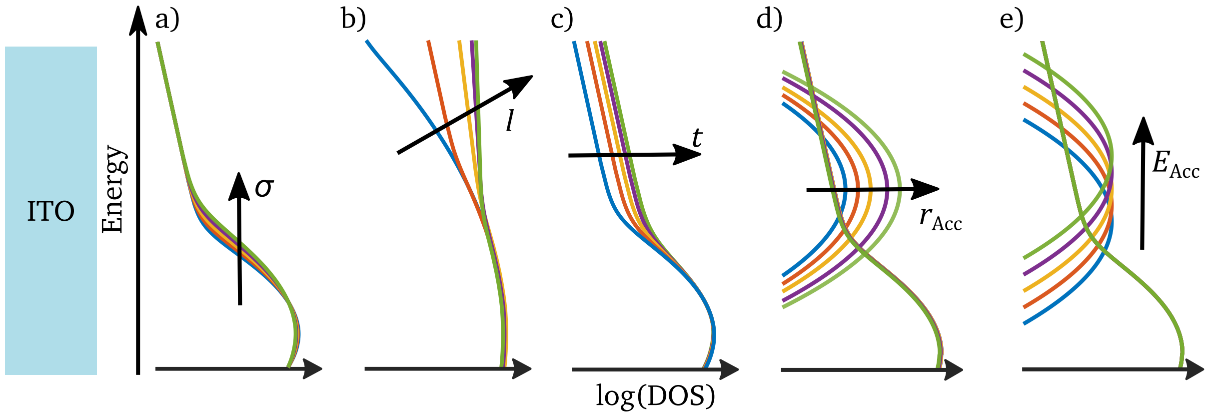

Figure 5.2-1: Illustration of the effect of several model parameters on the shape of the modeled DOS: a) the Gaussian standard deviation $\sigma$, b) the exponential decay parameter $l$, c) the tail states ratio $t$, d) the volumetric acceptor concentration $r_{\text{Acc}}$, and e) the energetic position of the acceptor states $E_{\text{Acc}}$ above the HOMO onset. The influence of an increasing parameter value is indicated by arrows. The DOS scale is in a logarithmic representation and the scaling varies among the parameters. Adapted from Frericks et al.[74]

The shape of the tailing gap states is defined by the parameters of the exponential decay function, the decay parameter $l$ (b) and the tail states ratio $t$ (c). Their influence can be best presented on a semi-logarithmic plot as in Figure 5.2-1. Here, the exponential function becomes a straight line where $l$ defines the slope and $t$ the offset. The total state density $N_0$ is kept constant. Thus, $t$ defines the ratio between Gaussian and exponential states and can be given as a percentage value of tail states with respect to the total number of states.

Finally, the volumetric acceptor concentration $r_{\text{Acc}}$ (d) and the energetic position of the acceptor states $E_{\text{Acc}}$ (e) define the doping effect in the model. Similar to $t$, $r_{\text{Acc}}$ defines the ratio between the matrix molecule state density and the dopant molecule state density. In a first approximation, the total density of states in a doped organic layer is assumed to be constant. Thus, it is assumed that if more dopant molecules occupy the space of matrix molecules for an increasing dopant concentration, they also take the according number of states from a fixed total state density. In other words, with increasing volumetric dopant concentration the number of matrix molecule states decreases while the density of dopant molecule states increases proportionally. As an advantage of this approximation, the model parameter $r_{\text{Acc}}$ can be directly compared to the measured dopant concentration $X$ (see next section). In Figure 5.2-1d, the decrease of the HOMO states is not visible due to the semi-logarithmic representation. The influence of $E_{\text{Acc}}$ can be simply understood as a shift of the acceptor states with respect to the HOMO onset of the material. In addition to $r_{\text{Acc}}$ and $E_{\text{Acc}}$, there is also a standard deviation for the Gaussian distribution of the acceptor states (not shown). Further details on this Gaussian distribution of the acceptor states and the effect of $r_{\text{Acc}}$ and $E_{\text{Acc}}$ are discussed below after the second component of the model, the convolution of electrical potential distribution and photoelectron emission decay, is explained.

### Peak Broadening by Convolution of Electrical Potential and Signal Decay

A photoelectron emission spectrum is influenced by different contributions. One is the characteristic spectral peak shape of the orbital emission $P$ that depends on the chemical shift (see Subsection 3.2.1) of the measured material. Furthermore, the position of this peak on the binding energy scale is influenced by the electrical potential $V$. If $V$ changes with the depth $x$ from the surface, an overlapping signal of different emission peaks shifted against each other by the distribution of $V(x)$ will be measured as broadening of the peak shape. In addition, the intensity of the emission $I$ decreases with $x$ (see Subsection 3.2.6). The following equation based on the work of Ohashi et al.[44] summarizes this convolution of depth-dependent electrical potential and intensity decay:

$$S(E_{\mathrm{BE}}) = \frac{1}{I_0}\int_0^d I\left(x, \lambda_{E_{\mathrm{kin}}}\right) P\left(E_{\mathrm{BE}}, V(x)\right) dx \; . \tag{27}$$

Here, the final measured peak shape is $S$. It is obtained by integrating the convolution from the surface ($x = 0$) to the depth of the measured layer thickness ($x = d$). $I_0$ is a normalization factor which is determined from the peak intensity at a layer thickness $d_{\mathrm{max}}$ that is thicker than the information depth:

$$I_0 = \int_0^{d_{\mathrm{max}}} I\left(x, \lambda_{E_{\mathrm{kin}}}\right) dx \; , \tag{28}$$

with $\lambda_{E_{\mathrm{kin}}}$ the effective attenuation length or inelastic mean free path of the electrons as discussed in Subsection 3.2.6. In that subsection, also the Beer-Lambert type exponential decay function is mentioned on which the description of $I$ is based:

$$I\left(x, \lambda_{E_{\mathrm{kin}}}\right) = \exp\left(\frac{x-d}{\lambda_{E_{\mathrm{kin}}}}\right) . \tag{29}$$

The whole method of potential-decay-convolution is visualized in Figure 5.2-2. As example the p-HTM-B spectrum at 3 nm layer thickness of the ITO | p-(6 vol%)-HTM-B interface experiment is chosen. The measured spectrum is plotted in the top right graph as black solid line. Here, the superposition of different spectral signals (red shaded peaks) coming from different depths $x$ is also shown. These signals are summed up to obtain the final spectral shape which is shown as grey shaded peak. The position of each red spectrum on the binding energy scale is defined by

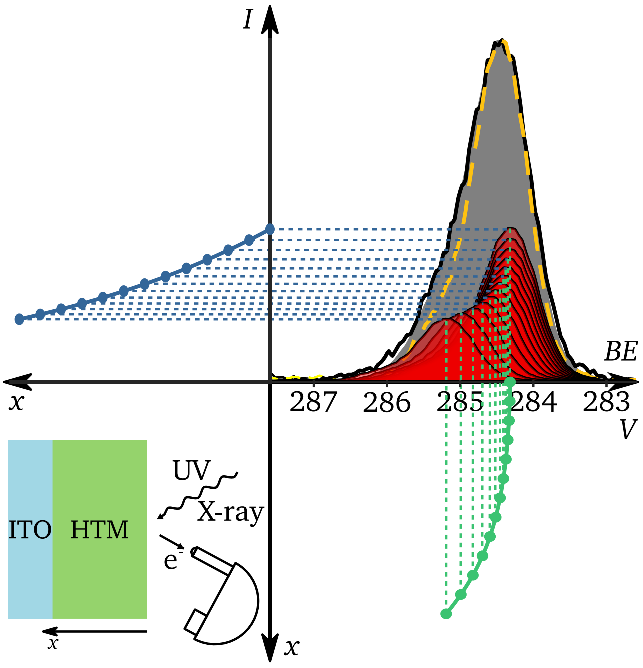

Figure 5.2-2: Illustration of the convolution of depth *x* dependent electrical potential *V(x)* (green) and intensity decay *I(x)* (blue) to obtain the modelled peak shape (grey shaded area). *V(x)* shifts the unaffected peak shape (red shaded areas) while *I(x)* scales their intensity. Summing up these shifted and scaled contributions the final peak shape is obtained. The red shaded peaks are drawn for every fifth integration point and scaled for better visibility. If the change of *V(x)* is significant in the information depth, the final peak shape will be broadened. The final modelled peak is compared to the measured p-HTM-B spectrum (black solid line) from the ITO | p-(6 vol%)-HTM-B interface experiment at 3 nm layer thickness which is affected by the potential drop in the SCR at the interface, and to the intensity adjusted peak shape which is unaffected by the potential distribution (yellow dashed line) at final layer thickness.

the electrical potential (green line on the bottom right) for the respective depth $x$. Its intensity for the respective depth is given by the exponential Beer-Lambert type decay function (blue line on the top left). For the illustration only every fifth integration point is shown, and the red shaded spectra are scaled to fit the representation. For the peak shape, the shape of the spectrum at final layer thickness of the interface experiment is used. Here, it can be expected that an influence from a SCR is no longer present. The spectral shape is interpolated, so it can be easily shifted and scaled. This unaffected spectrum is also shown for comparison as yellow dashed line. From the comparison to the unaffected spectrum and the good agreement between the modeled spectrum (gray shaded peak) and the measured spectrum, it can be clearly seen that the spectrum at 3 nm is broadened by the influence of the potential drop across the SCR which forms at the interface. This effect is especially strong if the change of the electrical potential is steep in the range of the information depth. In this work, the electrical potential is calculated by the DOS-based approach, which is described in the first part of this Section 5.2, and then photoelectron emission spectra are modelled by the just described convolution with the intensity decay. Thus, spectra for each deposition step of an interface experiment can be modeled and fitted to the measured ones. In the following, the implementation of this modeling and fitting procedure shall be described in more detail.

### Model Implementation, Parameters, and Fitting

Now, more practical information about the DOS-based modeling approach shall be given. The peak shapes for modeling and fitting of the spectra are taken either from measurements of the substrate before deposition or from the final deposition step at maximum layer thickness where only the adlayer spectra appear. To solve the above-mentioned Poisson Eq. (17) two boundary conditions are needed. The first boundary condition is of Dirichlet-type[p] and is given by the contact potential at the ITO interface, $V(0) = V_{\mathrm{Contact}}$. Here, it is assumed that due to its good conductivity the charge carrier density in ITO is much higher than that of the deposited organic HTMs. Thus, the potential in the ITO substrate will not change. The second boundary condition is of Neumann-type[p] and is defined by the vanishing electric field in the vacuum at the surface, $F(d) = 0$. As the electric field is the derivative of the electric potential, this second boundary potential indicates that the potential in the deposited layer has to be flat at the surface towards the vacuum. As mentioned above, the equation has to be solved numerically. Here, a multiple shooting method[189] based on a *Runge-Kutta 4(5)* algorithm[190] for each initial value problem is used. For a modeled DOS, the convolution with the Fermi-Dirac distribution is calculated for all Fermi level positions in the energy gap. As a consequence, for one modeled DOS the charge density vs. Fermi level position is known. The shift of the Fermi level in the energy gap is the same as shifting the DOS with respect to the Fermi level for a given electrical potential. For the effective attenuation length $\lambda_{E_{\mathrm{kin}}}$ of the XP spectra, the inelastic mean free path calculated by the *TPP-2M* equation[88] in the *NIST* database software[89] is used (see Subsection 3.2.6). For the UP spectra, the experimentally determined value of about 0.5 nm for the discussed materials is used (see Section 5.1). The deposited layer thickness $d$ which enters the calculation is determined from the damping of the substrate signal as described in Subsection 3.2.6. The

---

[p] A Dirichlet boundary condition defines the value of the function at a boundary while a Neuman boundary condition defines the value of the derivative of the function at a boundary.

Figure 5.2-3: Diagram of important energy levels in the DOS-based model. The charge neutrality levels of the undoped ($\mathrm{CNL}^{\mathrm{i}}$) and doped HTM ($\mathrm{CNL}^{\mathrm{p}}$) mark the position where, in thermodynamic equilibrium, the Fermi level will tend to be situated, far from the interface. $V_{\mathrm{Contact}}$ defines the energetic position of the Fermi level right at the interface. It is defined by the work function difference $\Delta_{\mathrm{WF}}$ of ITO and HTM and a potential drop $\Delta_{\mathrm{ID}}$ due to a possibly formed interface dipole. The difference $\Delta V$ of $V_{\mathrm{Contact}}$ and CNL is the potential that needs to be adjusted by formation of a SCR.

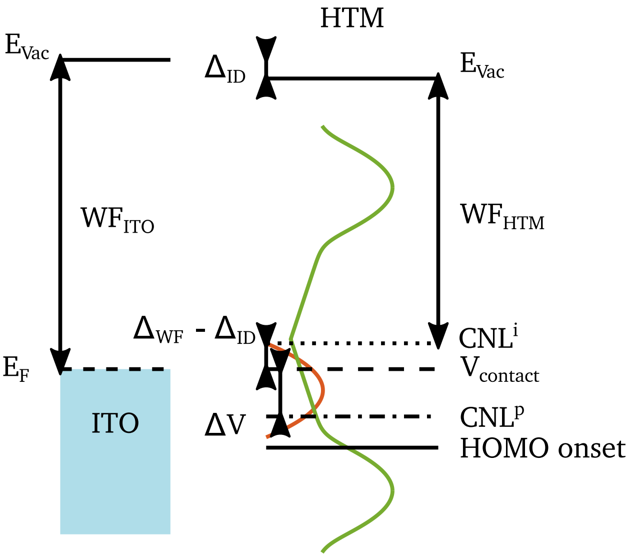

relative dielectric permittivity $\varepsilon_{\mathrm{r}}$ is set to 3. This is a common value for organic molecules[17] and the parameter is known to have only little influence in the order of some meV.[191] Furthermore, the temperature $T$ is needed and is set to 20 °C, i.e., 298.15 K. Finally, the total state density $N_0$ is estimated at $10^{27.3}$ $\mathrm{m}^{-3}$. This is again in a typical range for organic semiconductors.[192]

For a better understanding of the model implementation, Figure 5.2-3 shows important energy levels of the model. On the left are the energy levels of the ITO substrate and on the right are the ones of the deposited HTM. In the background, a DOS of the HTM in green, with acceptor states in orange, is drawn. For the modeling, all energy levels are defined with respect to the energy gap center which is set to 0. This center of the energy gap is called intrinsic charge neutrality level ($\mathrm{CNL}^{\mathrm{i}}$). Here, intrinsic stands for the case of an undoped layer and charge neutrality level means that for this energetic position of the Fermi level the charge densities for negative and positive charge carriers are equal. Furthermore, the energy gap and thereby the $\mathrm{CNL}^{\mathrm{i}}$ are defined by the energy difference of the HOMO onsets to the Fermi level, determined from the valence spectra of the two studied HTMs. The HOMO onset of undoped m-MTDATA is determined to be at 1.42 eV below the Fermi level and the HOMO onset of HTM-B at 1.88 eV (see Section 4.1). As mentioned in Subsection 3.2.4, the HOMO onset is typically determined by a tangent procedure at $2\sigma$ from the HOMO Gaussian maximum. Thus, $E_{\mathrm{HOMO}}$ of the modeled $DOS_{\mathrm{HOMO}}$ is placed by the respective value of the HOMO onset plus $2\sigma$ below $\mathrm{CNL}^{\mathrm{i}}$. As described above, the LUMO states are obtained by mirroring the HOMO states with respect to $\mathrm{CNL}^{\mathrm{i}}$. It should be noted that the DOS of the HOMOs in comparison to the DOS of the LUMOs depends on the chemical structure of the organic material and in reality, may deviate from a mirror like DOS.

The Fermi level will tend to reach the $\mathrm{CNL}^{\mathrm{i}}$ for thermodynamic electronic equilibrium in the undoped layer which is by design positioned at the measured Fermi level position above the HOMO onset. In the case of a doped HTM layer, the energetic position of the Fermi level, where the charge density of the positive and negative charge carriers compensates, is different from $\mathrm{CNL}^{\mathrm{i}}$ because of the acceptor states. Therefore, the charge neutrality level for the p-doped HTMs is abbreviated $\mathrm{CNL}^{\mathrm{p}}$ and is close to the HOMO onset. The exact position depends on the density and position of the acceptor states. In analogy to the undoped HTMs, the $\mathrm{CNL}^{\mathrm{p}}$ marks the energetic position where the Fermi level will tend to shift to reach thermodynamic equilibrium in the doped HTMs.

After the target values for the Fermi level far away from the interface are now set, the Fermi level position right at the substrate interface shall be further discussed, i.e., the boundary condition $V_{\mathrm{Contact}}$. In principle, $V_{\mathrm{Contact}}$ with respect to the $\mathrm{CNL}^{\mathrm{i}}$ is given by the difference in work function $\Delta_{\mathrm{WF}}$ between ITO and the deposited HTM. However, if an interface dipole, i.e., an instant change of the potential right at the interface, which can have different origins (see Section 5.1), is present, the related potential drop $\Delta_{\mathrm{ID}}$ is included as correction term to $\Delta_{\mathrm{WF}}$. As $V_{\mathrm{Contact}}$ defines the energetic position of the Fermi level in the energy gap right at the interface and the CNL defines the target position for the Fermi level shift, their difference gives the potential drop $\Delta V$ that is compensated by charge transfer and the formation of a SCR. $\Delta_{\mathrm{ID}}$ influences the magnitude of the modeled potential drop across the SCR via $V_{\mathrm{Contact}}$ and is therefore an important fitting parameter for the model.

To fit the modeled to the measured spectra, there are five more variable parameters whose influence is discussed by Figure 5.2-1: $\sigma, l, t, E_{\mathrm{Acc}},$ and $r_{\mathrm{Acc}}$. Unfortunately, the first tests of the model showed, that these are still too many variable parameters creating too many degrees of freedom to obtain consistent results across several interface experiments. Thus, the number of parameters was further reduced by assigning constant values to the Gaussian standard deviation $\sigma$ and the exponential slope parameter $l$. As mentioned above, the influence of $\sigma$ is small. In addition, a value could be well extracted from the valence spectra of pure m-MTDATA and HTM-B thin films. Here, the HOMO peak was fitted by a Gaussian function. The fit is corrected for the Gaussian broadening from the spectrometer. For m-MTDATA a value of 0.22 eV and for HTM-B a value of 0.18 eV is obtained. The Gaussian distribution of the acceptor states in the matrix cannot be measured (see Section 5.3) and is thus estimated at 0.20 eV. For $l$, it is considered that its influence on the DOS is similar to the one of the tail states ratio $t$. Thus, based on the first pre-tests, its value was set to 0.5 eV leaving $t$ as single descriptor of the tailing gap states.

The aim of the modeling is to fit the changes of XP and UP spectra for all deposition steps of one interface experiment with one set of parameters. The two sets of spectra are fitted manually in an alternating manner, starting with free parameters, and then constraining the variable parameters further and further to obtain the overall best fit for the spectra sets of both spectral regions.

For the fitting of one individual set of spectra, a semi-automated procedure is used. The parameters which can be varied are $t, E_{\mathrm{Acc}}, r_{\mathrm{Acc}},$ and $\Delta_{\mathrm{ID}}$. The algorithm is a nonlinear interior point algorithm which allows to set constraints to the fit parameters. The cost function is simply squared-error based. For the fitting, each parameter can individually be selected or deselected for fitting and restricted to a certain range. On the one hand, $t, E_{\mathrm{Acc}},$ and $r_{\mathrm{Acc}}$ influence the energetic position of $\mathrm{CNL}^{\mathrm{p}}$ and the course of the electrical potential as they determine the DOS shape. On the other hand, $\Delta_{\mathrm{ID}}$ only influences $V_{\mathrm{Contact}}$ and thereby $\Delta V$. Thus, usually, $t, E_{\mathrm{Acc}},$ and $r_{\mathrm{Acc}}$ are optimized first to obtain a good initial description of the spectral shapes and the overall shift, i.e., $\Delta V$. The resulting CNL might be off from the measured final Fermi level position with respect to the HOMO onset. This measured value is not intrinsically included in the model as the modeled electrical potential shift is applied relative to the spectra and not on an absolute binding energy scale. Therefore, it has to be manually taken care of to keep the final Fermi level position at the measured value above the HOMO onset. Here, the interface dipole $\Delta_{\mathrm{ID}}$ can be set to adjust the energetic starting point. As a consequence, there is a need for the CNL (thereby $t, E_{\mathrm{Acc}},$ and $r_{\mathrm{Acc}}$) to be adjusted and keep the overall measured spectral shift $\Delta V$. Multiple iterations of optimizing $t, E_{\mathrm{Acc}},$ and $r_{\mathrm{Acc}}$ and adjusting $\Delta_{\mathrm{ID}}$ might be necessary to obtain a good fit of the measured spectra and a Fermi level close to the measured value.

After one set of spectra, e.g., the C 1s spectra, are fit, the procedure is repeated for the other set of spectra, e.g., the valence spectra. Afterwards, a compromise between the different sets of parameters is chosen to obtain one set of parameters that leads to satisfying fits for both spectral ranges. This procedure is similar to calculating the mean value of binding energy shifts from different spectral regions in the classical approach (see Section 5.1). As will be discussed in the next section, valence and core level states should be in the same way influenced by the electrical potential leading to the same spectral shifts. However, as the regions are measured with two related but still different experimental techniques there are always some deviations. Still, at the end, all core level emissions and the valence emissions are fitted with the same parameter set and values.

Beside this compromise in finding one parameter set that fits both spectral regions, it should be pointed out that the number of variable fitting parameters is strongly reduced. This is necessary to avoid a meaningless overfitting; however, it also might lead to misleading values for the variable parameters. Several parameters are acting on certain parts of the model in a similar way and by fixing one parameter to a constant value, the remaining free parameters might compensate for this. Therefore, the absolute values of the parameters obtained from the fitting should be handled with care, and the evaluation should be rather done based on general trends and averages. The next section will show how well the model is able to fit the spectra of the interface experiments and which further benefits can be deduced from its application.

## 5.3 Testing the DOS-Based Model at the Heterointerface

This section is divided into two subsections. In the first subsection, the just described DOS-based model is used to analyze the ITO | (p-)HTM heterointerfaces. The results obtained by this analysis are then compared to the results obtained from the classical analysis in Section 5.1. In this comparison, the classically obtained results set the benchmark for the model, which needs to be able to deliver at least the same results as the classical method. However, as the model approach is not only more sophisticated but also more time-consuming, it is only useful if it provides additional benefits. Thus, the second subsection provides a detailed discussion of the additional results of the model, showcasing its advantages over the classical method in providing further insights.

### 5.3.1 Results of the DOS-Based Model and Comparison to the Classical Analysis

In this subsection, the photoemission spectra of the heterointerface experiments ITO | (p-)HTM discussed in Section 5.1 are analyzed using the density of states (DOS)-based modeling approach which is explained in detail in the previous Section 5.2. After demonstrating the method, the results are discussed and compared to the results of the before described classical procedure.

To briefly summarize the modeling approach, the DOS of the organic adlayer is modeled and the energetic position of $E_F$, which depends on the concentration of charge carriers in the adlayer, is calculated. The resulting electrical potential is obtained by solving the electrostatic Poisson equation. The emission line shape, which is simulated by the depth-dependent potential and intensity profile, is fitted to the experimental spectra. In an iterative fitting procedure, the root-mean-square deviation between modeled and measured spectra is minimized for both spectral ranges (C 1s and valence) of one interface experiment. The parameters of the modeled DOS are adjusted until the combined best fit for the sets of C 1s and valence emission spectra is found. As example, Figure 5.3-1 shows the fitted spectra for the interface experiments (a) ITO | p-(2 vol%)-m-MTDATA and (b) ITO | p-(6 vol%)-HTM-B. The measured spectra are plotted with black and the superposed fits with green lines. The modeled substrate and adlayer spectra are visualized by blue and red shaded areas, respectively. It can be seen that an overall good agreement between fit and measured spectra is obtained. The shift to lower binding energies with increasing layer thickness that is discussed in Subsection 5.1.2 as result of a SCR at the interface is well met by the fits and thereby by the underlying calculated DOS-dependent electrical potential. Also, from a detailed evaluation of the spectra from the single deposition steps (not shown) the broadening of the C 1s peaks at the early deposition steps due to the emission from molecules at different potentials is resembled by the fit. This effect (see Section 5.2, Figure 5.2-2) is especially strong for the interfaces with higher dopant concentrations. In these cases, the number of charge carriers is high, the electric field is strong, and the electric potential drop is steep within the range of the information depth. Thus, the signals from different depths also come from different potentials, meaning energetic positions.

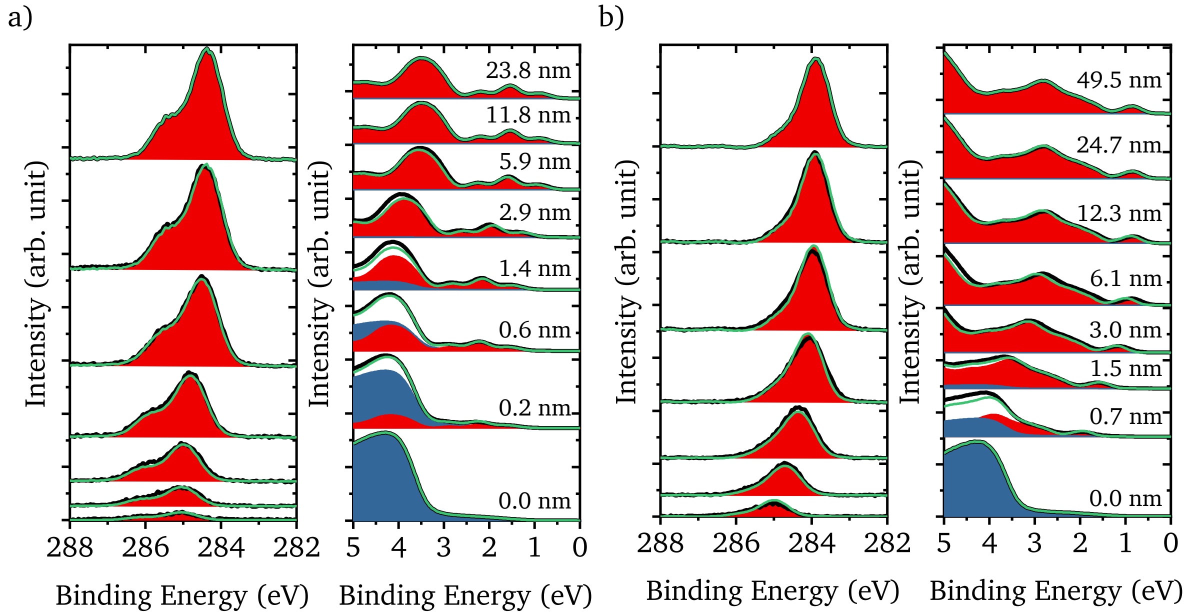

Figure 5.3-1: Photoemission spectra of the interface experiments a) ITO | p-(2 vol%)-m-MTDATA and b) ITO | p-(6 vol%)-HTM-B. For each interface, the spectra of the C 1s (left panel) and valence emissions (right panel) are shown. The measured spectra (black lines) are fitted by a superposition (green lines) of modeled substrate (blue shaded areas) and adlayer spectra (red shaded areas). Layer thicknesses of the deposition steps are stated in each right panel. The C 1s spectra start with the first deposition step. Adapted from Frericks et al.[74]

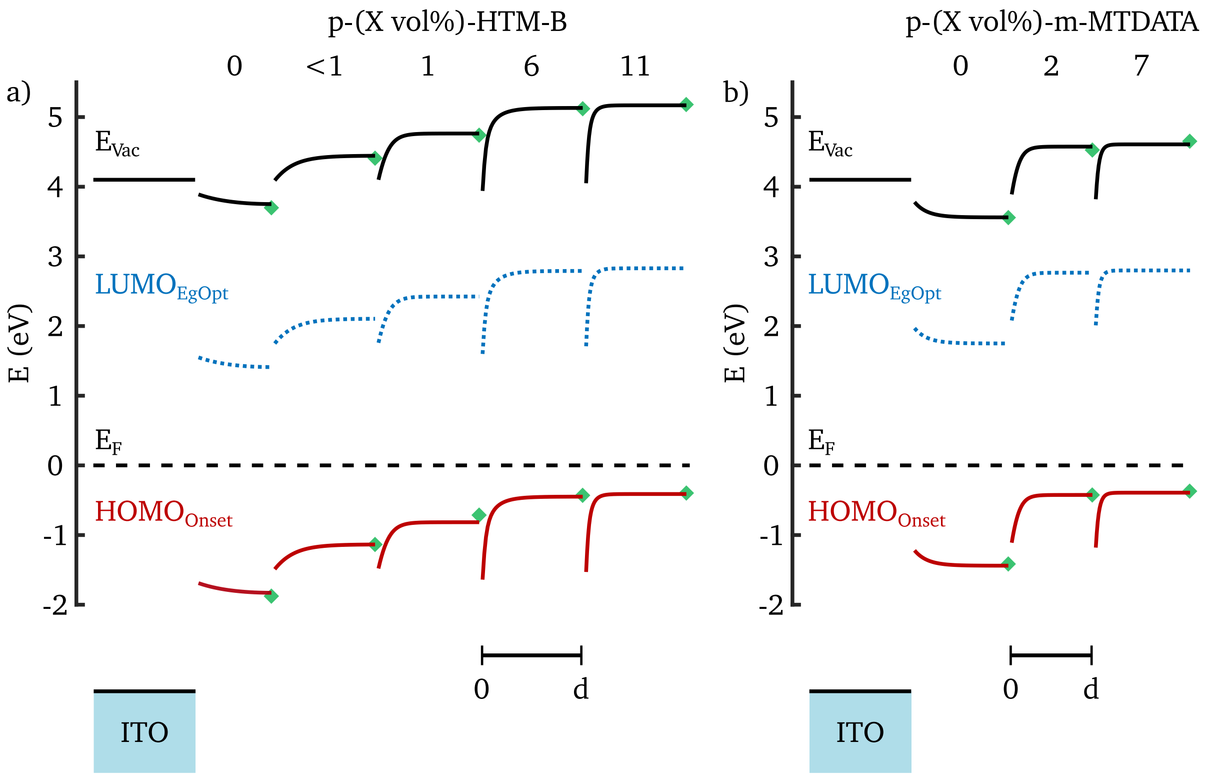

Figure 5.3-2: Energy level diagrams for the interfaces a) ITO | p-(X vol%)-m-MTDATA and b) ITO | p-(X vol%)-HTM-B. The dopant concentrations X are given above the energy levels of each (p-)HTM layer which are stacked horizontally. The course of the energy levels over the layer thickness d follows the modeled electrical potential obtained by fitting the photoemission spectra. The energetic positions of HOMO onsets and vacuum levels is determined by the IP and WF of the undoped material modified by the modeled interface dipole. LUMO onsets are situated at the values of the optical energy gap above the HOMO onsets. The green diamonds mark the energetic position of the measured WF and the energetic difference of the HOMO onset to $E_F$ at the final layer thicknesses. Adapted from Frericks et al.[74]

The model approach is used for all interface experiments of the differently doped HTMs. From the calculated electrical potential, the energy level alignment at the interface can be directly drawn and is shown in Figure 5.3-2. The energy level alignments of the ITO | (p-)m-MTDATA interfaces are presented in a) and the ones of the ITO | (p-)HTM-B interfaces in b). The ITO energy levels are drawn once for each material and then the energy levels of the differently doped adlayers are stacked to the right by increasing dopant concentration. The dopant concentration values are stated above the respective energy levels. The course of the energy levels is defined by the calculated electrical potential and is thus the same for HOMO onset (red solid), lowest unoccupied molecular orbital (LUMO) onset (blue dashed), and the vacuum level (black solid). The offsets of the HOMO onsets and the vacuum levels are set by the ionization potential (IP) and the WF of the undoped layers and modified by the modeled interface dipole for each interface. The energetic positions of the LUMO onsets are defined by the optical energy gap of each material.

As described in the two Subsections 5.1.1 and 5.1.2, there are SCRs at the interface that lead to an upwards bending of the energy levels towards the interface for the undoped HTMs and a downwards bending of the energy levels towards the interface for the doped HTMs. Also, electric dipoles at the interface are included in the model which follow from the offsets between the vacuum level of ITO and the starting points of the vacuum levels of the HTMs. The measured values of the HOMO onset and the WF (vacuum level) at the final layer thicknesses are added to the energy level diagram as green diamonds. They show a good agreement with the energetic positions of the modeled energy levels and highlight the accuracy of the model. For the doped HTMs, it can be observed that the bending of the energy levels becomes steeper, and the magnitude becomes larger with increasing dopant concentration as the energetic difference of $E_F$ to HOMO onset at final layer thickness becomes smaller.

For m-MTDATA, this energetic difference is saturated at 2 vol%, while for HTM-B the saturation is probably between 1 and 6 vol%. This is in agreement with the observations of Paula Connor, who determined a saturation point around 2 vol% for both HTMs in her master thesis.[102] In Subsection 4.2.7, when discussing the doping mechanism, this saturation is surprising when just comparing the $E_F$ and HOMO energetic positions of the undoped HTMs and the $E_F$ and LUMO energetic positions of the pure CPTCFA layers in Figure 4.1-25, it could be expected that the $E_F$ can be shifted much further into the HOMOs of the HTMs. However, this limited shift of $E_F$ is often observed in literature.[23,28,46,168,65] Many different factors may be considered as possible reasons. The internal interface charge transfer doping model by Mayer et al.[65] and the charge transfer complex (CTX) model by Salzmann et al.[46], Lüssem et al.[23] show that the saturation point is independent of the dopant molecule but depends on the host material. Furthermore, they argue that a substantial number of states that tail into the energy gap above the defined HOMO onset pin $E_F$. For the model in this work (for details, see Section 5.2), a combined approach is suggested to define the saturation point of $E_F$. First, the model uses acceptor states that are located above the HTMs' HOMOs as in the CTX model. Second, the model describes the DOS of the HOMO as combination of a Gaussian distribution and an exponential function where the exponential resembles the states which tail from the HOMO into the energy gap. The role of gap states in the electronic properties of organic semiconductors and their origin is further discussed in a review by Yang et al.[47] Both approaches are necessary to achieve the narrow SCRs with high dopant concentrations and still keeping $E_F$ pinned above the HOMO onset as is discussed below.

Continuing the discussion of the energy level alignment at the interface, with further increasing dopant concentration the magnitude of the potential drop does no longer change but still becomes steeper. This steeper potential change is directly related to a higher number of charge carriers leading to a narrower SCR. As already mentioned in the previous subsection, these observations are in line with classical inorganic semiconductor interface physics.[66,67,48,184] Following this classical understanding, often a simple Schottky model[66,67] is used to describe the potential in the SCR. The Schottky model assumes a constant charge carrier (ionized dopants) concentration in a SCR of a defined width. Based on the Poisson equation (see Section 5.2 Eq. (17)) the electrical potential is then described by a parabolic function. Thus, the potential drop across the SCR depends on the width of the SCR and dopant concentration. In Figure 5.3-3, a Schottky model (green line) is fitted to the observed binding energy shifts of the interface ITO | p-(2 vol%)-m-MTDATA and compared to the results of the DOS-based model (grey line). It should be noted, that both lines for the electrical potential (Schottky and DOS-based model) in Figure 5.3-3 represent the electrical potential distribution in the thick layer and do not match the binding energy shifts of the earlier deposition steps with thinner layer thicknesses. This is due to the surface sensitivity of photoelectron spectroscopy which causes

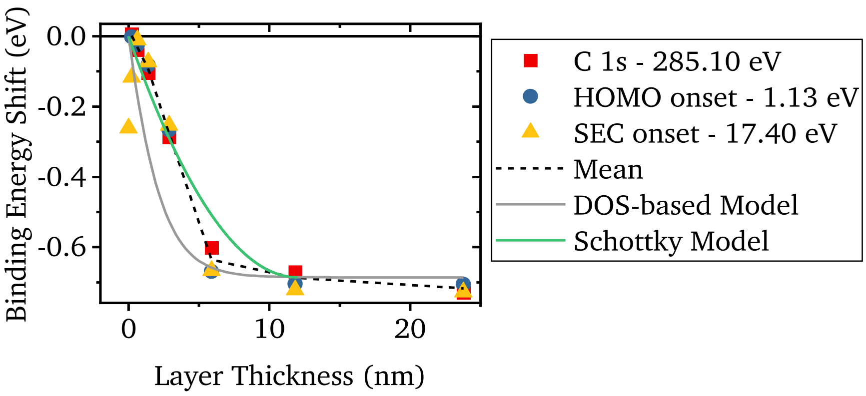

Figure 5.3-3: Comparison of DOS-based model and Schottky model. The adlayer binding energy shifts vs. deposition layer thickness for the interface of ITO with p-(2 vol%)-m-MTDATA as shown in Figure 5.1-6a are taken as example. Here, the modeled electric potentials from the classical Schottky model (green line) and from the DOS-based model (grey line) are added. For the Schottky model, the dopant concentration is far too low with about 0.08 vol%. In contrast, the dopant concentration used in the DOS-based model is much closer with 0.91 vol%. Adapted from Frericks et al.[74]

the measured shifts to be dominated by the electrical potential close to the surface and thus always represent mostly the evolution of the surface potential than the bulk potential.[49,191] As mentioned before, the interplay of electrical potential distribution and information depth depends on the effective attenuation length of the emitted electrons. The DOS-based model accounts for this by including the escape depth profile in the modeling of the spectra. Still, the measured potential distribution is dominated by the electrical potential close to the surface. However, the mismatch between the Schottky model and the binding energy shift value at about 6 nm layer thickness cannot be explained by the difference in surface and bulk potential distribution. If diverging, the bulk potential distribution should be steeper than the surface potential distribution.[49]

Furthermore, the dopant concentration, which is needed to match the estimated SCR width of 12 nm and the potential drop of 0.7 eV, is 0.08 vol%, assuming that every dopant is ionized. This is 25 times smaller than the measured dopant concentration of 2 vol%. Contrastingly, the DOS-based model which is drawn as grey line in Figure 5.3-3 leads to a dopant concentration of 0.91 vol% which is only about half of the actual value. Both models do not consider the probability for the dissociation of charges to generate free charge carriers (see Section 2.3). The higher dopant concentration in the DOS-based model is achieved because in the model charge carrier concentration is not assumed constant but is calculated dependent on the energetic position of $E_F$ in the DOS. As a result, the number of ionized dopants changes as the acceptor level energetic position changes with respect to $E_F$ due to the electric potential change. Right at the interface, $E_F$ is far from the HOMO onset of the HTM and well above the acceptor states. Hence, the acceptor states are occupied leading to a negative net charge, an electric field, and an electric potential change. Here, the density of ionized acceptors can directly be calculated from the modeled dopant concentration and ranges from $2 \times 10^{18}$ to $1 \times 10^{20}$ cm$^{-3}$ for lowly to highly doped layers. With the change of the electric potential, the states of the molecules far from the interface approach $E_F$ resulting in less ionized dopants, with a slower decrease of the electric field, and a more gradual change of the electric potential. If compared again to the Schottky model – this time for the same dopant concentration and potential drop –, the DOS-based model leads to wider SCRs. The SCRs of the Schottky model would be ranging from 1.5 to 8 nm for the highest (11 vol%) and lowest dopant concentrations (<1 vol%) while the SCRs of the DOS-based model are determined with widths from 4.5 to 24 nm, respectively. As the SCRs in the DOS-based model have no defined end, the width is taken at 99% of the potential drop.

The magnitudes of the SCR potential drop as determined by the classical approach $\Delta V^{\text{class.}}$ and the DOS-based model approach $\Delta V^{\text{Model}}$ are summarized in Table 5.3-1. Also, the interface dipole potential drops obtained by both procedures $\Delta_{\text{ID}}^{\text{class.}}$ and $\Delta_{\text{ID}}^{\text{Model}}$ are given for comparison. The agreement for the potential drop magnitude between the two methods is good with only one exception for the 1 vol% p-doped HTM-B where the classical procedure leads to a larger potential drop. While the classical approach just takes the mean value of the shifts obtained from the C 1s peak binding energy positions and the HOMO onsets, the model approach tries to find one set of DOS parameters that leads to one electrical potential distribution and the combined best fit for valence and C 1s region. These two regions are measured using different excitation sources and therefore are similar but not identical measurement techniques. In the model, the two techniques only differ in their information depth represented by the effective attenuation length of the electrons. In reality, this is not the only difference as, for example, the measurement spot area, the chamber pressure, and the incident angle of the photons are also different. For the interface dipole, the energy values vary more among one material in the case of the model approach than for the classical approach. While in the classical approach the dipole value is obtained by adjusting the energy level alignment at the interface to be self-consistent, in the model approach it is part of the fit parameters. It is thereby also not directly influenced by the measurement but depends on the other fit parameters. Still, the overall agreement between the values of the two methods is quite good with an average deviation of about 50 meV.

Table 5.3-1: Energy level alignment and model parameter values obtained by the classical analysis (class.) and DOS-based model approach (Model). X is the measured dopant concentration, $r_{\text{Acc}}$ is the modeled acceptor concentration, $E_{\text{Acc}}$ is the modeled acceptor level energetic position with respect to the HOMO onset, $\Delta_{\text{ID}}$ are the interface dipole potential drop, $\Delta V$ are the SCR potential drops, and $t$ is the modeled tail state concentration. Adapted from Frericks et al.[74]

| Molecule | X (vol%) | $r_{\text{Acc}}$ (vol%) | $E_{\text{Acc}}$ (eV) | $\Delta_{\text{ID}}^{\text{Model}}$ (eV) | $\Delta_{\text{ID}}^{\text{class.}}$ (eV) | $\Delta V^{\text{Model}}$ (eV) | $\Delta V^{\text{class.}}$ (eV) | $t$ (%) |
|---|---|---|---|---|---|---|---|---|
| HTM-B | 0.0 | 0.000 | 0.00 | -0.21 | -0.23 | 0.19 | 0.18 | 1.55 |
| | <1.0 | 0.099 | 1.12 | -0.01 | -0.13 | -0.36 | -0.41 | 1.11 |
| | 1.0 | 0.520 | 0.68 | 0.00 | -0.15 | -0.66 | -0.80 | 4.14 |
| | 6.0 | 4.790 | 0.96 | -0.16 | -0.10 | -1.19 | -1.11 | 0.17 |
| | 11.0 | 7.200 | 0.77 | -0.05 | -0.09 | -1.12 | -1.12 | 1.39 |
| m-MTDATA | 0.0 | 0.000 | 0.00 | -0.32 | -0.31 | 0.22 | 0.24 | 6.00 |
| | 2.0 | 0.910 | 0.33 | -0.21 | -0.24 | -0.69 | -0.70 | 3.20 |
| | 7.0 | 5.900 | 0.60 | -0.28 | -0.22 | -0.79 | -0.82 | 4.20 |

Hence, on average, the model approach is able to deliver the same results as the classical approach, but provides additional information as given by the fitting parameters.

### 5.3.2 Additional Insights from the Modeling Approach

At the same time, the model approach has the advantage of relating the obtained electronic structure at the interface directly to the density of states. With this information, the model sets the basis for a more detailed discussion. The model parameters of the DOS obtained from the fitting procedure are also given in Table 5.3-1. These fitting parameters define the shape of the DOS as explained in Section 5.2. The resulting DOS for the (p-)HTMs of the different ITO | (p-)HTM heterointerfaces are drawn in Figure 5.3-4 on a logarithmic scale to visualize the and exponential tail states Gaussian acceptor states.

Before the discussion of the three parameters starts with the acceptor concentration $r_{\mathrm{Acc}}$, it shall be again mentioned (see Section 5.2) that the absolute values of the parameters might not be perfectly exact as the number of fitting parameters was reduced. Otherwise, there would have been too many degrees of freedom. Thus, many parameters which enter the model were set constant. However, by constraining some parameters the remaining variable parameters might in some cases compensate for the restrictions of other parameters. The results for the fit parameters will therefore mainly be discussed in their trends and based on averaged values.

#### Discussion of the Model Parameters

As mentioned above together with the details of the model, the acceptor states are described by a Gaussian function. The overall density of states in terms of states per volume is assumed to be constant and the states for the host and dopant molecules are divided according to their volumetric ratio. This allows to give the $r_{\mathrm{Acc}}$ in units of vol% and compare it directly to the measured dopant concentrations X. Overall, the trend among the differently doped layers is

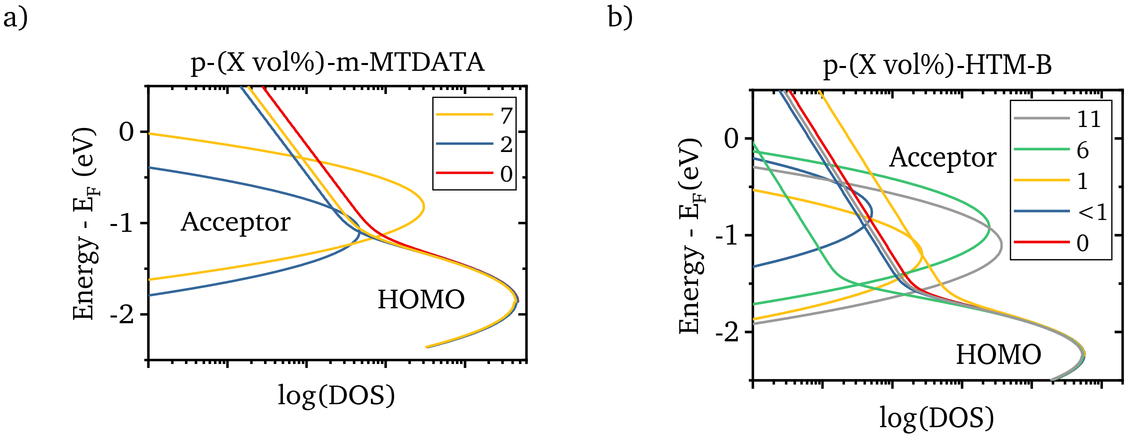

Figure 5.3-4: Modeled density of states for the different ITO | (p-)HTM heterointerfaces that where obtained from fitting C 1s and valence spectra of the sets of interface experiments a) ITO | p-(X vol%)-m-MTDATA and b) ITO | p-(X vol%)-HTM-B. Dopant concentrations X are given in the legend. The DOS scale is chosen as logarithmic to visualize the exponential tail states of the HOMO and the Gaussian distribution of the acceptor states. The energy scale is with respect to the intrinsic Fermi level. The variations of the parameters, e.g., the energetic position of the acceptor states, is mainly caused by restrictions on other parameters and the attempt to reduce the overall number of fitting parameters. Thus, the results should be rather viewed on average than discussing individual absolute values. Adapted from Frericks et al.[74]

well resembled. However, the model values are always below the measured concentrations. This is because the model already takes the disorder and related energetic distribution of the acceptor states and changed occupation due to the variation of the Fermi level into account. One source of error is probably the measurement of the dopant concentrations which is based on approximations and is especially inaccurate for low dopant concentrations, for which the dopants' F 1s signal to noise ratio is low (see Subsection 4.2.1). Furthermore, the model assumes that every dopant molecule is electronically active by directly translating the acceptor state density into a volumetric dopant molecule concentration.

It seems unlikely that the CPTCFA molecules form precipitates as in the report by Mayer et al.[65] because the concentrations are not as high, there might still be some small clusters of dopant molecules which might reduce the number of active dopants.[193,194] Also, polaronic effects on the energy level position of molecules in the surrounding of a charge are not considered in the model.[46,195] Especially if the doping mechanism follows the CTX model, the formation of CPTCFA molecule clusters could hinder the hybridization of the matrix and dopant frontier orbitals and thereby potentially the doping efficiency.

The energetic position of the acceptor states with respect to the HOMO onset of the host molecule is given by $E_{\mathrm{Acc}}$ in the model. For both HTMs the acceptor states are placed above the HOMO onset. As mentioned above, this energetic position is necessary to achieve the saturation of $E_F$ above the HOMO onset. As described by Salzmann et al.[46] and already discussed in Subsection 4.2.7, the formation of a CTX could explain the energetic position of the acceptor states. In fact, if the proposed Hückel-like equation (see Section 2.3) is used to calculate the energetic position of the LUMO of the formed donor-acceptor complex, values of 0.40 eV for m-MTDATA and 0.91 eV for HTM-B are obtained. In the calculation, a resonance integral value of 0.4 eV is chosen and the correction for the optical energy gap by Djurovich et al.[61] is used for the energetic position of the LUMO of CPTCFA (see Section 2.1). The average values of $E_{\mathrm{Acc}}$ are in good agreement with these theoretical values as they are 0.47 eV for m-MTDATA and 0.88 eV for HTM-B. This observation would support the CTX model of doping for both molecules and would justify the obtained energetic positions of the acceptor states. However, referring to the absorption spectra of the doped HTM layers in Subsection 4.2.6 and the following discussion on the doping mechanism in Subsection 4.2.7 this seems only a possible explanation for HTM-B but not for m-MTDATA. While for HTM-B no clear sign of an integer charge transfer is found, it seems to be clearly the case for m-MTDATA. Therefore, the energetic position of the acceptor states in the m-MTDATA case has to be considered as an effective position that allows a phenomenologically valid formation of space charge regions and their electronic structure while missing the foundation of a mechanistic description. As also mentioned before, further studies focusing on the doping mechanism in these systems are required for a better understanding.

Finally, the results for the tail state ratio parameter $t$ shall be discussed. As mentioned before, these tail states are found to be necessary to pin $E_F$ at high dopant concentrations and provide the observed saturation point. The existence of states that tail into the energy gap of organic semiconductors was observed before and is found to be the result of perturbations as for example steric and electrostatic disorder. It is considered to play a large role in understanding of the electronic properties of organic semiconductors.[47,170,171,185–188] For the interfaces studied here, the disorder could be introduced by the substrate (see Figure 5.1-4) or the doping (see

Figure 4.2-5) by inducing a change of orientation or conformation of the molecules.[173] On average, the results for m-MTDATA show higher tail state ratios than for HTM-B which suggests a greater disorder in m-MTDATA. As mentioned in Section 5.2, the Gaussian HOMO width, which is directly determined from the ultraviolet photoelectron (UP) valence spectra, is larger for m-MTDATA with 0.22 eV compared to HTM-B with 0.18 eV also indicating a greater disorder in m-MTDATA. It should be mentioned that, while for simplicity the model assumes a constant DOS and tail state ratio for the whole layer thickness, this might not necessarily be the case and the tail state ratio might change from close to far from the interface.

### Direct Comparison of Modeled DOS and Valence Spectra

UPS probes the occupied states, and therefore allows to compare the modeled DOS to the measured UP spectra. This is done for the examples of the ITO | p-(7 vol%)-m-MTDATA and ITO | p-(11 vol%)-HTM-B interface experiments where the dopant concentrations are considerably high. The observations are similar for m-MTDATA and HTM-B. The substrate signal is subtracted from the measured spectra and the resulting adlayer spectra are plotted in Figure 5.3-5. The modeled DOS is scaled and shifted to overlap with the measured HOMO to enable the comparison of the shape. The modeled DOS is plotted by two lines: blue lines for the HOMO states of the HTM and red lines for the acceptor states of CPTCFA. First, it can be seen that the Gaussian HOMO shape matches the measured spectra well. For thin layers, there is a slight mismatch where the modeled Gaussian HOMO is too narrow in comparison to the measured spectrum. This can be explained by the broadening which is induced by the steep electrical potential change at the very interface (see Section 5.2 Figure 5.2-2). In addition, there is a broadening of the spectrometer in the measured spectra which is not present in the modeled

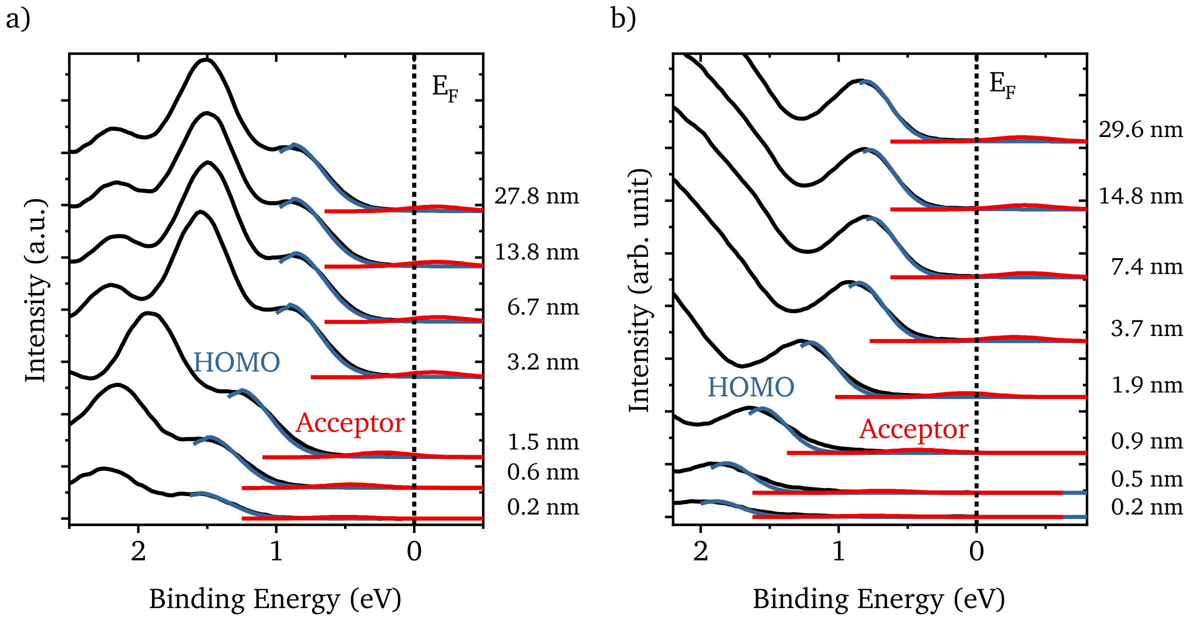

Figure 5.3-5: Comparison of the modeled DOS shape to the valence emissions (black lines) of the adlayer which is obtained by subtracting the substrate emissions from the measured spectra for each deposition step. The modeled HOMO states are the blue lines, and the acceptor states the red lines. The interfaces a) ITO | p-(7 vol%)-m-MTDATA and b) ITO | p-(11 vol%)-HTM-B are here chosen as examples. The energetic position of $E_F$ is highlighted by the dotted black line at 0 eV binding energy. Layer thicknesses of the deposition steps are stated next to the spectra on the right. Adapted from Frericks et al.[74]

DOS. Furthermore, the exponential states are too low in intensity to be visible and a comparison on the logarithmic scale, which in principle shows the tail states (as in Figure 5.3-4), is futile as the UPS measurement does not provide sufficiently low noise and is affected by the side lines of the excitation source (no monochromator). Even though the spectra were corrected for the ghost lines from the He-discharge lamp by a data post-treatment (see Subsection 3.2.4), the method is not precise enough to completely get rid of the corresponding signals. Thus, for future studies and investigations of the tailing gap states a different setup would be needed. Reports in literature which show measurements of the tailing gap states used more advanced low-noise, monochromatized setups.[171,196] Alternatively, one may use electrochemical impedance spectroscopy to map the density of states and reveal the presence of gap states in organic semiconductors.[197]

Finally, the question may be raised if the acceptor states, which were discussed before, can be detected in the UP spectra at all. Even though the concentrations of 7 and 11 vol% should be high enough (see red lines) to see an emission from the acceptor states, no corresponding spectral feature was detected in the measured spectra. For layer thicknesses above 3.2 nm this can be understood by the given energetic position of $E_F$ (black dotted vertical line at 0 eV binding energy). For these cases, $E_F$ is below the acceptor states which are therefore not occupied and cannot be detected by UPS. At lower thicknesses, however, the acceptor states are below $E_F$, thus should be occupied, and should appear in the measurement. A possible explanation why the states still do not show up in the measurement is that the energetic position of the acceptor states as used in the model are those of the neutral unoccupied states. Presumably, the energetic position of an acceptor state changes when it is occupied and shifts, due to the additional charge, to higher binding energies.[46,195] The occupied acceptor states would then overlap with the much more intense HOMO emission and hence remain undetected.

Concluding, it was shown that the two HTMs, m-MTDATA and HTM-B, behave very similar and form SCRs at the ITO interface as expected from classical semiconductor physics. For both materials, an interface dipolar layer is detected which persists for the p-doped HTMs. The doping leads to very narrow SCRs at higher dopant concentrations which could potentially be tunneled by charge carriers and thus reduce the contact resistance. For device fabrication, the ITO WF could be tuned to be closer to the one of the doped semiconductors. Furthermore, it becomes clear from the extensive discussion above that the DOS-based model approach provides a physical basis for the consideration of different effects like doping mechanisms or tailing gap states. There are still some deviations as fully consistent parameters are not obtained for an overall mechanistic picture. The model could still be improved, for example, by improving the algorithm and providing larger data sets. With larger data sets more degrees of freedom could be allowed and less parameters would need to be set constant. In addition, the fitting procedure could be altered to fit a complete series of experiments with a consistent parameter set. Also, the integration of a layer thickness dependent DOS might lead to further improvements of the fits and the understanding of the physical mechanisms as will be shown in the next section. Still, at this point, the model already has an advantage to the classical approach where SCRs can be identified but the quantification is at best based on very rough approximations like the Schottky model. With the inherent more sophisticated physical foundation, the DOS-based model provides good agreements with the measured spectra. It therefore also enables the analysis of homointerfaces for which a classical approach is no longer possible. These homointerfaces are analyzed and discussed in the following section.

## 5.4 Advancement of the Model at the (ITO/p-HTM) | HTM Homointerface

In this section, (ITO/p-HTM) | HTM homointerfaces are analyzed. The interfaces are called homointerfaces as it is the same HTM in the p-doped and undoped layer. These interfaces appear, e.g., in organic LEDs where a doped HTM layer is used to provide a better charge injection and a higher conductivity towards the contact, but also an undoped HTM layer is needed to separate the active emission layer from the doped HTM layer to avoid exciton quenching by the free charge carriers in the doped HTM.[22] However, the spectroscopic analysis of homointerfaces poses a problem as the spectral signature from the two involved layers is dominated by the same matrix molecule. Thus, it is difficult or impossible to separate the contributions from the two layers and, e.g., determine in which of the two layers a space charge region forms. The DOS-based model, which is introduced in Section 5.2 and proved to be superior to the classical analysis method in Section 5.3, also enables the analysis of homointerfaces as will be shown in this section. First, the initial results obtained from the model will be presented. The results show an unexpected space charge region in the doped HTM layer. The interdiffusion of CPTCFA molecules as origin for this SCR is discussed and excluded in the second part of this section. Finally, the DOS-based model is advanced towards a layer-depth-dependent DOS which then allows to successfully model the experiment data obtained for the homointerfaces.

### 5.4.1 Initial Modeling Results of the Homointerface Experiments

Following the experiments on the ITO | p-HTM interface discussed in the previous section, p-HTM sublayers of two different dopant concentrations for each HTM – 2 and 7 vol% for m-MTDATA and 1 and 5 vol% for HTM-B – were prepared. The interfaces were again analyzed by XPS and UPS during consecutive layer-by-layer deposition of the undoped HTMs. As mentioned before, homointerfaces are difficult to analyze as the spectral signal of the sub- and adlayer are dominated by the emission from the same host molecule. The signal from the dopant molecules which is only present in the sublayer is typically too weak to be analyzed carefully. Only at high dopant concentrations, the dopant signal is strong enough as distinguishing feature to be analyzed as unconcealed signal from the sublayer. To overcome the problem of indistinguishable signals, the DOS-based model, which was tested in the previous section and was found to deliver reliable description of the electrical potential at the interface, is used to model the homointerfaces in this section. The model allows for the separation of the sublayer and adlayer spectral contributions.

Figure 5.4-1 shows the photoemission spectra (black lines) of the (ITO/p-(2 vol%)-m-MTDATA) | m-MTDATA interface (a) and the (ITO/p-(1 vol%)-HTM-B) | HTM-B interface (c). Layer thicknesses of the adlayer are shown next to the valence spectra. The layer thicknesses were obtained by extrapolation based on the deposition rate which was determined from the signal damping of the ITO substrate during p-HTM layer deposition (see Subsection 3.2.6). As it was described for the homointerfaces, it can be clearly seen that there is hardly a difference between the spectral shapes of each deposition step. Overall, a shift to higher binding energies with increasing adlayer thickness can be seen without any fitting, however, it is less clear how much of the shift results from the sub- or adlayer. Thus, the figure also shows the best fit (green lines) by the DOS-based model. The modeled contributions to the fit are shown as blue shaded areas for the sublayer spectra and red shaded areas for the adlayer spectra. For the fitting, the electrical potential is again modeled as described in the previous section and Section 5.2. The electrical potential is modeled for the doped and undoped layer together. The model parameters for the doped layers are taken from the results of the ITO | p-HTM interfaces which are closest

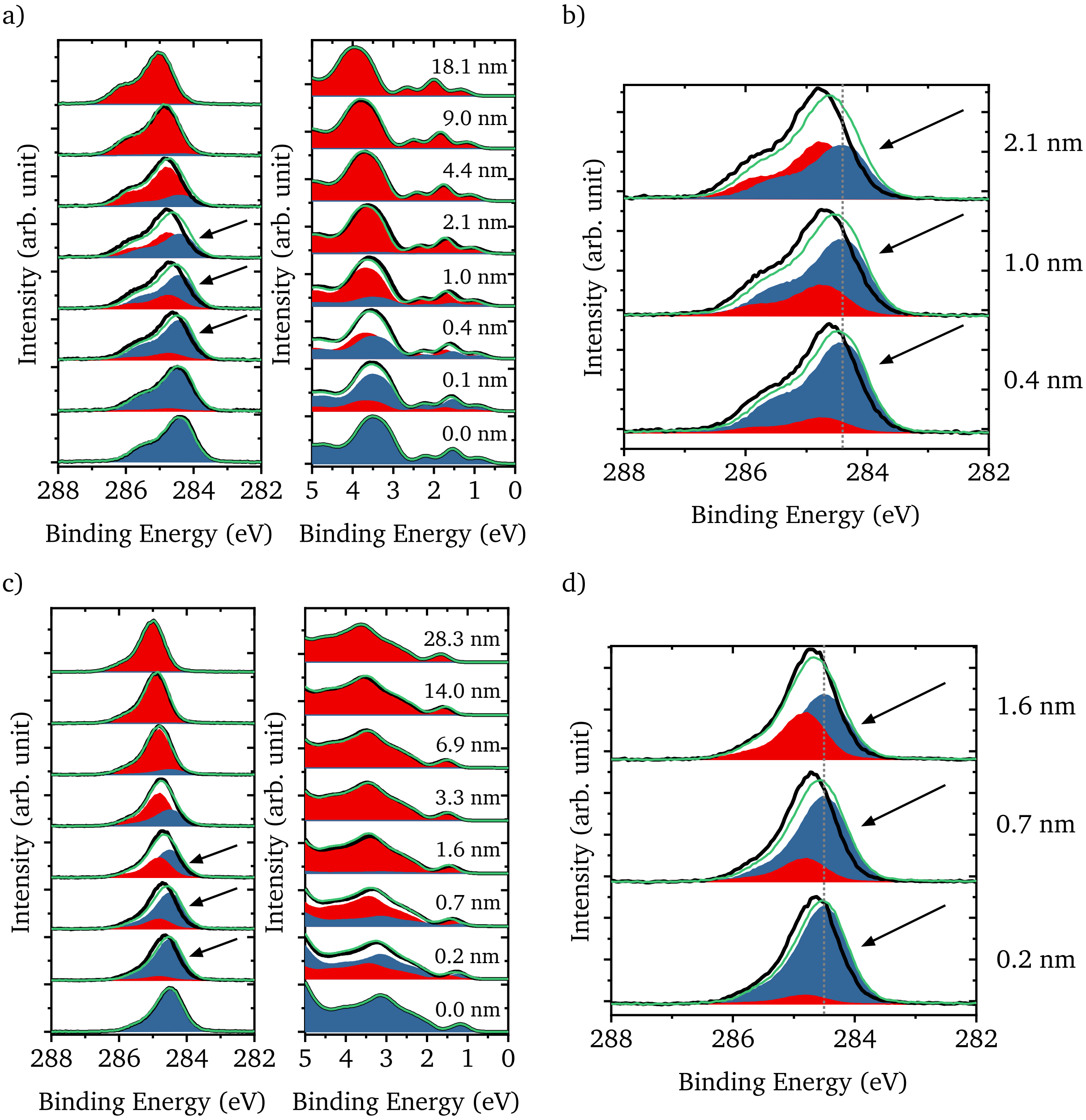

Figure 5.4-1: Photoemission spectra of the interface experiments a) (ITO/p-(2 vol%)-m-MTDATA) | m-MTDATA and c) (ITO/p-(1 vol%)-HTM-B) | HTM-B. For each interface, the spectra of the C 1s (left panel) and valence emissions (right panel) are shown. The measured spectra (black lines) are fit by a superposition (green lines) of modeled substrate (blue shaded areas) and adlayer spectra (red shaded areas). Layer thicknesses of the deposition steps are stated in each right panel. The mismatch between fit and measurement for some deposition steps is highlighted by black arrows and the spectra are shown magnified in b) and d), respectively. Grey dotted lines serve as guide to the eye. Adapted from Frericks et al.[74]

in dopant concentration (see Table 5.3-1) and are kept constant. Thus, only the model parameters for the undoped layers are free and serve as fitting parameters.

Figure 5.4-1 (b, d) show a magnification of some C 1s spectra of m-MTDATA and HTM-B, respectively, where the fit is found to not match the measured data (respective spectra in (a) and (c) are highlighted by the same black arrows). Here, the modeled sublayer spectra (blue shaded areas) do not shift while the modeled adlayer spectra shift to higher binding energies with increasing adlayer thickness. From the corresponding modeled electrical potential distribution (not shown), it can be seen that this behavior resembles the presence of a wide SCR with gradual changing electrical potential in the undoped layer. In the doped layer, a narrow SCR with barely any potential drop appears from the model. This distribution of the electrical potential agrees well with the physical expectation from a classical semiconductor interface formation.[67] The doped layer is expected to have a much higher number of charge carriers due to the present acceptors than the undoped layer. The doped layer has a lower energetic position of $E_F$ (higher WF) than the undoped layer and thus electrons will move from the undoped layer to the doped layer where they can recombine with the dopant induced holes. Due to the high charge carrier concentration the resulting negative charges in the doped layer are located in a narrow region while the counter charges in the undoped layer need a larger region because of the low charge density (see Section 2.4).[67] In contrast, the measured spectra of the doped layer at these deposition steps shift to higher binding energies resulting in the mismatch with the modeled fit. At these low adlayer thicknesses, the main contribution to the measured signal comes from the sublayer as can be seen by the larger blue shaded areas. Thus, to cause this spectral shift, a SCR with a significant potential drop has to form in the doped HTM during the early steps of interface formation with the undoped layer. In the UP spectra, the effect cannot be observed as the sublayer signal contribution vanishes too quickly with the deposition of the adlayer due to the much lower kinetic energy and therefore shorter effective attenuation length of the emitted electrons. The same shift of the doped layer is observed also for the cases with more highly doped sublayers (not shown). To find an explanation for this unexpected behavior, which is in contradiction to the just described typical semiconductor behavior, two assumptions were checked: first, the possibility of interdiffused dopants at the interface will be discussed and, second, the DOS-based model will be advanced assuming a layer thickness dependent increase of the density of states at the interface.

### 5.4.2 Excluding Dopant Interdiffusion

In this subsection, dopant interdiffusion at the (ITO/p-HTM) | HTM homointerfaces as possible explanation for the observed unexpected sublayer binding energy shift will be discussed. The discussion starts with a further analysis of the experimental results and concludes with model-based considerations.

For the (ITO/p-(7 vol%)-m-MTDATA) | m-MTDATA homointerface the dopant concentration is high enough that the F 1s signal from CPTCFA in the sublayer can be followed. Also, the p-HTM layer is thin enough that there is still some In 3d signal from the ITO substrate detectable. The spectra of both emissions are plotted in Figure 5.4-2(b, c), respectively. The peaks of both signals are integrated, the values are normalized and plotted in (a). Similar to the dopant distribution analysis in Subsection 4.2.2, the expected Beer-Lambert type exponential decay

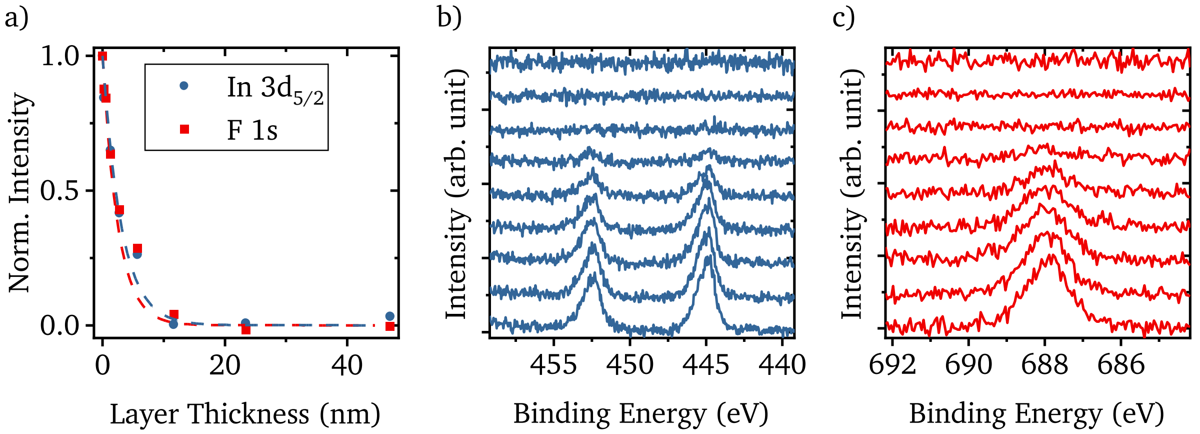

Figure 5.4-2: Data from the (ITO/p-(7 vol%)-m-MTDATA) | m-MTDATA homointerface experiment. a) Plots of the normalized integrated intensities of the F 1s emission (red squares) from CPTCFA in the sublayer and the In $3d_{5/2}$ emission (blue circles) from the ITO substrate. The dashed lines are the expected exponential signal decay functions in the respective colors. b) and c) Stacked plots of the In 3d and F 1s spectra, respectively. Adapted from Frericks et al.[74]

functions of the signal due to the damping by the adlayer (see Subsection 3.2.6 Eq. (6)) are plotted as dashed lines. Considering the low signal to noise ratio there is a good agreement between the expected and measured decay. Besides, the decay of the CPTCFA signal follows the decay of the ITO substrate signal and can thus be assumed not to diffuse into the undoped adlayer. Otherwise, the F 1s signal would decay slower than the one of In 3d.

In addition, the interdiffusion of CPTCFA was considered in the DOS-based model. The results of the electrical potential induced energy level bending are shown in Figure 5.4-3. The horizontal black dashed line marks the Fermi level while the vertical black dotted line marks the interface between doped and undoped layer. The 1 nm thick undoped layer is highlighted by a grey background. For an actual interdiffusion layer, the dopant molecule concentration would be expected to decay gradually over the range of the interdiffusion layer. Furthermore, the interdiffusion layer would extend into both (doped and undoped) previously well separated layers. To simulate the effect of interdiffusion, a very rough first approximation is used. Differently large regions of interdiffusion are considered (inset in a) serves as legend). The interdiffusion regions equally extend into the doped and undoped layer and the dopant concentration is set to half of the concentration of the doped sublayer. The graphs of the electrical potential induced energy level bending show that the potential drop at the interface (black dotted line) is rather low. For the observed shift of the sublayer spectra, a much larger shift of the energy levels in the p-HTM region (left from the vertical black dotted line) would be needed. The blue line from c) represents the required energy level bending towards the interface and is added in a) as a reference in light blue. Furthermore, it seems that the introduction of interdiffusion reduces the potential drop as the largest change is observed for the case where the interdiffusion range is the smallest. This can be understood by the schematic energy diagrams in b). Here, the energetic position of $E_F$ in the differently doped regions is drawn: doped layer with high dopant concentration and low $E_F$ (left, dark green), interdiffusion region with intermediate dopant concentration and slightly higher $E_F$ (center, striped), and undoped layer with no dopant and mid gap $E_F$ position (right, light green). The difference between the energetic positions of $E_F$ as indicated by the black arrows defines the required

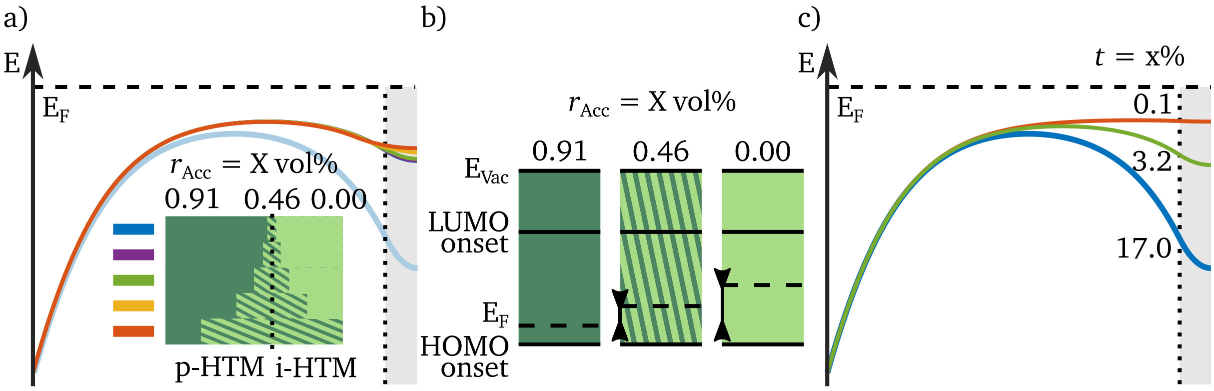

Figure 5.4-3: a) and c) Energy level bending due to a DOS-based modeled electrical potential distribution. The interface is indicated by a black dotted line and the undoped layer part highlighted in grey. a) Differently large interdiffusion regions with half of the dopant concentration parameter $r_{Acc}$ (see Section 5.2) of the doped layer are modeled. It equally extends into the doped and undoped layer. The inset depicts the regions and serves as legend. The blue line from c) is given as reference in a) (light blue). b) Schematic energy level diagrams of the differently doped regions in a). c) Differently high tailing gap state concentrations $t$ (see Section 5.2) right at the interface. Adapted from Frericks et al.[74]

potential change and can be considered as driving force for the charge transfer. In the interdiffusion region, $E_F$ will be further apart from the HOMO level than in the doped layer with higher dopant concentration but not as far as for the undoped layer. Thus, the potential drop from doped to interdiffusion region is indeed reduced compared to the undoped layer. In other words, to create a significant potential drop in the p-doped layer enough negative charges need to be transferred from the undoped layer. These negative charges cannot be provided by an interdiffusion layer where an intermediate concentration of p-dopants introduces already positively charged holes.

As the experimental observations of Figure 5.4-2 and theoretical considerations of Figure 5.4-3 both speak against interdiffusion as explanation for the observed potential drop in the p-doped layer, the next subsection will present an advancement of the DOS-based model that allows for the required negative charge transfer from the undoped layer. In this context, also Figure 5.4-3c will be discussed in more detail.

### 5.4.3 Towards a Model with a Layer-Depth-Dependent Density of States

The so far used DOS-based model is not able to produce fits that match the measured spectra of the homointerface experiments (see Figure 5.4-1). In particular, the density of occupied states in the undoped layer, which are energetically above $E_F$ of the doped layer, is too low in comparison to the high density of holes in the doped layer. Thus, the modeled potential drop resulting from the charge transfer at the interface is mainly located in the undoped layer and therefore the modeled sublayer peaks do not shift. In other words, to cause a shift of the sublayer peaks a substantial change of the electrical potential has to take place in the sublayer and thus more charges need to be transferred from the undoped layer. This can only be achieved by increasing the number of gap states of the undoped layer right at the interface which tail into the energy gap and are partially higher in energy than $E_F$ of the doped layer.

If this increased tail state concentration is applied to the DOS of the whole undoped layer, the overall number of transferred charges becomes so high, that the potential drops very quickly over the full range of the initial $E_F$ difference between doped and undoped layer. After a few nanometers of deposited adlayer, the energetic difference of $E_F$ to HOMO onset in the undoped layer is at the values of the pure HTM layers on ITO – about 1.4 eV for m-MTDATA and 1.9 eV for HTM-B (see Figure 4.1-25). However, these values are also in contradiction to the results of the homointerface experiments. Here, even at adlayer thicknesses around 20 nm the HOMO onsets shift to about 1 eV below $E_F$ (see green diamonds in Figure 5.4-7). Therefore, the model needs to be able to provide a significant charge transfer during the deposition of the first few nanometers by an increased DOS but must reduce the charge density for the following deposited

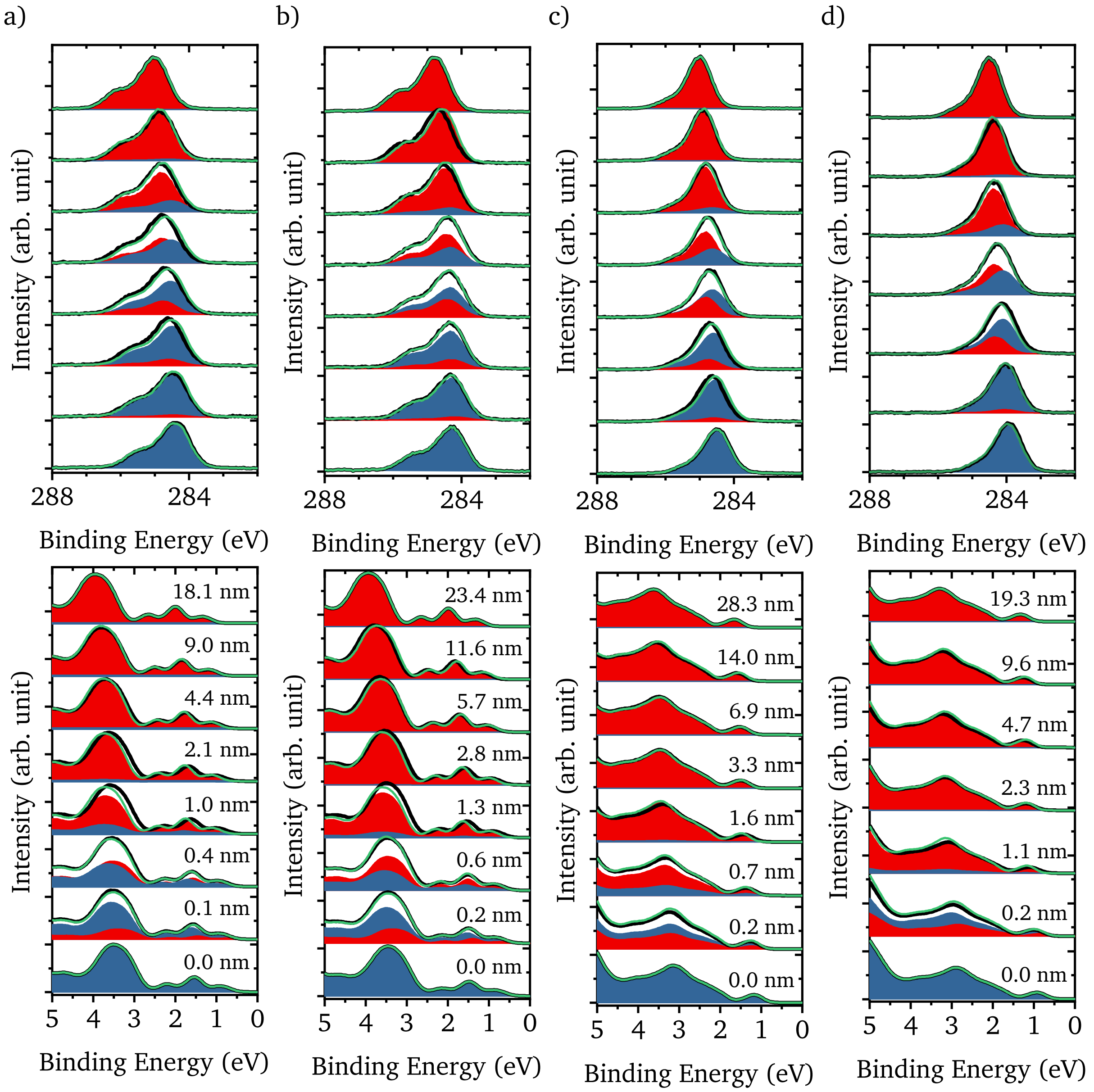

Figure 5.4-4: Photoemission spectra of the interface experiments a) (ITO/p-(2 vol%)-m-MTDATA) | m-MTDATA, b) (ITO/p-(7 vol%)-m-MTDATA) | m-MTDATA, c) (ITO/p-(1 vol%)-HTM-B) | HTM-B, and d) (ITO/p-(5 vol%)-HTM-B) | HTM-B. For each interface, the spectra of the C 1s (top panel) and valence emissions (bottom panel) are shown. The measured spectra (black lines) are fitted by a superposition (green lines) of modeled substrate (blue shaded areas) and adlayer spectra (red shaded areas) using the advanced DOS-based model. Layer thicknesses of the deposition steps are stated in each bottom panel. Adapted from Frericks et al.[74]

adlayer. This behavior cannot be modeled by using one constant DOS for the whole undoped adlayer. Thus, the model is advanced towards a DOS that depends on the deposited adlayer thickness. For simplicity, the layer is divided into two regions: one narrow region right at the interface, and one region for the rest of the layer further away from the interface. Next, two different DOS shapes can be used in these two regions. Right at the interface the concentration of tail states will be high to provide the required charge transfer and further away from the interface the tail state concentration will be low. The effect of different tail state concentrations in the first nanometer of deposited adlayer is shown in Figure 5.4-3c. It can be clearly seen that the electrical potential drop in the sublayer is the largest for the highest number of tail states (blue line, $t = 17\%$).

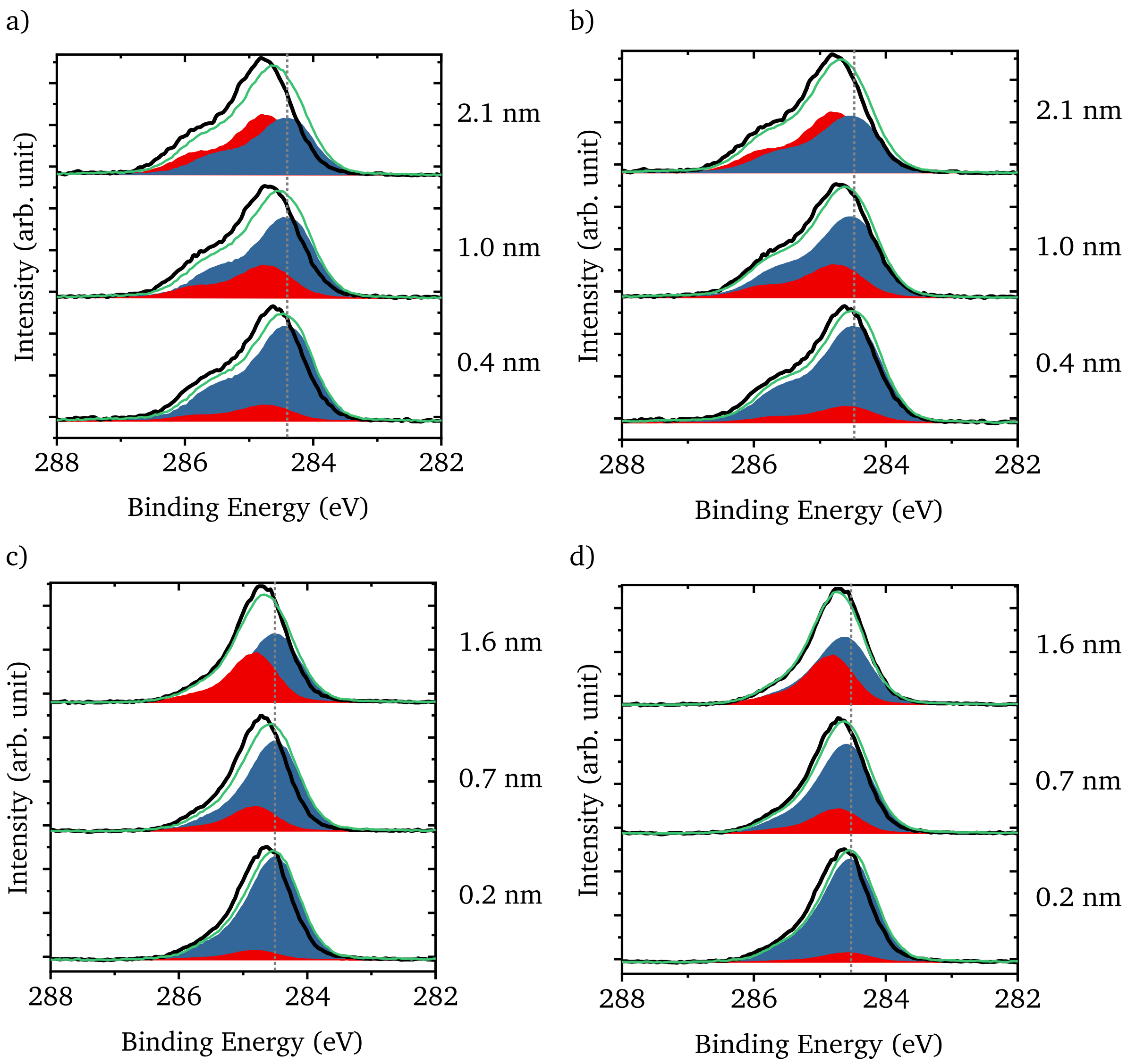

Figure 5.4-5: C 1s spectra of the (a, b) (ITO/p (2 vol%) m-MTDATA) | m-MTDATA and (c, d) (ITO/p (1 vol%) HTM-B) | HTM-B homointerface experiments. Measured spectra are plotted as black lines, modelled fits as green lines, modeled sublayer spectra are given as blue shaded areas, and modeled adlayer spectra as red shaded areas. In a) and c) the spectra using the initial DOS-based model fit with a low concentration of tail states (see Figure 5.4-1) are plotted, showing a strong mismatch. For the fits in b) and d), the advanced model with an increased concentration of tail states is used providing much better agreement with the measurements.

Figure 5.4-4 shows the C 1s and valence spectra of all homointerface experiments fitted by the advanced DOS-based model. Overall, a good agreement between fit and measured spectra is achieved by using high and low tail state concentrations close and far from the interface in the advanced DOS-based model. In Figure 5.4-5, the mismatching spectra (a, c) from the initial fits (see Figure 5.4-1 (b, d)) are compared with the fits from the advanced model (b, d), clearly showing an improvement of the agreement with the measured spectra. Given the combined fit of two techniques (UPS and XPS), the number of spectra, and the simplifications in the model, it is not surprising that there are still small deviations between fit and measurement. In contrast to the original mismatch, the deviations are now randomly scattered across the spectra and do not indicate a systematic error which would indicate wrong assumptions or trends in the model. Therefore, the modeled electrical potential seems to accurately describe the actual electric potential distribution at the interface.

As an example and for further evidence, the F 1s spectra from CPTCFA in the sublayer of the (ITO/p-(7 vol%)-m-MTDATA) | m-MTDATA homointerface experiment (see Figure 5.4-2c) are plotted in Figure 5.4-6a and fitted by pseudo-Voigt[198] type functions (blue lines). Highlighted by the black dotted line which serves as guide for the eye, a shift of the sublayer to higher binding energies is clearly visible in the first deposition steps. From the pseudo-Voigt fits, the shift is determined to be 80 meV in the first two deposition steps. Thus, this analysis of the sublayer's CPTCFA signal provides further evidence for the unexpected sublayer shift where only or mainly a shift in the undoped adlayer would be expected due to the lower charge density. Furthermore, the electrical potential, which is obtained from the fits shown in Figure 5.4-4b, is used to model the F 1s spectra. Due to the low signal to noise ratio, the spectrum from the bare sublayer (bottom spectrum) was fitted by a pseudo-Voigt profile which is then used to model the spectra of the following deposition steps. The modeled spectra are shown as blue shaded areas in Figure 5.4-6b. Red markers are positioned at the maxima and the shift to higher

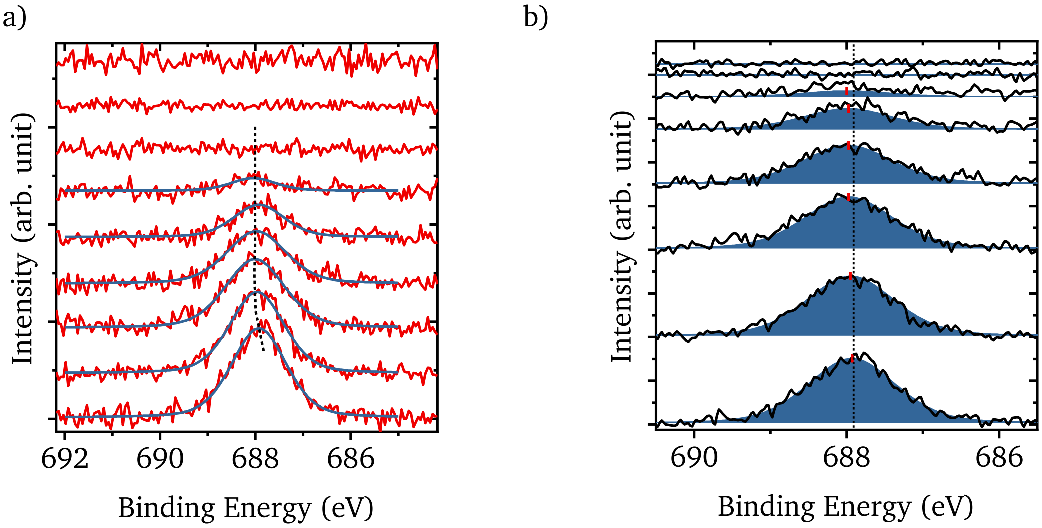

Figure 5.4-6: a) The F 1s spectra from the (ITO/p-(7 vol%)-m-MTDATA) | m-MTDATA homointerface experiment (see also Figure 5.4-2) are fitted by pseudo-Voigt type functions (black dashed). The black dotted line serves as guide for the eye and highlights the shift to higher binding energies. b) Stacked F 1s spectra as for (a) but fitted using the DOS-based model. Red markers highlight the maxima. The straight black dotted line serves as guide for the eye.

binding energies can be seen with respect to the horizontal black dotted line which is drawn at the binding energy position of the first spectrum and serves as guide for the eye.

It is clearly visible that the F 1s spectra modeled with the same electrical potential as the C 1s and valence spectra are also in good agreement with the measured spectra. Therefore, the validity of the modeled electric potential distribution is further supported, and the potential distribution can be used to draw energy level diagrams of the homointerfaces.

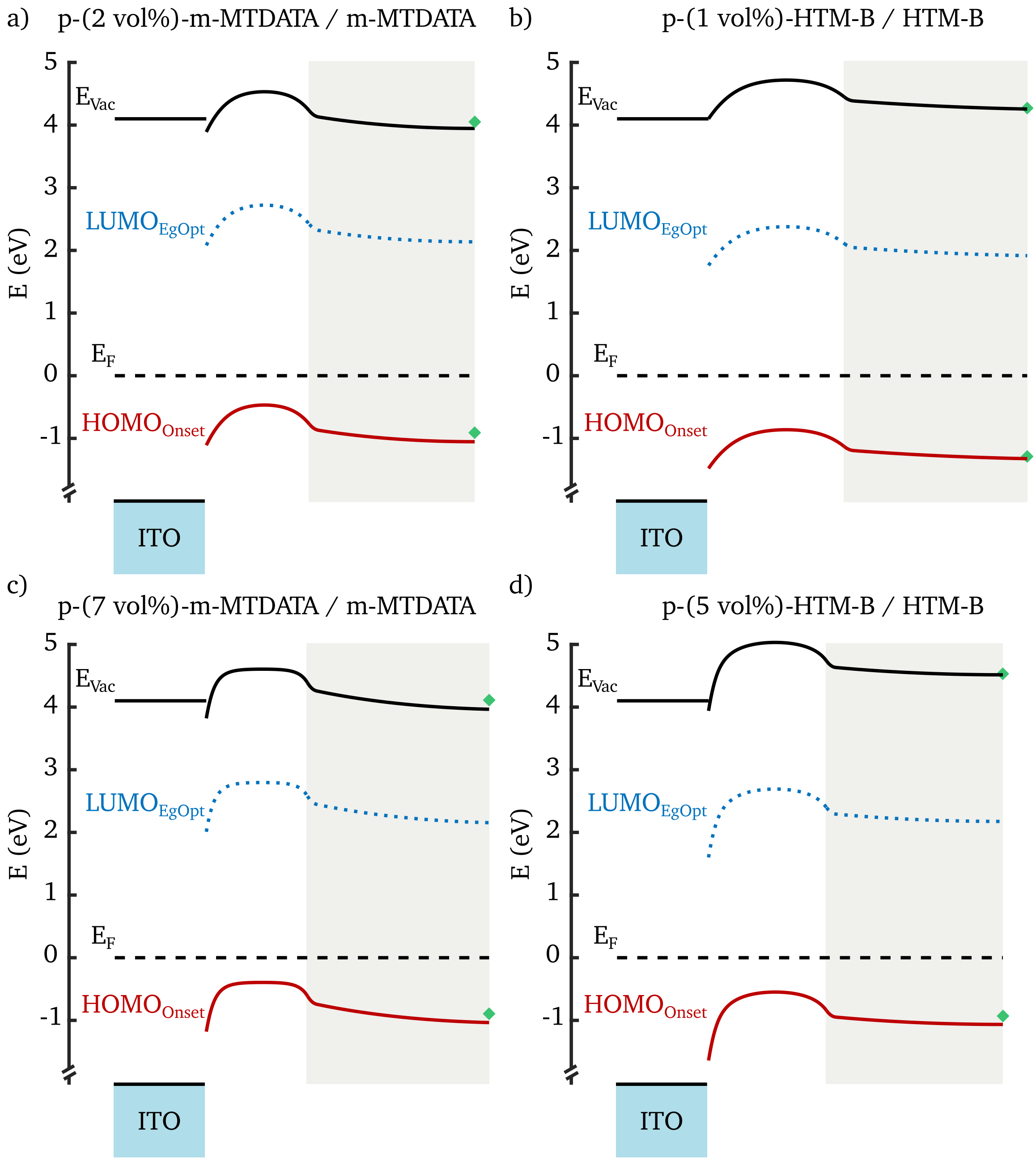

Figure 5.4-7: Energy level diagrams for the interfaces a) (ITO/p-(2 vol%)-m-MTDATA) | m-MTDATA, b) (ITO/p-(1 vol%)-HTM-B) | HTM-B, c) (ITO/p-(7 vol%)-m-MTDATA) | m-MTDATA, and d) (ITO/p-(5 vol%)-HTM-B) | HTM-B. The course of the energy levels follows the modeled electrical potential distribution obtained by fitting the photoemission spectra using the advanced DOS-based model. The energetic position of HOMO onset and vacuum levels is determined by the IP and WF of the undoped material modified by the modeled interface dipole. LUMO onsets are situated according to the values of the optical energy gap above the HOMO onsets. The green diamonds mark the energetic position of the measured WF and energetic difference of HOMO onset to $E_F$ at the final layer thicknesses. The undoped adlayer region is highlighted in grey. Adapted from Frericks et al.[74]

As result of the homointerface experiments, the electrical potentials, which are obtained from fitting with the advanced DOS-based model, are used to draw the energy level diagram of the homointerfaces in Figure 5.4-7. The course of the HOMO onset, LUMO onset, and vacuum level follows the calculated change of the electrical potential. The energetic positions of the HOMO onsets and vacuum levels is determined by the IPs and WFs of the pure undoped HTMs. The LUMO onset is situated according to the value of the optical energy gap above the HOMO onset.

There are three SCRs in the layer stacks. First, the energy levels of the doped layer bend downwards towards the ITO interface as discussed in Section 5.1. Second, the energy levels in the doped layer bend downwards towards the homointerface. Third, the energy levels in the undoped layer bend upwards towards the homointerface. As for the heterointerface, the potential drop at the homointerface is steeper in the more highly doped samples. This is again due to the higher charge density and thus more narrow SCRs.

The potential in the undoped layer can be divided into two parts. Right at the interface the potential drops quickly but then shows some kind of kink followed by a gradual change of the potential with further distance from the interface. These two regions correspond to the two regions with different tail state concentrations. Close to the interface where the tail state concentration is high, the resulting charge density, and thus the electrical field and electrical potential drop, is large. Further away from the interface where the tail state concentration is set low, only few charges can be transferred and thus, charge density, electric field, and electric potential drop are low.

As mentioned above, the energetic difference of HOMO onset to $E_F$ do not reach the values of the pure undoped HTMs on ITO. Therefore, it can generally be concluded that the p-doped sublayer influences the energetic position of $E_F$ in the undoped adlayer over a long range. It should also be mentioned that a corresponding steep change of the vacuum level during the first deposition steps is indeed detected by the shift of the SEC onset, i.e., a change of the WF. As a result and in contrast to the observations in the work of Fukagawa et al.[199], the IP of the molecules remains constant, and the observed shifts cannot be attributed to a change of the energetic position of the electronic states with respect to the vacuum level. Consequently, the shifts have to be the result of a charge transfer and resulting change of the electrical potential.

The parameters used to model the DOS for the fitting of the homointerfaces are listed in Table 5.4-1. As mentioned before, the parameters for the p-doped sublayer are chosen from the results of the heterointerfaces in Table 5.3-1 which are closest in dopant concentration. The thickness of the sublayer is given by $d_{\text{p-HTM}}$ and is calculated from the deposition rate which is obtained from the ITO signal damping. The concentration of the tail states $t$, which is used for the main part of the undoped layer, is rather low in comparison to the one obtained for the heterointerfaces. This might be interpreted as a reduced disorder in the undoped film when it is deposited on the same host molecule instead of ITO. As already discussed, it is found that the valence spectra are broadened at the interface to ITO and by incorporation of the CPTCFA molecules (see Figure 4.2-5 and Figure 5.1-4). In contrast to this low tail state concentration further apart from the interface, the concentration of tail states $t_{\text{IS}}$ that is needed to obtain the required potential drop in the sublayer is quite high. The thickness $d_{\text{IS}}$ of this region is quite

Table 5.4-1: DOS parameters from fitting the homointerface experiments using the advanced DOS-based model. X is the dopant concentration, $d_{\text{p-HTM}}$ is the thickness of the doped sublayer, $t$ is the tail state concentration in the undoped layer region further apart from the interface, and $d_{\text{IS}}$ is the thickness of the undoped layer region right at the interface where the increased tail state concentration $t_{\text{IS}}$ is used. The DOS parameters for the doped sublayer are taken from the results on the heterointerfaces which are closest in dopant concentration (see Table 5.3-1). Adapted from Frericks et al.[74]

| Molecule | X<br>in vol% | DOS parameter p-HTM | $d_{\text{p-HTM}}$<br>in nm | $t$<br>in % | $d_{\text{IS}}$<br>in nm | $t_{\text{IS}}$<br>in % |
|---|---|---|---|---|---|---|
| HTM-B | 1 | as for interface with ITO | 14.8 | 0.10 | 1.0 | 20.0 |
|  | 5 | as for interface with ITO | 12.9 | 0.10 | 1.0 | 20.0 |
| m-MTDATA | 2 | as for interface with ITO | 11.3 | 0.23 | 1.0 | 17.0 |
|  | 7 | as for interface with ITO | 11.1 | 0.20 | 1.0 | 17.0 |

narrow with 1 nm in comparison to the estimated molecule dimensions between 0.5-2 nm (see Section 4.1).

It can only be speculated about the origin for this high number of tail states right at the interface. In the following, different literature reports on this topic will be discussed.

There are reports on similar steep, dipole-like potential drops at organic-organic interfaces in literature.[30,32,51,52] In these reports, the interdiffusion of dopant molecules as possible explanation is also discarded. The authors then introduce the concept of an intrinsic charge neutrality level and an induced density of states. This induced density of states forms electronic states continuously distributed over the energy gap which allows to transfer charges across the interface depending on the position of the Fermi level with respect to the CNL. Overall, this method is quite similar to the assumed high tail state concentration in this work. Here, the tailing gap states correspond to the induced density of states and allow for the required charge transfer (see Figure 2.4-4 in Section 2.4). In the published articles, the origin for this induced density of states remains quite vague. The induced DOS has been introduced for experiments at metal-organic interfaces where the charge carrier concentration in the metal contact material might be high enough to justify such a strong interaction with the organic adlayer.[50] The idea of the induced states has then been transferred to organic-organic interfaces where – as pointed out by Braun et al. – the interaction is expected to be much weaker and an induced density of states seems less likely.[35]

Fukagawa et al.[182] performed experiments with pentacene on differently modified graphite substrates. They used an inert molecular dipole layer to decouple the pentacene from the graphite and realize different substrate WFs. As a result, they observe a charge transfer from the pentacene into the graphite when the modified substrate WF is larger than the IP of pentacene forming a dipolar layer between the substrate and the thin pentacene layer (1-1.6 nm). The charge transfer is explained by the presence of occupied gap states in the pentacene film which are situated above the substrate's $E_F$. These states appear together with structural inhomogenity.[182]

Furthermore, Opitz et al. report the change of the molecular orientation at an organic-organic heterointerface that leads to a change in the energetic position of the HOMO and LUMO states and a strong change of electrical potential right at the interface.[34]

If the electronic interaction of organic-organic heterointerfaces is generally considered to be weak, it seems even more surprising for the studied homointerfaces to show such a strong effect in the DOS at the interface. The only difference between the sub- and adlayer that marks the interface is the incorporation of dopant molecules in the doped sublayer. It therefore has to be assumed that the presence of the dopant molecules or their induced charge density lead to the presence of the predicted gap states in the undoped layer right at the interface – by a structural, orientational, conformational, or electronic influence on the adlayer molecules right at the interface. While the above-mentioned experiments in literature often examine molecules with a crystalline structure, the overall structure of the organic thin films of the studied molecules is expected to be amorphous (see Subsections 4.1.3 and 4.1.4). Still, a locally changing short range orientation of the molecules especially at the interface is conceivable.[200,201]

The presented experiments in combination with the DOS-based modeling provide a basis and a tool for further investigations. The advancement of the DOS-based model is still a rather simple description of a layer depth-dependent DOS. Further development in this direction providing a layer-by-layer changing DOS might be necessary for an even better in-depth characterization. Experimentally, future studies with a broader range of molecules including different crystalline or amorphous structures might help in the attempt to understand the mechanism not only for such homointerfaces as studied in this dissertation but also on the heterointerfaces examined in other investigations.

## 5.5 Conclusion

In this chapter, a new DOS-based modeling approach for the analysis of photoelectron spectroscopy interface experiments was shown. In these interface experiments, step-by-step deposition and consecutive photoemission spectroscopy were used to study the interface formation with emphasis on the electronic structure. ITO | (p-)HTM heterointerface were used as a test case. First, these heterointerfaces were analyzed by classical methods to lay the benchmark for the new approach. Next, the new model was introduced and then applied to the heterointerfaces. The ITO | (p-)HTM heterointerfaces were studied for two different HTMs, m-MTDATA and HTM-B, at different dopant concentrations. The classical analysis of the interface experiments reveals a typical semiconductor physics textbook behavior. During interface formation, charge transfer between ITO and the organic semiconductor occurs which leads to the formation of a SCR in the semiconductor. The potential drop across the SCR depends on the final energetic position of $E_F$ in the doped semiconductor which up to about 2 vol% shifts towards 0.4 eV above the HOMO onset where the energetic position saturates. With further increase of the dopant concentration the width of the SCR decreases. For both materials, a small interface dipole is measured at the interface.

The DOS-based modeling approach combines different ideas from literature in a new way and, for the first time, generates spectra for different emission regions that can be directly fitted to the measured ones. Here, a calculated distribution of the electrical potential, which is mainly influenced by assuming a model of the organic semiconductor's DOS, is considered. It further takes into account the variation of the layer-depth dependent signal intensity in convolution with the electrical potential distribution. The model demonstrated to deliver the same results on the energetic properties as by a classical analysis of the data. In addition, the model allows for a detailed discussion of the electronic states introduced by the dopant or potentially present in the energy gap of the organic semiconductor. The DOS-based model also gives a more accurate description of the electrical potential in the SCR than the often-used Schottky model. As it considers the change of the charge density with the change of the energetic position of $E_F$ it is more accurate in calculating SCR widths and ionized acceptor concentrations. This Fermi level dependent charge density is realized by using a constant acceptor DOS but calculating the occupation based on the relative energetic position of $E_F$ resulting in a varying charge distribution.

Next, the successful test of the DOS-based model allowed to analyze (ITO/p-HTM) | HTM homointerfaces. These homointerfaces are difficult to characterize as the sublayer and adlayer signals are dominated by the same spectral features which makes it impossible to distinguish them. Here, the model proves to be crucial as it provides the physical basis to discuss the observed spectral shifts. Again, m-MTDATA and HTM-B were used in the experiments to form the layer stacks with the same host molecule in the doped and undoped layer of the interface. Two different dopant concentrations in the doped layer were tested for each material. From the spectra, it is found that an unexpected SCR appears in the p-doped layer. Principle physical considerations, assuming a structurally perfect homointerface, would suggest that this should not be the case as the charge carrier density should be much higher in the doped sublayer compared to the undoped adlayer. A potential interdiffusion of the dopant during or after deposition is ruled out experimentally as well as by theoretical considerations using the model. In a next step, the DOS-based model was further advanced to allow for a different DOS right at the interface and further apart from the interface. With this advanced DOS-based model, it is shown that an increased density of gap states in the undoped layer right at the interface is able to create a sufficient charge transfer into the doped layer which causes the formation of a SCR in the doped layer. The origin of these gap states remains unclear, but it is suggested that they are induced by a structural change in the molecular orientation or conformation right at the interface. It is further discussed that similar effects are reported in literature for organic-organic heterointerfaces and that gap states often seem to play a significant role in the energy alignment of organic semiconductor interfaces. Still, it is surprising to detect that even at a homointerface – where only a few percent of dopant molecules define the difference between the two sides of the interface – modified electronic properties and their involvement in contact formation seem to occur. It is suggested that further studies are needed to investigate these predicted interface states in a more dedicated approach by a systematic variation of molecules that form amorphous and also crystalline layers.

# 6 The Aluminum Back Contact Interface in Hole-Only Devices

Even though, the interface between a cathode material and an HTM is generally not present in any full device, it is still relevant for so called hole-only devices.[40,17] These hole-only devices are often used in research and development efforts where the device structure is reduced to isolate the effects of certain layers and exclude further complicating processes, e.g., charge recombination. In these cases, a second electrode is still required to enable electrical measurements, and a cathode material is then often used as back contact. However, in the hole-only device study of Wißdorf et al. the influence of the Al cathode is found to play a main role in the observed effects.[17] In this section, the same material combination as in the work of Wißdorf et al. is investigated in heterointerface experiments. Aluminum is deposited step-by-step onto p-doped as well as undoped HTM-B thin films. In the first subsection the layer growth of Al will be analyzed and discussed, and then in the second subsection the interface experiments will be analyzed with respect to the electronic structure at the interface. Finally, the results will be discussed with respect to the observations made by Wißdorf et al., but also address the problems of Al interfaces in the general context of hole-only devices.

## 6.1 Layer Growth and Thin Film Formation

In this subsection, the growth of aluminum thin films on different sublayer materials and under different deposition conditions is analyzed. The results of the first interface experiments showed a behavior different from a simple layer-by-layer Frank-van der Merwe type of growth mode.[202] Therefore, further interface experiments were carried out to examine if a difference in thin film growth could be achieved. The parameters for the interface experiments are given in Table 6.1-1. The experiments with Si wafer substrates serve as references. The Si wafer substrates were treated by Ar-ion etching to remove the native oxide layer and avoid any reaction with Al. In the work by Wißdorf et al.[17], which is mentioned in the introduction to this chapter and is the motivation for these experiments, much higher deposition rates (about 300 vs 4 Å/min) and a higher base pressure ($<10^{-7}$ mbar) are used. In literature, there are statements that the deposition rate or base pressure in the vacuum chamber might influence the thin film growth.[161] Thus, the deposition rate and base pressure were increased for additional experiments. To increase the deposition rate, the temperature of the evaporation source was increased; the

Table 6.1-1: Deposition parameters for the different interface experiments.

| Sublayer | Ar-ion etched Si | Ar-ion etched Si | HTM-B | HTM-B | HTM-B | p-(14 vol%)-HTM-B | CPTCFA |
|---|---|---|---|---|---|---|---|
| Evap. Source Temp. | 915°C | 1005°C | 915°C | 915°C | 1005°C | 915°C | 915°C |
| Base Pressure | ~$5\cdot10^{-9}$ mbar | ~$5\cdot10^{-9}$ mbar | ~$5\cdot10^{-9}$ mbar | ~$3\cdot10^{-8}$ mbar | ~$5\cdot10^{-9}$ mbar | ~$5\cdot10^{-9}$ mbar | ~$5\cdot10^{-9}$ mbar |

experiments at higher evaporation source temperatures will be referred to as “high-rate”. To achieve a higher base pressure, the chamber was vented and no bake-out was performed afterwards; the experiment conducted at higher base pressure is referred to as “high P”. The base pressure in the chamber was measured after the Al evaporation source was heated up but the shutter was still closed. The exact values from the article by Wißdorf et al. could not be reached but the increased values might still give some ideas on the influence of these parameters.

### Core-Level Spectra Analysis

To analyze the deposition of Al in the different interface experiments, the evolution of the sublayer emission peaks is plotted against the deposition time in Figure 6.1-1. Examples of the corresponding photoemission spectra from the interface experiments can be seen later in Figure 6.1-3 and Figure 6.2-1. For the high-rate experiments, the deposition rate is expected to be about ten times higher than in the other experiments. This expectation is based on an increase in vapor pressure of about one order of magnitude for Al when going from about 900°C to 1000°C.[203,204] Thus, the deposition time steps were reduced to a tenth. The high-rate experiment data in Figure 6.1-1 are plotted with respect to the top x-axis which is scaled by a factor of 0.1 to the bottom x-axis. Figure 6.1-1a shows the evolution of the sublayer emission peak areas normalized to the initial value before deposition. In b), the natural logarithm of these normalized values is plotted. For the reference depositions on Si (brown squares, and dark green right pointing triangles), the Si 2p emission intensity decreases with increasing deposition time towards zero intensity as expected. The data points of the normal and high-rate depositions are close but do not exactly match. This indicates that the factor between the deposition rates for the high-rate and normal depositions is not ten as assumed for plot but slightly lower. The data points of the F 1s emission areas from the CPTCFA sublayer (dark orange down pointing triangles) evolve closely to the ones of the Si substrates. In contrast, the C 1s emission peak areas of the Al deposition at normal rate on doped and undoped HTM-B (red up pointing

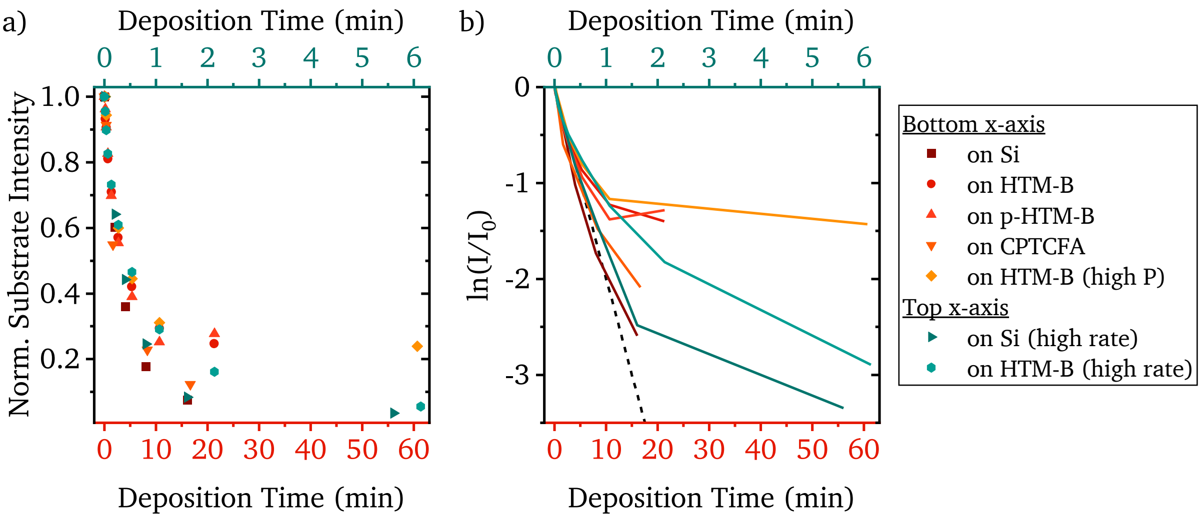

Figure 6.1-1: a) Peak areas of the sublayer core level emissions against Al deposition time normalized to the initial peak before deposition of Al. b) Natural logarithm of the normalized peak areas against Al deposition time. The data of the high-rate deposition experiments are plotted with respect to the top x-axis which is scaled by a tenth of the bottom axis to compensate for the higher deposition rate and allow for a comparison.

triangles, dark red circles, orange diamonds) show a slower decrease in intensity with increasing deposition time. Furthermore, the emissions do not tend towards zero but seem to saturate slightly above 0.2. For the high-rate Al deposition on HTM-B, the emission peak area decrease is slightly faster and reduces below 0.2 for a long deposition time. The plot of the natural logarithm of these normalized intensities is chosen to compare the intensity evolution with an exponential decay as it would be the case for a layer-by-layer growth. The dashed black line resembles such an exponential decay for a deposition rate of 4 Å/min and an effective attenuation length for the emitted electrons of 20 Å. It can be clearly seen that the data points do not follow this linear trend but start along a steep slope which then gets more and more gradual with further deposition time. If a layer-by-layer deposition is assumed this would be described as a high deposition rate that then becomes lower and lower. However, in the layer-by-layer picture there is no reason why the deposition rate should decrease. In his dissertation, Eric Mankel[59] models the sublayer emission intensity evolution for an island formation Volmer-Weber type growth mode[202] and compares it to the Frank-van der Merwe type[202]. He shows that the island growth leads to a more gradual slope in a semi-logarithmic plot than the layer-by-layer growth. Based on this model he finds examples in his experiments where he observes a change from a steep slope to a gradual slope which he then assigns to a Stranski-Krastanov type growth mode.[202] In this growth mode type, the deposition starts with a layer growth and then changes to the formation of islands with ongoing desposition.[59] The in this work observed change in the slope of the natural logarithm plot suggests a similar growth mode. For the depositions on Si and on the CPTCFA sublayer, the slope is rather constant up to the last deposition step in the high-rate deposition. However, instead of two regimes with two different slopes, the change of the slope is rather continuous from steep to gradual for the depositions on doped and undoped HTM-B sublayers. Also, the saturation above 20% of the initial intensity is unexpected for the formation of islands which would still be expected to continuously cover the surface with deposition time leading to a continuous decrease of the signal. In other words, this saturation could mean that the islands do not grow into certain areas on the surface leaving uncovered spots whose emission is not damped.

### Take-Off Angle Dependent X-ray Photoelectron Spectroscopy

To further investigate the growth of an Al thin film deposited at normal rate for 16:40 min on an HTM-B sublayer, the Al 2p and C 1s photoelectron emission were measured at different take-off angles θ with respect to the sample surface plane. With lowering the take-off angle the path from a certain depth in the sample to the surface for the detected electrons is increased. If the effective attenuation length of the electrons is considered to be independent of the take-off angle in a first approximation, the path length of the detected electrons can be assumed constant, and the effective information depth is lowered. In other words, the surface sensitivity is enhanced by lowering the take-off angle.[205,206] With lower θ, the detected intensity decreases overall. Thus, the change of the Al 2p peak area with θ has to be analyzed relative to the evolution of the C 1s peak area. Therefore, the Al 2p peak area is divided by the C 1s peak area for each take-off angle and then normalized to the ratio at normal emission, i.e., $\theta = 90°$.

The obtained values are plotted in Figure 6.1-2a. Due to the increased surface sensitivity with decreasing $\theta$, it would be expected that the adlayer signal increases relative to the sublayer signal with decreasing θ. In contrast, the data points in Figure 6.1-2a show exactly the opposite

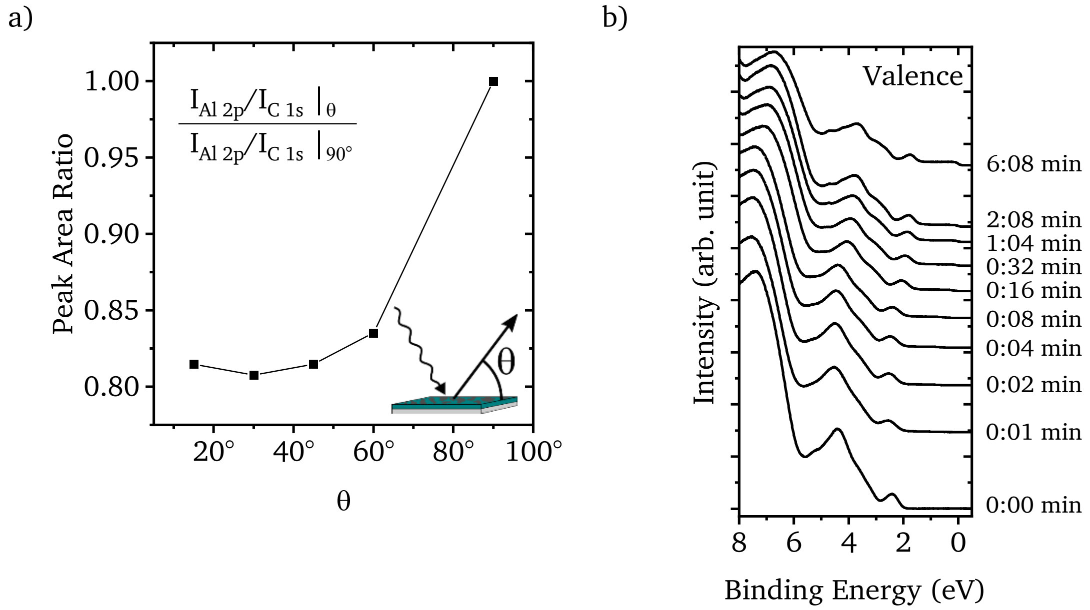

Figure 6.1-2: a) Take-off angle dependent Al 2p peak areas of an HTM-B | Al stack. The peak areas are divided by the ones of the C 1s sublayer peak and normalized to the ratio at 90° take-off angle θ. b) Evolution of the UP valence spectra for the HTM-B | Al high-rate interface experiment. Deposition times are stated on the right.

trend. In a simple picture, this trend would suggest that there are organic molecules above the deposited Al. However, it is also known that the surface roughness influences the results of take-off angle dependent measurements.[205,207] The aspect ratio of the underlying ITO grain morphology is within a value of about 0.1 (height/width) rather small (see Subsection 4.1.1) and thus the effect of the substrate roughness can be assumed to have no significant influence. However, the formation of Al islands during the growth might influence the take-off angle dependent results more strongly and the analysis is no longer straightforward.

### Valence Spectra Analysis

Besides the trends for the core level electron emissions, the evolution of the valence spectra with increasing Al deposition time does also deviate from a simple layer-by-layer growth mode. In Figure 6.1-2b, the valence spectra for the HTM-B | Al high-rate interface experiment are shown. It can be clearly seen that the spectral features from the organic sublayer with peaks around 2.5, 4.5, and 7 eV binding energy are well visible along the deposition of Al. Even after 6 min of high-rate deposition the spectral signature is still clearly visible while the C 1s core level emission is strongly reduced to about 5% of initial intensity at this point (see Figure 6.1-1). A quantification of the valence spectra is not possible as the spectral signature of the adlayer is not clear and thus cannot be subtracted from the measured data to obtain the pure sublayer signal. The effective attenuation length in Al for the emitted electrons with kinetic energies around 10 eV is reported with values between 4 and 40 Å.[208–210] In the work of Ashley et al., the inelastic mean free path of electrons at 10 eV is about 20 Å and close to the one at 1000 eV.[211]

In addition, the valence spectra measured with He-II excitation (hν = 40.8 eV) – not shown here – follow a similar trend even though this excitation energy results in electrons with kinetic energies around 30 eV and thus a much shorter expected effective attenuation length. Therefore, it seems that at least in some areas of the surface organic molecules stay at the surface, potentially, as the Al diffuses into the top layers of the HTM. However, an exclusive diffusion of Al into the organic layer seems unlikely as the valence spectra show the appearance of a Fermi edge feature after about 2-4 s of deposition time. This requires the formation of clusters or islands of Al atoms. In contrast to this evolution of the valence spectra for the depositions on doped and undoped HTM-B, the valence spectra of Si and the CPTCFA sublayer vanish after the first deposition step in the respective interface experiments (see Figure 6.1-3). This shows that in principle the effective attenuation length in Al is small for the UP spectra and a remaining sublayer signal with deposition has to be the result of diffusion or island formation. From these results up to here, it can be concluded that Al likely grows in islands on the doped and undoped HTM-B thin films and might also diffuse partially into these organic layers. While the diffusion of Al into the substrate seems unlikely for Si, it is noteworthy that the behavior on the organic molecules of the CPTCFA sublayer is completely different from the undoped or even doped HTM-B layers. Therefore, before the discussion of the Al thin film growth is concluded, a closer look is taken on the photoemission spectra of the CPTCFA | Al interface experiment.

### Reactive CPTCFA | Al Interface

In Figure 6.1-3, the evolution of the X-ray photoelectron (XP) and UP spectra of the pure CPTCFA | Al interface experiment are shown. The bottom Al 2p spectrum shows a broad peak around 76 eV after the first 20 s of deposition. Then, with continuing deposition a sharper doublet around 73 eV appears and grows in intensity. While the sharp peak at 73 eV can be assigned to metallic Al, the broad peak at higher binding energies marks the existence of a strongly oxidized Al species.[140]

Furthermore, the C 1s, N 1s, and F 1s spectra show a broadening of the peaks and a shoulder towards lower binding energies after the first deposition step of Al. The shoulder is especially well visible in the C 1s emission. These observations suggest that there is a charge transfer and potentially a reaction between the deposited Al and the CPTCFA molecules of the sublayer

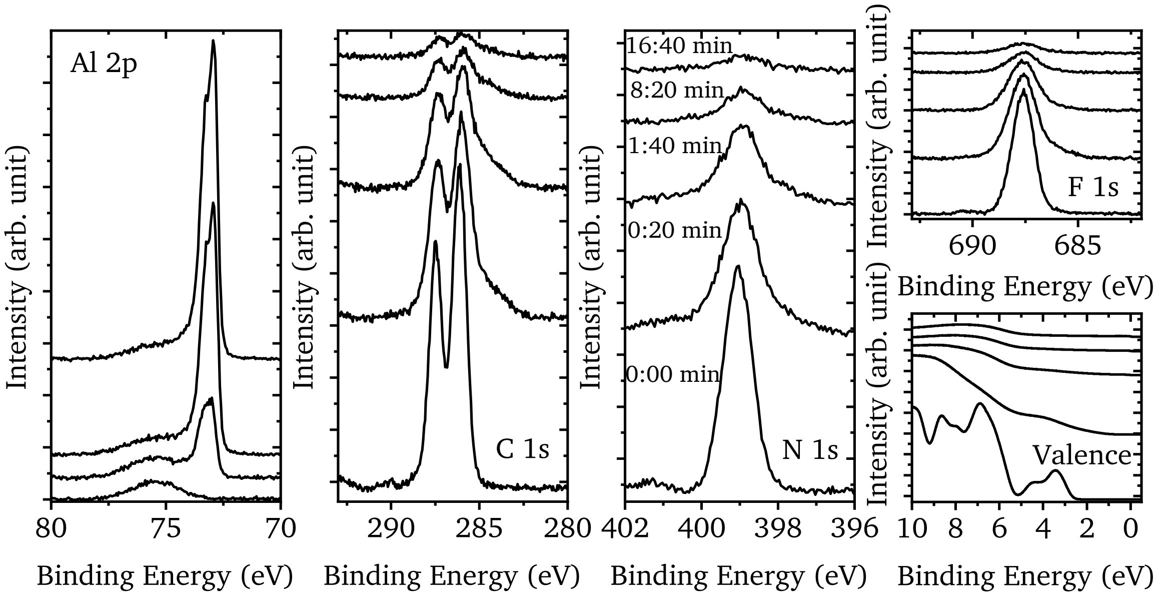

Figure 6.1-3: Photoemission spectra of the CPTCFA | Al interface experiment. The spectra are plotted from bottom to top for increasing deposition time. The total deposition time steps are given next to the N 1s spectra.

where Al is oxidized, transferring its electrons to the CPTCFA molecules. As a result, the binding energy of the Al 2p core level electrons on the positively charged Al-ions would increase while the increased electron density on the negatively charged CPTCFA molecules would cause a respective shift of the core level emissions to lower binding energies. Considering that Al is a rather reactive metal that is easily oxidized,[212,213] and that the p-dopant is designed with a large electron affinity to accept electrons (see Subsection 4.1.2), such a reaction seems likely. Furthermore, Fahlman et al. report the reaction of Al with cyano derivatives of poly(p-phenylene vinylene) and identifies that Al preferentially reacts with the C≡N groups which are also present in the here used CPTCFA molecule.[214] Based on this analysis of the CPTCFA | Al interface, the growth of the Al thin films can be further discussed.

In literature, similar effects to those observed here are found for Al and other metal contact materials like, e.g., Au, Ag, and Mg. The diffusion of thermally evaporated hot metal atoms into the organic semiconductor layers is observed using measurements of the signal evolution after heat treatment, capacity measurements, scanning electron microscopy on cross sections, and Auger electron spectroscopy depth profiling.[38,161,215–217] Often the diffusion is accompanied with a reactive interaction between the metal and the organic layer. Hirose et al. study the interface of several metal elements and see a trend for reactive metals to diffuse while noble metals tend to form abrupt interfaces.[218] Furthermore, there are reports where the valence features of the organic sublayer measured by UPS are found to only slowly decrease with Al deposition. As there is no sign for a reaction and thereby indication for diffusion, the authors assign this slow intensity decrease to a not fully covered surface, i.e., island formation.[164,219] In the work of Hill et al., similar observations are made for Ag and Mg. However, the authors detect a clear Fermi edge feature in the spectra for Ag but not for Mg. They interpret this as the formation of islands in the case of Ag and a diffusion into the organic layer in the case of Mg.[220] In contrast to the reports of reaction driven diffusion of metal atoms into the organic sublayers, the reports of Kaune et al. and Demirkan et al. describe limited diffusion and a Stranski-Krastanov type growth due to the formation of a reaction layer. In their picture, the reacting Al atoms are bound to the molecules at the surface forming many nucleation sites facilitating a quick layer growth.[163,221] The observations of the here studied CPTCFA | Al interface support these latter reports. They also indicate the formation of a closed layer as indicated by the quickly vanishing sublayer features in the valence spectra and the nearly linear decrease of the natural logarithm of the normalized C 1s peak. In addition, the spectra show a charge transfer or reaction between Al and the CPTCFA molecules. The reduced slope of the C 1s peak area at longer deposition times indicates the transition to island formation.

For the depositions of Al on undoped and doped HTM-B, the interpretation is more complex. The formation of a closed layer can be ruled out by the evolution of the XPS core level emissions and the UP valence spectra. Furthermore, the detection of a Fermi edge in the valence spectra shows the formation of metal clusters or islands at the surface. However, island formation alone does not explain the different sublayer signal damping in XPS and UPS data. If there would be only island formation on the surface, the ratio of covered and uncovered parts of the surface would be expected to affect the XPS and UPS signal in the same way. The signal damping of the surface parts covered by islands, however, would be expected to follow an exponential law with a shorter effective attenuation length and a faster signal decay in the case of UPS. As a result, and opposite to the observations here, the UPS signal would be expected to decrease faster than the XPS signal. It is therefore assumed that a combination of Al diffusion into the organic layer and island formation is taking place during deposition. The idea is that, on the one hand, the interdiffused layer leads to signal damping of the underlaying organic layer reducing the effective information depth of the core level emission intensities. On the other hand, the UPS valence signal is less affected as it results only from the topmost molecular layers which are still at the surface. As a result of this complex organic-metal interface that is not following a simple layer-by-layer growth and might include interdiffusion and the reaction of Al and CPTCFA molecules with each other, the data of the interface experiments are not suitable for an analysis using the DOS-based model. In the next subsection, the electronic structure at the interfaces is thus analyzed in a classical manner.

## 6.2 Electronic Structure at the Interface

After the growth type of deposited Al onto doped and undoped HTM-B was discussed in the previous subsection, the respective interface experiments will now be analyzed regarding the electronic structure and energy level alignment at the interface. As an example, the photoemission spectra of the p-HTM-B | Al interface experiment are presented in Figure 6.2-1. Shown are a) the Al 2p, b) C 1s, and c) valence spectra. The total deposition time for each deposition step is stated on the right. The first (bottom) Al 2p spectrum marks the first deposition step. The vertical dashed black lines serve as guide for the eye and mark the final Al 2p peak maximum, the initial C 1s peak maximum, and the initial HOMO onset binding energy positions.

Right after the first deposition for 10 s, the Al 2p signal is still quite weak but the C 1s and valence spectra show a strong shift to higher binding energies. For the C 1s peak, the shift is combined with a broadening of the peak. This shift continues up to 40 s total deposition time. After 20 s of deposition, a Fermi-edge-like spectral feature can be detected around 0.3 eV

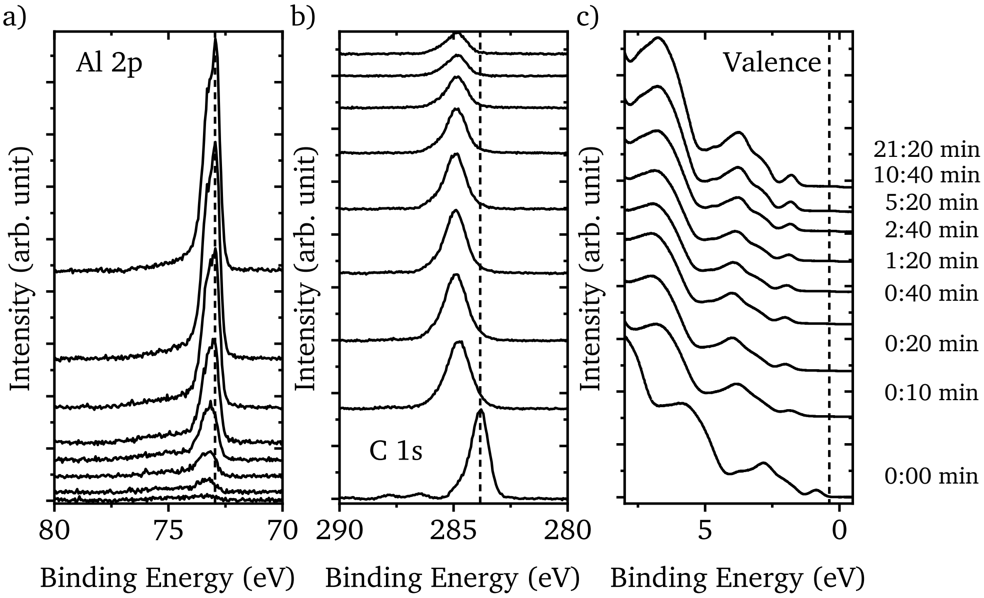

Figure 6.2-1: Photoemission spectra of the p-HTM-B | Al interface experiment for increasing deposition time from bottom to top. Shown are a) the Al 2p, b) C 1s, and c) valence emissions. The total deposition time for each step is stated on the right. The Al 2p spectra start with the first deposition step of 10 s.

binding energy. For the continued deposition up to about 5 min, a slight shift in the opposite direction towards lower binding energies is observed for the C 1s peak, the HOMO onset, and the Al 2p peak. Also, the Fermi edge in the valence spectra shifts towards 0 eV.

For the undoped HTM-B | Al interface experiments (spectra not shown), the spectra show no shift for the first 20 s of deposition. Afterwards, with continued deposition, a shift towards lower binding energies is observed for the spectral features. For the C 1s peaks, the shift is accompanied by a broadening of the peaks. Again, a Fermi edge is detected which analogously shifts from about 0.7 eV towards 0 eV. In Figure 6.2-2a, the HOMO onset binding energy positions vs. deposition time are plotted for the experiments with doped and undoped HTM-B. The evolution of the HOMO onset is representative for the observed shifts in the other emission spectra. It can be seen that there is barely any difference between the experiments on undoped HTM-B, thereby showing no influence of the varied deposition rate or base pressure. Due to the p-doping, the energetic position of $E_F$ of the p-HTM-B sublayer is closer to the HOMO onset prior to the Al deposition than in the undoped layer. However, right with the first deposition step the HOMO onset of the doped layer shifts to higher binding energies, i.e., towards the energetic position of the undoped layer. After around 20 to 40 s of Al deposition, the HOMO onsets of the undoped HTM-B layers start to shift towards lower binding energies. Also, the HOMO onset of the doped layer shifts to lower binding energies. This is accompanied by the detection of the Fermi edge. At about 5 min of Al deposition, the HOMO onset shifts in the doped and undoped sublayers, also starting to saturate around 1.4 eV below $E_F$. These observations can be understood as follows: During the first deposition steps most of the deposited Al diffuses into the organic layer, but the XP spectra of the undoped HTM-B | Al interface show no indication for a reaction. Thus, the Al atoms apparently do not react with the HTM-B molecules. In the doped HTM-B layer, however, the Al atoms can be expected to react with the p-dopant molecules as the results of the CPTCFA | Al experiment indicate. This reaction potentially revokes the p-doping effect and thereby leads to an $E_F$ shift away from the HOMO. Furthermore, the Al atoms could act as donors and simply release electrons which recombine with the holes, originally introduced by the p-dopant molecules. With continued deposition, Al starts to form islands on the surface as indicated by the appearance of the Fermi edge.

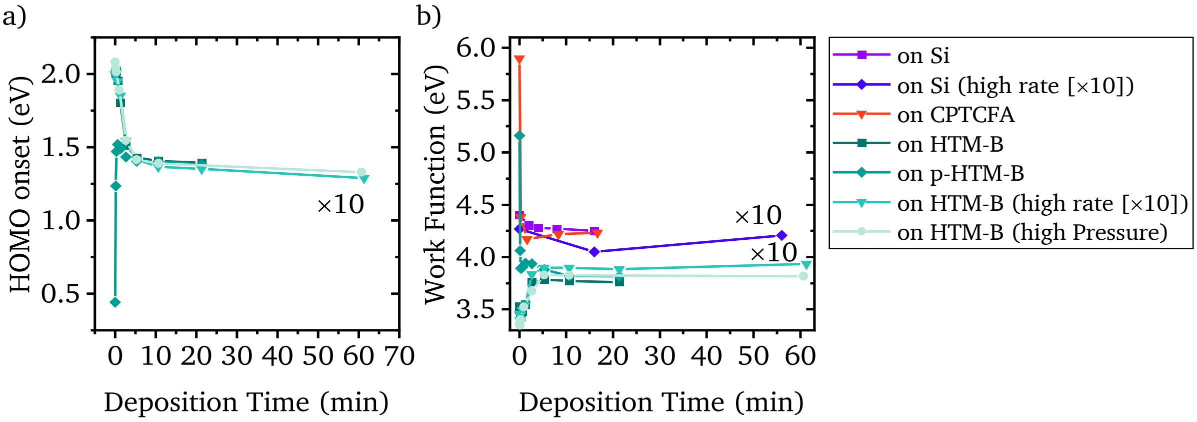

Figure 6.2-2: Evolution of a) the HOMO onsets and b) the WFs with Al deposition time for the different interface experiments. The deposition time of the high-rate experiment data is multiplied by ten (× 10) for plotting to allow for a better comparison.

At this point, a more classical interface energy level alignment between organic layer and metallic Al islands can be considered. For undoped HTM-B the WF is determined to be about 3.7 eV and for Al on Si a value of 4.2 eV is measured (see Subsection 4.1.5). This suggests the charge transfer of electrons from the organic layer into Al during interface formation. The charge transfer then would result into a SCR in the organic layer which causes an electrical potential and a respective upwards bending of the energy levels towards the interface – photoelectron binding energies shift towards lower values. The formation of a SCR also explains the broadening of the C 1s peaks. For the doped HTM-B layer, as discussed, the interdiffusion layer is also effectively undoped or at least much more weakly p-doped. Therefore, $E_F$ is also slightly above the one of a pure Al layer leading to a negative charge transfer from the organic layer to Al. This charge transfer then adjusts the $E_F$ energetic position and causes the slight shift in binding energy. If the Al islands are not interconnected on the surface towards the contacting sample holder screws on the side, they are only electrically connected through the underlaying organic layer. Thus, the Al islands electronically float on top of the organic layer and their Fermi edge and Al 2p emission will shift along with the change of the electrical potential in the organic layer. For the deposition of a metallic contact, usually, it is expected that the high density of charge carriers in the metal leads immediately to the required charge transfer and formation of the SCR. Thus, the Fermi level of Al should appear right away at 0 eV binding energy. Then, also, no layer-by-layer shift of the core level spectra would be observed. As a result, either the amounts of deposited Al are too low for an immediate formation of the full SCR, or there are other effects, e.g., charging[98,99] or surface photo voltages[222], which are present at early deposition steps but vanish when the Al layer is interconnected and grounded via the sample sides. However, no indications for comparable charging effects or surface photovoltages were observed in the ITO | HTM-B interface experiments in Chapter 5. As the magnitude of the observed binding energy shift is about 0.6 eV, such an effect should have a significant influence which would be unlikely to be missed.

In addition to the core level and valence spectra, the SECs are also measured to determine the WFs. The evolution of the WFs is plotted in Figure 6.2-2b. Here, the values of Al on Si and the CPTCFA sublayer are included. For these latter experiments, where the Al is expected to grow in a Stranski-Krastanov type, the WF is determined around 4.2 eV. In contrast, the WFs of the doped and undoped HTM-B experiments end up at about 3.8 eV. In addition, the shift of the WFs is larger than the shift of the HOMO onsets in the case of doped HTM-B and smaller than the shift of the HOMO onsets in the case of undoped HTM-B. This mismatch between HOMO onset and WF indicates the formation of an interface dipole. The results of the electronic structure analysis are summarized in the energy alignment in Figure 6.2-3. The exact course of the electrical potential is not known for the interface. Therefore, it is simply assumed that the electronic properties of the organic layer are constant over the whole layer thickness and that the formation of the SCR at the organic-Al interface is similar to the situation at the ITO-organic interface, resulting in a similar course of the electrical potential. The energy level course at the ITO-organic interface is thus adjusted to the respective potential drop and used at the organic-Al interface. The uncertainty about the exact energy level evolution is indicated by dashed lines. The magnitude of the potential drop across the energy level bending is taken from the initial and final HOMO onset energetic positions. The mismatch between WF and HOMO onset evolution is drawn as offset at the interface indicating an interface dipole.

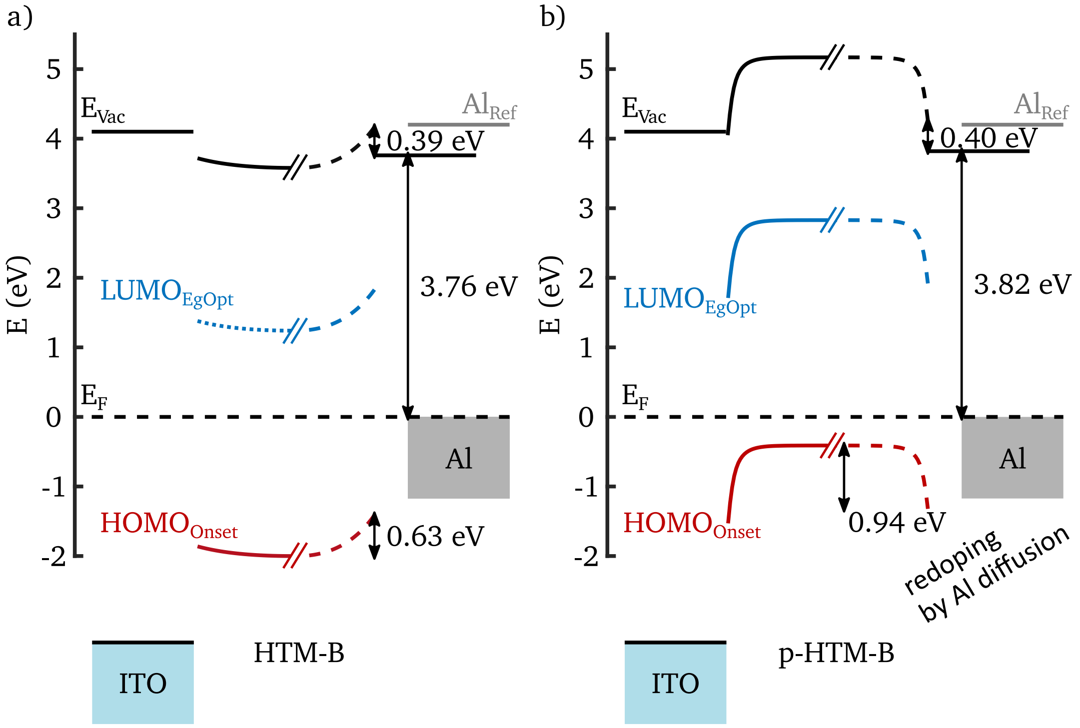

Figure 6.2-3: Energy level alignment of a) the HTM-B | Al and b) the p-(14 vol%)-HTM-B | Al interfaces. The left side interfaces towards ITO are taken from Figure 5.3-2. As the right interface is not abrupt and the exact electrical potential distribution is not known, the energy levels are drawn as dashed lines. The expected Al vacuum level energetic position (Al$_{Ref}$) is given as grey line slightly shifted to the right. LUMO onset and vacuum level of the organic layer are situated according to the IP and optical energy gap of the pure material above the HOMO onset.

The expected energetic position of the vacuum level of a pure Al layer is drawn as grey line slightly shifted to the right. It can be seen that this reference line of the expected Al vacuum level aligns perfectly with the vacuum level bending in the organic layer. In other words, as expected from classical semiconductor physics,[67] the observed potential drops across the SCRs in the organic semiconductors correspond well to the initial $E_F$ differences between organic layer and pure Al film. The observed WF of 3.8 eV suggests that the Al film on the doped and undoped HTM-B layers is different from the one on Si. Typically, a lower WF of an Al thin film indicates an increased oxidation.[162] Although the depositions are performed under UHV conditions, there are small amounts of oxygen detected by XPS (see Subsection 4.1.5). However, the amount of oxygen detected for the different depositions is about the same for all experiments and the highest values are measured for the experiments on Si and the CPTCFA layer which in contrast show the highest WF values. Another explanation for the low WF would be the island formation of Al. As it is well shown in the work by Schultz et al.,[86] the WF of an inhomogeneous surface measured by photoemission spectroscopy is dominated by the surface areas with the lowest WF. For a well-defined sharply patterned surface, the superposition of two SECs can be detected and the respective two WFs can be extracted. However, for less well-defined inhomogeneous surfaces, the different WF contributions to the SEC cannot be separated. The lowest WF does then mark the determined onset.[86] For the here studied interfaces, this effect could mean that the local WF at the Al islands on the surface is actually around 4.2 eV while the organic layer spots with potentially interdiffused Al atoms between the islands have a local WF of 3.8 eV. While the WF of the Al islands determines the shifts of the charge transfer, electrical potential, and observed binding energy shifts, the uncovered surface areas dominate the determined WFs leading to the observed mismatch. In the following subsection, the results of this subsection will be discussed with respect to the results published by Wißdorf et al.[17]

## 6.3 Discussion Regarding the Impedance Spectroscopy Results

As mentioned in the introduction to this section, the presented Al interface experiments are strongly motivated by the report of Wißdorf et al. Now, the results of the previous sections shall be discussed with respect to the work by Wißdorf et al. but concluding with a more general view on the topic. In this study, hole-only devices with the layer stacks of ITO/p-(x vol%)-HTM-B/Al with different dopant concentrations in the organic layer are characterized by current-voltage and capacitance-voltage measurements. The capacitance at 0 V is found to change with the dopant concentration of the p-HTM-B layer and a maximum of the capacitance is found for the devices with a dopant concentration around 5 vol%. To understand this effect, a combination of a differential equivalent circuit model and drift diffusion simulations is used to model the results of the impedance spectra. From this model, the capacitance can be linked to the charge carrier distribution. The stronger the charge carrier distribution varies over the thickness of the organic layer, the more the capacitance diverges from its low limit geometrical value. Similar to the DOS-based model used in this work, the Poisson equation is numerically solved to obtain the charge carrier distribution. As a result of the simulations, the authors find SCRs near the interfaces to the contacts. Especially the SCR at the Al interface is found to severely change and cause the observed capacitance effect. In their simulation, the SCRs get smaller, and the change of the charge carrier distribution gets steeper with increasing dopant concentration. In addition, the contact potential at the Al interface is altered with dopant concentration which reduces the potential drop and the energy level bending across the SCR. The reason for this changed contact potential is speculated to be a changed interface dipole.[17]

For the interface prepared in this work, the deposition conditions do not match the ones stated in the work of Wißdorf et al. Their Al thin films are deposited at a rate of 300 Å/min in a base pressure of smaller than $10^{-7}$ mbar.[17] In this work, the nominal deposition rate can be estimated to be around 4 Å/min or 40 Å/min in the case of the high-rate depositions. Even higher deposition rates could not be used for the interface experiments as the deposition time could have been no longer well controlled via the shutter. From the peak area evolution of the sublevel core level emissions (see Figure 6.1-1), it can be seen that an increased deposition rate might have some influence on the thin film formation. Whether the hotter atoms, which are evaporated at higher temperature to achieve the increased rate, will diffuse deeper into the organic layer or if the faster arriving atoms form more or broader growing islands cannot be told. The base pressure of $10^{-9}$ mbar or even $10^{-8}$ mbar used here is also well below the values for the reported hole-only device fabrication. A higher content of oxygen in the remaining gas of the chamber might act as surfactant for the formation of a closed thin film.[164] Still, the overall observed effects seem not to be influenced by a change of deposition rate or base pressure and the analysis of the electronic structure at the p-HTM-B | Al interface does also not reveal strong differences. Therefore, it is assumed that the results obtained here are also true for the p-HTM-B | Al interface of the hole-only devices of the literature report.

In the article, the SCR at the p-HTM-B | Al interface is predicted to play the dominant role in the capacitance effect. The interface experiment reveals a strong shift of the energy levels which confirms the existence of a SCR at the interface. Furthermore, the energy level shift is caused by the revoking of the p-doping and thus linking the SCR to the distribution of the CPTCFA molecules. Therefore, it can be assumed that the SCR gets narrower with increasing dopant concentration, i.e., increasing dopant molecule density. Potentially, the diffusion of Al atoms into the organic layer could also be influenced by the distribution of the CPTCFA molecules by the reaction between Al and CPTCFA. At lower dopant concentrations, the Al atoms could diffuse deeper into the material before getting trapped by a dopant molecule which at high dopant concentrations would occur closer to the surface. Overall, the SCRs which are observed in this work at the ITO interface tend to be narrower than the ones which are shown for the hole-only devices in the article. Still, the experiments presented here support the trend of narrower SCRs at higher dopant concentrations predicted by the simulations in the article by Wißdorf et al.[17] In contrast, no indication for a change of the contact potential at the interface caused by a dipole can be found. The observed potential drops across the SCR at the interface seem to be determined by the $E_F$ difference of p-doped HTM-B and pure Al thin films before contact. Thus, above a dopant concentration of about 2 vol%, where the energetic position of $E_F$ saturates and does not get closer to the HOMO onset, no change of the potential drop can be expected. If there is an interface dipole the results show that it is about the same for undoped and doped HTM-B (about 0.4 eV) and cannot be expected to change with dopant concentration. However, it shall be mentioned again that this potential interface dipole is more likely a measurement artifact by the inhomogeneous surface of Al islands. For the interpretation of the hole-only device simulation results, this could mean that the simulated change of the contact potential is compensating for very steep potential changes right at the interface of the narrow SCRs at high dopant concentrations which might be below the spatial resolution of the simulation grid. Furthermore, the diffusion of Al atoms into the organic layer and the non-abrupt interface might also have an influence on the capacitance which is not accounted for in the simulation.

Finally, it can be concluded that the predictions of the simulations by Wißdorf et al. can to some extend be confirmed by the results of the here presented interface experiment. Still, the experiments also highlight that the assumptions and approximations necessary for the simulation inherently cannot account for more complex less well-defined situations. In this case, it is the complex interface structure and the reaction of Al with the CPTCFA molecule. In conclusion to the results of the hole-only device impedance spectroscopy and the here analyzed interface experiments, the Al interface is found to have a strong influence on the characterization of the devices that cannot be easily modeled. This has to be carefully taken into account for further hole-only device studies which contain a similar layer structure. If the organic-Al interface dominates an observed effect in a hole-only device, the results might be not useful for a further understanding of the hole transport side of full devices as the Al contact is normally on the electron transport side. In other words, the goal of reducing the complexity by using hole-only devices might not be reached if the required auxiliary back contact introduces new effects. Further studies might investigate different back contact materials which have less influence on the device characteristics. In principle, there is no need to stick to the same back contact (or front contact) material as in the full device for a hole-only (or electron only) device as the created interface is never representative for the full device situation.

## 6.4 Conclusion

In this chapter, the (ITO/(p-)HTM-B) | Al heterointerface was studied. Interface experiments with step-by-step deposition and consecutive photoemission spectroscopy were used for characterization. The results are discussed with respect to a published article by Wißdorf et al. where hole-only devices of the same material combination were studied. Interface experiments with Al deposition on different sublayers and for different deposition conditions are analyzed. It is found that Al does not grow in a simple layer-by-layer type of growth mode on doped and undoped HTM-B. The evolution of the XPS and UPS sublayer signal with deposition time as well as measurements under different take-off angles suggest that Al diffuses into the amorphous organic layer and forms islands on the surface. In contrast, Al quickly forms a closed layer when it is deposited on a pure CPTCFA layer. Furthermore, it can be seen from the XP spectra that a reaction between Al and the CPTCFA molecules occurs where Al transfers electrons to the molecules redoping the layer to a more intrinsic value. Based on literature, the C≡N groups of CPTCFA could be the preferential reaction site for the Al atoms. This reaction would then bind the deposited Al atoms and keep them from diffusing. The analysis of the electronic structure at the interface shows that in the case of the undoped layer a SCR is formed that leads to an upwards bending of the energy levels in the organic layer towards the Al interface. For the case of the doped layer, the deposited Al quickly revokes the p-doping effect by reaction with the CPTCFA molecules or simple donation of electrons and leads to an $E_F$ shift away from the interface. The result is a SCR with a downwards bending of the energy level towards the Al interface. In both cases, the shift of the energy levels corresponds to the expected initial difference of $E_F$ in the materials before contact. The analysis of the WF evolution disagrees with the shift of the energy levels and could indicate the formation of an interface dipole. However, it is considered more likely that it is the result of the Al island formation and the therefore inhomogeneous surface where areas of low WF dominate the measurement result. Finally, the results are compared to the predictions from the published hole-only device study. The measurements of this work prove the existence of a SCR at the Al interface and agree with a decrease of the SCR width with increased dopant concentration. The results obtained here disagree with a change of the contact potential and the formation of an interface dipole. It is suggested that the interdiffusion of Al and the reaction with CPTCFA, which are not accounted for in the published model, affect the device characteristics. As a final remark it should be mentioned that the influence of the Al contact on the characteristics of hole-only devices have to be carefully evaluated and that the use of a different contact material, which forms a more abrupt surface and does not react with the dopant, might be advantageous. In future works, a combination of photoemission interface experiments and electrical characterization could be modeled by pairing the DOS-based model for the photoemission spectra from the previous chapter with the drift-diffusion-based model for the electrical characterization mentioned in the work by Wißdorf et al.[17] Potentially, the fabrication of devices which are afterwards electrically characterized should be first monitored by photoemission spectroscopy.

# 7 Low Excitation Energy Electron Emission – L4E

In this chapter, an unexpected side effect, which was observed during the experiments on the interfaces of indium tin oxide (ITO) and the undoped hole transport materials (HTMs) (see Section 5.1), is analyzed and discussed. During these interface experiments, it appeared that illumination by the ultraviolet (UV) light emitting diode (LED) – which is used to increase the conductivity and reduce charging effects (see Subsection 3.2.8) – strongly increases the intensity of the secondary electron cut-off (SEC) measured at thick HTM films. It is found that the UV-LED itself leads to emission of electrons although the excitation energy of the UV-LED is smaller than the ionization potential (IP) of the materials. While light up-conversion, where materials absorb low energy photons and emit photons of higher energy, is a well-known research field,[54–56] no description of this low excitation energy electron emission (L4E) effect where electrons are emitted could be found in literature. Among the materials from this work, the L4E effect is especially strong for m-MTDATA which is further studied here. In the following sections of this chapter, the observations will be further described, LEDs with different excitation energies will be tested, and their emission spectra will be compared to the absorption spectrum of the HTM. Furthermore, the dependency of the L4E effect on the HTM layer thickness, exposure to air, p-doping, temperature, and irradiation intensity will be analyzed. Overall, the goal is to address the origin of the L4E effect. Thus, potential mechanisms will be discussed and ideas for further experiments are given. In addition, the efficiency in terms of emitted electrons per incident photon will be estimated leading to a discussion about a potential application of the effect.

## 7.1 Dependencies of the L4E Effect in m-MTDATA

The data shown in this section were obtained together with Sun-Myung Kim within the scope of her bachelor thesis.[223] During the final deposition steps of the ITO | m-MTDATA interface experiment, it is observed that the intensity of the SEC increases with the layer thickness until the intensity exceeds the capacity of the detector of 1.6 $\cdot 10^7$ counts per second (cps). At this intensity, the measurement breaks down until the number of emitted electrons drops again below the limit, as otherwise this strong intensity would potentially damage the detector. The respective spectrum can be seen in Figure 7.1-1.

Triggered by this unexpected behavior and the question under which conditions this effect appears and what causes it, the measurement conditions are checked and varied until it is found that the high electron emission intensity is linked to the application of the UV-LED during the SEC measurements. After further testing, it is observed that the light from the UV-LED alone, i.e. without light from the X-ray source or He-discharge lamp, can be used to cause the emission of electrons which are detected as a SEC spectrum in a range of about 1.5 eV binding energy – difference SEC onset to low binding energy onsets (see Figure 7.1-2a).

A question which immediately arises is whether or not the detected electrons are primary electrons. If the detected electrons would be secondary electrons, they would have received

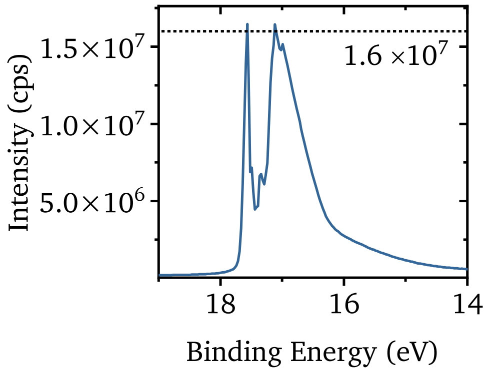

Figure 7.1-1: UP spectrum of a 28 nm thick m-MTDATA layer deposited onto ITO. A 365 nm UV-LED is used to enhance the conductivity of the layer. The measurement breaks down when the intensity exceeds the detector capacity of 1.6 $\cdot 10^7$ cps. Adapted from Sun-Myung Kim's bachelor thesis.[223]

energy from primary electrons which have the same or more energy. Then, some of these hypothetical primary electrons which have not lost any energy should be detected with higher kinetic energies, i.e., at lower binding energies. However, there is no further emission peak at lower binding energies which would mark the energy of such primary electrons. Thus, even though the measured peak is in the range where typically secondary electrons are detected, it can be assumed that the detected electrons are instead directly excited primary electrons. These electrons were probably excited into unoccupied states just above and below the vacuum level. However, only the electrons excited above the vacuum level can be transferred to the vacuum to be detected. Therefore, the same spectral cut-off shape as for the typical secondary electrons is measured. Hence, as long as there are no charging effects, the SEC onsets measured under He-I excitation alone, UV-LED excitation alone, or both excitations together are detected at the same binding energy. Even though the electrons excited by the LED are primary electrons, their spectra will be still referred to as SEC spectra due to the similar spectral shape and measurement conditions.

The effect is not only observed for the standard UV-LED with a nominal wavelength of 365 nm (3.40 eV), but also for LEDs with nominal wavelengths of 400 nm (3.10 eV) and 500 nm (2.50 eV) as shown in Figure 7.1-2a. Here, it can be seen that the intensity of the spectrum seems to scale with the excitation energy as the spectra decrease in intensity with increasing nominal wavelength of the LED, i.e., decreasing photon energy. The photon energies of the

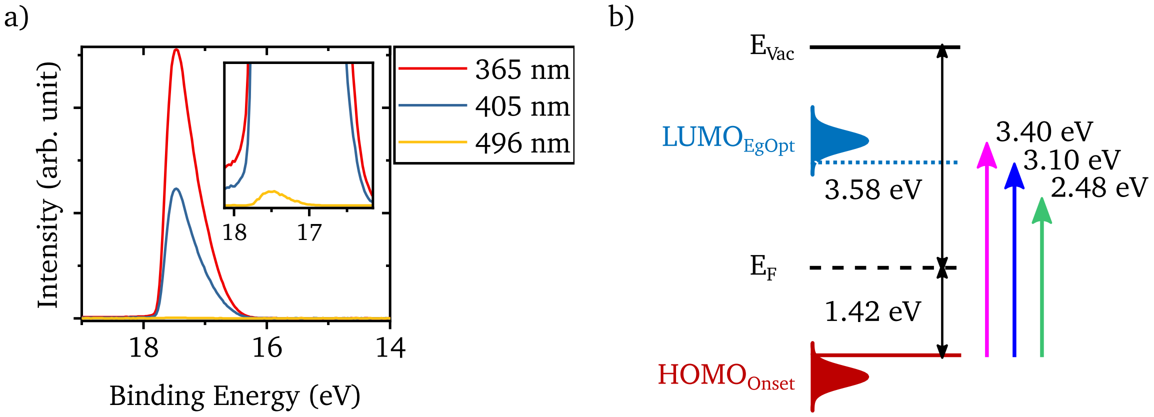

Figure 7.1-2: a) SEC spectra recorded for different UV-LED excitation energies. The inset presents a magnification of the lower intensity scale to show the weak spectrum of the 500 nm UV-LED. b) Energy level diagram of m-MTDATA including the nominal excitation energies of the three UV-LEDs used in a) drawn as pink (365 nm), blue (400 nm), and green (500 nm) arrow. Adapted from Sun-Myung Kim's bachelor thesis.[223]

LEDs are drawn in comparison to the m-MDTATA energy level diagram in Figure 7.1-2b. From the diagram it becomes clear that all excitation energies are much smaller than the IP of m-MTDATA (5 eV) and should not be able to excite an electron from the highest occupied molecular orbital (HOMO) to a state above the vacuum level. Thus, the excitation by none of the LEDs alone should lead to the emission of electrons as the electrons need to have more energy than the vacuum energy to be transferred from the sample to the vacuum (see Section 3.2).

Regardless of the excitation source, He-discharge lamp or LED, these electrons just above the vacuum energy have only very little kinetic energy, are very slow, and get easily reabsorbed or deflected. Thus, a bias of -5 V is applied to the sample to accelerate the electrons and let them reach the analyzer and detector. This bias will shift the potential of the whole sample including the vacuum level and thus does not change the energetic distance between HOMO and vacuum level. Therefore, the bias does not explain the L4E effect. Still, the bias does change the measured intensity as a higher bias accelerates the electrons more strongly and more electrons reach the analyzer and detector. Investigating the origin of this unexpected emission of electrons, the emission wavelengths of the LEDs are also analyzed. If the LEDs would emit photons of much higher energy besides their nominal wavelength, these photons could potentially provide the required energy. To check the energy of the emitted photons, the emitted spectra of the LEDs, nominal 365 nm, 400 nm, and 500 nm, are measured and plotted in Figure 7.1-3. The spectra are analyzed, and the peak intensities of the LEDs are obtained at energies of 3.36 eV for the 365 nm LED, 3.05 eV for the 400 nm LED, and 2.46 eV for the 500 nm LED. The uncertainty due to the energy step size of the data points is 0.01 eV. The full width at half maximum (FWHM) for the LEDs is 100 meV, 110 meV and 160 meV, respectively. In addition to the emission spectra, dashed lines in the graph mark the IP and WF of m-MTDATA on the energy scale. It is clear that the energy of all emitted photons for all three LEDs is much smaller than the IP of m-MTDATA. Still, it might be argued that there could be electrons in occupied gap states which tail into the energy gap up to the Fermi level ($E_F$). In this case, the electrons would not need to overcome the IP determined from the HOMO onset but the WF. However, even compared to the WF the LEDs do not provide photons with enough energy, especially in the case of the 400 nm and 500 nm LED. It has to be mentioned that the 365 nm LED shows an unexpected second smaller emission line at about 3 eV. The origin of this line is not known, but as it appears at lower energies it does not affect the analysis. Beside the emission spectra of the

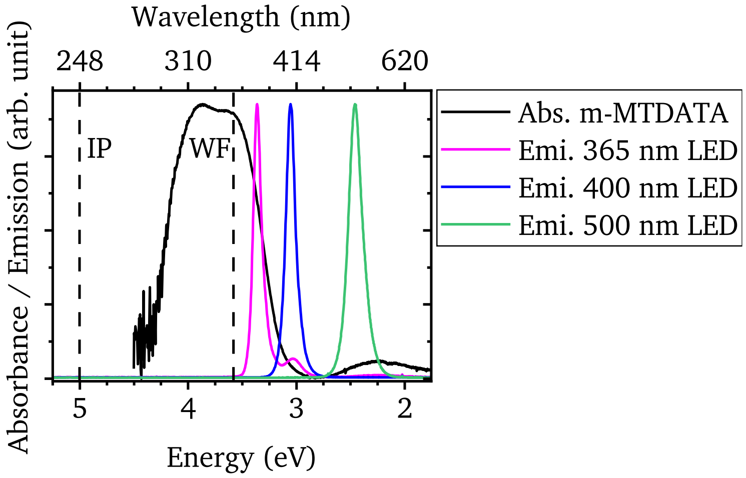

Figure 7.1-3: Normalized emission spectra of three LEDs plot together with the normalized optical absorption spectrum of m-MTDATA. The dashed lines mark the energy of the IP and WF of m-MTDATA. Adapted from Sun-Myung Kim's bachelor thesis.[223]

LEDs, the absorption spectrum of m-MTDATA is added to Figure 7.1-3. All spectra are normalized.

The graph shows that the overlap of LED emission spectrum and the m-MTDATA absorption spectrum becomes smaller with decreasing emission energy of the LEDs. In the case of the 500 nm LED, the tails of the LED emission and m-MTDATA main absorption peak touch but their overlap is in the range of the noise. The second absorption peak of m-MTDATA is likely an artifact of the simple absorption measurement setup (see Section 3.3) and is therefore not considered. This trend of increasing overlap between emission and absorption with excitation energy coincides with the increasing intensity of the respective SEC spectra. This observation is purely qualitative as the radiant flux of the LEDs is not the same. According to the data sheets of the LEDs, the radiant flux of the 400 nm LED (1800 mW) is higher than the one of the 365 nm LED (1200 mW) which means that there are more photons at 400 nm LED than at 365 nm. This should counteract the emission-absorption overlap dependency and thereby shows the strength of the overlap influence.[104] As a result of the LED emission spectra analysis, the LEDs do not emit photons with energies that are high enough to overcome either the IP or the WF of m-MTDATA. However, it is found that the overlap with the absorption spectrum seems to play a dominant role for the intensity of the L4E effect.

Next, it shall be mentioned that the L4E does not only appear for m-MDTATA thin films deposited on ITO but also for m-MDTATA thin films deposited on gold. In addition, L4E is also observed for the commercial HTM HTM-B and the known HTM N,N′-Di-[(1-naphthyl)-N,N′-diphenyl]-(1,1′-biphenyl)-4,4′-diamin (NPB).[224] As the effect is strongest in m-MTDATA, further experiments are performed using m-MTDATA as example assuming that the behavior of the other materials is similar.

The first observations during the interface experiments suggested that there is a dependence of the effect on the HTM layer thickness. To properly test the layer thickness dependency, 365 nm LED excited SEC spectra for different layer thicknesses of m-MTDATA are plotted in Figure 7.1-4a. A clear trend of increasing SEC intensity with increasing layer thickness is observed. This is remarkable as the intensity of a common photoemission process saturates when the layer thickness exceeds the information depth which depends on the effective attenuation length of the electrons.[48] Thus, the effective attenuation length of the emitted electrons is either much larger than for typical photoemission processes due to the very low kinetic energies,[48] or the effect does not stem from a normal photoemission process. Another possible influence might come from the substrate, as with increasing layer thickness also the distance to the substrate interface increases.

To check if the effect persists after the exposure of the sample to air, which would allow for further ex-situ characterization techniques, the sample was exposed to air for increasing time intervals with consecutive measurements in UHV. The results are shown in Figure 7.1-4b. It is clearly visible, that the measured SEC spectra decrease with cumulative air exposure time while also shifting to lower binding energies. The shift to lower binding energies is also observed for the HOMO onset in the valence spectra obtained from normal He-I excitation (spectra not shown). This means that $E_F$ is shifting closer to the HOMO onset resulting in an increase of the WF as it is typically observed for a p-doping effect. It is known that the exposure to oxygen can

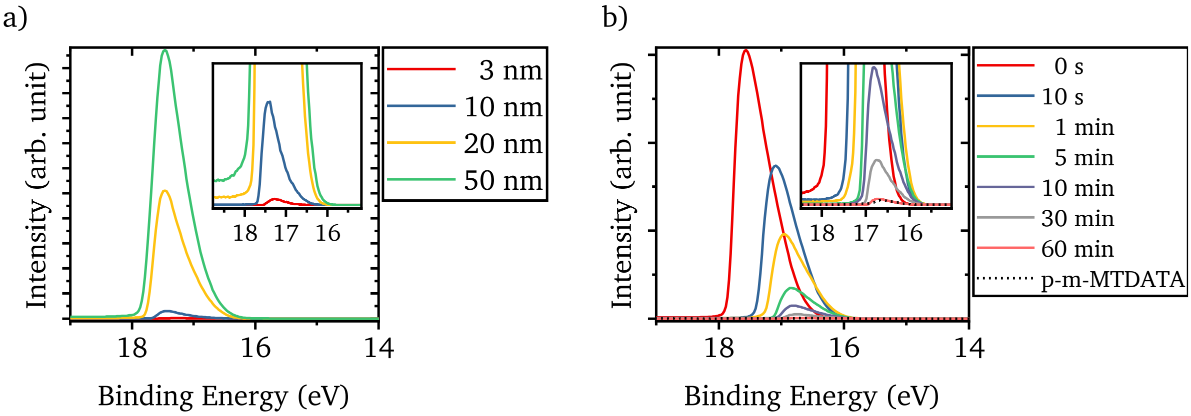

Figure 7.1-4: SEC spectra of m-MTDATA thin films excited by a 365 nm UV-LED. a) Different layer thicknesses are compared. b) The sample is exposed to air for increasing time intervals before it is again introduced into the UHV chamber for measurement. The spectrum of a p-doped sample is added for reference. The insets show magnifications of the low intensity peaks. Adapted from Sun-Myung Kim's bachelor thesis.[223]

lead to a p-doping effect in some organic semiconductor materials.[225–228] Furthermore, oxygen is known to quench excited molecular states, especially, excited triplet states (see later discussion in Section 7.2), due to its triplet ground state and its first excited singlet state only about 1 eV higher.[13] To further test if p-doping affects the L4E effect, an intentionally p-doped layer of m-MTDATA is prepared by co-evaporation of m-MTDATA with a commercial p-dopant molecule, herein called CPTCFA, (see Subsection 4.1.2). The resulting SEC spectrum from the 365 nm LED excitation is also plotted in Figure 7.1-4b. In the inset, it can be seen that the spectrum of the undoped sample after 60 min of air exposure is very similar to the spectrum of the intentionally p-doped m-MTDATA film. The spectra agree in binding energy position as well as intensity. In conclusion, p-doping by exposure to air or by co-evaporating a p-dopant molecule strongly weakens the L4E effect and thus an ex-situ characterization of the effect is not possible.

Based on the observations of the p-doped m-MTDATA films, the involvement of intermediate excited states into the excitation process was considered. The lifetime of electrons in such excited states then will play a dominant role. The lifetime might be reduced by quenching due to the p-doping of the active layer reducing the intensity of the L4E effect. For example, for organic LEDs it is known that an undoped layer is needed to separate the doped transport layer from the emission layer, as otherwise the excitons in the emission layer get quenched by the holes in the doped transport layer.[22] To further investigate excited state lifetime effects, the temperature dependence of the L4E effect was studied. Usually, the lifetime of electrons in

Figure 7.1-5: SEC spectra of a m-MTDATA thin film excited by a 365 nm UV-LED, recorded at different temperatures. The intensity clearly decreases with increasing temperature. The inset shows a magnification of the low intensity peak. Adapted from Sun-Myung Kim's bachelor thesis.[223]

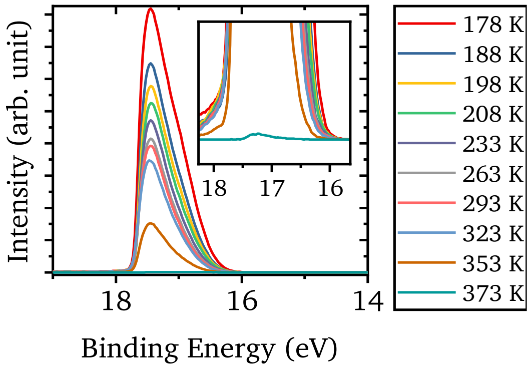

excited states is expected to increase with decreasing temperature, as higher temperatures favor thermally activated non-radiative decay.[156,229] Therefore, a 20 nm thick m-MTDATA thin film deposited on an ITO substrate was cooled down in the photoemission spectroscopy chamber. Then, heating of the sample against the cooling was used to measure the L4E effect at defined temperatures. The LED excited SEC spectra recorded between temperatures of 178 K to 373 K are shown in Figure 7.1-5. It is clearly visible that the intensity of the SEC spectra decreases with increasing temperature, supporting the idea of the dependency of the L4E effect on the excited state lifetime.

Finally, the relation between irradiation intensity and electron emission intensity is analyzed. The irradiation intensity of the 365 nm UV-LED is varied by changing the forward current driving the UV-LED. The SEC spectra recorded at different irradiation intensities are integrated to determine the area under the spectrum, i.e., the sum of the detected electrons per second. The SEC integrated intensities are plotted against the UV-LED forward current in Figure 7.1-6a. The relation between the radiant flux emitted by the UV-LED and the forward current is extracted from the data sheet provided by the manufacturer of the UV-LED. It is added to the graph as guidance to the eye (dotted black line) and scaled on the y-axis to overlap with part of the SEC area data points. Overall, the relation between radiant flux and forward current is close to linear. Therefore, the SEC area vs. forward current can be directly translated into SEC area vs. radiant flux. Unfortunately, the relation of the UV-LED radiant flux vs. forward current is not given for the low forward current regime. Thus, it can only be assumed that the trend is similar to the known behavior and also close to linear. The inset shows a zoom into the low forward current region. Here, it can be seen that the SEC area increases more than linearly with the forward current. With higher forward current, the SEC area increases more slowly, i.e., more linearly, and the data points follow the radiant flux vs. forward current relation. Finally, at a forward current above 400 mA the SEC area seems to saturate and get constant. Based on the nearly linear relation between forward current and radiant flux of the UV-LED, the SEC area vs. radiant flux can be characterized as a higher order dependence at low radiant flux, a linear

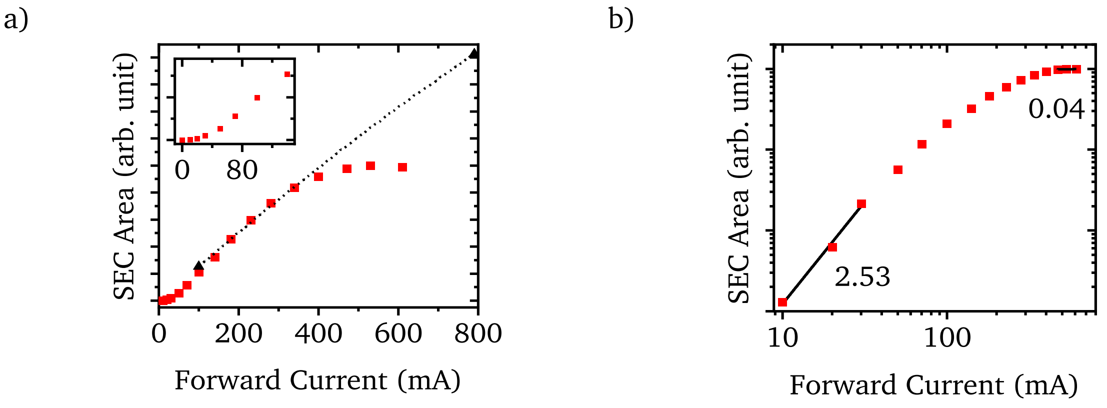

Figure 7.1-6: a) SEC integrated intensities measured at different UV-LED (365 nm) forward current, i.e., irradiation intensity. The inset presents a zoom into the region of low forward current. The dotted black line shows the radiant flux vs. forward current relation extracted from the UV-LED data sheet; it serves as guidance to the eye. The curve was scaled to overlap with the SEC area data points, where the start and end points are indicated by black triangles. b) Same SEC areas vs. forward current data as in a) but plotted on a double logarithmic scale to check for potential power-law dependencies. The black lines and values in the graph mark the slope of the curve in this representation for low and high forward currents.

dependence at medium radiant flux, and a lower order dependence or even independence at high radiant flux.

This change of the SEC area dependence on the radiant flux becomes clearer when plotting the data in a double logarithmic graph as it is done in Figure 7.1-6b. The slope of the data points in this representation is determined at low forward current (low radiant flux) and high forward current (high radiant flux). The slopes are indicated by black lines and the values of 2.53 and 0.04 are given in the graph. In a double logarithmic plot, the slope shows the power dependence in its relation. This means that the L4E effect has a more than quadratic dependence on the forward current (radiant flux) at low values and a transition to be independent from the forward current (radiant flux) at high values. In the next section, possible mechanisms for the L4E effect will be discussed. In literature, power dependencies are usually discussed in similar light excitation effects and thus will play an important role.

## 7.2 Mechanistic Discussion of the L4E effect

As explained in more detail in Subsection 3.2.5, the model behind the SEC consists of three steps. (i) Primary electrons are excited from occupied states into excited states, (ii) the excited primary electrons scatter on their transport to the sample surface with other electrons transferring energy and exciting these secondary electrons to excited states, and (iii) all electrons at the surface which are in excited states above the vacuum level can be transferred to the vacuum leaving the sample while the lower energy electrons cannot overcome the vacuum level and remain in the sample.[62,230] As mentioned before, in the case of primary and secondary electrons, some of the primary electrons will reach the surface without inelastic scattering, transfer to the vacuum, and will be detected at their characteristic kinetic energy.[48] In the case of the low excitation energy from the LED, no signal at lower binding energies from the main cut-off peak is detected. Thus, it is assumed that the detected electrons are primary electrons which are excited in states above and below the vacuum level but only the once above the vacuum level can leave the sample and get detected. As a result, the normal optical transition from HOMO to lowest unoccupied molecular orbital (LUMO) is not sufficient as the LUMO lies well below the vacuum energy (see the energy level diagram in Subsection 4.1.3). Please note, that an optical transition should be generally treated in a state picture rather than an orbital picture (see Section 2.2) and that the following discussion is simplified in this regard. Figure 7.2-1 illustrates different excitation mechanisms in a simplified scheme. In a), the two-photon excitation (2PE) is depicted. Here, an electron in an occupied HOMO state simultaneously absorbs two photons gaining the energy of both photons and getting excited into an unoccupied state above the vacuum level.[231] In b), two different two-step processes adapted from the article "Power dependence of up-conversion luminescence in lanthanide and transition-metal-ion systems" by Pollnau et al.[54] are shown. The solid black arrows mark the excitation processes while the dashed black arrows indicate the decay process which will be further discussed below.

In both cases, the first step (1) is a photon absorption excitation (PAE) where an electron gets excited from an occupied HOMO into an unoccupied LUMO state by absorption of a single photon. In the second step, two different processes are distinguished.

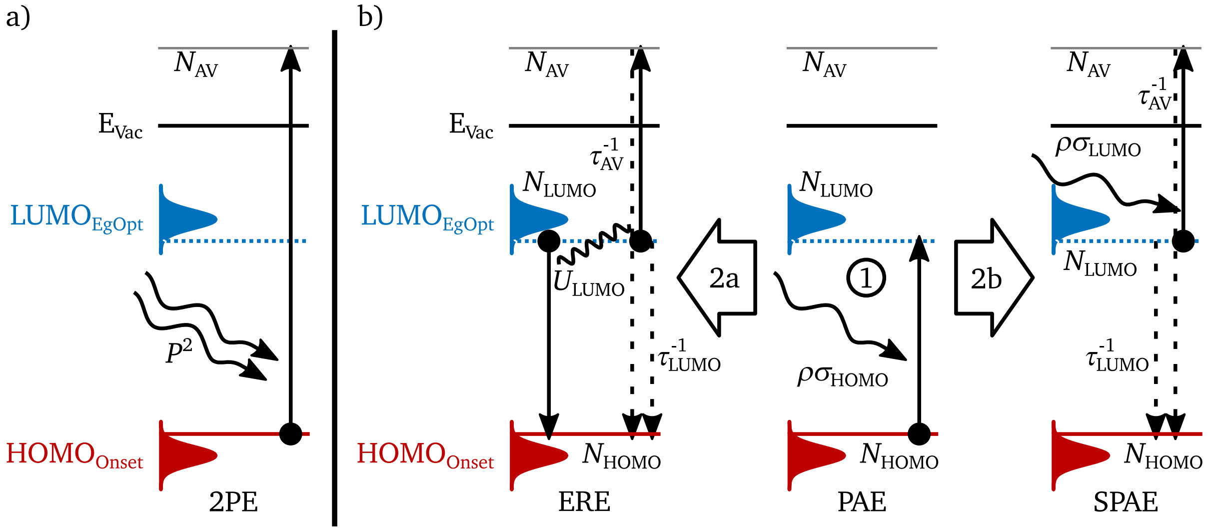

Figure 7.2-1: Illustration of different excitation processes that will lead to an electron in an excited state above the vacuum level. a) Two-photon excitation (2PE), which is a simultaneous absorption of two photons by one electron. Adapted from Pawlicki et al.[234] b) Two-step processes where first (1) a single photon absorption excitation (PAE) takes place. Here, an electron gets excited by one photon to the LUMO. This step is followed by one of two subsequent steps. Either (2a) an electron relaxation excitation (ERE) or (2b) a second photon absorption excitation (SPAE) takes place. In the ERE process, a second electron in a LUMO relaxes to the HOMO, transferring the energy to the electron in the LUMO similar to an Auger process. In the SPAE, the electron in the LUMO absorbs a second photon. Adapted from a general two excited states up-conversion schematic in "Power dependence of up-conversion luminescence in lanthanide and transition-metal-ion systems" by Pollnau et al.[54]

One possibility (2a) would be an electron relaxation excitation (ERE) where another excited electron relaxes from a LUMO into a HOMO state transferring the energy to the electron in the LUMO which gets excited into a state above the vacuum level. This process is similar to an Auger process.[48,232] The other possibility (2b) would be a second photon absorption excitation (SPAE) where the excited electron in the LUMO state absorbs another photon and thereby gets excited into a state above the vacuum level. The 2PE is a very unlikely process where the number of electrons, which got excited into a state above the vacuum level $N_{AV}$, is proportional to the square of the incident radiation power $P$, i.e., $N_{AV} \propto P^2$.[231] For the L4E effect, it can be expected that the number of detected electrons is proportional to $N_{AV}$ and thus $N_{AV}$ will be representative for the L4E effect. In addition, the radiant flux of the LED marks the emitted light power and is therefore assumed to be proportional to the incident radiation power $P$. As a result, it is expected that a 2PE process would lead to a parabolic dependency of SEC area and radiant flux in Figure 7.1-6a, i.e., a slope of 2 in the double logarithmic plot of Figure 7.1-6b. It is, however, not expected that the dependency would change with the increase of the radiant flux. Furthermore, a 2PE process seems unlikely to be the origin of the L4E effect as 2PE is typically only observed at very high radiant intensities which are provided by lasers.[231,233]

For the discussion of the two step processes ERE and SPAE, the considerations in the article by Pollnau et al.[54] will be used and their simplified model for photon up-conversion will be repeated in the following.

Beside the excitation steps of the ERE and SPAE as two step processes, there is the competing process of relaxation. The relaxation process of an electron, i.e., the transition from an excited LUMO state to a HOMO state, is defined by the lifetime $\tau$ of the excited state. The rate for the relaxation is then given as $\tau^{-1}$. In a first approximation, it is assumed that the electrons from any excited state decay to the HOMO state. Furthermore, a pump parameter $\rho$ is introduced which is proportional to the incident radiation power $P$ and, based on a Beer-Lambert type law, approximates the absorption process so that $\rho\sigma_i N_i$ is an absorption rate with the dimension of $\mathrm{s}^{-1}$ for the state $i$. Here, $N_i$ is the number of electrons in state $i$ and $\sigma_i$ is the absorption cross section for this state and the incident radiation. Finally, it is assumed that the number of electrons in the HOMO states $N_{\mathrm{HOMO}}$ is large and can be considered constant. Next, the processes of ERE and SPAE are discussed separately assuming that either one or the other process is dominating.

For the whole two step ERE process, the rate with which the number of electrons in excited LUMO states changes can be described as:

$$\frac{dN_{\mathrm{LUMO}}}{dt} = \rho\sigma_{\mathrm{HOMO}}N_{\mathrm{HOMO}} - 2U_{\mathrm{LUMO}}N_{\mathrm{LUMO}}^2 - \tau_{\mathrm{LUMO}}^{-1}N_{\mathrm{LUMO}}\,, \tag{30}$$

where $U$ is the rate parameter of the ERE process.

The equation consists of three terms. The first term describes the PAE process where an electron is added to a LUMO state. The second term represents the ERE process where one electron is removed from a LUMO state by relaxation and a second electron is further excited to a state above the vacuum level. The last term describes the decay of an electron from a LUMO to a HOMO state without transferring its energy to another electron, i.e., a radiative or a non-radiative decay process. In a similar manner, the rate with which the number of electrons in excited states above the vacuum level changes is given by:

$$\frac{dN_{\mathrm{AV}}}{dt} = U_{\mathrm{LUMO}}N_{\mathrm{LUMO}}^2 - \tau_{\mathrm{AV}}^{-1}N_{\mathrm{AV}} \tag{31}$$

Here, the first term describes the addition of an electron to an excited state above the vacuum (AV) level by the ERE process, and the second term the removal of an electron by decay from the excited state to a HOMO state. Next, it can be considered that under continuous irradiation by the LED a steady state condition is reached:

$$\frac{dN_{\mathrm{LUMO}}}{dt} = \frac{dN_{\mathrm{AV}}}{dt} = 0 \tag{32}$$

The steady state condition changes Eq. (31) to:

$$U_{\mathrm{LUMO}}N_{\mathrm{LUMO}}^2 = \tau_{\mathrm{AV}}^{-1}N_{\mathrm{AV}}\,, \tag{33}$$

which leads to the proportionality of $N_{\mathrm{LUMO}}^2 \propto N_{\mathrm{AV}}$.

Under steady state conditions, Eq. (30) yields:

$$\rho\sigma_{\mathrm{HOMO}}N_{\mathrm{HOMO}} = 2U_{\mathrm{LUMO}}N_{\mathrm{LUMO}}^2 + \tau_{\mathrm{LUMO}}^{-1}N_{\mathrm{LUMO}}\,, \tag{34}$$

which requires a case-by-case analysis.

In the first case, the relaxation process is considered to dominate the ERE process, i.e., $2U_{\mathrm{LUMO}}N_{\mathrm{LUMO}}^2 \ll \tau_{\mathrm{LUMO}}^{-1}N_{\mathrm{LUMO}}$, and the ERE term in Eq. (34) is neglected. This yields the relation of $\rho \propto N_{\mathrm{LUMO}}$. In combination with the proportionality of $N_{\mathrm{LUMO}}^2 \propto N_{\mathrm{AV}}$ the relation of $N_{\mathrm{AV}} \propto N_{\mathrm{LUMO}}^2 \propto \rho^2$ is obtained. This would mean that the L4E process has a parabolic dependence on the radiant flux.

In the second case, instead, the ERE process is considered to dominate the relaxation process, i.e., $2U_{\mathrm{LUMO}} N_{\mathrm{LUMO}}^2 \gg \tau_{\mathrm{LUMO}}^{-1} N_{\mathrm{LUMO}}$, and the relaxation term in Eq. (34) is neglected. This yields the relation of $\rho \propto N_{\mathrm{LUMO}}^2$ and thus with $N_{\mathrm{LUMO}}^2 \propto N_{\mathrm{AV}}$ the proportionality of $N_{\mathrm{AV}} \propto N_{\mathrm{LUMO}}^2 \propto \rho$ is obtained. As a result, the L4E process would have a linear dependence on the radiant flux.

For the whole two step SPAE process, similar equations and results are obtained. The rate with which the number of electrons in LUMO states changes is given by:

$$\frac{dN_{\mathrm{LUMO}}}{dt} = \rho\sigma_{\mathrm{HOMO}} N_{\mathrm{HOMO}} - \rho\sigma_{\mathrm{LUMO}} N_{\mathrm{LUMO}} - \tau_{\mathrm{LUMO}}^{-1} N_{\mathrm{LUMO}} \tag{35}$$

Here, the first term represents again the PAE process, and the last term describes the relaxation process. Unlike Eq. (30), the second term describes the SPAE process where an electron in the excited state absorbs another photon to get into an excited state above the vacuum level. The rate with which the number of electrons in these excited states above the vacuum level changes is defined by:

$$\frac{dN_{\mathrm{AV}}}{dt} = \rho\sigma_{\mathrm{LUMO}} N_{\mathrm{LUMO}} - \tau_{\mathrm{AV}}^{-1} N_{\mathrm{AV}}\,, \tag{36}$$

where the first term describes the addition of an electron by the SPAE process and the second term the removal of an electron by decay to a HOMO state.

As for the ERE process steady state conditions are assumed (see Eq. (32)). This yields for Eq. (36) the relation:

$$\rho\sigma_{\mathrm{LUMO}} N_{\mathrm{LUMO}} = \tau_{\mathrm{AV}}^{-1} N_{\mathrm{AV}}\,, \tag{37}$$

from which the proportionality of $\rho N_{\mathrm{LUMO}} \propto N_{\mathrm{AV}}$ can be obtained.

For Eq. (35), steady state conditions result in:

$$\rho\sigma_{\mathrm{HOMO}} N_{\mathrm{HOMO}} = \rho\sigma_{\mathrm{LUMO}} N_{\mathrm{LUMO}} + \tau_{\mathrm{LUMO}}^{-1} N_{\mathrm{LUMO}}\,, \tag{38}$$

which again requires a case-by-case analysis.

In the first case, the relaxation process is considered to dominate the SPAE process, i.e., $\rho\sigma_{\mathrm{LUMO}} N_{\mathrm{LUMO}} \ll \tau_{\mathrm{LUMO}}^{-1} N_{\mathrm{LUMO}}$, and the SPAE term in Eq. (38) is neglected. This yields the relation of $\rho \propto N_{\mathrm{LUMO}}$. In combination with the proportionality of $\rho N_{\mathrm{LUMO}} \propto N_{\mathrm{AV}}$ the relation of $N_{\mathrm{AV}} \propto N_{\mathrm{LUMO}}^2 \propto \rho^2$ is obtained. As for the ERE process, this would mean that the L4E process has a parabolic dependence on the radiant flux.

In the second case, instead, the SPAE process is considered to dominate the relaxation process, i.e., $\rho\sigma_{\mathrm{LUMO}} N_{\mathrm{LUMO}} \gg \tau_{\mathrm{LUMO}}^{-1} N_{\mathrm{LUMO}}$, and the relaxation term in Eq. (38) is neglected. This results in a number of electrons in excited LUMO states that is independent of $\rho$, i.e., $N_{\mathrm{LUMO}} = \mathrm{const.}$

Thus, the relation $\rho N_{\text{LUMO}} \propto N_{\text{AV}}$ changes to $N_{\text{AV}} \propto \rho N_{\text{LUMO}} \propto \rho$. As in the case of the ERE process the result is that the L4E process would have a linear dependence on the radiant flux.

This simplified model adapted from Pollnau et al.[54] shows that there are situations where a two-step process either by ERE or SPAE can lead to an irradiation power dependency that is linear instead parabolic. Furthermore, it is expected that the relaxation of the excited LUMO state is dominating at lower radiant flux where $N_{\text{LUMO}}$ is small, yielding an order of two dependence. At higher radiant flux, where $N_{\text{LUMO}}$ is larger, the ERE or SPAE process is dominating leading to an order of one dependence. Coming back to the discussion of Figure 7.1-6b where the SEC areas vs. forward current, i.e., approximately the radiant flux, is presented in a double logarithmic plot, it can be seen that the order of the L4E effect changes indeed with increasing radiant flux. At low radiant flux, the dependence is about 2.54 and then decreases steadily with increasing radiant flux to an order of 0.04 which is close to independency. These values do not exactly match the theoretical values of 2 and 1 derived from the simple model. In reality, not all of the assumptions, which were taken for the simplification of the model, might be valid and could lead to a deviation from the theoretical values. It should be kept in mind that the relation between LED forward current and LED radiant flux is not known but is extrapolated for low forward currents. If this relation is not linear, it will influence the experimentally obtained power law value of 2.54. Pollnau et al. also extend their model to mechanisms where they consider more than two excited states with multiple step excitation processes. In these scenarios, the highest order dependency is equal to the number of excitation steps involved. Furthermore, the dependency of the excitation to the highest state is taken to be 1 but the dependency of the excitation to intermediate states may also be smaller than 1.[54] This could mean that the value of 2.54 represents a process where 3 excitation steps take place and that at higher radiant flux the emitted electrons are coming from intermediate excited states which are above the vacuum level. Overall, after this analysis and the comparison to the results of the simple model, a two-step process seems likely to be the origin of the L4E effect. Such a two-step process involves an intermediate excited state that would be influenced by p-doping or the temperature as experimentally observed. If the two-step process is a ERE or SPAE process, however, is still an open question. For both processes, a long lifetime of the excited LUMO state is required to exceed the decay process and, in both cases, the simple model shows the same linear dependence at high radiant flux. To distinguish between the two processes, Pollnau et al. investigated the luminescence dependence of the intermediate states and the finally excited states.[54] Unfortunately, this is not possible in the case of the L4E effect. The L4E effect just detects the electrons which come from excited states above the vacuum level but does not provide any further information about their energy or the electrons which were excited into intermediate states below the vacuum energy.

For further experiments, it would be helpful to build up a setup that can also measure the luminescence of the sample without breaking the vacuum. As described in the previous subsection, the exposure to air strongly reduces the intensity of the effect, which does not allow to investigate the L4E effect outside the vacuum chamber.

As the number of electrons which get excited to a LUMO state is expected to be high, it was attempted to measure these electrons by He-I excitation. To avoid the ghost lines of a normal He-discharge lamp the measurements were performed at a monochromatized ultraviolet

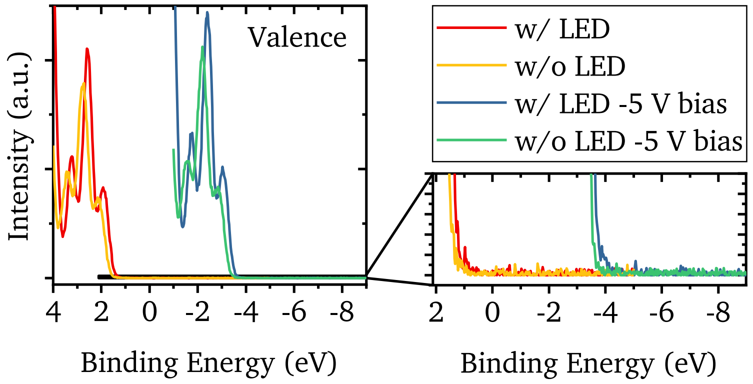

Figure 7.2-2: Valence spectra of a m-MTDATA thin film recorded at a monochromatized UPS setup with or without additional excitation by a 365 nm LED and applied bias of -5 V. The spectra with an applied bias were not corrected for the bias and are thus shifted by -5 eV binding energy. A zoom into the region above 0 eV binding energy is shown on the right.

photoelectron spectroscopy (UPS) setup at TU Darmstadt. The spectra recorded with this setup are shown in Figure 7.2-2. Spectra were taken with and without irradiation by the 365 nm LED and an applied bias of -5 V. The spectra which were recorded with applied bias are shifted by -5 eV (for visibility no correction was applied). Even though it is expected to see the signal from electrons, which are in an excited state about 3 eV above the HOMO onset, for the spectra irradiated by the LED, no difference to the measurements without the LED can be found. Thus, the existence of a significant number of electrons in an excited LUMO state cannot be confirmed. Possibly, the number of electrons is still too low to show up as a signal above the noise of the measurement.

So far, the excited LUMO state was not further defined. The LUMO state is reached by an electron from a HOMO state which absorbs a photon. For the following description, it should be kept in mind that optical transitions are usually discussed by transitions between the ground state and excited states which do not resemble single electronic configurations (see Section 2.2). However, for the excitation of free electrons a single electron description with certain electronic configurations is more practical. Therefore, the here presented excitation processes should be taken as dominating electronic configurations of a certain molecular excited state. An optical transition preserves the spin of the electron. In the occupied HOMO state, two electrons with opposite spin can occupy the same state, i.e., a singlet ground state $S_0$. As the optical transition to an excited state preserves the spin of the electron, the excited state is still a singlet state labeled $S_1$ with two electrons of opposite spin.[235,236] Now, for some organic molecules, a process called intersystem crossing (ISC) is known. This means the transition from an excited singlet state to a triplet state in which the spin of the two electrons is the same. Thus, ISC requires a spin flip. The first excited triplet state is labeled $T_1$.[56,235,236] The optical transition from the $T_1$ to $S_0$ state is forbidden which leads to a longer lifetime of the $T_1$ state compared to the $S_1$ state. As a consequence, the $T_1$ state could serve as intermediate excited state in which the electrons live long enough for a second excitation process to occur.

In the case of an SPAE process, it could be expected that the energy of the highest excited electron and thus the highest kinetic energy (low binding energy) depends on the excitation energy. An excited electron of the $T_1$ state absorbs the whole energy of a photon and thus with higher energy of the absorbed photon a higher energy of the final excited state is reached. As a result, the low binding energy onset would be different for the 365 nm LED compared to the 400 nm LED. However, this is not the case in the experiment as can be seen in Figure 7.1-2. In the case of ERE, the energy for the second excitation step would come from another electron relaxing as part of a $T_1$ state. Thus, this amount of energy depends on the energetic difference between the $T_1$ and $S_0$ state and thus is independent from the excitation energy that is used. As a result, no difference in low binding energy onsets for the 365 nm and 400 nm LEDs is expected. This is in agreement with the observations made (Figure 7.1-2) and thereby suggests an ERE instead of an SPAE process. Still, it could be that a higher excited state which is reached using the 365 nm LED is decaying so fast into an excited state of lower energy that the difference between the excitation energies cannot be measured.

Seo et al. studied m-MTDATA thin films by time-resolved photoluminescence spectroscopy and determined lifetimes of 1.3 ns for the $S_1$ state and 1.2 $\mu$s for the $T_1$ state.[156] In comparison, Goushi et al. reported a triplet state lifetime of 2.9 ns for NPB, which also shows an L4E effect but with lower intensity.[237] This lower L4E intensity could correspond to the shorter triplet state lifetime and thereby supports the involvement of the triplet state in the excitation process. In addition, Seo et al. observed delayed fluorescence for m-MTDATA which suggests that the $S_1$ state gets repopulated by a process of triplet-triplet annihilation (TTA).[13,156] This TTA process requires two triplet states where one of them decays transferring its energy to the other triplet state which then gets excited into a higher state and potentially decays right away into the $S_1$ state. As the fluorescence from this repopulated $S_1$ state depends on the lifetime of the $T_1$ state, it is delayed with respect to the fluorescence from the directly optically excited $S_1$ states.[236] For the dependence of the intensity of delayed fluorescence on the irradiation intensity there is also a quadratic dependence at low irradiation intensities and a linear dependence at high irradiation intensities.[236] The TTA process describes exactly a type of ERE process and as such could be the explanation for the L4E effect. Interestingly, Hertel et al. [238] showed that the intensity of the above mentioned delayed fluorescence originating from TTA saturation at high excitation intensities is similar to the observations in Figure 7.1-6. However, their measurements were laser-pulse-excited, time-dependent measurements which might not be fully comparable to the here studied continuous excitation. Especially, as Hertel et al. showed that there is a different decay behavior of the delayed fluorescence in different time regimes after the excitation pulse.

Seo et al. reported a $T_1$ state energy of 2.58 eV above the $S_0$ state. By the TTA process, double the amount of energy would be available for an excitation which is 5.16 eV and thus above the 5 eV IP of m-MTDATA. The difference of 0.16 eV is not enough to reach a low binding energy onset that is about 1.5 eV above the SEC onset. However, the disorder in the amorphous molecular layer that leads to the energetic broadening of the molecular state distribution might lead to $T_1$ states of higher energy, providing more energy for the excitation and ground states that are energetically closer to the vacuum level (effectively lower IP). It should be noted, again, that the comparison of single electron orbital energies and state energies is not exactly valid (see Section 2.2). Furthermore, an exciton would also first need to dissociate, overcoming the Coulomb energy, before the electron could diffuse to the surface.[13] Still, at this point, the TTA process seems to be the most likely explanation for the L4E effect, but an excitation by a second photon absorption cannot be excluded. To further clarify the mechanism behind the L4E effect, time resolved experiments seem necessary in addition.

Some experimental ideas were already created but could not be performed within this work. One idea for a time resolved measurement is based on a current measurement, e.g., to measure the sample current vs. time after switching off the LED. If the current signal persists after the LED is off, an electron relaxation process would be the valid mechanism as, e.g., the triplet-triplet-annihilation could still take place within the lifetime of the triplet states after the LED is off. This experiment requires very fast measurement of very low current. The nanoampere meter, which is used to measure the sample current, converts the signal to a voltage output, however, first tests with an oscilloscope showed a high noise level of the setup to measure the current vs. time. Therefore, the setup would need to be better shielded for this method to potentially work. Another idea would be to build up an in-situ time resolved photoluminescence spectroscopy setup which would allow to use this technique without breaking the vacuum and exposing the sample to air which would reduce the L4E effect. With time resolved photoluminescence spectroscopy different optical transitions and lifetimes could be studied to get further information. Potentially, also the irradiation intensity dependence of different luminescence process could be studied as in the work of Pollnau et al.[54] to gain information on the intermediate excited states and mechanism involved. Moreover, in highly sensitive low energy valence band spectroscopy one could try to probe the occupied excited states. Finally, a time-resolved two-photon photoelectron spectroscopy setup could be used to study the electron emission process of the intermediate excited states with time relation.

## 7.3 Photon to Electron Efficiency Estimation

The goal of this section is to estimate the efficiency of the L4E effect in terms of the ratio of emitted electrons per incident photons. Furthermore, a potential application of the L4E effect in m-MTDATA as electron source in an electron gun setup shall be discussed.

The following equation gives the ratio of emitted electrons to incident photons. The different quantity symbols are explained below.

$$\frac{\text{emitted Electrons}}{\text{incident Photons}} = \frac{{I_{\text{Sample}}}/{e}}{\frac{P_{\text{Measure}}}{E_{\text{Photon}}} \cdot \frac{\Omega_{\text{Sample}}}{\Omega_{\text{Measure}}}} \tag{39}$$

The number of emitted electrons is determined by the measurement of the sample current $I_{\text{Sample}}$. The electrons that are emitted from the sample need to be replaced during the measurement as otherwise the sample would get positively charged. This replacement current, i.e., the sample current, can be measured by a nanoampere meter that is connected between sample stage and ground. Furthermore, a 9 V battery is also connected in series to apply a bias of -9 V to the sample and enable the measurement of otherwise too slow electrons. The current drawn from the battery is small enough that the voltage can be considered constant during the measurement. The sample current divided by the elementary charge $e$ yields the number of emitted electrons per second. The current measured for a 20 nm thick m-MTDATA thin film deposited on gold, excited by the 365 nm LED at a forward current of 700 mA is 375 nA with an estimated error of $\pm 25$ nA based on the observed fluctuations.

For the number of incident photons on the sample surface, first, the radiant intensity of the LED, i.e., the radiant flux $P_{\text{Measure}}$ per solid angle $\Omega_{\text{Measure}}$, needs to be determined. Therefore, a *SM1PD1A* photo diode from *Thorlabs* is used. A radiant flux of 0.689 mW with an error of

0.059 mW is measured at a solid angle of 0.00239 sr with an error of 0.00012 sr. The error in the radiant flux is estimated from the uncertainties in reading off the diode sensitivity factor from a graph while the solid angle error originates from the uncertainties in the distance measurement. The radiant flux and solid angle lead to radiant intensity of 0.288 $Wsr^{-1}$ ± 0.029 $Wsr^{-1}$. From the radiant flux and angular displacement given in the data sheet of the LED and considering that only three of the four pixels of the LED are working (see Subsection 3.2.8) a similar value of 0.310 $Wsr^{-1}$ is calculated. The radiant intensity divided by the energy of the photons $E_{\mathrm{Photon}}$ yields the number of photons per second and steradian. The photon energy is taken from Section 7.1 with a value of 3.36 eV ± 0.05 eV. Finally, the solid angle of the sample in the measurement setup $\Omega_{\mathrm{Sample}}$ is estimated to be 0.00785 sr with an error of 0.00314 sr. The error stems from the distance estimation.

Using all these values and Eq. (39) to calculate the emitted electron to incident photon ratio an efficiency of 0.06% ± 0.02% is obtained. The incident photons were chosen as reference rather than the driving current or power consumption of the LED, because only a fraction of the emitted light hits the sample which for an application could be easily corrected with proper optics. For comparison, the $LaB_6$ electron source used for the X-ray generation in the X-ray photoelectron spectrometer *VersaProbe 5000* by *Physical Electronic* is heated with a current of about 1.5 A to generate an emission current of 4 mA.[75] This yields an emission to heating current ratio of 0.27%. Furthermore, emission current densities for conventional electron sources used in electron microscopes are reported to range from $10^4$ $Am^{-2}$ for thermionic tungsten emitters to $10^9$ $Am^{-2}$ for field emitters. In this field, not only the absolute current but also the electron-optical brightness is important which depends on the emitting area and thus current density.[239] For the L4E effect studied here, the sample current of 375 nA and the sample area of about 5 $cm^2$ lead to a current density of only $8 \times 10^{-4}$ $Am^{-2}$. However, it should be kept in mind that the measured m-MTDATA thin film sample and the use of a simple LED is not optimized to harvest the L4E effect. In terms of absolute current, the difference to the conventional sources is minimal, as the products of current densities and effective emission areas of conventional electron sources yield currents of about 100 nA to 10 $\mu$A.[239] Potentially, well designed and optimized setups, which might use more bulk-like samples or even small organic crystals could lead to more compatible current densities. In addition, a better understanding of the effect might lead to a targeted organic material selection or even a tailored design of new molecules. Also, the use of a laser instead of a simple LED is likely to improve the performance and could reduce the emission area. The use of a pulsed laser or LED could also enable the application as pulsed electron source for ultrafast electron microscopy.[240] However, the life time of the $T_1$ state which seems to be responsible for the L4E effect might be a limiting factor for the pulse time. Further studies will have to investigate if the L4E effect in organic materials can be successfully used for an electron source or some other application.

## 7.4 Conclusion

In this chapter, the low excitation energy electron emission (L4E) effect was investigated. During interface experiments it was observed that the irradiation with an UV-LED led to the emission of electrons even though the excitation energy of the LED should have been insufficiently low. Later, it was confirmed that the light of LEDs with excitation energies of about 3.36, 3.05, and 2.46 eV causes the emission of electrons from a 20 nm thick m-MTDATA layer with an IP of 5.00 eV and a WF of 3.58 eV. The intensity of the electron emission scaled with the excitation energy of the LEDs. The comparison of the LED emission spectra with the m-MTDATA absorption spectrum showed that the intensity of the L4E effect correlates with the overlap of emission and absorption spectra. Furthermore, it was found that the L4E effect increases with greater layer thickness or lower temperature. The p-doping of the m-MTDATA layer led to a strong decrease of the effect. Unfortunately, it was also observed that the contact to air caused a strong reduction of the L4E intensity which does not allow for an ex-situ characterization. The contact to air seem to p-dope the material, presumably due to the influence of oxygen as it was already reported before for organic semiconductors.[225–228] The effect occurred for the deposition of m-MTDATA on ITO or gold substrates and was also observed for HTMs NPB and HTM-B.

The qualitative analysis of the dependence of the achieved L4E intensity on the irradiation intensity showed different behaviors in different irradiation intensity regimes. At low irradiation intensity the dependency follows a power law with a value of 2.5. In the medium range of the irradiation intensity, the behavior was about linear and at high irradiation intensity the L4E intensity saturated. This analysis then led to a discussion of possible mechanism of the L4E effect. The suggested mechanism involves the excitation of electrons into an excited state above the vacuum level for the electrons to be able to leave the sample. A simultaneous two-photon absorption was discarded, as the dependency should be of the order of 2 and is not expected to change with increasing irradiation intensity. Furthermore, this effect is typically only observed at very high radiation intensities obtained using lasers. Thus, a consecutive two-step excitation process was considered to be more likely. Here, a photon gets absorbed first, leading to the excitation of an electron into an intermediate excited state and then two following processes were distinguished: the absorption of a second photon by an electron from the intermediately excited state, or the relaxation of one electron from the intermediately excited state by transferring its energy to another excited electron which thereby gets excited into a state above the vacuum level equivalent to an Auger process. The adaptation of a simple model from Pollnau et al.[54] showed that such two-step processes can change their power law dependency order with increasing irradiation intensity as it was observed for the L4E effect. In addition, the lifetime of the intermediate excited state must be long which agrees to the observations regarding temperature and p-doping. A lower temperature is expected to increase the lifetime leading to a higher L4E intensity while the p-doping is expected to lead to a quenching of the excited state reducing the L4E intensity. Which of the two two-step processes is responsible for the L4E effect could not be clarified definitively, but the Auger-like effect of electron relaxation excitation seems more likely, as it fits to the excitation independent low binding energy onset of the L4E emission peak. The effect of triplet-triplet-annihilation was also reported before for m-MTDATA.[156] The triplet-triplet-annihilation involves two excited states of which one relaxes while the other gets further excited. To further clarify the mechanism behind the L4E effect, time resolved experiments would be necessary. Some ideas for an adaptation of electric measurement, the application of in-situ time resolved photoluminescence, or two-photon photoelectron spectroscopy were presented.

Beside further experiments to further investigate the involved mechanism of the L4E effect, tests for potential applications should be performed. Here, it was discussed that the effect could be used for a time- and energy-controlled electron source. The advantage would be that the material does not need to be heated as in the case of conventional thermionic emitters like tungsten or $LaB_6$. So far, the measured current densities are too small to compete, but some future optimization work should allow to reach competitive conditions with higher intensities and reduced emission area. As the effect is light induced, the effect might, e.g., be used to generate electron pulses by using a pulsed light source as it is done in electron sources for ultrafast electron microscopy.

# 8 Summary

The field of organic semiconductors (OSCs) spans a broad range of applications from organic field effect transistors and organic photovoltaics to organic light emitting diodes (OLEDs). The presented work in this dissertation is related to OSC materials for OLED applications investigated together with the project partner Merck KGaA. The overall framework for this work was driven by the goal to understand all effects and mechanisms which are involved ranging from the molecular properties to the final device characteristics. One often stated advantage of OSCs is the chemical flexibility to easily synthesize new molecules. Thus, a deeper understanding of the connection between molecular structure and device characteristics could lead to faster material screening and development. As all semiconductor devices include several functional layers, one important contribution to the device characteristics are the interface properties. The main contribution of the here presented work is related to the analysis and discussion of the properties of hole transport materials (HTMs) and especially their electronic interface properties. Two different HTMs were examined as pure thin films as well as p-doped HTM layers by a combination of experimental and modeling methods.

The presentation of the results is divided into four Chapters (4-7). It starts with the general characterization of the used materials as thin films (Chapter 4). In this chapter, also the p-doping of the investigated hole transport materials (HTMs) was studied. On this basis, the electronic structure at hetero- and homointerfaces of the doped and undoped HTMs was analyzed in the following Chapter 5. Here, a new model-based fitting used for investigating the contact of hetero- and homointerfaces by photoelectron spectroscopy is introduced. This model combines different approaches from literature and, for the first time, generates complete sets of spectra for different emission regions which can be fit with one set of parameters to the experimental data. Chapter 6 deals with the interface at the Al back contact in hole-only devices. Finally, the Chapter 7 exploits a curious low excitation energy electron emission for which no reports in literature could be found. In the following paragraphs, the conclusions of each chapter will be summarized. For a more detailed summary, please refer to the individual conclusions at the end of each chapter.

In Chapter 4, at first, thin films of the pure materials relevant for this work were characterized using photoelectron spectroscopy (PES), ultraviolet-visible-near-infrared (UV-vis-NIR) absorption spectroscopy and infrared reflection absorption (IRA) spectroscopy, here after, the p-doping of the used hole transport materials was investigated. Density functional theory (DFT) calculations were used to assist the interpretation of the experimental data. Indium tin oxide (ITO) substrates, a commercially available p-dopant, CPTCFA, a literature-known HTM, m-MTDATA, a commercial HTM from Merck KGaA, HTM-B, and aluminum are characterized as thin films. The main focus of the characterization of the pure materials is related to the electronic structure which is summarized in energy level diagrams in Figure 4.1-25. In the second part of Chapter 4, the p-doping of the HTMs is addressed. It is found that the dopant distribution in the host matrix is homogeneous and stable against diffusion. Furthermore, the p-doping lowers the energetic position of the Fermi level towards the HOMO onset of the HTM and introduces a broadening of the density of states. Finally, the doping mechanism in m-MTDATA and HTM-B is discussed; mainly on the basis of UV-vis-NIR absorption and IRA spectroscopy data. For m-MTDATA the p-doping seems to follow the integer charge transfer model, while for HTM-B the formation of a charge transfer complex seems more likely.

In Chapter 5, a new DOS-based modeling approach for the analysis of PES interface experiments is introduced. These interface experiments were performed with the two different HTMs, m-MTDATA and HTM-B, using step-by-step deposition and consecutive PES to study the interface formation with emphasis on the electronic structure. ITO | (p-)HTM heterointerfaces were used as a test case. First, these heterointerfaces were analyzed by classical methods to lay the benchmark for the new approach. The classical analysis of the interface experiments reveals a typical semiconductor physics textbook behavior. During interface formation, a charge transfer between ITO and organic semiconductor occurs which leads to the formation of a space charge region (SCR) in the semiconductor. This behavior is well reproduced by the novel model-based fitting approach. This DOS-based modeling approach combines different ideas from literature in a new way and, for the first time, generates spectra for different emission regions that can directly be fitted to the measured ones. Here, a calculated distribution of the electrical potential, which is mainly influenced by a model of the organic semiconductor's DOS, is considered. Further, the variation of the layer-depth-dependent signal intensity in convolution with the electrical potential distribution is taken into account. The model demonstrated to deliver the same results as by a classical analysis of the data. But, in addition, the model allows for a detailed discussion of the electronic states introduced by the dopant or potentially present in the energy gap of the organic semiconductor. The DOS-based model also delivers a more accurate description of the electrical potential distribution of the SCR than the often-used Schottky model.

Next, the successful test of the DOS-based model allowed the analysis of (ITO/p-HTM) | HTM homointerfaces. These homointerfaces are difficult to analyze as the spectral sublayer and adlayer signals are dominated by the same spectral features which makes them impossible to distinguish. Here, the model proves to be crucial as it provides the physical basis to deduce the observed spectral shifts. It is found that an unexpected SCR appears in the p-doped layer. Typically, this should not be the case as its charge carrier density should be much higher compared to the undoped adlayer. After the DOS-based model was further advanced to allow for a different DOS right at the interface and further from the interface, it could be shown that an increased density of gap states in the undoped layer right at the interface is able to create a sufficient charge transfer into the doped layer and thus cause the formation of a SCR in the doped layer. The origin of these gap states remains unclear. However, similar effects have already been reported in literature for organic-organic heterointerfaces and newly formed gap states often seem to play a significant role in the energy alignment. Still, it is surprising to find that even at homointerfaces – where only a few percent of dopant molecules are sufficient to adjust the contact potential difference – such effects seem to occur.

In Chapter 6, the (ITO/(p-)HTM-B) | Al heterointerface was investigated in PES interface experiments. The results are discussed with respect to a published article by Wißdorf et al. where hole-only devices of the same material combination were studied. From the interface experiments, it is found that Al does not deposit in a simple layer-by-layer type of growth mode on doped and undoped HTM-B. Al seems to partially diffuse into the amorphous organic layer and form islands on the surface. The analysis of the electronic structure at the interface shows that in the case of the undoped layer a SCR is formed that leads to an upwards bending of the energy levels in the organic layer towards the Al interface. For the case of the doped layer, the deposited Al quickly revokes the p-doping effect by reaction with the CPTCFA molecules or simple donation of electrons, leading to an upward $E_F$ shift. Regarding the work by Wißdorf et al., the electric measurements performed in this work prove the existence of a SCR at the Al interface and agree with a decrease of the SCR width with increased dopant concentration. The results obtained here disagree with the proposed change of the contact potential and the formation of an interface dipole. It is suggested that the interdiffusion of Al and the reaction with CPTCFA, which are not accounted for in the published paper, instead affect the device characteristics. As a final remark, it be emphasized that the influence of the Al contact on the characteristics of hole-only devices has to be carefully evaluated and that the use of a different contact material which forms a more abrupt surface and does not react with the dopant might be advantageous.

In Chapter 7, a low excitation energy electron emission (called L4E) effect was investigated. It is found that the light from an LED with an excitation energy around 3 eV can lead to the emission of electrons from a m-MTDATA thin film with an ionization potential of 5 eV. A description of this effect could not be found in literature. A set of experiments showed that the intensity of the effect increases with the overlap of LED emission and m-MTDATA absorption spectrum. The effect decreases with p-doping and contact to air. Furthermore, it increases at lower temperatures and for thicker layers. The analysis of the irradiation intensity dependence leads to a discussion of the mechanism which most likely is based on a two-step excitation process. Here, a photon gets absorbed leading to the excitation of an electron into an intermediate excited state and then two possible subsequent processes are distinguished: the absorption of a second photon by an electron in such an intermediate excited state, or the relaxation of one electron from an intermediate excited state transferring its energy to another electron in an intermediate excited state which thereby gets excited into a state above the vacuum level. For such processes, long excited state lifetimes are required which suggests that a triplet state is involved. A triplet-triplet-annihilation involved as second excitation process is considered as the most likely one, but further experiments are required. Ideas for such experiments and potential applications of the L4E effect are discussed and will be summarized in the following outlook.

In conclusion, this work demonstrates the strength which lies in the interplay between experiment and theory. It shows how simple DFT calculations can assist in the interpretation of experimental data, and how the attempt to model PES experiments can result in an in-depth discussion of the underlying physics. At the same time, the presented approach suggests the importance of experimental verification. In the case of the Al back contact interface, the experiments reveal a more complicated picture regarding the layer growth and the interaction of the involved materials as originally assumed in an idealized model. In the case of homointerfaces of organic semiconductors, the novel DOS-based model of interface formation allows the precise analysis of the data in the first place, but the obtained results require the further advancement of the model which leads to new open but severe characterization needs for further research.

# 9 Outlook

In conclusion of this PhD work there are some open questions remaining which shall be summarized here, to inspire further investigations.

From the analysis of the doping mechanism in m-MTDAT and HTM-B, it is found that m-MTDATA seems to follow the integer charge transfer model. However, it is not clear why the energetic position of the Fermi level saturates above the HOMO onset even though the electronic structure of the CPTCFA molecule suggests further charge transfer. For HTM-B, the formation of a charge transfer complex seems plausible but no clear experimental evidence, e.g., from related spectral absorption features of the complex states, could be found. Further experiments using inverse PES may provide a proof of these new acceptor states in the CPTCFA:HTM-B system.

The DOS-based model fitting of the PES interface experiments, have been shown to be quite successful, but several restrictions and assumptions in the model leave room for improvement. But, it should be kept in mind that a more complex model with more fitting parameters might also require larger data sets to avoid overfitting. Here, different emission regions or data from parameter variation experiments, e.g., different dopant concentrations might be combined to one large data set, which is fitted in one automated procedure, to further improve the reached consistency.

In addition, the results from the model-based analysis suggest an increased density of tail states at homointerfaces of organic semiconductors. The discussion with respect to reports in literature show that similar effects, e.g., induced density of interface states (IDIS) or disorder related density of gap states (DOGS), have repeatedly been used to explain deviating electronic structures at interfaces of organic semiconductors without clear experimental evidence. It is suggested that further studies to investigate these predicted interface states by a systematic variation of molecules that form amorphous and also crystalline layers are needed. Sophisticated experimental setups, which are able to reveal low densities of states in the energy gap, must be developed to detect this interfacial density of states.

As another way to continue this work, a combination of photoemission interface experiments and electrical characterization could attempted to be modeled by pairing the DOS-based model for the analysis of photoemission spectra from Chapter 5 with the drift-diffusion-based model for the electrical characterization mentioned in the work by Wißdorf et al..[17] Potentially, the fabrication of devices which are afterwards electrically characterized could be first monitored by photoemission spectroscopy. Here, different, interface forming more ideal back contacts using other materials could be tested.

To further clarify the mechanism leading to the L4E effect, time resolved experiments are necessary. Here, electric measurements of the sample current, the application of an in-situ time resolved photoluminescence setup, or two-photon photoelectron spectroscopy should be considered.

Beside further experiments to investigate the valid mechanism of the L4E effect, tests for potential applications could be considered. The effect could, e.g., be used for a flexible electron source. The advantage would be that the material does not require heating as in the case of conventional thermionic emitters, like tungsten or $LaB_6$. So far, the measured current densities are too small to compete, but some future work is suggested to optimize the conditions to obtain higher intensities while reducing the emission area. As the effect is light induced, the effect might be used to generate electron pulses by using a pulsed light source as it is done in electron sources for ultrafast electron microscopy.

## References

(1) Pope, M.; Kallmann, H. P.; Magnante, P., Electroluminescence in organic crystals. *The Journal of Chemical Physics* **1963**, *38* (8), 2042–2043. DOI: 10.1063/1.1733929.

(2) Helfrich, W. and Schneider, W. G., Recombination radiation in anthracene crystals. *Phys. Rev. Lett.* **1965**, *14* (7), 229–231. DOI: 10.1103/physrevlett.14.229.

(3) Helfrich, W. and Schneider, W. G., Transients of volume-controlled current and of recombination radiation in anthracene. *The Journal of Chemical Physics* **1966**, *44* (8), 2902–2909. DOI: 10.1063/1.1727152.

(4) Tang, C. W. and VanSlyke, S. A., Organic electroluminescent diodes. *Appl. Phys. Lett.* **1987**, *51* (12), 913–915. DOI: 10.1063/1.98799.

(5) Shirakawa, H.; Louis, E. J.; MacDiarmid, A. G.; Chiang, C. K.; Heeger, A. J., Synthesis of electrically conducting organic polymers: halogen derivatives of polyacetylene, $(CH)_x$. *J. Chem. Soc., Chem. Commun.* **1977**, *0* (16), 578. DOI: 10.1039/C39770000578.

(6) Shirakawa, H.; McDiarmid, A.; Heeger, A., Focus article: Twenty-five years of conducting polymers. *Chem. Commun.* **2003**, *0* (1), 1–4. DOI: 10.1039/B210718J.

(7) Distler, A.; Brabec, C. J.; Egelhaaf, H.-J., Organic photovoltaic modules with new world record efficiencies. *Prog Photovolt Res Appl* **2021**, *29* (1), 24–31. DOI: 10.1002/pip.3336.

(8) Yuvaraja, S.; Nawaz, A.; Liu, Q.; Dubal, D. *et al.*, Organic field-effect transistor-based flexible sensors. *Chem. Soc. Rev.* **2020**, *49* (11), 3423–3460. DOI: 10.1039/c9cs00811j.

(9) Chen, H.-W.; Lee, J.-H.; Lin, B.-Y.; Chen, S.; Wu, S.-T., Liquid crystal display and organic light-emitting diode display: present status and future perspectives. *Light Sci Appl* **2018**, *7* (3), 17168. DOI: 10.1038/lsa.2017.168.

(10) Yao, L.; Rahmanudin, A.; Guijarro, N.; Sivula, K., Organic semiconductor based devices for solar water splitting. *Adv. Energy Mater.* **2018**, *8* (32), 1802585. DOI: 10.1002/aenm.201802585.

(11) Chorsi, M. T.; Curry, E. J.; Chorsi, H. T.; Das, R. *et al.*, Piezoelectric biomaterials for sensors and actuators. *Adv. Mater.* **2019**, *31* (1), e1802084. DOI: 10.1002/adma.201802084.

(12) Russ, B.; Glaudell, A.; Urban, J. J.; Chabinyc, M. L.; Segalman, R. A., Organic thermoelectric materials for energy harvesting and temperature control. *Nat Rev Mater* **2016**, *1* (10). DOI: 10.1038/natrevmats.2016.50.

(13) Köhler, A. and Bässler, H. *Electronic processes in organic semiconductors: An introduction*; Wiley-VCH Verlag GmbH & Co, 2015.

(14) Kühn, M.; Pflumm, C.; Jaegermann, W.; Mankel, E., Detailed evaluation of in-operando potentials in OLED devices: A combined experimental and drift-diffusion study. *Organic Electronics* **2016**, *37*, 336–345. DOI: 10.1016/j.orgel.2016.07.006.

(15) Kühn, M.; Pflumm, C.; Glaser, T.; Harbach, P. *et al.*, Band alignment in organic light emitting diodes - On the track of thickness dependent onset voltage shifts. *Organic Electronics* **2017**, *41*, 79–90. DOI: 10.1016/j.orgel.2016.11.018.

(16) Shirota, Y.; Kobata, T.; Noma, N., Starburst molecules for amorphous molecular materials. 4,4′,4″-Tris(N ,N-diphenylamino)triphenylamine and 4,4′,4″-Tris[N-(3-methylphenyl)-N-phenylamino]triphenylamine. *Chem. Lett.* **1989**, *18* (7), 1145–1148. DOI: 10.1246/cl.1989.1145.

(17) Wißdorf, V.; Frericks, M.; Tzschoppe, M.; Connor, P. *et al.*, Impedance spectra analysis of p-doped organic thin films by charge carrier distribution evaluation. *ACS Appl. Electron. Mater.* **2019**, *1*, 1994–2006. DOI: 10.1021/acsaelm.9b00279.

(18) Braun, S.; Jong, M. P. de; Osikowicz, W.; Salaneck, W. R., Influence of the electrode work function on the energy level alignment at organic-organic interfaces. *Appl. Phys. Lett.* **2007**, *91*, 202108. DOI: 10.1063/1.2806938.

(19) Zhang, T.; Brumboiu, I. E.; Lanzilotto, V.; Grazioli, C. *et al.*, Electronic structure modifications induced by increased molecular complexity: from triphenylamine to m-MTDATA. *Physical chemistry chemical physics : PCCP* **2019**, *21* (32), 17959–17970. DOI: 10.1039/c9cp02423a.

(20) Zhang, T.; Chu, B.; Li, W.; Su, Z. *et al.*, Efficient triplet application in exciplex delayed-fluorescence OLEDs using a reverse intersystem crossing mechanism based on a ΔES-T of around zero. *ACS applied materials & interfaces* **2014**, *6* (15), 11907–11914. DOI: 10.1021/am501164s.

(21) Gao, W. and Kahn, A., Electronic structure and current injection in zinc phthalocyanine doped with tetrafluorotetracyanoquinodimethane: Interface versus bulk effects. *Organic Electronics* **2002**, *3*, 53–63. DOI: 10.1016/S1566-1199(02)00033-2.

(22) Matsushima, T. and Adachi, C., Extremely low voltage organic light-emitting diodes with p-doped α-sexithiophene hole transport and n-doped phenyldipyrenylphosphine oxide electron transport layers. *Appl. Phys. Lett.* **2006**, *89*, 253506. DOI: 10.1063/1.2410236.

(23) Lüssem, B.; Riede, M.; Leo, K., Doping of organic semiconductors. *Phys. Status Solidi A* **2013**, *210* (1), 9–43. DOI: 10.1002/pssa.201228310.

(24) Pfeiffer, M.; Leo, K.; Zhou, X.; Huang, J. *et al.*, Doped organic semiconductors: Physics and application in light emitting diodes. *Organic Electronics* **2003**, *4*, 89–103. DOI: 10.1016/j.orgel.2003.08.004.

(25) Walzer, K.; Maennig, B.; Pfeiffer, M.; Leo, K., Highly efficient organic devices based on electrically doped transport layers. *Chem. Rev. (Chemical reviews)* **2007**, *107*, 1233–1271. DOI: 10.1021/cr050156n.

(26) Ante, F.; Kälblein, D.; Zschieschang, U.; Canzler, T. W. *et al.*, Contact doping and ultrathin gate dielectrics for nanoscale organic thin-film transistors. *Small (Weinheim an der Bergstrasse, Germany)* **2011**, *7* (9), 1186–1191. DOI: 10.1002/smll.201002254.

(27) Méndez, H.; Heimel, G.; Winkler, S.; Frisch, J. *et al.*, Charge-transfer crystallites as molecular electrical dopants. *Nature communications* **2015**, *6*, 8560. DOI: 10.1038/ncomms9560.

(28) Salzmann, I. and Heimel, G., Toward a comprehensive understanding of molecular doping organic semiconductors (review). *Journal of Electron Spectroscopy and Related Phenomena* **2015**, *204*, 208–222. DOI: 10.1016/j.elspec.2015.05.001.

(29) Koch, N., Organic electronic devices and their functional interfaces. *ChemPhysChem* **2007**, *8*, 1438–1455. DOI: 10.1002/cphc.200700177.

(30) Gao, W. and Kahn, A., Effect of electrical doping on molecular level alignment at organic–organic heterojunctions. *Appl. Phys. Lett.* **2003**, *82* (26), 4815–4817. DOI: 10.1063/1.1585123.

(31) Zhao, W. and Kahn, A., Charge transfer at n-doped organic-organic heterojunctions. *J. Appl. Phys. (Journal of Applied Physics)* **2009**, *105*, 123711. DOI: 10.1063/1.3153962.

(32) Kahn, A.; Zhao, W.; Gao, W.; Vázquez, H.; Flores, F., Doping-induced realignment of molecular levels at organic–organic heterojunctions. *Chemical Physics* **2006**, *325*, 129–137. DOI: 10.1016/j.chemphys.2005.09.015.

(33) Tang, J. X.; Lau, K. M.; Lee, C. S.; Lee, S. T., Substrate effects on the electronic properties of an organic/organic heterojunction. *Appl. Phys. Lett.* **2006**, *88*, 232103. DOI: 10.1063/1.2209212.

(34) Opitz, A.; Wilke, A.; Amsalem, P.; Oehzelt, M. *et al.*, Organic heterojunctions: Contact-induced molecular reorientation, interface states, and charge re-distribution. *Scientific reports* **2016**, *6*, 21291. DOI: 10.1038/srep21291.

(35) Braun, S.; Salaneck, W. R.; Fahlman, M., Energy-level alignment at organic/metal and organic/organic interfaces. *Adv. Mater.* **2009**, *21*, 1450–1472. DOI: 10.1002/adma.200802893.

(36) Gao, W. and Kahn, A., Electrical doping: the impact on interfaces of π-conjugated molecular films. *J. Phys.: Condens. Matter* **2003**, *15*, S2757-S2770. DOI: 10.1088/0953-8984/15/38/014.

(37) Greiner, M. T.; Helander, M. G.; Tang, W.-M.; Wang, Z.-B. *et al.*, Universal energy-level alignment of molecules on metal oxides. *Nature materials* **2012**, *11*, 76–81. DOI: 10.1038/nmat3159.

(38) Kahn, A.; Koch, N.; Gao, W., Electronic structure and electrical properties of interfaces between metals and π-conjugated molecular films. *J. Polym. Sci. B Polym. Phys.* **2003**, *41*, 2529–2548. DOI: 10.1002/polb.10642.

(39) Chen, B.; Zuo, L.; Li, A.; Sheng, R. *et al.*, High-efficiency orange and white phosphorescent organic light-emitting diodes based on homojunction structure. *Organic Electronics* **2017**, *44*, 183–188. DOI: 10.1016/j.orgel.2017.02.019.

(40) Cai, C.; Su, S.-J.; Chiba, T.; Sasabe, H. *et al.*, High-efficiency red, green and blue phosphorescent homojunction organic light-emitting diodes based on bipolar host materials. *Organic Electronics* **2011**, *12* (5), 843–850. DOI: 10.1016/j.orgel.2011.01.021.

(41) Hamwi, S.; Riedl, T.; Kowalsky, W., An organic p-i-n homojunction as ultra violet light emitting diode and visible-blind photodiode in one. *Appl. Phys. Lett.* **2011**, *99* (5), 53301. DOI: 10.1063/1.3617427.

(42) Harada, K.; Riede, M.; Leo, K.; Hild, O. R.; Elliott, C. M., Pentacene homojunctions: Electron and hole transport properties and related photovoltaic responses. *Phys. Rev. B* **2008**, *77* (19), 435. DOI: 10.1103/PhysRevB.77.195212.

(43) Kao, P.-C. and Chiu, C.-T., $MoO_3$ as p-type dopant for Alq3-based p–i–n homojunction organic light-emitting diodes. *Organic Electronics* **2015**, *26*, 443–450. DOI: 10.1016/j.orgel.2015.08.018.

(44) Ohashi, N.; Yoshikawa, H.; Yamashita, Y.; Ueda, S. *et al.*, Determination of Schottky barrier profile at Pt/$SrTiO_3$: Nb junction by x-ray photoemission. *Appl. Phys. Lett.* **2012**, *101*, 251911. DOI: 10.1063/1.4772628.

(45) Oehzelt, M.; Koch, N.; Heimel, G., Organic semiconductor density of states controls the energy level alignment at electrode interfaces. *Nature communications* **2014**, *5*, 4174. DOI: 10.1038/ncomms5174.

(46) Salzmann, I.; Heimel, G.; Oehzelt, M.; Winkler, S.; Koch, N., Molecular electrical doping of organic semiconductors: Fundamental mechanisms and emerging dopant design rules. *Acc. Chem. Res. (Accounts of chemical research)* **2016**, *49*, 370–378. DOI: 10.1021/acs.accounts.5b00438.

(47) Yang, J.-P.; Bussolotti, F.; Kera, S.; Ueno, N., Origin and role of gap states in organic semiconductor studied by UPS: as the nature of organic molecular crystals. *J. Phys. D: Appl. Phys.* **2017**, *50* (42), 423002. DOI: 10.1088/1361-6463/aa840f.

(48) Klein, A.; Mayer, T.; Thissen, A.; Jaegermann, W., Photoelectron spectroscopy in materials science and physical chemistry: Analysis of composition, chemical bonding, and electronic structure of surfaces and interfaces. In *Methods in physical chemistry,* First Edition; Schäfer, R., Schmidt, P. C., Eds.; Wiley-VCH Verlag GmbH & Co. KGaA, 2012; pp 477–512.

(49) Mankel, E.; Hein, C.; Kühn, M.; Mayer, T., Electric potential distributions in space charge regions of molecular organic adsorbates using a simplified distributed states model. *Phys. Status Solidi A* **2014**, *211* (9), 2040–2048. DOI: 10.1002/pssa.201330432.

(50) Vázquez, H.; Flores, F.; Oszwaldowski, R.; Ortega, J. *et al.*, Barrier formation at metal–organic interfaces: Dipole formation and the charge neutrality level. *Applied Surface Science* **2004**, *234* (1-4), 107–112. DOI: 10.1016/j.apsusc.2004.05.084.

(51) Vázquez, H.; Gao, W.; Flores, F.; Kahn, A., Energy level alignment at organic heterojunctions: Role of the charge neutrality level. *Phys. Rev. B* **2005**, *71* (4), 41306. DOI: 10.1103/PhysRevB.71.041306.

(52) Vázquez, H.; Flores, F.; Kahn, A., Induced density of states model for weakly-interacting organic semiconductor interfaces. *Organic Electronics* **2007**, *8*, 241–248. DOI: 10.1016/j.orgel.2006.07.006.

(53) Wißdorf, V., Elektrische Charakterisierung organischer Lochtransportmaterialien: Vergleich von Experiment und Simulation. Dissertation, Technische Universität Darmstadt, Darmstadt, 2020.

(54) Pollnau, M.; Gamelin, D. R.; Lüthi, S. R.; Güdel, H. U.; Hehlen, M. P., Power dependence of upconversion luminescence in lanthanide and transition-metal-ion systems. *Physical review. B, Condensed matter* **2000**, *61* (5), 3337–3346. DOI: 10.1103/PhysRevB.61.3337.

(55) Raišys, S.; Adomėnienė, O.; Adomėnas, P.; Rudnick, A. *et al.*, Triplet exciton diffusion and quenching in matrix-free solid photon upconversion films. *J. Phys. Chem. C* **2021**, *125* (7), 3764–3775. DOI: 10.1021/acs.jpcc.0c11048.

(56) Bharmoria, P.; Bildirir, H.; Moth-Poulsen, K., Triplet-triplet annihilation based near infrared to visible molecular photon upconversion. *Chem. Soc. Rev.* **2020**, *49* (18), 6529–6554. DOI: 10.1039/D0CS00257G.

(57) Kühn, M., Heterokontakte organischer Leuchtdioden: Schichtdickenabhängiges Strom-Spannungsverhalten. Dissertation, Technische Universität Darmstadt, Darmstadt, 2017.

(58) Tsiper, E. V.; Soos, Z. G.; Gao, W.; Kahn, A., Electronic polarization at surfaces and thin films of organic molecular crystals: PTCDA. *Chemical Physics Letters* **2002**, *360*, 47–52. DOI: 10.1016/S0009-2614(02)00774-1.

(59) Mankel, E., Elektronische Eigenschaften von Heterosystemen organischer und anorganischer Halbleiter: Präparation, Modifikation und Charakterisierung von Grenzflächen und Kompositen. Dissertation, Technische Universität Darmstadt, Darmstadt, 2010.

(60) Hill, I. G.; Kahn, A.; Soos, Z. G.; Pascal, J. R., Charge-separation energy in films of π-conjugated organic molecules. *Chemical Physics Letters* **2000**, *327* (3-4), 181–188. DOI: 10.1016/S0009-2614(00)00882-4.

(61) Djurovich, P. I.; Mayo, E. I.; Forrest, S. R.; Thompson, M. E., Measurement of the lowest unoccupied molecular orbital energies of molecular organic semiconductors. *Organic Electronics* **2009**, *10*, 515–520. DOI: 10.1016/j.orgel.2008.12.011.

(62) Hüfner, S. *Photoelectron spectroscopy*: *Principles and applications*, Third Revised and Enlarged Edition; Advanced Texts in Physics; Springer, 2003. DOI: 10.1007/978-3-662-09280-4.

(63) Salzmann, I.; Heimel, G.; Duhm, S.; Oehzelt, M. *et al.*, Intermolecular hybridization governs molecular electrical doping. *PRL (Physical review letters)* **2012**, *108*, 35502. DOI: 10.1103/PhysRevLett.108.035502.

(64) Méndez, H.; Heimel, G.; Opitz, A.; Sauer, K. *et al.*, Doping of organic semiconductors: Impact of dopant strength and electronic coupling. *Angew. Chem.* **2013**, *125* (30), 7905–7909. DOI: 10.1002/ange.201302396.

(65) Mayer, T.; Hein, C.; Mankel, E.; Jaegermann, W. *et al.*, Fermi level positioning in organic semiconductor phase mixed composites: The internal interface charge transfer doping model. *Organic Electronics* **2012**, *13*, 1356–1364. DOI: 10.1016/j.orgel.2012.03.028.

(66) Schottky, W., Zur Halbleitertheorie der Sperrschicht- und Spitzengleichrichter. *Zeitschrift für Physik* **1939**, 367–414. DOI: 10.1007/BF01340116.

(67) Ibach, H. and Lüth, H. *Festkörperphysik*: *Einführung in die Grundlagen; mit 18 Tafeln und 104 Übungen*, 7. Aufl.; Springer-Lehrbuch; Springer, 2009. DOI: 10.1007/978-3-540-85795-2.

(68) Anderson, R. L., Germanium-gallium arsenide heterojunctions. *IBM J. Res. & Dev.* **1960**, *4* (3), 283–287. DOI: 10.1147/rd.43.0283.

(69) Schlaf, R.; Lang, O.; Pettenkofer, C.; Jaegermann, W., Band lineup of layered semiconductor heterointerfaces prepared by van der Waals epitaxy: Charge transfer correction term for the electron affinity rule. *Journal of Applied Physics* **1999**, *85* (5), 2732–2753. DOI: 10.1063/1.369590.

(70) Ranke and Xing, Surface dipole and Fermi-level position on clean, oxygen-, and water-covered cylindrical Si crystals: A photoelectron spectroscopy study. *Physical review. B, Condensed matter* **1985**, *31* (4), 2246–2253. DOI: 10.1103/physrevb.31.2246.

(71) Heimel, G.; Romaner, L.; Zojer, E.; Bredas, J.-L., The interface energetics of self-assembled monolayers on metals. *Accounts of chemical research* **2008**, *41* (6), 721–729. DOI: 10.1021/ar700284q.

(72) Tung, R. T., Recent advances in Schottky barrier concepts. *Materials Science and Engineering: R: Reports* **2001**, *35* (1-3), 1–138. DOI: 10.1016/S0927-796X(01)00037-7.

(73) Benneckendorf, F. S.; Hillebrandt, S.; Ullrich, F.; Rohnacher, V. *et al.*, Structure-property relationship of phenylene-based self-assembled monolayers for record low work function of indium tin oxide. *The journal of physical chemistry letters* **2018**, *9* (13), 3731–3737. DOI: 10.1021/acs.jpclett.8b01242.

(74) Frericks, M.; Pflumm, C.; Mankel, E.; Mayer, T.; Jaegermann, W., Space charge regions at organic p-i-homointerfaces from advanced modeling of in situ-prepared interfaces analyzed by photoelectron spectroscopy. *ACS Appl. Electron. Mater.* **2021**, *3* (3), 1211–1227. DOI: 10.1021/acsaelm.0c01062.

(75) Physical Electronics. *Technician's PHI 5000 VersaProbe installation, calibration, & maintenance manual.*

(76) Samson, J. A. R., Line broadening in photoelectron spectroscopy. *Review of Scientific Instruments* **1969**, *40* (9), 1174–1177. DOI: 10.1063/1.1684192.

(77) Turner, D. W., Photoelectron spectroscopy. *Annu. Rev. Phys. Chem.* **1970**, *21* (1), 107–128. DOI: 10.1146/annurev.pc.21.100170.000543.

(78) Burger, F. and Maier, J. P., Vacuum ultraviolet source of the line radiation of the rare gas ions suitable for photoelectron spectroscopy. *J. Phys. E: Sci. Instrum.* **1975**, *8* (5), 420–422. DOI: 10.1088/0022-3735/8/5/026.

(79) Peel, J. B. and Nagy-Felsobuki, E. I. von, The far ultraviolet emission of a helium discharge source studied by photoelectron spectroscopy. *J. Chem. Educ.* **1987**, *64* (5), 463. DOI: 10.1021/ed064p463.

(80) Reiser, P., Modifying and controlling diffusion properties of molecular dopants in organic semiconductors. Dissertation, Technische Universität Darmstadt, Darmstadt, 2019.

(81) Tietze, M. L.; Burtone, L.; Riede, M.; Lüssem, B.; Leo, K., Fermi level shift and doping efficiency in p-doped small molecule organic semiconductors: A photoelectron spectroscopy and theoretical study. *Phys. Rev. B* **2012**, *86*, 35320. DOI: 10.1103/PhysRevB.86.035320.

(82) Endres, J.; Egger, D. A.; Kulbak, M.; Kerner, R. A. *et al.*, Valence and conduction band densities of states of metal halide perovskites: A combined experimental-theoretical study. *The journal of physical chemistry letters* **2016**, *7* (14), 2722–2729. DOI: 10.1021/acs.jpclett.6b00946.

(83) Hellmann, T., Advanced understanding of the electronic properties of perovskite solar cells: Contact formation, band energy diagrams and involved surface photovoltages. Dissertation, Technische Universität Darmstadt, Darmstadt, 2021.

(84) Helander, M. G.; Greiner, M. T.; Wang, Z. B.; Lu, Z. H., Pitfalls in measuring work function using photoelectron spectroscopy. *Applied Surface Science* **2010**, *256* (8), 2602–2605. DOI: 10.1016/j.apsusc.2009.11.002.

(85) Schultz, T.; Lenz, T.; Kotadiya, N.; Heimel, G. *et al.*, Reliable work function determination of multicomponent surfaces and interfaces: The role of electrostatic potentials in ultraviolet photoelectron spectroscopy. *Adv. Mater. Interfaces* **2017**, *4* (19), 1700324. DOI: 10.1002/admi.201700324.

(86) Schultz, T.; Amsalem, P.; Kotadiya, N. B.; Lenz, T. *et al.*, Importance of substrate work function homogeneity for reliable ionization energy determination by photoelectron spectroscopy. *Phys. Status Solidi B* **2019**, *256*, 1800299. DOI: 10.1002/pssb.201800299.

(87) Seah, M. P. and Dench, W. A., Quantitative electron spectroscopy of surfaces: A standard data base for electron inelastic mean free paths in solids. *Surface and Interface Analysis* **1979**, *1* (1), 2–11. DOI: 10.1002/sia.740010103.

(88) Tanuma, S.; Powell, C. J.; Penn, D. R., Calculations of electron inelastic mean free paths. V. Data for 14 organic compounds over the 50-2000 eV range. *Surf Interface Anal* **1994**, *21*, 165–176. DOI: 10.1002/sia.740210302.

(89) Powell, C. J. and Jablonski, A. *NIST electron inelastic-mean-free-path database*: *NIST standard reference database 71*, Version 1.2; National Institute of Standards and Technology: Gaithersburg, 2010.

(90) Jablonski, A. and Powell, C., Relationships between electron inelastic mean free paths, effective attenuation lengths, and mean escape depths. *Journal of Electron Spectroscopy and Related Phenomena* **1999**, *100* (1-3), 137–160. DOI: 10.1016/S0368-2048(99)00044-4.

(91) Cumpson, P. J. and Seah, M. P., Elastic scattering corrections in AES and XPS. II. Estimating attenuation lengths and conditions required for their valid use in overlayer/substrate experiments. *Surface and Interface Analysis* **1997**, *25* (6), 430–446. DOI: 10.1002/(SICI)1096-9918(199706)25:6<430:AID-SIA254>3.0.CO;2-7.

(92) Ozawa, Y.; Nakayama, Y.; Machida, S.; Kinjo, H.; Ishii, H., Maximum probing depth of low-energy photoelectrons in an amorphous organic semiconductor film. *Journal of Electron Spectroscopy and Related Phenomena* **2014**, *197*, 17–21. DOI: 10.1016/j.elspec.2014.08.001.

(93) Graber, T.; Forster, F.; Schöll, A.; Reinert, F., Experimental determination of the attenuation length of electrons in organic molecular solids: The example of PTCDA. *Surface Science* **2011**, *605* (9-10), 878–882. DOI: 10.1016/j.susc.2011.01.033.

(94) Shirley, D. A., High-resolution X-ray photoemission spectrum of the valence bands of gold. *Phys. Rev. B* **1972**, *5* (12), 4709–4714. DOI: 10.1103/PhysRevB.5.4709.

(95) Proctor, A. and Sherwood, P. M. A., Data analysis techniques in X-ray photoelectron spectroscopy. *Anal. Chem.* **1982**, *54*, 13–19. DOI: 10.1021/ac00238a008.

(96) Scofield, J. H., Hartree-Slater subshell photoionization cross-sections at 1254 and 1487 eV. *Journal of Electron Spectroscopy and Related Phenomena* **1976** (8), 129–137. DOI: 10.1016/0368-2048(76)80015-1.

(97) Reilman, R. F.; Msezane, A.; Manson, S. T., Relative intensities in photoelectron spectroscopy of atoms and molecules. *Journal of Electron Spectroscopy and Related Phenomena* **1976**, *8* (5), 389–394. DOI: 10.1016/0368-2048(76)80025-4.

(98) Cros, A., Charging effects in X-ray photoelectron spectroscopy. *Journal of Electron Spectroscopy and Related Phenomena* **1992**, *59* (1), 1–14. DOI: 10.1016/0368-2048(92)85008-U.

(99) Yu, X. and Hantsche, H., Some aspects of the charging effect in monochromatized focused XPS. *Fresenius J Anal Chem* **1993**, *346* (1-3), 233–236. DOI: 10.1007/BF00321421.

(100) Koch, N.; Pop, D.; Weber, R.; Böwering, N. *et al.*, Radiation induced degradation and surface charging of organic thin films in ultraviolet photoemission spectroscopy. *Thin Solid Films* **2001**, *391*, 81–87. DOI: 10.1016/S0040-6090(01)00961-0.

(101) Koch, N.; Dürr, A. C.; Ghijsen, J.; Johnson, R. L. *et al.*, Optically induced electron transfer from conjugated organic molecules to charged metal clusters. *Thin Solid Films* **2003**, *441*, 145–149. DOI: 10.1016/S0040-6090(03)00925-8.

(102) Paula Connor, Dotierung und Charakterisierung von organischen Halbleiterschichten. Masterthesis, TU Darmstadt, 2016.

(103) Roschwege GmbH. *Datasheet - High efficacy UV LED emitter 365nm / 11W: RSW-P11-365-0*, 2012.

(104) Roschwege GmbH. *Datasheet - High efficacy UV LED emitter 400nm / 10W: RSW-P10-400-0*, 2012.

(105) Kalinowski, J.; Cocchi, M.; Virgili, D.; Fattori, V.; Williams, J., Evidence for electric field dependent dissociation of exciplexes in electron donor–acceptor organic solid films. *Chemical Physics Letters* **2006**, *432* (1-3), 110–115. DOI: 10.1016/j.cplett.2006.10.059.

(106) Jaegermann, W., Adsorption of $Br_2$ on n-$MoSe_2$: modelling photoelectrochemistry in the UHV. *Chemical Physics Letters* **1986**, *126* (3-4), 301–305. DOI: 10.1016/S0009-2614(86)80087-2.

(107) Schellenberger; Schlaf; Pettenkofer; Jaegermann, Synchrotron-induced surface-photovoltage saturation at intercalated Na/$WSe_2$ interfaces. *Physical review. B, Condensed matter* **1992**, *45* (7), 3538–3545. DOI: 10.1103/PhysRevB.45.3538.

(108) Brown, C. W., Ultraviolet, visible, and near-infrared spectrophotometers. *Applied Spectroscopy Reviews* **2000**, *35* (3), 151–173. DOI: 10.1081/ASR-100101223.

(109) Anderson, R. J.; Bendell, D. J.; Groundwater, P. W. *Organic spectroscopic analysis*; Tutorial chemistry texts, Vol. 22; Royal Society of Chemistry, 2004.

(110) Hasegawa, T. *Quantitative infrared spectroscopy for understanding of a condensed matter*; Springer Japan, 2017. DOI: 10.1007/978-4-431-56493-5.

(111) Hillebrandt, S., Infrarotspektroskopische Untersuchung von Elektrodenmodifikationen und deren Auswirkung auf die angrenzenden organischen Halbleiter. Dissertation, Ruprecht - Karls - Universität, Heidelberg, 2017.

(112) Tamanai, A.; Dao, T. D.; Sendner, M.; Nagao, T.; Pucci, A., Mid-infrared optical and electrical properties of indium tin oxide films. *Phys. Status Solidi (a)* **2017**, *214* (3), 1600467. DOI: 10.1002/pssa.201600467.

(113) Brewer, S. H. and Franzen, S., Indium tin oxide plasma frequency dependence on sheet resistance and surface adlayers determined by reflectance FTIR spectroscopy. *J. Phys. Chem. B* **2002**, *106* (50), 12986–12992. DOI: 10.1021/jp026600x.

(114) Martin, R. M. *Electronic structure*: *Basic theory and practical methods*; Cambridge University Press, 2004. DOI: 10.1017/CBO9780511805769.

(115) Hohenberg, P. and Kohn, W., Inhomogeneous electron gas. *Phys. Rev.* **1964**, *136* (3B), B864-B871. DOI: 10.1103/PhysRev.136.B864.

(116) Kohn, W. and Sham, L. J., Self-consistent equations including exchange and correlation effects. *Phys. Rev.* **1965**, *140* (4A), A1133-A1138. DOI: 10.1103/PhysRev.140.A1133.

(117) Barragan-Yani, D. A., First-principles study of dislocations in Cu(In,Ga)$Se_2$ solar cell absorbers. Dissertation, Technische Universität Darmstadt, Darmstadt, 2018. urn://nbn:de:tuda-tuprints-81954.

(118) Mortensen, J. J.; Hansen, L. B.; Jacobsen, K. W., Real-space grid implementation of the projector augmented wave method. *Phys. Rev. B* **2005**, *71* (3), 4351. DOI: 10.1103/PhysRevB.71.035109.

(119) Enkovaara, J.; Rostgaard, C.; Mortensen, J. J.; Chen, J. *et al.*, Electronic structure calculations with GPAW: a real-space implementation of the projector augmented-wave method. *Journal of physics. Condensed matter : an Institute of Physics journal* **2010**, *22* (25), 253202. DOI: 10.1088/0953-8984/22/25/253202.

(120) Hjorth Larsen, A.; Jørgen Mortensen, J.; Blomqvist, J.; Castelli, I. E. *et al.*, The atomic simulation environment-a Python library for working with atoms. *Journal of physics. Condensed matter : an Institute of Physics journal* **2017**, *29* (27), 273002. DOI: 10.1088/1361-648X/aa680e.

(121) Blöchl, P. E.; Först, C. J.; Schimpl, J., Projector augmented-wave method: ab-initio molecular dynamics with full wave functions. *Physical review. B, Condensed matter* **1994**, *50* (24), 17953–17979. DOI: 10.1103/PhysRevB.50.17953.

(122) Ljungberg, M. P.; Mortensen, J. J.; Pettersson, L., An implementation of core level spectroscopies in a real space Projector Augmented Wave density functional theory code. *Journal of Electron Spectroscopy and Related Phenomena* **2011**, *184* (8-10), 427–439. DOI: 10.1016/j.elspec.2011.05.004.

(123) Måtensson, N. and Nilsson, A., On the origin of core-level binding energy shifts. *Journal of Electron Spectroscopy and Related Phenomena* **1995**, *75*, 209–223. DOI: 10.1016/0368-2048(95)02532-4.

(124) Walter, M.; Moseler, M.; Pastewka, L., Offset-corrected Δ-Kohn-Sham scheme for the prediction of X-ray photoelectron spectra of molecules and solids. *Phys. Rev. B* **2016**, *94* (4). DOI: 10.1103/PhysRevB.94.041112.

(125) Holme, A.; Børve, K. J.; Sæthre, L. J.; Thomas, T. D., Accuracy of calculated chemical shifts in carbon 1s ionization energies from single-reference ab initio methods and density functional theory. *Journal of chemical theory and computation* **2011**, *7* (12), 4104–4114. DOI: 10.1021/ct200662e.

(126) Hanwell, M. D.; Curtis, D. E.; Lonie, D. C.; Vandermeersch, T. *et al.*, Avogadro: an advanced semantic chemical editor, visualization, and analysis platform. *J Cheminform* **2012**, *4* (1), 17. DOI: 10.1186/1758-2946-4-17.

(127) Perdew; Burke; Ernzerhof, Generalized gradient approximation made simple. *Physical review letters* **1996**, *77* (18), 3865–3868. DOI: 10.1103/PhysRevLett.77.3865.

(128) Porezag and Pederson, Infrared intensities and Raman-scattering activities within density-functional theory. *Physical review. B, Condensed matter* **1996**, *54* (11), 7830–7836. DOI: 10.1103/PhysRevB.54.7830.

(129) Pederson, M. R.; Quong, A. A.; Broughton, J. Q.; Feldman, J. L., Fullerene molecules and tubules polarizabilities, vibrational modes and nanocapillarity. *Computational Materials Science* **1994**, *2* (3-4), 536–542. DOI: 10.1016/0927-0256(94)90084-1.

(130) Stukowski, A., Visualization and analysis of atomistic simulation data with OVITO–the Open Visualization Tool. *Modelling Simul. Mater. Sci. Eng.* **2010**, *18* (1), 15012. DOI: 10.1088/0965-0393/18/1/015012.

(131) Bistricić, L.; Volovsek, V.; Dananić, V.; Sapić, I. M., Conformational stability and vibrations of aminopropylsilanol molecule. *Spectrochimica acta. Part A, Molecular and biomolecular spectroscopy* **2006**, *64* (2), 327–337. DOI: 10.1016/j.saa.2005.07.027.

(132) Afre, R. A.; Sharma, N.; Sharon, M.; Sharon, M., Transparent conducting oxide films for various applications: A review. *REVIEWS ON ADVANCED MATERIALS SCIENCE* **2018**, *53* (1), 79–89. DOI: 10.1515/rams-2018-0006.

(133) Klein, A.; Körber, C.; Wachau, A.; Säuberlich, F. *et al.*, Transparent conducting oxides for photovoltaics: Manipulation of Fermi level, work function and energy band alignment. *Materials* **2010**, *3* (11), 4892–4914. DOI: 10.3390/ma3114892.

(134) Hamberg, I. and Granqvist, C. G., Evaporated Sn-doped $In_2O_3$ films: Basic optical properties and applications to energy-efficient windows. *Journal of Applied Physics* **1986**, *60* (11), R123-R160. DOI: 10.1063/1.337534.

(135) Gassenbauer, Y. and Klein, A., Electronic and chemical properties of tin-doped indium oxide (ITO) surfaces and ITO/ZnPc interfaces studied in-situ by photoelectron spectroscopy. *J. Phys. Chem. B* **2006**, *110* (10), 4793–4801. DOI: 10.1021/jp056640b.

(136) Wachau, A., Sauerstoffaustausch polykristalliner kathodenzerstäubter Indiumoxid-Dünnschichten: Volumen-, Oberflächen- und Grenzflächeneigenschaften. Dissertation, Technische Universität Darmstadt, Darmstadt, 2015.

(137) Sugiyama, K.; Ishii, H.; Ouchi, Y.; Seki, K., Dependence of indium–tin–oxide work function on surface cleaning method as studied by ultraviolet and X-ray photoemission spectroscopies. *Journal of Applied Physics* **2000**, *87* (1), 295–298. DOI: 10.1063/1.371859.

(138) Chaney, J. A. and Pehrsson, P. E., Work function changes and surface chemistry of oxygen, hydrogen, and carbon on indium tin oxide. *Applied Surface Science* **2001**, *180* (3-4), 214–226. DOI: 10.1016/S0169-4332(01)00347-6.

(139) Klein, A., Electronic properties of $In_2O_3$ surfaces. *Appl. Phys. Lett.* **2000**, *77*, 2009–2011. DOI: 10.1063/1.1312199.

(140) Moulder, J. F.; Stickle, W. F.; Sobol, P. E.; Bomben, K. D. *Handbook of X-ray photoelctron spectroscopy: A reference book of standard spectra for identification and interpretation of XPS data*; Physical Electronics, Inc., 1992.

(141) Turgeon, S. *On the determination of carbon* $sp^2/sp^3$ *ratios in polystyrene–polyethylene copolymers by photoelectron spectroscopy*, Vol. 394, 2001. DOI: 10.1016/S0040-6090(01)01134-8.

(142) Barr, T. L. and Seal, S., Nature of the use of adventitious carbon as a binding energy standard. *Journal of Vacuum Science & Technology A* **1995**, *13* (3), 1239–1246. DOI: 10.1116/1.579868.

(143) Walsh, A.; Da Silva, J. L. F.; Wei, S.-H.; Körber, C. *et al.*, Nature of the band gap of $In_2O_3$ revealed by first-principles calculations and X-ray spectroscopy. *Physical review letters* **2008**, *100* (16), 167402. DOI: 10.1103/PhysRevLett.100.167402.

(144) Weiher, R. L. and Ley, R. P., Optical properties of indium oxide. *Journal of Applied Physics* **1966**, *37* (1), 299–302. DOI: 10.1063/1.1707830.

(145) Necas, D. and Klapetek, P., Gwyddion: an open-source software for SPM data analysis. *Cent. Eur. J. Phys.* **096**, *2012* (10), 181–188. DOI: 10.2478/s11534-011-0096-2.

(146) Klapetek, P.; Necas, D.; Anderson, C. *Gwyddion user guide*, 2021. http://gwyddion.net/documentation/.

(147) Zeika, O.; Willmann, S.; Dorok, S.; Werner, A.; Bachmann, C., Radialene compounds and their use: United States Patent 8,057,712 B2. Nov. 15, 2011.

(148) Shard, A. G., Detection limits in XPS for more than 6000 binary systems using Al and Mg Kα X-rays. *Surf Interface Anal* **2014**, *46* (3), 175–185. DOI: 10.1002/sia.5406.

(149) Kampar, E. and Neilands, O., Degree of Charge Transfer in Donor–Acceptor Systems of the π–π Type. *Russ. Chem. Rev.* **1986**, *55* (4), 334–342. DOI: 10.1070/RC1986v055n04ABEH003193.

(150) Meneghetti, M. and Pecile, C., Charge–transfer organic crystals: Molecular vibrations and spectroscopic effects of electron–molecular vibration coupling of the strong electron acceptor $TCNQF_4$. *The Journal of Chemical Physics* **1986**, *84* (8), 4149–4162. DOI: 10.1063/1.450086.

(151) Kuwabara, Y.; Ogawa, H.; Inada, H.; Noma, N.; Shirota, Y., Thermally stable multilared organic electroluminescent devices using novel starburst molecules, 4,4′,4″-Tri(N-carbazolyl)triphenylamine (TCTA) and 4,4′,4″-Tris(3-methylphenylphenylamino)triphenylamine (m-MTDATA), as hole-transport materials. *Adv. Mater.* **1994**, *6* (9), 677–679. DOI: 10.1002/adma.19940060913.

(152) Dänekamp, B.; Droseros, N.; Tsokkou, D.; Brehm, V. *et al.*, Influence of hole transport material ionization energy on the performance of perovskite solar cells. *J. Mater. Chem. C* **2019**, *7* (3), 523–527. DOI: 10.1039/C8TC05372C.

(153) Matsushima, T.; Jin, G.-H.; Kanai, Y.; Yokota, T. *et al.*, Interfacial charge transfer and charge generation in organic electronic devices. *Organic Electronics* **2011**, *12* (3), 520–528. DOI: 10.1016/j.orgel.2011.01.001.

(154) Ogawa, H.; Okuda, R.; Shirota, Y., Tuning of the emission color of organic electroluminescent devices by exciplex formation at the organic solid interface. *Applied Physics A: Materials Science & Processing* **1998**, *67* (5), 599–602. DOI: 10.1007/s003390050829.

(155) Stampor, W.; Mężyk, J.; Kalinowski, J.; Cocchi, M. *et al.*, Organic electroluminescent devices containing phosphorescent molecules in molecularly doped hole transporting layer. *Macromol. Symp.* **2004**, *212* (1), 509–514. DOI: 10.1002/masy.200450866.

(156) Seo, J. H.; Han, N. S.; Shim, H. S.; Park, S. M. *et al.*, Triplet state and phosphorescence of hole-transport layer and its triplet exciton confinement. *Chemical Physics Letters* **2010**, *499* (4-6), 226–230. DOI: 10.1016/j.cplett.2010.09.057.

(157) Schwoerer, M. and Wolf, H. C. *Organische molekulare Festkörper*, 1. Aufl.; Lehrbuch Physik; Wiley-VCH, 2012.

(158) Pflumm, C.; Parham, A. H.; Brocke, C.; Montenegro, E. *et al.*, Materials for organic electroluminescent devices: United States Patent 9,312,495 B2. Apr. 12, 2016.

(159) Burroughes, J. H.; Bradley, D. D. C.; Brown, A. R.; Marks, R. N. *et al.*, Light-emitting diodes based on conjugated polymers. *Nature* **1990**, *347* (6293), 539–541. DOI: 10.1038/347539a0.

(160) Burn, P. L.; Holmes, A. B.; Kraft, A.; Bradley, D. D. C. *et al.*, Chemical tuning of electroluminescent copolymers to improve emission efficiencies and allow patterning. *Nature* **1992**, *356* (6364), 47–49. DOI: 10.1038/356047a0.

(161) Koch, N.; Pogantsch, A.; List, E. J. W.; Leising, G. *et al.*, Low-onset organic blue light emitting devices obtained by better interface control. *Appl. Phys. Lett.* **1999**, *74* (20), 2909–2911. DOI: 10.1063/1.123962.

(162) Blyth, R. I. R.; Sardar, S. A.; Netzer, F. P.; Ramsey, M. G., Influence of oxygen on band alignment at the organic/aluminum interface. *Appl. Phys. Lett.* **2000**, *77* (8), 1212–1214. DOI: 10.1063/1.1289497.

(163) Demirkan, K.; Mathew, A.; Weiland, C.; Reid, M.; Opila, R. L., Reactivity and morphology of vapor-deposited Al/polymer interfaces for organic semiconductor devices. *Journal of Applied Physics* **2008**, *103* (3), 34505. DOI: 10.1063/1.2837883.

(164) Ivanco, J.; Winter, B.; Netzer, F. P.; Ramsey, M. G. *et al.*, Oxygen as a surfactant for Al contact metallization of organic layers. *Appl. Phys. Lett.* **2004**, *85* (4), 585–587. DOI: 10.1063/1.1775284.

(165) Dhaka, R. S.; Biswas, C.; Shukla, A. K.; Barman, S. R.; Chakrabarti, A., Xe and Ar nanobubbles in Al studied by photoemission spectroscopy. *Phys. Rev. B* **2008**, *77* (10). DOI: 10.1103/PhysRevB.77.104119.

(166) Mills, I.; Cvitas, T.; Homann, K.; Kallay, N.; Kuchitsu, K. *Quantities, units and symbols in physical chemistry*, 2. ed., reprinted.; Blackwell Science, 1993.

(167) Brune, H.; Wintterlin, J.; Trost, J.; Ertl, G. *et al.*, Interaction of oxygen with Al(111) studied by scanning tunneling microscopy. *The Journal of Chemical Physics* **1993**, *99* (3), 2128–2148. DOI: 10.1063/1.465278.

(168) Olthof, S.; Tress, W.; Meerheim, R.; Lüssem, B.; Leo, K., Photoelectron spectroscopy study of systematically varied doping concentrations in an organic semiconductor layer using a molecular p-dopant. *J. Appl. Phys. (Journal of Applied Physics)* **2009**, *106*, 103711. DOI: 10.1063/1.3259436.

(169) Duhm, S.; Salzmann, I.; Bröker, B.; Glowatzki, H. *et al.*, Interdiffusion of molecular acceptors through organic layers to metal substrates mimics doping-related energy level shifts. *Appl. Phys. Lett.* **2009**, *95*, 93305. DOI: 10.1063/1.3213547.

(170) Zhang, F. and Kahn, A., Investigation of the high electron affinity molecular dopant $F_6$-TCNNQ for hole-transport materials. *Adv. Funct. Mater.* **2018**, *28* (1), 1703780. DOI: 10.1002/adfm.201703780.

(171) Bussolotti, F.; Kera, S.; Kudo, K.; Kahn, A.; Ueno, N., Gap states in pentacene thin film induced by inert gas exposure. *PRL (Physical review letters)* **2013**, *110*, 267602. DOI: 10.1103/PhysRevLett.110.267602.

(172) Yang, J.; Li, Y.; Duhm, S.; Tang, J. *et al.*, Molecular structure-dependent charge injection and doping efficiencies of organic semiconductors: Impact of side chain substitution. *Adv. Mater. Interfaces* **2014**, *1* (3), 1300128. DOI: 10.1002/admi.201300128.

(173) Koch, N.; Heimel, G.; Wu, J.; Zojer, E. *et al.*, Influence of molecular conformation on organic/metal interface energetics. *Chemical Physics Letters* **2005**, *413* (4-6), 390–395. DOI: 10.1016/j.cplett.2005.08.004.

(174) Tietze, M. L.; Wölzl, F.; Menke, T.; Fischer, A. *et al.*, Self-passivation of molecular n-type doping during air exposure using a highly efficient air-instable dopant. *Phys. Status Solidi (a)* **2013**, *210* (10), 2188–2198. DOI: 10.1002/pssa.201330049.

(175) Tietze, M. L.; Pahner, P.; Schmidt, K.; Leo, K.; Lüssem, B., Doped organic semiconductors: Trap-filling, impurity saturation, and reserve regimes. *Adv. Funct. Mater.* **2015**, *25*, 2701–2707. DOI: 10.1002/adfm.201404549.

(176) Tietze, M. L.; Benduhn, J.; Pahner, P.; Nell, B. *et al.*, Elementary steps in electrical doping of organic semiconductors. *Nature communications* **2018**, *9*, 1182. DOI: 10.1038/s41467-018-03302-z.

(177) Pingel, P. and Neher, D., Comprehensive picture of p-type doping of P3HT with the molecular acceptor $F_4TCNQ$. *Phys. Rev. B* **2013**, *87* (11). DOI: 10.1103/PhysRevB.87.115209.

(178) Glaser, T.; Beck, S.; Lunkenheimer, B.; Donhauser, D. *et al.*, Infrared study of the $MoO_3$ doping efficiency in 4,4′-bis(N-carbazolyl)-1,1′-biphenyl (CBP). *Organic Electronics* **2013**, *14* (2), 575–583. DOI: 10.1016/j.orgel.2012.11.031.

(179) Ueda, Y.; Nakanotani, H.; Hosokai, T.; Tanaka, Y. *et al.*, Role of spontaneous orientational polarization in organic donor–acceptor blends for exciton binding. *Adv. Optical Mater.* **2020**, *8* (21), 2000896. DOI: 10.1002/adom.202000896.

(180) Lögdlund; Lazzaroni; Stafström; Salaneck; Brédas, Direct observation of charge-induced π-electronic structural changes in a conjugated polymer. *Physical review letters* **1989**, *63* (17), 1841–1844. DOI: 10.1103/PhysRevLett.63.1841.

(181) Hill, I. G.; Mäkinen, A. J.; Kafafi, Z. H., Distinguishing between interface dipoles and band bending at metal/tris-(8-hydroxyquinoline) aluminum interfaces. *Appl. Phys. Lett.* **2000**, *77* (12), 1825. DOI: 10.1063/1.1310637.

(182) Fukagawa, H.; Kera, S.; Kataoka, T.; Hosoumi, S. *et al.*, The role of the ionization potential in vacuum-level alignment at organic semiconductor interfaces. *Adv. Mater.* **2007**, *19* (5), 665–668. DOI: 10.1002/adma.200601678.

(183) Ishii, H.; Hayashi, N.; Ito, E.; Washizu, Y. *et al.*, Kelvin probe study of band bending at organic semiconductor/metal interfaces: examination of Fermi level alignment. *Phys. Status Solidi A* **2004**, *201* (6), 1075–1094. DOI: 10.1002/pssa.200404346.

(184) Sze, S. M. and Ng, K. K. *Physics of semiconductor devices*, 3. ed.; Wiley-Interscience, 2007. DOI: 10.1002/0470068329.

(185) Lange, I.; Blakesley, J. C.; Frisch, J.; Vollmer, A. *et al.*, Band bending in conjugated polymer layers. *PRL (Physical review letters)* **2011**, *106*, 216402. DOI: 10.1103/PhysRevLett.106.216402.

(186) Lin, X.; Purdum, G. E.; Zhang, Y.; Barlow, S. *et al.*, Impact of a low concentration of dopants on the distribution of gap states in a molecular semiconductor. *Chem. Mater.* **2016**, *28*, 2677–2684. DOI: 10.1021/acs.chemmater.6b00165.

(187) Sueyoshi, T.; Fukagawa, H.; Ono, M.; Kera, S.; Ueno, N., Low-density band-gap states in pentacene thin films probed with ultrahigh-sensitivity ultraviolet photoelectron spectroscopy. *Appl. Phys. Lett.* **2009**, *95*, 183303. DOI: 10.1063/1.3258351.

(188) Yogev, S.; Matsubara, R.; Nakamura, M.; Zschieschang, U. *et al.*, Fermi level pinning by gap states in organic semiconductors. *PRL (Physical review letters)* **2013**, *110*, 36803. DOI: 10.1103/PhysRevLett.110.036803.

(189) Morrison, D. D.; Riley, J. D.; Zancanaro, J. F., Multiple shooting method for two-point boundary value problems. *Commun. ACM* **1962**, *5* (12), 613–614. DOI: 10.1145/355580.369128.

(190) Dormand, J. R. and Prince, P. J., A family of embedded Runge-Kutta formulae. *Journal of Computational and Applied Mathematics* **1980**, *6* (1), 19–26. DOI: 10.1016/0771-050X(80)90013-3.

(191) Oehzelt, M.; Akaike, K.; Koch, N.; Heimel, G., Energy-level alignment at organic heterointerfaces. *Sci. Adv.* **2015**, *1*, e1501127. DOI: 10.1126/sciadv.1501127.

(192) Blakesley, J. C. and Greenham, N. C., Charge transfer at polymer-electrode interfaces: The effect of energetic disorder and thermal injection on band bending and open-circuit voltage. *J. Appl. Phys. (Journal of Applied Physics)* **2009**, *106*, 34507. DOI: 10.1063/1.3187787.

(193) Lee, J.-H.; Kim, H.-M.; Kim, K.-B.; Kim, J.-J., Origin of charge generation efficiency of metal oxide p-dopants in organic semiconductors. *Organic Electronics* **2011**, *12* (6), 950–954. DOI: 10.1016/j.orgel.2011.03.008.

(194) Fediai, A.; Emering, A.; Symalla, F.; Wenzel, W., Disorder-driven doping activation in organic semiconductors. *Phys. Chem. Chem. Phys.* **2020**, *22* (18), 10256–10264. DOI: 10.1039/D0CP01333A.

(195) Winkler, S.; Amsalem, P.; Frisch, J.; Oehzelt, M. *et al.*, Probing the energy levels in hole-doped molecular semiconductors. *Mater. Horiz.* **2015** (2), 427–433. DOI: 10.1039/C5MH00023H.

(196) Levine, I.; Shimizu, K.; Lomuscio, A.; Kulbak, M. *et al.*, Direct probing of gap states and their passivation in halide perovskites by high-sensitivity, variable energy ultraviolet photoelectron spectroscopy. *J. Phys. Chem. C* **2021**, *125* (9), 5217–5225. DOI: 10.1021/acs.jpcc.0c11627.

(197) Bässler, H.; Kroh, D.; Schauer, F.; Nádaždy, V.; Köhler, A., Mapping the density of states distribution of organic semiconductors by employing energy resolved–electrochemical impedance spectroscopy. *Advanced Functional Materials* **2020**, 2007738. DOI: 10.1002/adfm.202007738.

(198) Wertheim, G. K.; Butler, M. A.; West, K. W.; Buchanan, D. N. E., Determination of the Gaussian and Lorentzian content of experimental line shapes. *Review of Scientific Instruments* **1974**, *45* (11), 1369–1371. DOI: 10.1063/1.1686503.

(199) Fukagawa, H.; Yamane, H.; Kataoka, T.; Kera, S. *et al.*, Origin of the highest occupied band position in pentacene films from ultraviolet photoelectron spectroscopy: Hole stabilization versus band dispersion. *Phys. Rev. B* **2006**, *73* (24). DOI: 10.1103/PhysRevB.73.245310.

(200) Blasini, D. R.; Rivnay, J.; Smilgies, D.-M.; Slinker, J. D. *et al.*, Observation of intermediate-range order in a nominally amorphous molecular semiconductor film. *J. Mater. Chem.* **2007**, *17* (15), 1458–1461. DOI: 10.1039/B700505A.

(201) Eiermann, R.; Parkinson, G. M.; Baessler, H.; Thomas, J. M., Amorphous organic molecular solids. Vapor-deposited tetracene. *J. Phys. Chem.* **1982**, *86* (3), 313–315. DOI: 10.1021/j100392a003.

(202) Venables, J. A.; Spiller, G. D. T.; Hanbucken, M., Nucleation and growth of thin films. *Rep. Prog. Phys.* **1984**, *47* (4), 399–459. DOI: 10.1088/0034-4885/47/4/002.

(203) Alcock, C. B.; Itkin, V. P.; Horrigan, M. K., Vapour pressure equations for the metallic elements: 298–2500K. *Canadian Metallurgical Quarterly* **1984**, *23* (3), 309–313. DOI: 10.1179/cmq.1984.23.3.309.

(204) Mattox, D. M. *Handbook of physical vapor deposition (PVD) processing*, 2. ed.; William Andrew; Elsevier William Andrew, 2010.

(205) Fadley, C. S.; Baird, R. J.; Siekhaus, W.; Novakov, T.; Bergström, S., Surface analysis and angular distributions in X-ray photoelectron spectroscopy. *Journal of Electron Spectroscopy and Related Phenomena* **1974**, *4* (2), 93–137. DOI: 10.1016/0368-2048(74)90001-2.

(206) Fraser, W. A.; Florio, J. V.; Delgass, W. N.; Robertson, W. D., Surface sensitivity and angular dependence of X-ray photoelectron spectra. *Surface Science* **1973**, *36* (2), 661–674. DOI: 10.1016/0039-6028(73)90410-X.

(207) Martín-Concepción, A. I.; Yubero, F.; Espinós, J. P.; Tougaard, S., Surface roughness and island formation effects in ARXPS quantification. *Surface and Interface Analysis* **2004**, *36* (8), 788–792. DOI: 10.1002/sia.1765.

(208) Callcott, T. A. and Arakawa, E. T., Volume and surface photoemission processes from plasmon resonance fields. *Phys. Rev. B* **1975**, *11* (8), 2750–2758. DOI: 10.1103/PhysRevB.11.2750.

(209) Kanter, H., Slow-Electron Mean Free Paths in Aluminum, Silver, and Gold. *Phys. Rev. B* **1970**, *1* (2), 522–536. DOI: 10.1103/PhysRevB.1.522.

(210) Gesell, T. F. and Arakawa, E. T., Attenuation length for photoelectrons excited in aluminum by 21.2 eV photons. *Phys. Rev. Lett.* **1971**, *26* (7), 377–380. DOI: 10.1103/PhysRevLett.26.377.

(211) Ashley, J. C.; Tung, C. J.; Ritchie, R. H., Electron inelastic mean free paths and energy losses in solids. *Surface Science* **1979**, *81* (2), 409–426. DOI: 10.1016/0039-6028(79)90109-2.

(212) Heil, H.; Steiger, J.; Karg, S.; Gastel, M. *et al.*, Mechanisms of injection enhancement in organic light-emitting diodes through an Al/LiF electrode. *Journal of Applied Physics* **2001**, *89* (1), 420–424. DOI: 10.1063/1.1331651.

(213) Lee, J. H.; Yi, Y.; Moon, D. W., Direct evidence of Al diffusion into tris-(8-hydroquinoline) aluminum layer: medium energy ion scattering analysis. *Appl. Phys. Lett.* **2008**, *93* (15), 153307. DOI: 10.1063/1.3002290.

(214) Fahlman, M.; Salaneck, W. R.; Moratti, S. C.; Holmes, A. B.; Brhdas, J. L., A joint experimental and theoretical study of the interaction between aluminum and electroluminescent polymers: Cyano derivatives of poly(p-phenylene vinylene). *Chrm Eur J* **1997** (2). DOI: 10.1002/chem.19970030218.

(215) Dannetun, P.; Boman, M.; Stafström, S.; Salaneck, W. R. *et al.*, The chemical and electronic structure of the interface between aluminum and polythiophene semiconductors. *The Journal of Chemical Physics* **1993**, *99* (1), 664–672. DOI: 10.1063/1.466217.

(216) Shen, C.; Kahn, A.; Schwartz, J., Chemical and electrical properties of interfaces between magnesium and aluminum and tris-(8-hydroxy quinoline) aluminum. *Journal of Applied Physics* **2001**, *89* (1), 449–459. DOI: 10.1063/1.1333740.

(217) Zhang, G.; Hawks, S. A.; Ngo, C.; Schelhas, L. T. *et al.*, Extensive penetration of evaporated electrode metals into fullerene films: intercalated metal nanostructures and influence on device architecture. *ACS applied materials & interfaces* **2015**, *7* (45), 25247–25258. DOI: 10.1021/acsami.5b06944.

(218) Hirose; Kahn; Aristov; Soukiassian *et al.*, Chemistry and electronic properties of metal-organic semiconductor interfaces: Al, Ti, In, Sn, Ag, and Au on PTCDA. *Physical review. B, Condensed matter* **1996**, *54* (19), 13748–13758. DOI: 10.1103/physrevb.54.13748.

(219) Hwang, J.; Wan, A.; Kahn, A., Energetics of metal–organic interfaces: New experiments and assessment of the field. *Materials Science and Engineering: R: Reports* **2009**, *64* (1-2), 1–31. DOI: 10.1016/j.mser.2008.12.001.

(220) Hill, I. G.; Rajagopal, A.; Kahn, A., Energy-level alignment at interfaces between metals and the organic semiconductor 4,4′-N,N′-dicarbazolyl-biphenyl. *Journal of Applied Physics* **1998**, *84* (6), 3236–3241. DOI: 10.1063/1.368477.

(221) Kaune, G.; Metwalli, E.; Meier, R.; Körstgens, V. *et al.*, Growth and morphology of sputtered aluminum thin films on P3HT surfaces. *ACS applied materials & interfaces* **2011**, *3* (4), 1055–1062. DOI: 10.1021/am101195m.

(222) Hellmann, T.; Das, C.; Abzieher, T.; Schwenzer, J. A. *et al.*, The electronic structure of MAPI-based perovskite solar cells: Detailed band diagram determination by photoemission spectroscopy comparing classical and inverted device stacks. *Adv. Energy Mater.* **2020**, *10* (42), 2002129. DOI: 10.1002/aenm.202002129.

(223) Kim, S.-M., Photoemission by low photon energies in organic hole transport materials. Bachelor Thesis, Technische Universität Darmstadt, Darmstadt, 2019.

(224) van Slyke, S. A.; Chen, C. H.; Tang, C. W., Organic electroluminescent devices with improved stability. *Appl. Phys. Lett.* **1996**, *69* (15), 2160–2162. DOI: 10.1063/1.117151.

(225) Lu, C.-K. and Meng, H.-F., Hole doping by molecular oxygen in organic semiconductors: Band-structure calculations. *Phys. Rev. B* **2007**, *75* (23). DOI: 10.1103/PhysRevB.75.235206.

(226) Abdou, M. S. A.; Orfino, F. P.; Son, Y.; Holdcroft, S., Interaction of oxygen with conjugated polymers: Charge transfer complex formation with poly(3-alkylthiophenes). *Journal of the American Chemical Society* **1997**, *119* (19), 4518–4524. DOI: 10.1021/ja964229j.

(227) Ogawa, S.; Naijo, T.; Kimura, Y.; Ishii, H.; Niwano, M., Photoinduced doping of organic field effect transistors studied by displacement current measurement and infrared absorption spectroscopy in multiple internal reflection geometry. *Jpn. J. Appl. Phys.* **2006**, *45* (1B), 530–533. DOI: 10.1143/JJAP.45.530.

(228) Meijer, E. J.; Detcheverry, C.; Baesjou, P. J.; van Veenendaal, E. *et al.*, Dopant density determination in disordered organic field-effect transistors. *Journal of Applied Physics* **2003**, *93* (8), 4831–4835. DOI: 10.1063/1.1559933.

(229) Robin, I. C.; Gauron, B.; Ferret, P.; Tavares, C. *et al.*, Evidence for low density of nonradiative defects in ZnO nanowires grown by metal organic vapor-phase epitaxy. *Appl. Phys. Lett.* **2007**, *91* (14), 143120. DOI: 10.1063/1.2794790.

(230) Berglund, C. N. and Spicer, W. E., Photoemission studies of copper and silver: Theory. *Phys. Rev.* **1964**, *136* (4A), A1030-A1044. DOI: 10.1103/PhysRev.136.A1030.

(231) Albota, M.; Beljonne, D.; Brédas, J. L.; Ehrlich, J. E. *et al.*, Design of organic molecules with large two-photon absorption cross sections. *Science* **1998**, *281* (5383), 1653–1656. DOI: 10.1126/science.281.5383.1653.

(232) Auger, P., The Auger effect. *Surface Science* **1975**, *48* (1), 1–8. DOI: 10.1016/0039-6028(75)90306-4.

(233) Kaiser, W. and Garrett, C. G. B., Two-Photon Excitation in $CaF_2$: $Eu^{2+}$. *Phys. Rev. Lett.* **1961**, *7* (6), 229–231. DOI: 10.1103/PhysRevLett.7.229.

(234) Pawlicki, M.; Collins, H. A.; Denning, R. G.; Anderson, H. L., Two-photon absorption and the design of two-photon dyes. *Angew. Chem. Int. Ed.* **2009**, *48* (18), 3244–3266. DOI: 10.1002/anie.200805257.

(235) Moliton, A. *Optoelectronics of Molecules and Polymers*; Springer, 2006.

(236) Schwoerer, M. and Wolf, H. C. *Organic molecular solids*; Wiley-VCH, 2008.

(237) Goushi, K.; Kwong, R.; Brown, J. J.; Sasabe, H.; Adachi, C., Triplet exciton confinement and unconfinement by adjacent hole-transport layers. *Journal of Applied Physics* **2004**, *95* (12), 7798–7802. DOI: 10.1063/1.1751232.

(238) Hertel, D.; Bässler, H.; Guentner, R.; Scherf, U., Triplet-triplet annihilation in a poly(fluorene)-derivative. *The Journal of Chemical Physics* **2001**, *115* (21), 10007–10013. DOI: 10.1063/1.1415446.

(239) Egerton, R. F. *Physical principles of electron microscopy*: *An introduction to TEM, SEM, and AEM*, Corr. 3. print; Springer, 2008.

(240) Zhu, P. F.; Zhang, Z. C.; Chen, L.; Li, R. Z. *et al.*, Ultrashort electron pulses as a four-dimensional diagnosis of plasma dynamics. *Review of Scientific Instruments* **2010**, *81* (10), 103505. DOI: 10.1063/1.3491994.

## Publications and Conference Contributions

### Publications

Grenier, S.; Bailly, A.; Ramos, A. Y.; de Santis, M.; Joly, Y.; Lorenzo, J. E.; Garaudée, S.; **Frericks, M**. *et al.,* Verwey transition in a magnetite ultrathin film by resonant X-ray scattering. *Phys. Rev. B* **2018,** 97 (10). DOI: 10.1103/PhysRevB.97.104403.

Charfi, O.; **Frericks, M.**; Cehovski, M.; Johannes, H.-H.; Kowalsky, W., Electrochemical Synthesis of Transition Metal Oxides and Polymer Layers for OPV Fabrication. *Twenty-fourth Microoptics Conference MOC2019,* November 17-20, **2019**, Toyama International Conference Center, Toyama, Japan. [Piscataway, NJ]: IEEE. DOI: 10.23919/MOC46630.2019.8982882

Wißdorf, V.; **Frericks, M.**; Tzschoppe, M.; Connor, P.; Beck, S.; Pflumm, C.; Pucci, A.; Jaegermann, W.; Mankel, E., Impedance Spectra Analysis of p-Doped Organic Thin Films by Charge Carrier Distribution Evaluation. *ACS Appl. Electron. Mater.* **2019,** 1 (10), 1994. DOI: 10.1021/acsaelm.9b00279.

Schackmar, F.; Eggers, H.; **Frericks, M.**; Richards, B. S.; Lemmer, U.; Hernandez-Sosa, G.; Paetzold, U. W., Perovskite Solar Cells with All-Inkjet-Printed Absorber and Charge Transport Layers. *Adv. Mater. Technol.* **2020**, 6 (2), 2000271. DOI: 10.1002/admt.202000271.

**Frericks, M.**; Pflumm, C.; Mankel, E.; Mayer, T.; Jaegermann, W., Space Charge Regions at Organic p-i-Homointerfaces from Advanced Modeling of In Situ-Prepared Interfaces Analyzed by Photoelectron Spectroscopy. *ACS Appl. Electron.* Mater. **2021,** 3 (3), 1211. DOI: 10.1021/acsaelm.0c01062.

Gharibzadeh, S.; Fassl, P.; Hossain, I. M.; Rohrbeck, P.; **Frericks, M.**; Schmidt, M.; Khan, M. R.; Abzieher, T. *et al.*, Two birds with one stone: dual grain-boundary and interface passivation enables >22% efficient inverted methylammonium-free perovskite solar cells. *Energy Environ. Sci.* **2021,** 14, 5875. DOI: 10.1039/D1EE01508G.

Eliwi, A. A.; Byranvand, M. M.; Fassl, P.; Khan, M. R.; Hossain, I. M.; **Frericks, M.;** Ternes, S.; Abzieher, T. *et al.,* Optimization of $SnO_2$ electron transport layer for efficient planar perovskite solar cells with very low hysteresis. *Materials Advances* **2022,** 3, 456.
DOI: 10.1039/D1MA00585E

### Conference Contributions

DPG-Spring Meeting **2018** (Berlin), *Electronic and Surface Chemical Properties of the Interface Diethyl Carbonate/Zirconia* – presentation

4th International Fall School on Organic Electronics IFSOE **2018** (Moscow region, Russia), *Electronic structure at interfaces of hole transport materials* –
best poster presentation

DPG-Spring Meeting **2019** (Regensburg), *Measuring and Modelling Electric Potential Distributions at Organic Semiconductor Interfaces* – presentation

10th International Conference on Materials for Advanced Technologies ICMAT **2019** (Singapore), *Modelling of XPS-Experiments for the Analysis of Organic Semiconductor Interfaces* – presentation

E-MRS Fall Meeting **2021** (Warsaw, Poland – online), *Measuring and Modelling Space Charge Regions at Organic p-i-Homointerfaces* – outstanding student presentation award

# Curriculum Vitae

For the protection of data privacy this section is not available.